Constrained Buckling of Variable Length Elastica

A DISSERTATION

SUBMITTED TO THE FACULTY OF THE GRADUATE SCHOOL

OF THE UNIVERSITY OF MINNESOTA

BY

Anna Liakou

IN PARTIAL FULFILLMENT OF THE REQUIREMENTS

FOR THE DEGREE OF

Doctor of Philosophy

ADVISER

Emmanuel Detournay

CO-ADVISER

Vincent Denoël

October, 2017

Acknowledgements

I would like to express my appreciation to my academic advisor Professor Emmanuel Detournay for his encouragement, guidance and for allowing me to grow as a research scientist. I'd like to thank him for participating to our long conversations and the constructive feedback, I received from him during my PhD studies. The combination of my mathematical point of view and his physical vision, was unambiguously powerful and lead to the final form of my research. I would also like to thank my co-advisor Professor Vincent Denoel for his vision on the subject and his suggestions.

Now I can admit that I am more confident on conveying my research ideas in a convincing manner, in accordance with the research community under consideration.

I would also like to thank the committee members, Professor Bojan Guzina, Professor Henryk Stolarski, and Professor Yoichiro Mori for their insightful comments, suggestions and encouragement.

My sincere gratitude is reserved for Professor Yoichiro Mori whose invaluable lectures in applied mathematics were both influential and inspirational. This allowed me to carry-on my research, and helped me broaden my knowledge and understanding, especially in the area of asymptotic and dimensional analysis.

Special thanks to the Civil, Environmental and Geo Engineering (CEGE) Department for the financial support I received throughout my studies at the U of MN. I would also like to express my sincere appreciation and thanks to the CEGE Department Head, Professor Joseph Labuz for giving me the opportunity to carry out my doctoral research in a wonderful academic environment, and for his invaluable advice and suggestions.

Words cannot express my gratitude and the unconditional support I received from my parents and my brother. It was due to their unconditional support and constant encouragement that ultimately became possible for me to see this project through to the end. I thank them for that and for a lifetime of love and care.

In addition, I would like to thank a former PhD graduate of the U of MN and this Department and a family friend, Dino Xykis, who was instrumental in convincing me to apply to the U of MN for graduate studies, and his support, encouragement, and follow-up since the beginning of my

studies. I am also indebted to my friends Eduardo and Kaixiao for being there when I needed an ear to listen, and for all the incredible time that we spent together during the graduate studies.

Abstract

The physical understanding of the response of slender elastic bodies restrained inside constraints under various loading and boundary conditions is of a great importance in engineering and medical applications. The research work presented in this thesis is especially concerned with the buckling response of an elastic rod (the elastica) subjected to unilateral constraints under axial compression. It seeks to address two main issues: (i) the conditions that lead to the onset of instability, and (ii) the factors that define the bifurcation diagram.

Two distinct classes of problems are analyzed; (i) the classical buckling problem of a constant length elastica and (ii) the insertion buckling problem of a variable length elastica. Their main difference is the generation of a configurational force at the insertion point of the sliding sleeve in the insertion problem, which is not present in the classical problem.

The thesis describes two distinct methodologies that can solve these constrained buckling problems; (1) a geometry-based method, and (2) an optimal control method.

The geometry-based method is used to analyze the post-buckling response of a weightless planar elastica subjected to unilateral constraints. The method rests on assuming a deformed shape of the elastica and on uniquely segmenting the elastica consistent with a single canonical segment (clamped-pinned). An asymptotic solution of the canonical problem is then derived and the complete solution of the constrained elastica is constructed by assembling the solution for each segment.

Nevertheless, the application of the optimal control method is more generic. It can be used to solve any constrained buckling problem under general boundary and loading conditions. Based on Hamiltonian mechanics, the optimality conditions, which constitute the Pontryagin's minimum principle, involve the minimization of the Hamiltonian with respect to the control variables, the canonical equations and the transversality conditions.

The main advantage of the optimal control method is the assumption of strong rather than weak variation of the involved variables, which leads to the additional Weierstrass necessary condition ("optimal" equilibrium state). Based on it, several factors such as the effect of the self-weight of the elastica and the clearance of the walls are investigated.

Contents

List of Tables

List of Figures

Chapter 1

Introduction

1.1 Motivation

Rods are slender elastic bodies characterized by lengths that are much greater than their diameters, $L \gg D$. They can therefore be considered as one-dimensional structures, which can experience bending, torsion, extension and shearing. This thesis is concerned with the buckling response of an elastic rod under the presence of unilateral constraints.

The foremost application of this research concerns the petroleum industry, which relies on a kilometers long elastic drillstring to transmit axial force and torque to the bit, to drill deep boreholes. The history of deformation of a rod under compression, constrained by a borehole, is complex as the derived contact conditions (discrete and/or continuous) depend on multiple factors, such as the geometry of the wellbore, the boundary conditions and the clearance between the rod and the conduit. The stability of drillstrings has been extensively investigated by a number of authors (Miller, 2014; Wicks et al., 2008; Gao and Huang, 2015), starting with the pioneering work of Lubinski (1950).

There are also medical applications to the problem of a constrained rod. The insertion of guidewire and catheters for interventional radiology procedures requires very precise understanding of their deformation behavior as any potential mistake can lead to damage of vital tissues and blood vessel walls (Alderliesten et al., 2007; Konings et al., 2003; Li et al., 2011a). In this area of research, however, the interest is limited to real-time simulations of constrained rods rather than stability analysis.

This thesis describes methodologies that can be applied to investigate the buckling response of elastic rods in the presence of rigid discrete and longitudinal obstacles. It seeks to address some important questions: (i) what are the conditions leading to the loss of stability of an elastic rod inside a rigid straight conduit and (ii) which are the factors that define the complete form of the bifurcation diagram.

The thesis explains the difficulties that arise from the presence of the unilateral constraints, first in the derivation of an equilibrium state and most importantly in the stability analysis. The reasons behind the failure of classical techniques are clarified and alternative approaches that overcome these numerical barriers are provided. In few words, the thesis suggests two distinct methodologies; (1) a geometry-based method and (2) an optimal control method. Both methodologies are novel and their application is analyzed in the following Chapters.

1.2 Classes of problems

The post-buckling analysis of constrained elastic rods under axial compression is the main concern of the thesis. A buckling problem always involves two parts: (i) derivation of a particular equilibrium state depending on the loading and the boundary conditions; and (2) stability analysis of the equilibrium state. The former part requires a first-order analysis that can be performed in a variety of ways, using analytical, semi-analytical, and numerical approaches. A novel semi-analytical geometry-based approach is suggested in Chapter 3.

To extract information regarding the stability of a particular equilibrium configuration further analysis is required. If we apply the calculus of variations, a second-order analysis should be performed. Nevertheless, this classical method involves several numerical difficulties due to the presence of unilateral constraints, as explained in detail in Chapters 2 and 4. Therefore an optimization-based stability analysis is a more appropriate choice and can provide the solution of the constrained buckling problem in a simple and elegant manner.

Through this study, we analyze two distinct classes of problems. The first class of problems involves a weightless planar unit-length elastica resting in its unstressed configuration at mid-distance between two frictionless rigid horizontal walls (see Figure1.1 a)). The left end of the elastica is fixed while the right end is constrained to move horizontally. The extremities of the elastica are either clamped at zero inclination or pinned. We seek to determine the post-buckling behavior of the elastica under the action of a predefined compressive force R (force-controlled) or an imposed relative displacement $\delta = 1 - x(1)$ at the right end (displacement-controlled). This problem is referred to as the "classical buckling problem". The graph of the compressive force in terms of the end-shortening δ is a bifurcation diagram, where every equilibrium position corresponds to a particular contact pattern (see Figure 1.2).

This problem can be slightly modified. We consider that the horizontal distance between the two supports is fixed $x(l) = 1$ and the elastica is inserted gradually from the right end. This implies that the length of the elastica is variable. Hence, in this case, we are looking for the post-buckling behavior of the elastica assuming a fixed compressive force R (force-controlled), or a predefined change of the arc-length of the elastica (displacement-controlled). This leads to a different bifurcation diagram as we derive the compressive force in terms of the change of the arc-length of the elastica. This class of problem is denoted as "insertion buckling problem" (see

Figure 1.1b)).

The above buckling problems are our main concern. Several extensions are also included. One extension includes the analysis of the post-buckling response of a spatial rather than planar elastica. Another extension involves the investigation of the weight effect in the constrained stability analysis. Detailed analysis of all examples can be found in Chapters 3-7.

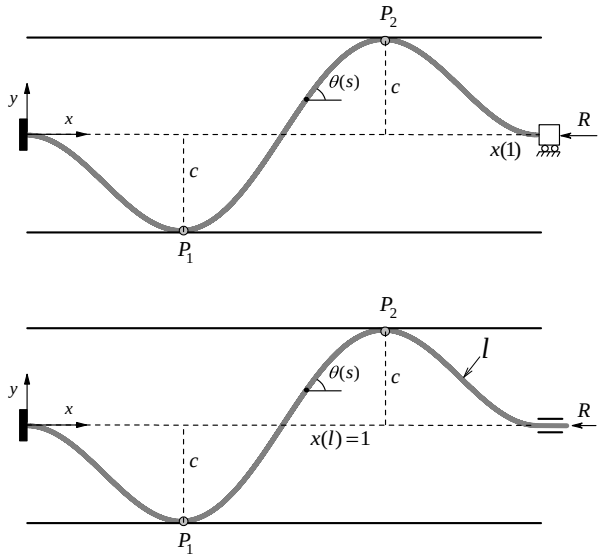

Figure 1.1: Classes of problems: a) the classical buckling problem Domokos et al. (1997); Manning and Bulman (2005) and b) the insertion buckling problem Ro et al. (2010).

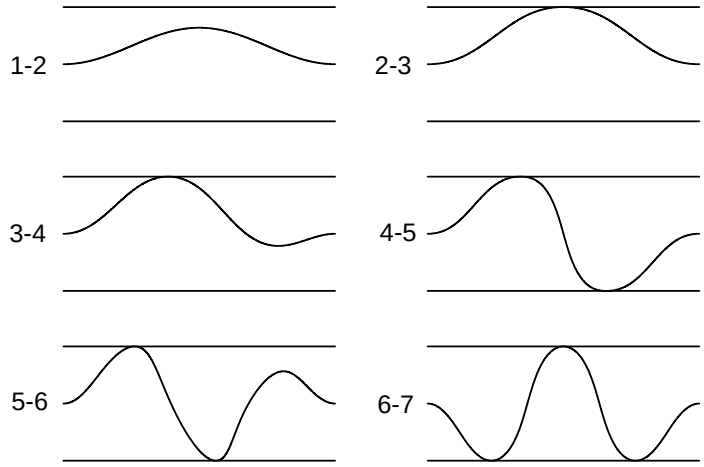

Figure 1.2: Contact patterns (equilibrium configurations) for different applied axial loads.

1.3 Outline

The thesis starts with a state-of-the-art literature review on the post-buckling analysis of elastic rods in the absence of unilateral constraints, see Chapter 2. More attention is placed on inextensible-unshearable elastic rods (planar or spatial elastica). The difference between the post-buckling response of a planar and a spatial elastica is illustrated, while several factors are also investigated. In the second part of Chapter 2, the constrained buckling problem is then analyzed by applying variational calculus. Through a concrete example, we then illustrate the limitation of the calculus of variations when unilateral constraints are present.

In Chapter 3, we study the post-buckling response of a weightless planar elastica in the presence of two symmetrically located rigid frictionless walls. Both classes of problems are analyzed. The main focus is placed on the insertion problem, where a configurational force is generated at the insertion point and leads to a reduced value of the applied force. The proposed method is a geometry-based technique. More specifically, assuming a particular buckling mode, a sequence of contact patterns of the elastica is derived by starting from an unconstrained shape and leading gradually to shapes with discrete and/or continuous contact. For every known configuration of the planar elastica, the phase portait of the inclination θ- curvature θ' is derived. Based on it, the elastica can be divided into distinct segments, which are consistent with a single canonical problem with clamped-pinned boundary conditions. Instead of using elliptic integrals, an asymptotic solution of the canonical problem is derived. After solving all distinct canonical subproblems, the complete solution is obtained by satisfying continuity properties at

the common extremities. Several bifurcation diagrams of the constrained elastica are computed by adopting this novel approach. A simple geometry-based rule for the stability analysis of every configuration state is also suggested based on the number of inflection points (i.e., $\theta' = 0$) and the nature of the contact conditions.

A novel approach for the stability analysis of constrained elastic structures is presented in Chapter 4. Inspired by Maurer and Mittelmann (1991) and Liberzon (2012), we show that a constrained buckling problem can be solved by applying an optimal control method (Berkovitz, 1961). First, we illustrate the advantage of adopting an optimal control approach rather than a calculus of variations method and their equivalence. Based on Hamiltonian mechanics, the general framework of an optimal control problem with pure-state constraints is described. This formulation is consistent with our constrained buckling problem. The optimality conditions are then derived by applying the Pontryagin's minimum principle. The available numerical methods for the solution of an optimal control problem are also described, with the main focus on the direct method.

Based on the optimal control theory, we investigate the buckling response of elastic rods constrained by frictionless rigid longitudinal obstacles in Chapters 5, 6 and 7. In particular, in Chapter 5, we compute the bifurcation diagram of a planar elastica constrained by two rigid horizontal walls. Both the classical and the insertion buckling problems are analyzed. Force-controlled and displacement-controlled conditions are studied, separately. The same buckling problems are then solved for the spatial case. The derived results are compared with previous numerical and experimental works (Manning and Bulman, 2005; Ro et al., 2010; Fang et al., 2013; Domokos et al., 1997).

Chapter 6 involves the analysis of the buckling response of a planar elastica with non-negligible self-weight (i.e., heavy elastica) constrained by either a rigid one-sided straight foundation, or two rigid horizontal walls. The one-sided foundation case is a classical problem, which was first studied by Wang (1986). A comprehensive literature review around this problem, also called the ribbon problem, is first performed. Its solution by the optimal control method is also included. Then we study the constrained stability problem with two-sided foundations. Several factors are analyzed, such as the effects of the boundary conditions, the clearance of the walls and the self-weight of the elastica.

The insertion problem for the spatial elastica is then analyzed in Chapter 7. Based on the calculus of variations, the configurational or Eshelby-like force is first computed. A concrete example is accordingly solved by applying the optimal control method, which illustrates the effect of this configurational force.

The thesis concludes with a short summary of the most remarkable results of the study. Other examples that can be solved by the geometry-based method and the optimal control method are also mentioned. The advantages and limitations of both numerical techniques when compared to other approaches are also explained.

Chapter 2

Stability Analysis of Elastica: The Calculus of Variations Method

In this Chapter, we first perform a comprehensive literature review about the buckling response of elastic rods under axial compression. The description starts with the stability analysis of an unconstrained elastic rod. Classical and novel approaches are presented. The main focus is placed on the post-buckling response of an inextensible-unshearable elastic rod, the planar or the spatial elastica. The assumption of the inextensibility and unshearability constraints is appropriate as we further investigate the buckling response of an elastic cylindrical rod with a large length/diameter ratio inside a rigid conduit with a clearance much smaller than the length of the rod. This constrained buckling problem is then studied by applying the calculus of variations. Through a concrete example, we also illustrate the limitations arising from the application of the calculus of variations in the analysis of a constrained buckling problem.

2.1 Buckling of elastic rods

The stability analysis of an inextensible and unshearable elastic rod —the elastica— is nowadays a classical problem that can be found in many books (Bigoni, 2016; Antman, 2005; Love, 2013; Timoshenko, 2009).

The equations of the elastica were first derived by J. Bernoulli (1692) for the particular case of the so-called rectangular elastica. The next important step took place in 1742 with the recognition by D. Bernoulli that the general problem of the elastica could be treated as an isoperimetric problem. This was the origin of variational calculus. Based on this pioneering idea, Euler (1744) computed a family of curves, known as Euler's elastica figures, which were then verified experimentally by Born (1906) (see (Levien, 2008) for an historical account). The

governing equation of the planar elastica is analogous to the equation of motion of a pendulum (Goss, 2008), while for the spatial case, Kirchhoff (1859) recognized that the deflection curve of the elastica is governed by the same set of differential equations as the motion of a heavy spinning top (Lazarus et al., 2013; Davies and Moon, 1993). The elastica has gained a lot of interest as it is used for the design of multiple mechanical systems from hair simulation (Spillmann and Teschner, 2007; Daviet et al., 2011) to the simulation of drill-strings in oil-drilling operations (Miller, 2014; Wicks et al., 2008; Su et al., 2013) and the animation of a locomotion (Zhou et al., 2015).

A short review of the methods used in the stability of a planar elastica is included herein. The stability analysis of an inflectional elastica is only presented as Born (1906) has shown that any elastic arc without inflection points is stable (Sachkov, 2008a,b).

Let us analyze the buckling response of a planar elastica under the action of an axial compressive load. The most classical problem is the Dirichlet-Dirichlet case (Gelfand, 2000; Liberzon, 2012; Love, 2013). The dimensionless potential energy of the elastica is given by

$$\Pi\left(\theta,\theta'\right)=\int_0^1\mathcal{F}\left(\theta,\theta'\right)ds=\frac{1}{2}\int_0^1\theta'^2\mathrm{d}s+\mathcal{Q}\int_0^1\left(\cos\theta-1\right)\mathrm{d}s \tag{2.1}$$

where $s=\sigma/L\in[0,1]$ is the normalized arc-length with L the total length of the elastica, $\theta(s)$ is the inclination angle with boundary conditions $\theta(0)=\theta(1)=0$, $\theta'(s)$ is the curvature and $\mathcal{Q}=QL^2/EI$ is the normalized axial load. The first term is the bending elastic energy, while the second term is the external work of the applied force $\mathcal{Q}$.

We assume a variation of the form $\theta(s,\varepsilon)=\theta^*(s)+\varepsilon\eta(s)$, where " $*$ " denotes the extremal variable, $\eta(s)$ is a sufficiently smooth function that vanishes at end-points $\eta(0)=\eta(1)=0$ and $0<\varepsilon\ll 1$ is an independent parameter. Based on it, the first variation of the potential energy $\delta\Pi\left(\theta,\theta'\right)=\lim_{\varepsilon\to 0}d\Pi/d\varepsilon$ can be derived as

$$\delta\Pi=\int_0^1\left\{\frac{\partial\mathcal{F}\left(\theta^*,\theta'^*\right)}{\partial\theta}\eta+\frac{\partial\mathcal{F}\left(\theta^*,\theta'^*\right)}{\partial\theta'}\eta'\right\}\mathrm{d}s \tag{2.2}$$

which after applying integration by parts becomes

$$\delta\Pi=\int_0^1\left\{\theta^{*\prime\prime}+\mathcal{Q}\sin\theta^*\right\}\eta\mathrm{d}s \tag{2.3}$$

An extremal solution is then obtained by vanishing the first variation (2.3). This equilibrium state $\theta^{*\prime\prime}+\mathcal{Q}\sin\theta^*=0$ is the Euler-Lagrange equation. Its analytical solution is given in terms of elliptic integrals.

Several studies are restricted to the first order analysis from which either the critical (linearized) buckling load is computed (i.e. first bifurcation point assuming $\sin\theta^*\approx\theta^*$) (Wang,

1997; Wang et al., 2004; Timoshenko, 2009), or a post-buckling analysis is performed (Mikata, 2007; Wang, 1997). For this problem the critical buckling load is $\mathcal{Q} = \pi^2$, which is identical to the first buckling load of a pinned-pinned elastica. This value becomes $\mathcal{Q} = 4\pi^2$, when the isoperimetric constraint $\int_0^1 \sin\theta ds = 0$ is additionally imposed.

Nevertheless the stability of an extremal solution can be determined by the second variation of the functional (2.1), which is given by

$$\delta^2 \Pi = \frac{1}{2}\int_0^1 \left\{ \frac{\partial^2 \mathcal{F}\left(\theta^*, \theta'^*\right)}{\partial\theta\partial\theta}\eta^2 + 2\frac{\partial^2 \mathcal{F}\left(\theta^*, \theta'^*\right)}{\partial\theta\partial\theta'}\eta'\eta + \frac{\partial^2 \mathcal{F}\left(\theta^*, \theta'^*\right)}{\partial\theta'\partial\theta'}\eta'^2 \right\} \mathrm{d}s \tag{2.4}$$

Let us transform (2.4) in a more convenient form. Applying an integration by parts, we get

$$\int_0^1 2\frac{\partial^2 \mathcal{F}\left(\theta^*, \theta'^*\right)}{\partial\theta\partial\theta'}\eta'\eta \mathrm{d}s = -\int_0^1 \frac{\mathrm{d}}{\mathrm{ds}}\left(\frac{\partial^2 \mathcal{F}\left(\theta^*, \theta'^*\right)}{\partial\theta\partial\theta'}\right)\eta^2 \mathrm{d}s$$

and substituting into (2.4) the following expression is obtained

$$\delta^2 \Pi = \int_0^1 \left\{ \mathrm{P(s)}\eta'^2 + \mathrm{G(s)}\eta^2 \right\} \mathrm{d}s \quad or \quad \delta^2 \Pi = \int_0^1 \left\{ -\frac{\mathrm{d}}{\mathrm{ds}}\left(\mathrm{P(s)}\eta'\right) + \mathrm{G(s)}\eta \right\} \eta \mathrm{d}s \tag{2.5}$$

where

$$P(s) = \frac{1}{2}\frac{\partial^2 \mathcal{F}\left(\theta^*, \theta'^*\right)}{\partial\theta'\partial\theta'}, \qquad G(s) = \frac{1}{2}\left(\frac{\partial^2 \mathcal{F}\left(\theta^*, \theta'^*\right)}{\partial\theta\partial\theta} - \frac{d}{ds}\left(\frac{\partial^2 \mathcal{F}\left(\theta^*, \theta'^*\right)}{\partial\theta\partial\theta'}\right)\right)$$

Hence, the second variation of the potential energy of the planar elastica becomes

$$\delta^2 \Pi = \int_0^1 \left\{ \eta'^2 - \mathcal{Q}\cos\theta^*\eta^2 \right\} \mathrm{d}s \tag{2.6}$$

A necessary condition for deriving the minimum of the functional $\Pi\left(\theta, \theta'\right)$ is the Legendre condition $P(s) \geq 0$. An extremal that satisfies the strengthened Legendre condition $P(s) > 0$ (strict inequality) is also said to be regular and it implies that θ and its variation η are of class C^2. In the above example, the strengthened Legendre condition is always satisfied as $P(s) = 1$. Nevertheless the Legendre condition is not a sufficient condition for the quadratic functional $\delta^2\Pi$ to be ≥ 0 for all admissible variations $\eta(s)$. If we satisfy $\delta^2\Pi > 0$, or $\delta^2\Pi < 0$, the corresponding extremal solution is stable, or unstable, respectively. In the case $\delta^2\Pi = 0$, higher order variation is required.

The positive definiteness of the second variation can be studied in a variety of ways; (i) considering the solution of an auxiliary Riccati equation (Gelfand, 2000; O ' Reilly and Peters, 2011), (ii) applying the conjugate point theory (Manning et al., 1998; Manning, 2009), or (iii) computing the eigensolution of an auxiliary Sturm–Liouville problem (Kuznetsov and Levyakov, 2002; Levyakov and Kuznetsov, 2010).

The oldest method in the derivation of the sign of the second variation of energy is based on a very simple mathematical idea. If the second variation of energy can be transformed to a perfect square, its sign is always non-negative (Gelfand, 2000). To make this possible, a vanishing quantity is added into (2.5)

$$\int_0^1 \frac{d}{ds}\left(w(s)\eta^2\right) ds = 0$$

where $w(s)$ is an arbitrary differentiable function. A new form of (2.5) can be accordingly obtained

$$\delta^2\Pi = \int_0^1 \left\{ P(s)\left(\eta' + \frac{w}{P(s)}\eta\right)^2 \right\} ds$$

if and only if a bounded solution of the following Riccati equation can be found

$$P\left(G + \frac{dw}{ds}\right) = w^2 \tag{2.7}$$

which, in the case of the planar elastica, is simply given by $w^2 = dw/ds - \mathcal{Q}\cos\theta^*$. The Riccati equation can be further reduced to a linear differential equation if we apply a simple change of variables. In fact, setting $w(s) = -\left(Pdu/ds\right)/u$ into (2.7), it gives

$$-\frac{d}{ds}\left(P(s)u'\right) + G(s)u = 0 \tag{2.8}$$

which is the Euler equation corresponding to the functional (2.5) with boundary conditions $u(0) = u(1) = 0$. A point $\alpha \in (0,1)$ is conjugate to the point $s = 0$ if (2.8) has a solution, which vanishes at $s = 0$ and $s = \alpha$ but it is not identically zero. If there is at least one conjugate point, the corresponding extremal solution is unstable.

In summary, the necessary and sufficient conditions for the stability of the elastica (i.e., $\delta^2 \Pi > 0$ for all admissible non-trivial variations $\eta(s)$) involve the following requirements; (i) the strengthened Legendre condition $P(s) > 0$ and (ii) the absence of the conjugate points at the interval $[0, 1]$, which can be established by solving the Euler equation, or deriving a bounded solution of the Riccati equation.

An alternative transformation of (2.4) has been suggested by Manning (2009), who applied a different type of integration by parts

$$\frac{1}{2}\int_0^1 \left\{ \frac{\partial^2 \mathcal{F}\left(\theta^*, \theta'^*\right)}{\partial\theta\partial\theta'}\eta'\eta + \frac{\partial^2 \mathcal{F}\left(\theta^*, \theta'^*\right)}{\partial\theta'\partial\theta'}\eta'^2 \right\} \mathrm{d}s =$$
$$-\int_0^1 \frac{d}{ds}\left(\frac{\partial^2 \mathcal{F}\left(\theta^*, \theta'^*\right)}{\partial\theta\partial\theta'}\eta + \frac{\partial^2 \mathcal{F}\left(\theta^*, \theta'^*\right)}{\partial\theta'\partial\theta'}\eta' \right) \eta \mathrm{d}s$$

that leads to

$$\delta^2\Pi = \int_0^1 \left\{ \mathcal{D}(s) - \frac{d}{ds}\mathcal{D}(s) \right\} \eta ds = \langle \eta, S\eta \rangle$$

where $\langle \cdot, \cdot \rangle$ denotes the L^2 inner product $\langle h, g \rangle = \int_0^1 h(s)g(s)ds$ and S is a self-adjoint operator which is a natural analogue of a Hessian matrix

$$S\eta = \mathcal{D}(s) - \frac{d}{ds}\mathcal{D}(s)$$

and

$$\mathcal{D}(s) = \frac{\partial^2 \mathcal{F}\left(\theta^*, \theta'^*\right)}{\partial\theta\partial\theta'}\eta + \frac{\partial^2 \mathcal{F}\left(\theta^*, \theta'^*\right)}{\partial\theta'\partial\theta'}\eta'$$

To deduce whether an extremal solution is stable, the spectrum of S is studied. In particular, there is a conjugate point α if we can find the solution of $S\eta = 0$ with boundary conditions $\eta(0) = \eta(\alpha) = 0$. On the other hand the absence of conjugate points implies $\langle \eta, S\eta \rangle > 0$ and thus positive definiteness of the second variation of the potential energy. For unconstrained problems, Morse (2013) showed that the Morse index corresponds exactly to the number of conjugate points. Quite recently, Manning et al. (1998)) showed that the classical index theory is also applicable to an isoperimetrically constrained problem except for Neumann-Neumann boundary conditions, where some adjustment is required (Manning, 2009).

Another methodology is to start with (2.6) and apply an integration by parts in order to get

$$\delta^2\Pi = -\int_0^1 \left\{ \eta'' + \mathcal{Q}\cos\theta^*\eta \right\} \eta \mathrm{d}s \tag{2.9}$$

For every admissible $\eta(s)$, the sign of (2.9) is studied by considering the decomposition $\eta = \sum_{i=1}^{\infty} A_i f_i$, where A_i are arbitrary coefficients, f_i are the eigenfunctions of the problem with boundary conditions $f(0) = f(1) = 0$ and λ_i are the eigenvalues that solves the following Sturm-Liouville problem

$$f'' + \lambda\mathcal{Q}\cos\theta^* f = 0 \tag{2.10}$$

For an imposed eigenvalue λ_i, the corresponding eigenfunction f_i satisfies $f_i'' + \lambda_i\mathcal{Q}\cos\theta^* f_i = 0$. If we multiply this expression by f_i and integrate from $s = 0$ to $s = 1$, we get

$$\int_0^1 \mathcal{Q}\cos\theta^* f_i^2 ds = \frac{1}{\lambda_i}\int_0^1 f_i'^2 ds$$

Taking also into account the orthogonality condition $\int_0^1 \mathcal{Q}\cos\theta^* f_i f_j ds = 0$ for $i \neq j$, we arrive

at the following expression

$$\delta^2 \Pi = \sum_{i=1}^{\infty} A_i^2 \left(1 - \frac{1}{\lambda_i}\right) \int_0^1 f_i'^2 ds$$

If all eigenvalues lie outside the interval $(0, 1)$, the second variation of energy is positive and the extremal solution becomes stable. The opposite holds if at least one eigenvalue $\lambda_i \in (0, 1)$. If there is an eigenvalue $\lambda_i = 0$, or $\lambda_i = 1$, higher variations should be evaluated to deduce whether the equilibrium state is stable. These stability criteria formulate a theorem, whose complete proof is contained in (Levyakov and Kuznetsov, 2010).

To solve (2.10), the interval $s \in [0, 1]$ is divided into m-subintervals leading to a constant step $h_i = 1/m$. For every subinterval, the solution of the second order ordinary differential equation (ODE) is a trigonometric function. For a fixed value of $\lambda \in (0, 1)$, (2.10) is solved piece-by-piece as an initial value problem. Starting from $s = 0$ and imposing the left boundary condition $f(0) = 0$ and an arbitrary value of $f'(0) = f_o^{'}$, we piecewisely compute the solution of the problem at the right end. If the boundary condition $f(1) = 0$ is satisfied, the solution is complete. Otherwise, a different assigned value λ should be chosen until convergence. If there is no eigenvalue $\lambda \in (0, 1)$ that can satisfy the boundary conditions, the corresponding extremal solution is stable. More details can be found in (Levyakov and Kuznetsov, 2010).

The stability behavior of the elastica can be also studied by taking into account the fundamentals of catastrophe theory. If we apply a spectral decomposition method (i.e., a Fourier expansion) to the first variation of the potential energy (2.3), we get a function equivalent to an algebraic equation $\lambda x - x^3 = 0$, which exhibits a pitchfork bifurcation point at $\lambda = 0$. The addition of a parameter $\alpha \neq 0$ into the algebraic equation $\alpha + \lambda x - x^3 = 0$ can be understood as an initial imperfection (e.g., initial curvature) that leads to a modification of the bifurcation diagram (see Figure 2.1) (Peterson and Manning, 2010). In this manner, we can indirectly deduce about the stability of the elastica by analyzing an equivalent algebraic equation with known stability behavior (i.e., unfolding).

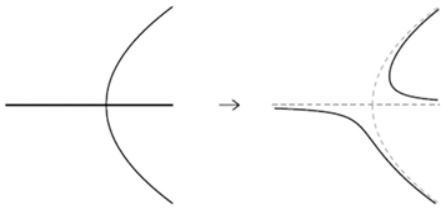

Figure 2.1: Pitchfork

As explained in detail in (Lazarus et al., 2015, 2013), an elastic structure can be also discretized by using methods, such as finite differences and finite elements. The stability, or instability of an equilibrium state can be then deduced by the positive, or negative definitiness of the Hessian matrix, respectively.

The classical problem of Dirichlet-Dirichlet boundary conditions can be further extended to any type of boundary conditions. When isoperimetric constraints are included, we cannot solve the stability problem by solving a Riccati equation and the "unfolding" is also impossible for similar reasons. The other numerical techniques, mentioned above, are applicable, but the most efficient approach, even for Newmann-Newmann boundary conditions, has been proposed recently by Levyakov and Kuznetsov (2010). A comprehensive review of the general buckling problem of a planar elastica under the action of an axial compressive load can be found in (Bigoni, 2016).

Quite recently, the sufficient conditions of the stability of the elastica have been also studied by taking into account the number of inflection points along the arc-length of the elastica. In particular, Jin and Bao (2008) investigated the case of a planar elastica clamped at one end and guided at the other end and showed that any equilibrium configuration with a number of inflection points less or equal to one is stable. This simple geometry-based criterion for the derivation of the stability of the elastica for a variety of boundary conditions has been also used by Sachkov (2007, 2008a,b), who applied a method of topology optimization.

For the stability analysis of a spatial elastica, or Kirchhoff rod model, multiple studies can be found (Maddocks, 1984; Majumdar et al., 2012; Goyal et al., 2005). For an isotropic Kirchhoff elastic rod with circular cross section, the energy functional can be written as

$$\Pi\left(\theta,\phi,\psi,\theta',\phi',\psi'\right)=\frac{1}{2}\int_0^1\left(\kappa_1^2(s)+\kappa_2^2(s)\right)ds+\frac{\gamma}{2}\int_0^1\tau^2(s)ds + \mathcal{Q}\int_0^1\cos\theta\cos\psi ds$$

where $s=\sigma/L\in[0,1]$ is the normalized arc-length with L the total length of the elastica, $\theta(s),\phi(s),\psi(s)$ are the three Euler angles and $\mathcal{Q}=QL^2/EI$ is the applied axial load. The energy functional involves the bending strain energy with curvatures $\{\kappa_1(s),\kappa_2(s)\}$, the torsional strain energy with torsion τ (Antman, 2005; Majumdar et al., 2012) and γ the ratio of torsional to bending moduli and the external work of the applied force $\mathcal{Q}$. For clamped clamped boundary conditions, we have $x(0)=y(0)=z(0)=y(1)=z(1)=0$ and $\psi(0)=\psi(1)=\theta(0)=\theta(1)=\phi(0)=\phi(1)=0$. The detailed derivation can be found in Chapter 5.

Goyal et al. (2005) studied the post-buckling behavior of a clamped-clamped spatial elastica and compared its response with the post-buckling response of a planar elastica (see Figure 2.2). The initial response of the planar elastica coincides with the minimum root of the first buckling

mode. When the applied force becomes $\mathcal{Q}/4\pi^2 \approx 2.18$, the two ends come in contact (end-shortening $\delta = 1$) and its shape is the so-called "figure-of-eight" Euler (1744). Beyond this point, a transition to the second root of the first buckling mode is obtained with a second type of "figure-of-eight". van der Heijden et al. (2003) explains that the first shape is held at the edge and requires a compression, while the second shape is held at the center and requires a tension.

As shown in Figure 2.2, the post-buckling behavior of the spatial elastica with $\gamma = 5/7$ coincides with the response of the planar elastica until $\delta = 0.559$. Beyond this value, an out-of-plane deformation initiates with gradually decreasing horizontal force, because bending strain energy is exchanged for torsional strain energy (Goyal et al., 2005). This branch continues until the rod deforms into a circular loop with $\delta = 1$ and $\mathcal{Q}/4\pi^2$ slightly tensile. An analytical description of this problem can be found in Goyal et al. (2005) and in van der Heijden et al. (2003) and is also used as a verification example in Chapter 5.

The onset of the out-of plane deformation depends on the value of γ. In particular, van der Heijden et al. (2003) computed the initiation of the out-of-plane bifurcation for clamped-clamped boundary conditions, which is represented by the following parametrized form:

$$\delta = 2\left(1 - \frac{E(k)}{K(k)}\right)$$

$$\gamma = \frac{K(k)\left[2(1-k^2)K(k) + \left(4k^2-3\right)E(k)\right]}{2(1-k^2)K(k) + (4k^2-5)\,K(k)E(k) + 3E^2(k)}$$

where the applied load is $\mathcal{Q} = 4(n+1)^2K^2(k)$, n is the buckling mode, $K(k)$ and $E(k)$ are the complete elliptic integrals of the first and the second kind and k $(0 \leq k \leq 1)$ is the elliptic modulus.

So far, we have only described the stability behavior of isotropic Kirchhoff rods. Nevertheless, factors such as anisotropy and non-uniformity can affect the buckling reponse of an elastic rod.

The effect of anisotropy in the stability behavior of an elastic rod has been investigated by Maddocks (1984), who showed that an anisotropic rod can only undergo planar buckling in either its plane of minimum, or maximum stiffness. Independently of the boundary conditions, any extremal in the plane of maximum stiffness is unstable to out of the plane perturbations. With regard to spatial stability, Maddocks (1984) deduced that equilibria of an anisotropic rod are at least as stable as those of an isotropic rod, whose constitutive relation coincides with that of the anisotropic rod in its weakest plane.

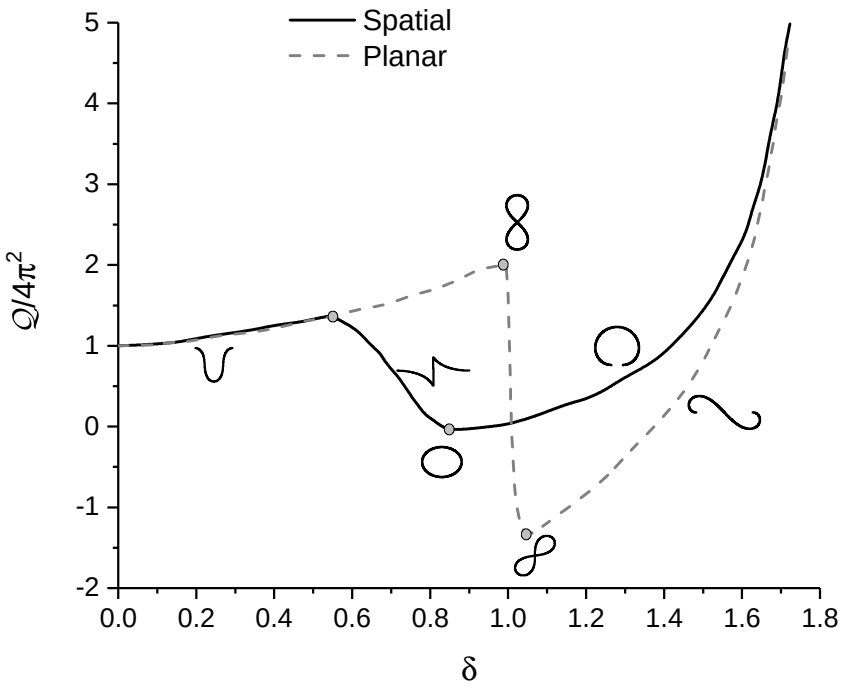

Figure 2.2: Comparison planar-spatial

On the other hand, the stability behavior of a non-uniform rod remarkably differs from a uniform elastic rod. One representative example is shown in Figure 2.3. In Figure 2.3a), the solid and dashed lines represent the first symmetrical mode of a uniform rod and its perturbed configuration, respectively. This equilibrium state is unstable, while the equilibrium configuration shown in Figure 2.3b) (dark lines denote stiffer parts than the light) is stable.

Another factor, the extensibility effect in the stability analysis of the elastica has been investigated by (Jin and Bao, 2013; Manning, 2014). Taking into account the extensibility effect, Jin and Bao (2013) showed that the first critical load is higher than Euler buckling load derived in the classical case, while their difference diminishes if the elastica becomes more slender.

The effect of a twist in the stability behavior of elastica has gained recently a lot of interest, especially in the DNA loop formations (see (Goyal et al., 2005; Manning et al., 1998; van der Heijden, 2001; Lazarus et al., 2013; Clauvelin et al., 2009)). Nevertheless the current study is restricted to the compression buckling of the elastic rods in the absence of a twist and thus the demonstration of this effect is omitted here.

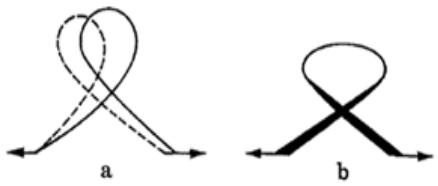

Figure 2.3: Elastic rod; (a) uniform and (b) non-uniform

2.2 Constrained buckling of elastic rods

The buckling of a slender elastic body constrained by discrete or continuous walls is a problem widely encountered in engineering and medical applications. Examples include the constrained buckling of drill-pipes in deep drilling for oil and gas (Wicks et al., 2008; Gao and Huang, 2015; Huang et al., 2015; Sun et al., 2015; Miller et al., 2015), the uplift buckling of a heavy elastic sheet from a one-sided rigid foundation in handling operations (Kolinski et al., 2009; Vella et al., 2009; Wang, 1981b, 1984b), and the insertion of a guide-wire or catheter into blood vessels (Duriez et al., 2006; Li et al., 2011b; Tang et al., 2012; Lenoir et al., 2006). There are actually two distinct classes of constrained buckling problems. The classical problem, which deals with constant length structures (Domokos and Holmes, 1993; Domokos et al., 1997; Holmes et al., 1999; Manning and Bulman, 2005), and the insertion problem, which is concerned with variable length slender objects (Denoel and Detournay, 2011; Huynen et al., 2016; Lu and Chen, 2008; Ro et al., 2010).

Due to the existence of unilateral constraints, most studies are restricted to a first-order analysis using either a discrete (i.e., finite differences or finite elements (Lazarus et al., 2015)) or a continuous (i.e., closed-form solutions (Domokos et al., 1997; Holmes et al., 1999; Chai, 1998)) formulation.

Methods that include second-order analysis have recently been proposed (Manning and Bulman, 2005; Chen and Wu, 2011; Ro et al., 2010). Manning and Bulman (2005) have reformulated Domokos et al. (1997)'s problem by replacing the unilateral constraint with a smooth potential. Furthermore, they have assessed the stability of an equilibrium state on the basis of the conjugate point theory. Ro et al. (2010) provide an Eulerian description of the problem that takes into account the variation of the contact points between the elastica and the walls during vibration. Accordingly a shooting method is applied from which natural values of the lowest frequencies can be derived, when the equilibrium configuration is stable.

Nevertheless, only preliminary studies can be found (see (Miersemann and Mittelmann, 1989;

Miersemann et al., 1986; Miersemann and Mittelmann, 1991)) that attempt to solve the constrained buckling problem by applying variational calculus. The reason behind that is the presence of the unilateral constraints, which affect the space of allowed variations. More specifically, Manning and Bulman (2005) state that " the space of allowed variations is no longer a vector space, but only a half-space". Hence, a second-order analysis cannot be easily performed, especially for the solution of the general constrained buckling problem with *a priori* unknown contact conditions.

In the following Section, we limit our attention to the constrained buckling response of a constant length elastica with known contact conditions. Based on this assumption, the unilateral constraints are transformed to bilateral constraints (i.e., closed contacts). Using the known positions of the contact points, the elastica is divided into distinct segments. For every distinct segment, we then derive the associated potential energy and its variations, while continuity requirements at the common extremities are also applied in order to get the complete solution of the problem.

The presentation starts with the simplest possible case, the presence of a single discrete contact. The general problem with a variety of discrete and continuous contacts is also demonstrated. The aim of this analysis is to illustrate the limitation of the classical calculus of variation method for the analysis of a constrained buckling problem, which can be overcome by applying an optimal control method, as explained in Chapter 4.

2.2.1 Description of the constrained buckling problem

Based on the calculus of variation, we analyze the buckling response of a weightless planar elastica of length L and uniform bending stiffness EI, which is constrained by two rigid horizontal walls. In the initial state, we assume that the elastica rests at mid-distance between two frictionless rigid horizontal walls. The left end of the elastica is fixed while the right end is constrained to move horizontally. The extremities of the elastica are either clamped at zero inclination or pinned, i.e., free to rotate.

A system of coordinates (X, Y) is defined with origin at the left extremity of the elastica and with the X-axis pointing towards the elastica right end. Relative to it, the two horizontal walls are located at $Y = +C_u$ and $Y = -C_l$. To describe an equilibrium state of the elastica, the arc-length coordinate S is introduced with its origin $S = 0$ at $X = 0$ and $Y = 0$, and the local inclination angle $\Theta(S)$ of the elastica on the X-axis. This implies that, in its unstressed configuration, the elastica is described by $\Theta(S) = 0$ with $S \in [0, L]$. The cartesian components are then derived by applying the inextensibility and unshearability constraints. In particular, a deformed configuration of the elastica $\bar{X}(S)$, $\bar{Y}(S)$ is obtained by the local inclination angle $\Theta(S)$ and the conditions $\bar{X}(0) = 0$ and $\bar{Y}(0) = 0$. In addition $\bar{Y}(L) = 0$, the imposed relative displacement is $\Delta = L - \bar{X}(L)$ and the presence of the two walls is described by the inequality

condition $-C_l \leq \bar{Y}(S) \leq C_u$ with $S \in [0, L]$.

The internal force transmitted by the elastica is denoted by $R(S)$, while its inclination is $\alpha(S)$ on the X-axis, as shown in Fig. 3.1. The functions $R(S)$ and $\alpha(S)$ become piecewise uniform whenever there is a discrete or a continuous contact with the walls. The axial force $Q = R\cos\alpha$ is uniform, however, due to the assumed frictionless nature of the contact.

Figure 3.1 illustrates a particular post-buckling configuration for an elastica with clamped ends, which touches the top wall at a single point P_1.

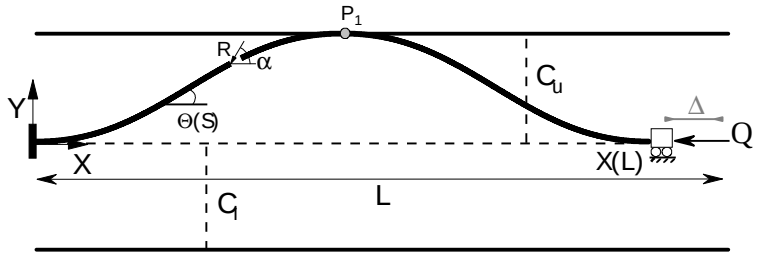

Figure 2.4: An elastica constrained by two rigid horizontal walls, which are symmetrically located with respect to the centerline. The left end is fixed while the right end is clamped. Sliding is allowed along the horizontal axis.

Scaling follows from adopting L as length scale and EI/L^2 as force scale;

$$s = \frac{S}{L}, \quad x = \frac{X}{L}, \quad y = \frac{Y}{L}, \quad \delta = \frac{\Delta}{L}, \quad c_{u,l} = \frac{C_{u,l}}{L}, \quad \mathcal{R} = \frac{RL^2}{EI}, \quad \mathcal{Q} = \frac{QL^2}{EI} \tag{2.11}$$

The inextensibility and unshearability constraints are then given by $\partial\bar{x}(s)/\partial s = \cos\theta(s)$ and $\partial\bar{y}(s)/\partial s = \sin\theta(s)$. The cartesian components are accordingly derived by imposing the boundary conditions $\bar{x}(0) = \bar{y}(0) = 0$, leading to

$$\bar{x}(s) = \int_0^s \cos\theta \mathrm{d}\xi, \qquad \bar{y}(s) = \int_0^s \sin\theta \mathrm{d}\xi \tag{2.12}$$

Stability analysis of the elastica for a single discrete contact

The potential energy of the elastica involves its bending energy

$$\mathcal{U} = \frac{1}{2}\int_0^1 \theta'^2(s) ds \tag{2.13}$$

under the presence of the equality and inequality constraints

$$\begin{array}{c} \int_0^s \sin\theta d\zeta - c_u \leq 0 \\ -\int_0^s \sin\theta d\zeta + c_l \leq 0 \\ \int_0^1 \sin\theta ds = 0 \end{array} \tag{2.14}$$

while $\theta(0) = \theta(1) = 0$, $\theta'(0) = \theta'(1) = 0$ denote the clamped-clamped and pinned-pinned boundary conditions, respectively. There are two distinct loading conditions; (1) force-controlled conditions, where the axial compressive force $\mathcal{Q}$ is predefined and (2) displacement-controlled conditons, where an axial distance between the supports is imposed. The potential energy also involves

$$\mathcal{Q}\left(\int_0^\ell \cos\theta(s) - 1\right) ds$$

which is the external work of the axial compressive force $\mathcal{Q}$ for force-controlled loading conditions. On the other hand, for displacement-controlled loading conditions, the axial force $\mathcal{Q}$ plays the role of a Lagrange multiplier for the associated bilateral constraint, which is the imposed axial distance between the extremities of the elastica.

To study the stability behavior of the constrained elastica, we assume that the positions of the discrete, or continuous contacts are known. To better explain the procedure, let us first investigate the simple case of a single discrete contact at $s = \ell_1$ with the upper wall (see Figure 3.1). This means that we get the following bilateral constraint

$$\int_0^{\ell_1} \sin\theta d\zeta - c_u = 0 \tag{2.15}$$

while the other inequality constraint (2.14) ii) is inactive. Based on this discrete contact, the elastica can be divided into two distinct segments with inclination angles $\theta_1(s_1)$ for $s_1 \in [0, \ell_1]$ and $\theta_2(s_2)$ for $s_2 \in [\ell_1, 1]$, respectively. Hence, the potential energy can be splitted into two parts;

$$\Pi(\theta_1, \theta_1^{'}, \theta_2, \theta_2^{'}) = \int_0^{\ell_1} \mathcal{F}_1(\theta_1, \theta_1^{'})\mathrm{d}s_1 + \int_{\ell_1}^1 \mathcal{F}_2(\theta_2, \theta_2^{'})\mathrm{d}s_2 \tag{2.16}$$

where

$$\begin{aligned} \int_0^{\ell_1} \mathcal{F}_1(\theta_1, \theta_1^{'})\mathrm{d}s_1 &= \frac{1}{2}\int_0^{\ell_1} \left(\theta_1^{'}\right)^2 \mathrm{d}s_1 \\ &\quad + \mathcal{Q}\left\{\int_0^{\ell_1} \cos\theta_1 \mathrm{d}s_1 - \ell_1\right\} \end{aligned}$$

$$+\mu_1 \left\{ \int_0^{\ell_1} \sin\theta_1 \mathrm{d}s_1 - c_u \right\} \tag{2.17}$$

$$\begin{aligned} \int_{\ell_1}^1 \mathcal{F}_2(\theta_2, \theta_2^{'}) \mathrm{d}s_2 \quad &= \quad \frac{1}{2} \int_{\ell_1}^1 \left(\theta_2^{'}\right)^2 \mathrm{d}s_2 \\ &\quad +\mathcal{Q} \left\{ \int_0^1 \cos\theta_2 \mathrm{d}s_2 - (1-\ell_1) \right\} \\ &\quad +\mu_2 \left\{ \int_{\ell_1}^1 \sin\theta_2 \mathrm{d}s + c_u \right\} \end{aligned} \tag{2.18}$$

are the potential energies of the two distinct segments and μ_1, μ_2 are the Lagrange multipliers associated with the bilateral constraints, derived by combining (2.14)(iii) with (2.15).

To perform a stability analysis, a weak variation of the involved variables is assumed, which is consistent with the 1-norm;

$$\|\chi\|_1 = \max_{0\leq s\leq 1} |\chi(s)| + \max_{0\leq s\leq 1} |\chi'(s)| \tag{2.19}$$

where $\chi : [0,1] \to \mathbb{R}$ is some arbitrary variable. A variation of the position of the contact point $\ell_1 + \varepsilon\gamma$ is also assumed. In this manner, the variations of the involved variables can be written as

$$\theta_i(s_i, \varepsilon) = \theta_i^*(s_i) + \varepsilon\eta_i(s_i), \qquad i = 1, 2 \tag{2.20}$$

$$\mathcal{Q} = \mathcal{Q}^* + \varepsilon\bar{\mathcal{Q}} \tag{2.21}$$

$$\mu_i = \mu_i^* + \varepsilon\bar{\mu}_i, \qquad i = 1, 2 \tag{2.22}$$

where $\theta_i^*(s_i)$, $\mathcal{Q}^*$, μ_i^* are the extremal values of the inclination angles, the axial compressive load and the Lagrange multipliers, respectively, while their corresponding variations are $\eta_i(s)$, $\bar{\mathcal{Q}}$ and $\bar{\mu}_i$ and $\varepsilon \ll 1$ is a positive parameter.

The continuity at the discrete contact is given by

$$\theta_1(\ell_1 + \varepsilon\gamma, \varepsilon) = \theta_2(\ell_1 + \varepsilon\gamma, \varepsilon) \tag{2.23}$$

which leads to

$$\theta_1^*(\ell_1 + \varepsilon\gamma) + \varepsilon\eta_1(\ell_1 + \varepsilon\gamma) = \theta_1^*(\ell_1 + \varepsilon\gamma) + \varepsilon\eta_1(\ell_1 + \varepsilon\gamma) = 0 \tag{2.24}$$

using (2.20). Taking the first and second derivatives of (2.24) with respect to ε and setting

$\varepsilon \to 0$, we get the following compatibility equations

$$\gamma\theta_1^{*'}(\ell_1) + \eta_1(\ell_1) = \gamma\theta_2^{*'}(\ell_1) + \eta_2(\ell_1) = 0 \tag{2.25}$$

$$\gamma^2\theta_1^{*''}(\ell_1) + 2\gamma\eta_1'(\ell_1) = \gamma^2\theta_2^{*''}(\ell_1) + 2\gamma\eta_2'(\ell_1) \tag{2.26}$$

where the first derivative is zero in order to satisfy the boundary condition at the discrete contact (i.e., zero inclination angle) after its variation.

Replacing ℓ_1 by $\ell_1 + \varepsilon\gamma$ and substituting (2.20-2.22) into (2.16), the potential energy becomes a function of ε. The first variation of the potential energy is then obtained by utilizing the following derivation

$$\delta\Pi(\theta_1, \theta_1^{'}, \theta_2, \theta_2^{'}) = \lim_{\varepsilon\to 0}\frac{\mathrm{d}\Pi}{\mathrm{d}\varepsilon} \tag{2.27}$$

Based on the Leibniz rule, the first variation of (2.17) for the two distinct segments is first obtained

$$\begin{aligned}\delta\int_0^{\ell_1+\varepsilon\gamma}\mathcal{F}_1(\theta_1,\theta_1^{'})\mathrm{d}s_1 = &\int_0^{\ell_1}\left[-\theta_1^{*''} - \mathcal{Q}^*\sin\theta_1^* + \mu_1^*\cos\theta_1^*\right]\eta_1 ds_1\\ &+ \theta_1^{*'}(\ell_1)\eta_1(\ell_1) - \theta_1^{*'}(\ell_o)\eta_1(\ell_o)\\ &+ \gamma\mathcal{F}_1\left(\theta_1^*(\ell_1), \theta_1^{*'}(\ell_1)\right) - \gamma\mathcal{Q}^*\\ &+ \bar{\mathcal{Q}}\left\{\int_0^{\ell_1}\cos\theta_1^*\mathrm{d}s_1 - \ell_1\right\}\\ &+ \bar{\mu}_1\left\{\int_0^{\ell_1}\sin\theta_1^*\mathrm{d}s_1 - c_u\right\}\end{aligned} \tag{2.28}$$

$$\begin{aligned}\delta\int_{\ell_1+\varepsilon\gamma}^1\mathcal{F}_2(\theta_2,\theta_2^{'})\mathrm{d}s_2 = &\int_{\ell_1}^1\left[-\theta_2^{*''} - \mathcal{Q}^*\sin\theta_2^* + \mu_2^*\cos\theta_2^*\right]\eta_2\mathrm{d}s_2\\ &+ \theta_2^{*'}(\ell_2)\eta_2(\ell_2) - \theta_2^{*'}(\ell_1)\eta_2(\ell_1)\\ &- \gamma\mathcal{F}_2\left(\theta_2^*(\ell_1), \theta_2^{*'}(\ell_1)\right) + \gamma\mathcal{Q}^*\\ &+ \bar{\mathcal{Q}}\left\{\int_{\ell_1}^1\cos\theta_2^*\mathrm{d}s - (\ell_2 - \ell_1)\right\}\\ &+ \bar{\mu}_2\left\{\int_{\ell_1}^1\sin\theta_2^*\mathrm{d}s + c_u\right\}\end{aligned} \tag{2.29}$$

where $\ell_o = 0$ and $\ell_2 = 1$ and leads to the following final form

$$\begin{aligned}\delta\Pi(\theta_1,\theta_1^{'},\theta_2,\theta_2^{'}) &= \sum_{i=1}^{2}\int_{\ell_{i-1}}^{\ell_i}\left[-\theta_i^{*''}-\mathcal{Q}^*\sin\theta_i^*+\mu_i^*\cos\theta_i^*\right]\eta_i \mathrm{d}s_i \\ &+\sum_{i=1}^{2}(-1)^{i+1}\gamma\mathcal{F}_i\left(\theta_i^*(\ell_1),\theta_i^{*'}(\ell_1)\right) \\ &+\sum_{i=1}^{2}\left[\eta_i\left(\ell_i\right)\theta_i^{*'}(\ell_i)-\eta_i\left(\ell_{i-1}\right)\theta_i^{*'}(\ell_{i-1})\right] \\ &+\sum_{i=1}^{2}\bar{\mathcal{Q}}\left\{\int_{\ell_{i-1}}^{\ell_i}\cos\theta_i^*\mathrm{d}s_i-(\ell_i-\ell_{i-1})\right\} \\ &+\sum_{i=1}^{2}\bar{\mu}_i\left\{\int_{\ell_{i-1}}^{\ell_i}\sin\theta_i^*\mathrm{d}s_i+(-1)^i c_u\right\} \end{aligned} \tag{2.30}$$

The additional compatibility requirements at the discrete contact involve the Weierstrass corner conditions, which are given by

$$\begin{aligned}\frac{\partial\mathcal{F}_1}{\partial\theta'}\left(\theta_1^*(\ell_1),\theta_1^{*'}(\ell_1)\right)=\frac{\partial\mathcal{F}_2}{\partial\theta'}\left(\theta_2^*(\ell_1),\theta_2^{*'}(\ell_1)\right)\Rightarrow \\ \theta_1^{*'}(\ell_1)=\theta_2^{*'}(\ell_1)\end{aligned} \tag{2.31}$$

$$\begin{aligned}&\theta_1^{*'}(\ell_1)\frac{\partial\mathcal{F}_1}{\partial\theta'}\left(\theta_1^*(\ell_1),\theta_1^{*'}(\ell_1)\right)-\mathcal{F}_1\left(\theta_1^*(\ell_1),\theta_1^{*'}(\ell_1)\right)= \\ &\theta_2^{*'}(\ell_1)\frac{\partial\mathcal{F}_2}{\partial\theta'}\left(\theta_2^*(\ell_1),\theta_2^{*'}(\ell_1)\right)-\mathcal{F}_2\left(\theta_2^*(\ell_1),\theta_2^{*'}(\ell_1)\right)\end{aligned} \tag{2.32}$$

Equations (2.31)-(2.32) are automatically satisfied as the inclination angles and the curvatures are continuous at the contact point, $\theta_1^*(\ell_1) = \theta_2^*(\ell_1)$ and $\theta_1^{*'}(\ell_1) = \theta_2^{*'}(\ell_1)$. This implies that the second term of (2.30) vanishes. Then by vanishing the first variation of the potential energy $\delta\Pi = 0$, the equilibrium state of the elastica is derived;

$$\theta_i^{*''}+\mathcal{Q}^*\sin\theta_i^*-\mu_i^*\cos\theta_i^*=0,\quad i=1,2 \tag{2.33}$$

with boundary conditions

$$\eta_i\left(\ell_{i-1}\right)\theta_i^{*'}(\ell_{i-1})=0,\quad i=1,2 \tag{2.34}$$

$$\eta_i\left(\ell_i\right)\theta_i^{*'}(\ell_i)=0,\quad i=1,2 \tag{2.35}$$

and the following additional requirements for the bilateral constraints

$$\bar{\mathcal{Q}}\left\{\int_{\ell_{i-1}}^{\ell_i}\cos\theta_i^* ds_i-(\ell_i-\ell_{i-1})\right\}=0,\quad i=1,2 \tag{2.36}$$

$$\bar{\mu}_i\left\{\int_{\ell_{i-1}}^{\ell_i}\sin\theta_i^* ds_i+(-1)^i c_u\right\}=0\quad i=1,2 \tag{2.37}$$

For force-controlled loading conditions, the axial compressive force is fixed $\bar{\mathcal{Q}}=0$, while for displacement-controlled conditions, the associated isoperimetric constraint remains unchanged. On the other hand, the bilateral constraint related to the vertical distance of the extremities of every discrete segment should be always satisfied. This implies a non-vanishing variation of the Lagrange multiplier $\bar{\mu}_i$, except the special case, where the elastica first touches one of the walls (i.e., no shear force is present).

Combining (2.25) with (2.34-2.35), there are two potential boundary conditions; (1) constant position of the contact point $\gamma=0$, which leads to $\eta_1(\ell_1)=\eta_2(\ell_1)=0$ and (2) change of the position of the contact point $\gamma\neq 0$ that gives $\eta_1(\ell_1)=\eta_2(\ell_1)=\theta_1^{*'}(\ell_1)=\theta_2^{*'}(\ell_1)=0$. The derived boundary conditions imply that variation of a contact point can be assumed only if a continuous contact is present. In other words, configurations with variable positions of discrete contacts cannot be studied by following this derivation.

To deduce about the stability behavior of a particular equilibrium state of the elastica, the second variation of the potential energy is required, which is denoted as

$$\delta^2\Pi(\theta_1,\theta_1^{'},\theta_2,\theta_2^{'})=\lim_{\varepsilon\to 0}\frac{\mathrm{d}^2\Pi}{\mathrm{d}\varepsilon^2} \tag{2.38}$$

and involves the following two parts

$$\begin{aligned}\delta^2\int_0^{\ell_1+\varepsilon\alpha}\mathcal{F}_1(\theta_1,\theta_1^{'})\mathrm{d}s=&\int_0^{\ell_1}\left[-\eta_1^{''}-\mathcal{Q}^*\cos\theta_1^*\eta_1-\mu_1^*\sin\theta_1^*\eta_1\right]\eta_1\mathrm{d}s_1\\&+\left[\eta_1(\ell_1)\,\eta_1^{'}(\ell_1)-\eta_1(\ell_o)\,\eta_1^{'}(\ell_o)\right]\\&+\gamma\theta_1^{*'}(\ell_1)\left\{\gamma\theta_1^{*''}(\ell_1)+2\eta_1^{'}(\ell_1)\right\}\\&+\gamma\left[-\mathcal{Q}^*\sin\theta_1^*(\ell_1)+\mu_1^*\cos\theta_1^*(\ell_1)\right]\left\{\gamma\theta_1^{*'}(\ell_1)+2\eta_1(\ell_1)\right\}\\&+2\bar{\mathcal{Q}}\left[-\int_0^{\ell_1}\sin\theta_1^*\eta_1\mathrm{d}s_1-\gamma\left(1-\cos\theta_1^*(\ell_1)\right)\right]\\&+2\bar{\mu}_1\left[\int_0^{\ell_1}\cos\theta_1^*\eta_1\mathrm{d}s_1+\gamma\sin\theta_1^*(\ell_1)\right]\end{aligned}$$

$$\begin{aligned}\delta^2\int_{\ell_1+\varepsilon\alpha}^{\ell_2}\mathcal{F}_2(\theta_2,\theta_2^{'})\mathrm{d}s = &\int_{\ell_1}^{\ell_2}\left[-\eta_2^{''}-\mathcal{Q}^*\cos\theta_2^*\eta_2-\mu_2^*\sin\theta_2^*\eta_2\right]\eta_2\mathrm{d}s_2\\ &+\left[\eta_2\left(\ell_2\right)\eta_2^{'}(\ell_2)-\eta_2\left(\ell_1\right)\eta_2^{'}(\ell_1)\right]\\ &-\gamma\theta_2^{*^{'}}(\ell_1)\left\{\gamma\theta_2^{*^{''}}(\ell_1)+2\eta_2^{\prime}(\ell_1)\right\}\\ &-\gamma\left[-\mathcal{Q}^*\sin\theta_2^*(\ell_1)+\mu_2^*\cos\theta_2^*(\ell_1)\right]\left\{\gamma\theta_2^{*^{'}}(\ell_1)+2\eta_2(\ell_1)\right\}\\ &+2\bar{\mathcal{Q}}\left[-\int_{\ell_1}^{\ell_2}\sin\theta_2^*\eta_2\mathrm{d}s_2+\gamma\left(1-\cos\theta_2^*\left(\ell_1\right)\right)\right]\\ &+2\bar{\mu}_2\left[\int_{\ell_1}^{\ell_2}\cos\theta_2^*\eta_2\mathrm{d}s_1-\gamma\sin\theta_2^*(\ell_1)\right]\end{aligned}$$

Considering $\theta_1^*\left(\ell_1\right)=\theta_2^*\left(\ell_1\right)=0$, $\gamma\theta_1^{*^{'}}(\ell_1)=\gamma\theta_2^{*^{'}}(\ell_1)=0$ and $\eta_1(\ell_1)=\eta_2(\ell_1)=0$, the second variation of energy (2.38) takes the following form

$$\begin{aligned}\delta^2\Pi(\theta_1,\theta_1^{'},\theta_2,\theta_2^{'}) &= \sum_{i=1}^{2}\int_{\ell_{i-1}}^{\ell_i}\left[-\eta_i^{''}-\mathcal{Q}^*\cos\theta_i^*\eta_i-\mu_i^*\sin\theta_i^*\eta_i\right]\eta_i\mathrm{d}s_i\\ &+\sum_{i=1}^{2}\left[\eta_i\left(\ell_i\right)\eta_i^{'}(\ell_i)-\eta_i\left(\ell_{i-1}\right)\eta_i^{'}(\ell_{i-1})\right]\\ &-2\sum_{i=1}^{2}\bar{\mathcal{Q}}\int_{\ell_{i-1}}^{\ell_i}\sin\theta_i^*\eta_{\mathrm{i}}\mathrm{d}s_i\\ &+2\sum_{i=1}^{2}\bar{\mu}_i\int_{\ell_{i-1}}^{\ell_i}\cos\theta_i^*\eta_{\mathrm{i}}\mathrm{d}s_i \qquad (2.39)\end{aligned}$$

which becomes

$$\delta^2\Pi(\theta_1,\theta_1^{'},\theta_2,\theta_2^{'})=\sum_{i=1}^{2}\int_{\ell_{i-1}}^{\ell_i}\left[-\eta_i^{''}-\mathcal{Q}^*\cos\theta_i^*\eta_i-\mu_i^*\sin\theta_i^*\eta_i\right]\eta_i\mathrm{d}s_i \qquad (2.40)$$

under the following variations of the boundary conditions and the bilateral constraints

$$\eta_i(\ell_{i-1})\eta_i^{\prime}(\ell_{i-1})=0,\quad i=1,2 \qquad (2.41)$$

$$\eta_i(\ell_i)\eta_i^{\prime}(\ell_i)=0,\quad i=1,2 \qquad (2.42)$$

$$\bar{\mathcal{Q}}\int_{\ell_{i-1}}^{\ell_i}\sin\theta_i^*\eta_{\mathrm{i}}\mathrm{d}s_i=0,\quad i=1,2 \qquad (2.43)$$

$$\bar{\mu}_i\int_{\ell_{i-1}}^{\ell_i}\cos\theta_i^*\eta_{\mathrm{i}}\mathrm{d}s_i=0,\quad i=1,2 \qquad (2.44)$$

The sign of the second variation of energy (2.40) determines the stability of an equilibrium state of the elastica (a positive sign implies a stable solution).

Stability analysis of the elastica for a multiple number of contacts

If the elastica comes in contact with the wall at $\mathcal{N}$ contact points (i.e., discrete contacts and/or entry and exit points of continuous contacts), we divide the elastica into $\mathcal{N}+1$ segments. The start and end segments (i.e., $\{1\}$ and $\{\mathcal{N}+1\}$) involve a contact point and a pinned, or clamped end, depending on the boundary conditions of the elastica. The intermediate segments always involve two contact points with one of the walls, or a combination of them.

Following the above approach, we can generalize the expressions for the first and second variations of the potential energy. By vanishing the first variation of the total potential energy of the elastica, the equilibrium configurations can be written as

$$\theta_i^{*''} + \mathcal{Q}^* \sin\theta_i^* - \mu_i^* \cos\theta_i^* = 0, \quad i = 1, \mathcal{N}+1 \tag{2.45}$$

under the boundary conditions and the bilateral constraints

$$\eta_i\left(\ell_{i-1}\right)\theta_i^{*'}\left(\ell_{i-1}\right) = 0, \quad i = 1, \mathcal{N}+1 \tag{2.46}$$

$$\eta_i\left(\ell_{i}\right)\theta_i^{*'}\left(\ell_{i}\right) = 0, \quad i = 1, \mathcal{N}+1 \tag{2.47}$$

$$\bar{\mathcal{Q}}\left\{\int_{\ell_{i-1}}^{\ell_i} \cos\theta_i^* \mathrm{d}s - \left(\ell_i - \ell_{i-1}\right)\right\} = 0, \quad i = 1, \mathcal{N}+1 \tag{2.48}$$

$$\bar{\mu}_i\left\{\int_{\ell_{i-1}}^{\ell_i} \sin\theta_i^* \mathrm{d}s \pm \left(\beta_u c_u \pm \beta_l c_l\right)\right\} = 0, \quad i = 1, \mathcal{N}+1 \tag{2.49}$$

where $c = c_u$, or $c = c_l$ depending on the contact conditions, while $\beta_u = \{-1, 0, 1\}$, $\beta_l = \{-1, 0, 1\}$. For instance, if there is a segment with its ends in contact with the same wall, $\beta_u = \beta_l = 0$.

Similarly to (2.40), the second variation of the potential energy of the elastica is given by

$$\delta^2\Pi = \sum_{i=1}^{\mathcal{N}+1} \int_{\ell_{i-1}}^{\ell_i} \left[-\eta_i^{''} - \mathcal{Q}^* \cos\theta_i^* \eta_i - \mu_i^* \sin\theta_i^* \eta_i\right] \eta_i \mathrm{d}s_i \tag{2.50}$$

with variations of the boundary conditions and the bilateral constraints

$$\eta_i(\ell_{i-1})\eta_i'(\ell_{i-1}) = 0, \quad i = 1, \mathcal{N}+1 \tag{2.51}$$

$$\eta_i(\ell_i)\eta_i'(\ell_i) = 0, \qquad i = 1, \mathcal{N}+1 \tag{2.52}$$

$$\bar{\mathcal{Q}} \int_{\ell_{i-1}}^{\ell_i} \sin\theta_i^* \eta_{\mathrm{i}} \mathrm{d}s_i = 0, \quad i = 1, \mathcal{N}+1 \tag{2.53}$$

$$\bar{\mu}_i \int_{l_{i-1}}^{l_i} \cos\theta_i^* \eta_{\mathrm{i}} \mathrm{d}s_i = 0, \quad i = 1, \mathcal{N}+1 \tag{2.54}$$

Limitation of the calculus of variation

To perform the stability analysis of every distinct segment, we can derive the eigensolution of an associated Sturm-Liouville problem, as explained by (Levyakov and Kuznetsov, 2010). O Reilly and Tresierras (2011) explains that if at least one segment is unstable, the elastica loses stability as a whole. This stability criterion is usually valid for force-controlled conditions. Nevertheless, for displacement-controlled conditions, there are cases, where a "stable segment" stabilizes the instability of another neighboring "unstable segment", leading to a final stable solution. This phenomenon is met in asymmetrical configurations, or symmetrical configurations, such as the "free-standing fold".

Nevertheless, these configurations cannot be studied by applying the above procedure as a variation of the contact position should be included, which violates (2.25). This is the main limitation of the calculus of variation. We cannot also avoid the analysis of these particular configurations for two main reasons; (1) the onset of them typically coincides with critical points, such as bifurcation points or limit points and (2) their analysis can make clear the distinction between force- and displacement-controlled loading conditions.

The above limitation becomes even more evident, if we analyze the stability behavior of an elastica with a non-negligible self-weight, where the greater number of the equilibrium states is asymmetrical, or symmetrical with variable positions of the contact points (see Chapter 6).

Chapter 3

Constrained Buckling of Variable Length Elastica: Solution by Geometrical Segmentation

The main focus of this Chapter is the development of a method to calculate the equilibrium states of a variable-length elastica (the constant length elastica being a particular case), which is loaded along its axis and constrained by rigid longitudinal obstacles.

Numerous papers have been published on the unconstrained buckling of thin elastic structures (Wang et al., 2004; Timoshenko, 2009; Bigoni, 2016) in contrast to the relatively small number of studies concerned with constrained buckling. The unconstrained deflection of a variable-length elastica has also been the subject of a few recent investigations (Humer and Irschik, 2011; Pulngern et al., 2013; Thongyothee and Chucheepsakul, 2015; Chucheepsakul et al., 2003; Athisakul et al., 2011). The *a priori* unknown length of an inserted elastica loaded by a compressive force introduces an additional challenge compared to the classical problem of a constant length elastica and several methods have been proposed to address this specific issue (Chucheepsakul et al., 1995; Chucheepsakul and Monprapussorn, 2000; Chucheepsakul and Phungpaigram, 2004; Humer and Irschik, 2009, 2011). Furthermore, a configurational or Eshelby-like force at the insertion point, not present in the classical problem, needs to be accounted as recently discovered (Bosi et al., 2015; Bigoni et al., 2015).

In the constrained buckling problem, the unknown position and nature of the contact conditions add new numerical difficulties. Discrete methods have been proposed to compute the

deformed configuration of a constant length elastica with unilateral constraints (Lazarus et al., 2015; Klarbring, 1988; Schulz and Pellegrino, 2001), but these methods face numerical issues if weakly active constraints are present, or when the contact patterns evolve discontinuously.

Therefore, most methods of solution are based on a continuous formulation of the constrained elastica problem. One approach is to solve the constrained problem analytically using elliptic integrals (Vaillette and Adams, 1983; Domokos et al., 1997), or assuming small displacements (Chai, 1998). An alternative to the classical continuation method is the simplex method, typically used to solve linear programming problems. In combination with analytical solutions, the simplex method makes it possible to compute all possible equilibrium states in a given domain, the adjacent branches and even isolated solutions (Domokos and Holmes, 1993; Domokos et al., 1997; Holmes et al., 1999).

These methods are restricted, however, for solving the constrained buckling of a constant length elastica. Approaches specifically developed for simulating the insertion of an elastica inside a conduit have been proposed by a few authors (Huynen et al., 2016; Denoel and Detournay, 2011; Ro et al., 2010). In particular, an Eulerian formulation of the constrained planar elastica in combination with a shooting method has been suggested (Huynen et al., 2016; Denoel and Detournay, 2011). The Eulerian formulation provides a simple definition of the distance between the elastica and an obstacle when compared to a Lagrangian-based method, but the application of this technique is not straightforward. In addition the shooting method requires an accurate guess of the involved variables, which is necessary for the solution of the initial value problem, and a precise definition of the contact pattern. The same numerical issues are also present in a similar technique suggested by Ro et al. (2010).

This Chapter proposes a novel technique to calculate the equilibrium configurations of a planar weightless elastica subjected to unilateral constraints that overcomes the above numerical difficulties and in particular the issue related to the *a priori* unknown length of the elastica in insertion problems under force control. The method is contingent on assuming a deformed shape of the elastica that is consistent with an assumed buckling mode and given unilateral constraints. The key concept, which can be traced to Euler (Love, 2013) and Domokos et al. (1997), is to divide the elastica into segments, each one being characterized by a zero curvature at one end. The segmentation takes into account the contact constraints, the number of inflection points, and the boundary conditions of the elastica for a specific buckling mode. This technique enables the construction of the elastica solution, by assembling the solution for each segment, each one being a particular realization of the same canonical problem. The method further depends on deriving a closed-form asymptotic solution for the canonical problem using a perturbation technique. The solution assembly entails solving a nonlinear system of equations that embodies continuity conditions between the segments and the contact constraints.

The proposed approach is first validated by computing the post-buckling response of a pinned-pinned elastica constrained by two symmetrically located walls, a particular instance

of the class of classical problems. The solution is shown to be in excellent agreement with previously published numerical and experimental results (Domokos et al., 1997). Also, a detailed comparison of the asymptotic solution of the canonical problem — the building block of the segmentation technique — with the closed-form solution based on elliptic integrals and an asymptotic expansion of this solution is documented. This comparison shows that the proposed asymptotic solution is the most efficient within the framework of the segmentation technique and at the same time is accurate enough for solving the constrained buckling problem for a significant range of clearances.

The proposed approach is then applied to solve related constant and variable length elastica problems. The similarities and differences between the two classes of problems are discussed. For small clearances and displacements, these two problems are comparable. Nonetheless, the development of a configurational force in the insertion problem leads to a reduction of the external axial compressive force. Other factors such as the effect of the boundary conditions and the loading conditions (i.e., force- or displacement-controlled conditions) are also investigated for the insertion problem.

Special attention is placed on the bifurcation points, when either the bending moment at a discrete contact vanishes, or a continuous contact with the wall buckles as the first buckling mode of a clamped-clamped elastica. The first case is observed in the constrained buckling problem of a clamped-clamped or clamped-pinned elastica with symmetrical walls, while the second case is obtained in the classical buckling problem of a pinned-pinned elastica with symmetrically located walls. Taking into account these geometrical characteristics, the corresponding equilibrium configurations of the elastica can easily be obtained by applying the proposed geometry-based method. Then, based on the principle of minimum energy (see Appendix B), the most favorable or optimal configurations of the elastica among candidates can be determined. Throughout this study, an optimal configuration is also called stable. A simply geometry-based stability criterion, based on the number of the inflection points of the elastica, is also included. A more rigorous stability analysis is required, however, which is beyond the scope of this study.

3.1 Constrained buckling problem of elastica

While the proposed method to calculate the equilibrium configuration of a planar elastica subject to unilateral constraints is very general, we introduce it within the context of a specific problem involving either a constant or a variable length elastica.

3.1.1 Problem definition

Consider a weightless planar elastica of uniform bending rigidity EI, whose deflection is constrained by two frictionless rigid horizontal walls that are symmetrically located on either side

of the elastica in its unstressed configuration (Fig. 3.1). Two different problems are under consideration: (i) the classical problem, where the elastica has a fixed length L (Fig. 3.1a); and (ii) the insertion problem, where the inserted length $\bar{L}$ changes with the loading (Fig. 3.1b). In both problems, one end of the elastica is fixed and is either clamped or pinned. In the first problem, the other end of the elastica —either clamped or pinned — is constrained to move horizontally. In the second problem the elastica is inserted through a frictionless sliding sleeve that functions as a clamped end, with the distance L between the fixed end of the elastica and the point of insertion maintained constant. In both cases, the axial loading is either under force or displacement control.

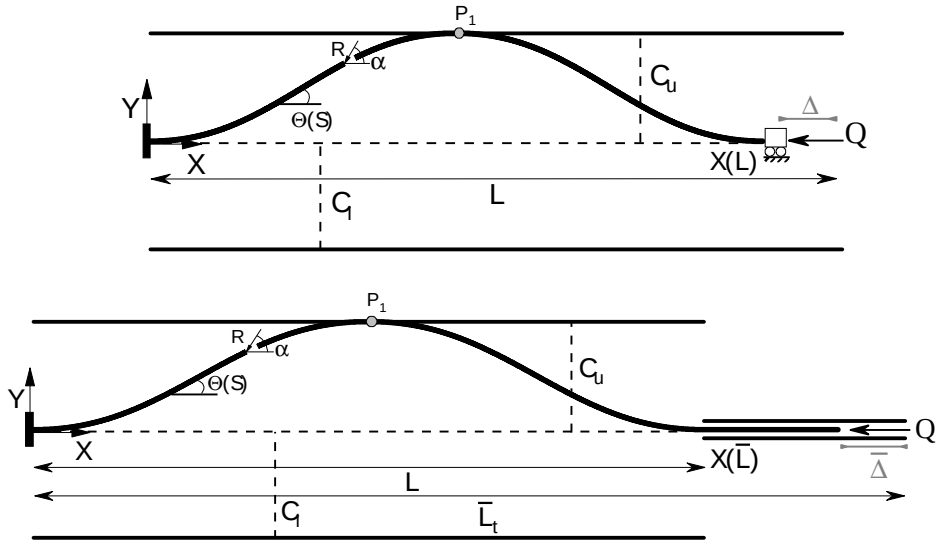

Figure 3.1: An elastica constrained by two rigid horizontal walls with clearances C_u, C_l located with respect to the centerline with the left end fixed and clamped; (a) Classical problem: the right end is clamped on a slider restricted to move along the horizontal axis, (b) Insertion problem: while the elastica is gradually inserted through a fixed frictionless sleeve at the right end.

For both problems, we seek to determine the post-buckling behavior of the elastica to an axial loading applied under either static or kinematic control. For force-controlled conditions, an axial compressive force Q is progressively applied. For displacement-controlled conditions, either the displacement Δ at the right end of the elastica or the inserted length increment $\bar{\Delta} = \bar{L} - L$ is gradually increased. Specifically, we aim to establish the relation $Q(\Delta)$ or $Q(\bar{\Delta})$ between the axial load and the end displacement or the change in inserted length. This relation reflects the buckling mode, the pattern of contacts, and the nature of the boundary conditions at the ends of the elastica.

We define a system of coordinates (X, Y) with origin at the left extremity of the elastica and with the X-axis pointing towards the elastica right end. The initial clearances between the elastica and the upper and lower walls are denoted as C_u and C_l, respectively. Thus in a representation of the planar elastica as a 1D object, the two horizontal walls are located at $Y = +C_u$ and $Y = -C_l$.

To describe the post-buckling configuration of the elastica, we introduce the arc-length coordinate S with its origin $S = 0$ at $X = 0$ and $Y = 0$, and the local inclination angle $\Theta(S)$ of the elastica on the X-axis. In its rest configuration, the elastica is thus described by $\Theta(S) = 0$ with $S \in [0, L]$ for the classical problem and $S \in \left[0, \bar{L}_t\right]$ for the insertion problem, where $\bar{L}_t$ is the total length of the elastica. In view of the inextensibity and unshearability constraints characterizing the elastica, its deformed configuration $\hat{X}(S)$, $\hat{Y}(S)$ is fully defined by the function $\Theta(S)$ and the condition that the end $S = 0$ is fixed, i.e., $\hat{X}(0) = \hat{Y}(0) = 0$. Additionally, $\hat{Y}(L) = 0$ or $\hat{Y}(\bar{L}) = 0$ in accordance with the imposed boundary conditions, and $\Delta = L - X(L)$ or $\bar{\Delta} = \bar{L} - X(\bar{L})$. The unilateral constraints associated with the presence of the two walls are represented by the inequality condition $-C_l \leq \hat{Y}(S) \leq C_u$ with $S \in [0, L]$ or $S \in \left[0, \bar{L}\right]$.

Let $R(S)$ denote the magnitude of the internal force transmitted by the elastica and $\alpha(S)$ its inclination on the X-axis, see Fig. 3.1 for the sign convention. The functions $R(S)$ and $\alpha(S)$ are actually piecewise uniform, as they experience only a jump at contact points (either discrete or at the ends of continuous contacts). The axial force $Q = R\cos\alpha$ is uniform, however, due to the assumed frictionless nature of the contact for the classical problem. In the insertion problem, the applied compressive force Q does not coincide with the axial force $R\cos\alpha$. More specifically, an Eshelby-like force develops at the point of insertion (Bosi et al., 2015; Bigoni et al., 2015). The existence of a configurational force implies that the external force Q is smaller than the axial force $R\cos\alpha$.

3.1.2 Governing equations of elastica

Assuming that the elastica is unstressed in its initial state, L represent either the initial distance between the ends of the elastica in the classical problem or the initial inserted length in the other problem. Hence, scaling follows from adopting L as length scale and EI/L^2 as force scale and defining the dimensionless quantities

$$s = \frac{S}{L}, \quad x = \frac{X}{L}, \quad y = \frac{Y}{L}, \quad c_{u,l} = \frac{C_{u,l}}{L}, \quad \mathcal{R} = \frac{RL^2}{EI}, \quad \mathcal{Q} = \frac{QL^2}{EI} \tag{3.1}$$

that are common to both problems, as well as

$$\delta = \frac{\Delta}{L} \quad or \quad \bar{\delta} = \frac{\bar{\Delta}}{L}$$

where δ represents the end-shortening and $\bar{\delta}$ the change of inserted length of the elastica.

The cartesian parametrization of the elastica, $\hat{x}(s)$, $\hat{y}(s)$, is deduced from $\theta(s)$ through integration

$$\hat{x}(s) = \int_0^s \cos\theta \mathrm{d}\xi, \qquad \hat{y}(s) = \int_0^s \sin\theta \mathrm{d}\xi \tag{3.2}$$

where the boundary conditions $\hat{x}(0) = \hat{y}(0) = 0$ have been taken into account.

Insertion Problem

Under force-controlled conditions, the dimensionless form of the potential energy of the elastica for the insertion problem can be written as

$$\Pi = \frac{1}{2}\int_0^\rho \theta'^2(s)ds - \mathcal{Q}\left(\rho_t - \int_0^{\rho_t} \cos\theta(s)ds\right) \tag{3.3}$$

where $\rho = \bar{L}/L = 1+\bar{\delta}$, $\rho_t = \bar{L}_t/L$ are the inserted and total lengths of the elastica, respectively. The first term of Π is the elastic bending energy of the elastica, while the second term is the external work of force $\mathcal{Q}$ under the following equality and inequality constraints

$$\int_0^s \sin\theta d\xi - c_u \leq 0, \quad s \in [0,\rho] \tag{3.4}$$

$$-\int_0^s \sin\theta d\xi + c_l \leq 0, \quad s \in [0,\rho] \tag{3.5}$$

$$\int_0^\rho \sin\theta ds = 0 \tag{3.6}$$

$$\int_0^\rho \cos\theta ds = 1 \tag{3.7}$$

and the boundary conditions, either $\theta(0) = 0$ or $\theta'(0) = 0$, and $\theta(\rho) = 0$. For displacement-controlled conditions, the external force $\mathcal{Q}$ is the Lagrange multiplier associated with the bilateral constraint $\rho_t - \int_0^{\rho_t} \cos\theta(s)ds = \bar{\delta}$.

The equations governing the equilibrium configuration of the elastica are now derived for a configuration involving a single discrete contact with the upper wall, see Fig. 3.1b. The derivation can be readily extended to multiple contact points. Taking into account the constraints (3.4)-(3.7), Π can be expressed as

$$\begin{aligned}\Pi = \frac{1}{2}\int_0^\rho \theta'^2(s)ds - \mathcal{Q}\left(\rho_t - \int_0^{\rho_t} \cos\theta(s)ds\right) - \lambda_x\left(1 - \int_0^\rho \cos\theta ds\right) \\ + \lambda_y \int_0^\rho \sin\theta ds - F\left(\int_0^{\ell_l} \sin\theta d\xi - c_u\right)\end{aligned} \tag{3.8}$$

where λ_x, λ_y, F are the Lagrange multipliers for the corresponding equality constraints, F is the contact force at the discrete contact P_1 and ℓ_l is the length of the segment from $s = 0$ to the discrete contact P_1, as shown in Fig. 3.1b.

The variations of the involved variables can be written as

$$\theta(s, \varepsilon) = \theta^*(s) + \varepsilon\eta(s) \tag{3.9}$$

$$\rho(\varepsilon) = \rho^* + \varepsilon\gamma \tag{3.10}$$

$$\ell_l\left(\varepsilon\right) = \ell_l^* + \varepsilon\gamma_l \tag{3.11}$$

where $\theta^*(s)$, ρ^*, ℓ_l^* are the extremal values of the inclination angle, the inserted length of the elastica and the length of the segment from $s = 0$ to the discrete contact P_1, respectively, while their corresponding variations are $\eta(s)$, γ , γ_l and $\varepsilon \ll 1$ is a positive parameter.

Taking into account that $\theta(\rho) = \theta^*(\rho^*) = 0$ and $\theta\left(\ell_l\right) = \theta^*\left(\ell_l^*\right) = 0$ and using (3.9), we obtain the following compatibility equations

$$\gamma\frac{d\theta^*(\rho^*)}{ds} + \eta(\rho^*) = 0 \tag{3.12}$$

$$\gamma_l\frac{d\theta^*(\ell_l^*)}{ds} + \eta(\ell_l^*) = 0 \tag{3.13}$$

Then the first variation of the potential energy is obtained as

$$\delta\Pi(\theta, \theta^{'}) =_{\varepsilon\to 0} \left|\frac{\mathrm{d}\Pi}{\mathrm{d}\varepsilon}\right. \tag{3.14}$$

Using Leibniz rule, the first variation of (3.8) can be written as

$$\begin{aligned}\delta\Pi(\theta, \theta^{'}) = &\int_0^{\rho^*}\frac{d\theta^*}{ds}\frac{d\eta}{ds}ds - (\mathcal{Q} + \lambda_x)\int_0^{\rho^*}\sin\theta^*\eta ds\\ &+ \left[\lambda_y - F\mathrm{H}\left(s - \ell_l\right)\right]\int_0^{\rho^*}\cos\theta^*\eta ds\\ &+ \gamma\left[\frac{1}{2}\left(\frac{d\theta^*(\rho^*)}{ds}\right)^2 + \lambda_x\cos\theta^*\left(\rho^*\right)\right]\\ &+ \gamma\lambda_y\sin\theta^*\left(\rho^*\right) - \gamma_l F\sin\theta^*\left(\ell_l^*\right)\end{aligned} \tag{3.15}$$

where $\mathrm{H}(s)$ is the Heaviside function. Integrating by parts the first term of (3.15) and considering the compatibility equation (3.12) yield

$$\int_0^{\rho^*}\frac{d\theta^*}{ds}\frac{d\eta}{ds}ds = \left.\frac{d\theta^*}{ds}\eta\right|_0^{\rho^*} - \int_0^{\rho^*}\frac{d^2\theta^*}{ds^2}\eta ds$$

$$= -\gamma \left(\frac{d\theta^*(\rho^*)}{ds} \right)^2 - \int_0^{\rho^*} \frac{d^2\theta^*}{ds^2} \eta ds \tag{3.16}$$

After substituting (3.16) into (3.15) and noting that $\theta^*(\rho^*) = \theta^*(\ell_l^*) = 0$, the first variation of the potential energy becomes

$$\delta\Pi(\theta, \theta') = -\int_0^{\rho^*} \left\{ \frac{d^2\theta^*}{ds^2} + [\mathcal{Q} + \lambda_x] \sin\theta^* - [\lambda_y - F\mathrm{H}(s - \ell_l)] \cos\theta^* \right\} \eta ds \tag{3.17}$$
$$+ \gamma \left[-\frac{1}{2} \left(\frac{d\theta^*(\rho^*)}{ds} \right)^2 + \lambda_x \right]$$

The governing equation of the elastica is then obtained by setting $\delta\Pi(\theta, \theta') = 0$

$$\frac{d^2\theta^*}{ds^2} + \left[\mathcal{Q} + \frac{1}{2} \left(\frac{d\theta^*(\rho^*)}{ds} \right)^2 \right] \sin\theta^* - [\lambda_y - F\mathrm{H}(s - \ell_l)] \cos\theta^* = 0$$

Omitting *, the final form of the governing equation of the elastica can be written as

$$\frac{d^2\theta}{ds^2} + \mathcal{R}\cos\alpha \sin\theta - \mathcal{R}\sin\alpha\cos\theta = 0 \tag{3.18}$$

where $\mathcal{R}\cos\alpha = \mathcal{Q} + (d\theta(\rho)/ds)^2/2$, $\mathcal{R}\sin\alpha = \lambda_y - F_{[2]}\mathrm{H}(s - \ell_l)$ and $s \in [0, \rho]$ (i.e., the absolute values of the resultant force $\mathcal{R}$ and its inclination angle are constant along the arc-length of the elastica as the configuration is symmetrical). The difference between the applied load and the axial force $P = \mathcal{R}\cos\alpha - \mathcal{Q} = (d\theta(\rho)/ds)^2/2$ is an Eshelby-like force that appears at the point of insertion (Bigoni, 2016; Bigoni et al., 2015; Bosi et al., 2015; Misseroni et al., 2015).

Classical Problem

For the classical problem, the total length of the elastica is $\rho = 1$ and thus the variation of the total length (3.10) is not applied. In addition (3.7) is replaced by $\int_0^1 \cos\theta ds = \delta$, which is identical to the displacement produced by the applied compressive force $\mathcal{Q}$. Hence, there is no Eshelby-like force and $\mathcal{Q} = \mathcal{R}\cos\alpha$. Following the above derivation, the same governing equation of the elastica (3.18) is obtained with boundary conditions $\theta(0) = 0$ or $\theta'(0) = 0$ and $\theta(1) = 0$ or $\theta'(1) = 0$.

3.2 Canonical problem

In this section we formulate and solve a canonical problem that constitutes the building block for the segmentation technique described in Section 3.3. Indeed, this technique involves dividing the elastica into contiguous segments, each one of them having characteristics similar to those

of the canonical problem. The solution of the canonical problem can thus serves as a general solution for each segment. Construction of the solution for the whole elastica is then reduced to assembling the segment solutions that have to satisfy various conditions, such as continuity of the solution between two successive segments or the unilateral constraints. The whole approach thus hinges on obtaining a solution of the canonical problem in terms of three numbers that fully define it.

3.2.1 Problem Definition

Consider the unit length elastica depicted in Fig. 3.2. Let $\xi \in [0,1]$ denote the arc length coordinate. The elastica is pinned at $\xi = 0$ and clamped at $\xi = 1$, i.e., $\vartheta'(0) = 0$ and $\vartheta(1) = \vartheta_1$. A dimensionless compressive force $\tilde{\mathcal{R}}$ inclined by an angle $\alpha \in [-\pi/2, \pi/2]$ on the x-axis is applied at extremity $\xi = 1$. Note that the force has here been scaled by EI/ℓ^2 with ℓ denoting the physical length of the segment. The solution $\vartheta(\xi)$ is obtained by solving

$$\frac{d^2\vartheta}{d\xi^2} + \tilde{\mathcal{R}}\cos\alpha\sin\vartheta - \tilde{\mathcal{R}}\sin\alpha\cos\vartheta = 0 \tag{3.19}$$

subjected to $\vartheta'(0) = 0$ and $\vartheta(1) = \vartheta_1$, given also $\tilde{\mathcal{R}}$ and α. The form of (3.19) suggests to rewrite this equation in terms of the relative inclination $\psi(\xi) = \vartheta(\xi) - \alpha$. Furthermore, we replace the input parameter $\tilde{\mathcal{R}}$ by the boundary condition $\vartheta(0) = \vartheta_0$. The canonical problem is thus reformulated as

$$\frac{d^2\psi}{d\xi^2} + \tilde{\mathcal{R}}\sin\psi = 0 \tag{3.20}$$

with $\psi'(0) = 0$, $\psi(0) = \psi_0 = \vartheta_0 - \alpha$, and $\psi(1) = \psi_1 = \vartheta_1 - \alpha$, noting that $\tilde{\mathcal{R}}$ is now part of the solution.

Once $\psi(\xi)$ has been determined, the cartesian components $\tilde{x}(\xi)$, $\tilde{y}(\xi)$ of a point ξ of the elastica are given by

$$\tilde{x}(\xi) = \tilde{x}(0) + \int_0^\xi \cos(\psi+\alpha)d\zeta, \quad \tilde{y}(\xi) = \tilde{y}(0) + \int_0^\xi \sin(\psi+\alpha)d\zeta \tag{3.21}$$

The canonical problem depends therefore on three angles: α, ϑ_0, and ϑ_1. It can in principle be solved analytically, but the presence of incomplete elliptic integrals in the solution makes it difficult to compute, see Appendix. However, an asymptotic solution to this problem can readily be obtained by transforming the nonlinear equation (3.20) into a system of linear equations, which can be solved as boundary value subproblems.

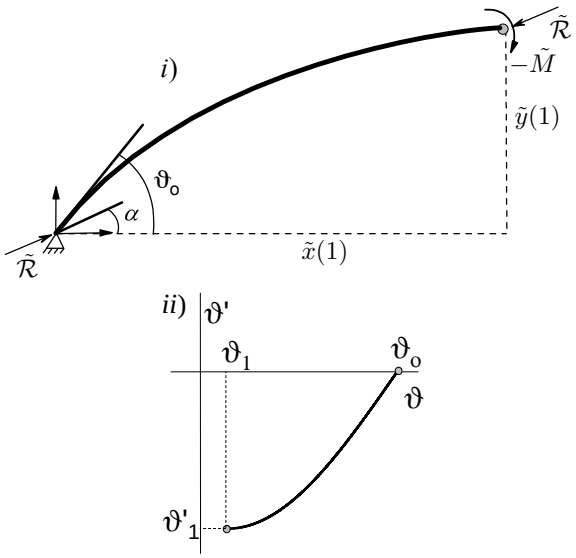

Figure 3.2: a) Canonical problem and b) Phase portrait

3.2.2 Asymptotic Solution

Inspired by (Challamel et al., 2015), we seek an asymptotic expansion of the solution in the form

$$\tilde{\mathcal{R}} = \tilde{\mathcal{R}}^{(0)} + \varepsilon\tilde{\mathcal{R}}^{(1)} + \varepsilon^2\tilde{\mathcal{R}}^{(2)} + \varepsilon^3\tilde{\mathcal{R}}^{(3)} + O(\varepsilon^4) \tag{3.22}$$

$$\psi(\xi) = \varepsilon\Psi^{(1)}(\xi) + \varepsilon^2\Psi^{(2)}(\xi) + \varepsilon^3\Psi^{(3)}(\xi) + O(\varepsilon^4) \tag{3.23}$$

where $\varepsilon = \psi_0$ is the small parameter. The second expansion starts with an order of $\mathcal{O}(\varepsilon)$ because of the post-buckling nature of the analysis. It results from this choice of expansion that $\mathcal{R}^{(0)}$ is the Euler buckling for a pinned-clamped beam subjected to an inclined load.

Inserting the asymptotic expansions (3.22) and (3.23) into (3.20), after first replacing $\sin\psi$ by $\psi - \frac{1}{6}\psi^3$, and balancing terms of same order yields a sequence of linear ODEs that replaces the original nonlinear ODE. Limiting the enforcement of (3.20) to the first three orders, we obtain

$$\mathcal{O}(\varepsilon): \ \frac{\mathrm{d}^2\Psi^{(1)}}{\mathrm{d}\xi^2} + \tilde{\mathcal{R}}^{(0)}\Psi^{(1)} = 0 \tag{3.24}$$

$$\mathcal{O}(\varepsilon^2): \ \frac{\mathrm{d}^2\Psi^{(2)}}{\mathrm{d}\xi^2} + \tilde{\mathcal{R}}^{(0)}\Psi^{(2)} = -\tilde{\mathcal{R}}^{(1)}\Psi^{(1)} \tag{3.25}$$

$$\mathcal{O}(\varepsilon^3): \ \frac{\mathrm{d}^2\Psi^{(3)}}{\mathrm{d}\xi^2} + \tilde{\mathcal{R}}^{(0)}\Psi^{(3)} = -\tilde{\mathcal{R}}^{(2)}\Psi^{(1)} - \tilde{\mathcal{R}}^{(1)}\Psi^{(2)} + \tfrac{1}{6}\tilde{\mathcal{R}}^{(0)}\Psi^{(1)3} \tag{3.26}$$

The first order solution $\Psi^{(1)}$ satisfies the boundary conditions

$$\Psi^{(1)}(0) = 1, \quad \frac{\mathrm{d}}{\mathrm{d}\xi}\Psi^{(1)}(0) = 0, \quad \Psi^{(1)}(1) = \beta \tag{3.27}$$

where β is defined as

$$\beta = \frac{\psi_1}{\psi_0} \tag{3.28}$$

while the higher order solutions $\Psi^{(i)}$, satisfy the homogeneous boundary conditions

$$\Psi^{(i)}(0) = 0, \quad \frac{\mathrm{d}}{\mathrm{d}\xi}\Psi^{(i)}(0) = 0, \quad \Psi^{(i)}(1) = 0, \quad i > 1 \tag{3.29}$$

Solving (3.24) with (3.27) yields

$$\Psi^{(1)}(\xi) = \cos\left(\sqrt{\tilde{\mathcal{R}}^{(0)}}\,\xi\right) \tag{3.30}$$

with $\tilde{\mathcal{R}}^{(0)}$ given by

$$\tilde{\mathcal{R}}^{(0)} = \arccos^2\beta \tag{3.31}$$

which reduces to $\tilde{\mathcal{R}}^{(0)} = \pi^2/4$ if $\beta = 0$. The next order solution $\Psi^{(2)}(\xi)$ is of the form

$$\Psi^{(2)}(\xi) = -\frac{\tilde{\mathcal{R}}^{(1)}}{2\sqrt{\tilde{\mathcal{R}}^{(0)}}}\xi\sin\left(\sqrt{\tilde{\mathcal{R}}^{(0)}}\,\xi\right) \tag{3.32}$$

However, necessarily $\tilde{\mathcal{R}}^{(1)} = 0$, in order to satisfy the boundary condition at $\xi = 1$. Finally, the terms $\Psi^{(3)}(\xi)$ and $\tilde{\mathcal{R}}^{(2)}$ of the asymptotic expansion of the solution are obtained by solving (3.26) with (3.29)

$$\Psi^{(3)}(\xi) = \frac{1}{192}\left[\cos\left(\sqrt{\tilde{\mathcal{R}}^{(0)}}\,\xi\right) - \cos\left(3\sqrt{\tilde{\mathcal{R}}^{(0)}}\,\xi\right)\right] + \frac{\tilde{\mathcal{R}}^{(0)} - 8\tilde{\mathcal{R}}^{(2)}}{16\sqrt{\tilde{\mathcal{R}}^{(0)}}}\xi\sin\left(\sqrt{\tilde{\mathcal{R}}^{(0)}}\,\xi\right) \tag{3.33}$$

$$\tilde{\mathcal{R}}^{(2)} = \tfrac{1}{8}\arccos\beta\left[\frac{\beta\left(1-\beta^2\right)}{3\sqrt{1-\beta^2}} + \arccos\beta\right] \tag{3.34}$$

with $\tilde{\mathcal{R}}^{(2)} = \pi^2/32$ if $\beta = 0$.

In summary, the asymptotic expansion of the solution reads

$$\tilde{\mathcal{R}} = \tilde{\mathcal{R}}^{(0)} + \psi_0^2\tilde{\mathcal{R}}^{(2)} + \mathcal{O}(\psi_0^4) \tag{3.35}$$

$$\psi(\xi) = \psi_0\Psi^{(1)}(\xi) + \psi_0^3\Psi^{(3)}(\xi) + \mathcal{O}(\psi_0^5) \tag{3.36}$$

3.2.3 Unscaling the Canonical Solution

As shown above, three numbers completely define the solution of the canonical problem, e.g., ϑ_0, ϑ_1, and α. Indeed force $\tilde{\mathcal{R}}$ and moment $\tilde{\mathcal{M}} = \mathrm{d}^2\vartheta/\mathrm{d}\xi^2$ at $\xi = 1$ depend on $\vartheta_0 - \alpha$ and $\vartheta_1 - \alpha$, while $\Delta\tilde{x}$ and $\Delta\tilde{y}$ depend on $\vartheta_0, \vartheta_1, \alpha$. An additional parameter, the scaled length ℓ of the segment (i.e., the physical length of a segment scaled by the length of the elastica) needs to be known, however, to translate the solution of the canonical problem in terms of quantities defined for the original elastica.

It is easy to show that

$$\mathcal{R} = \ell^{-2}\tilde{\mathcal{R}}(\vartheta_0 - \alpha, \vartheta_1 - \alpha)$$

$$\mathcal{M} = \ell^{-1}\tilde{\mathcal{M}}(\vartheta_0 - \alpha, \vartheta_1 - \alpha)$$

$$\Delta\bar{x} = \ell\Delta\tilde{x}(\vartheta_0, \vartheta_1, \alpha)$$

$$\Delta\bar{y} = \ell\Delta\tilde{y}(\vartheta_0, \vartheta_1, \alpha)$$

Hence four parameters define the solution of a segment.

3.3 Segmentation

3.3.1 Principle

The proposed approach to solve the elastica is based on presupposing a configuration of the elastica corresponding to a given buckling mode, and on slicing the elastica into a series of contiguous segments. The segmentation is carried out in such a way that each segment has a zero curvature ($\theta' = 0$) at one end, a non-zero curvature ($\theta' \neq 0$) and an expression for θ at the other end that is either implicit or explicit. The segment is further characterized by a monotonically varying curvature, with the trivial case of a straight segment being the only exception. The length of the segments is unknown a priori, except for particular cases where the configuration exhibits symmetry or anti-symmetry. As each segment is a particular realization of the canonical problem, the segmentation technique leads to the formulation of a system of equations to be solved for the unknown quantities that determine inclination $\vartheta(\xi)$ and length ℓ of each segment.

Defining as nodes the two ends of the elastica and the interior points at which the elastica is segmented, the elastica is thus marked by an alternate sequence of "pinned" ($\theta' = 0$) and "clamped" nodes ($\theta' \neq 0$). The interior pinned nodes are inflection points of the elastica. The segmentation leads to the definition of m segments which forms a set $\mathcal{I}_\ell = \{1, 2, ..m\}$ and $n = m + 1$ nodes with a set $\mathcal{I} = \{1, 2, ..n\}$ consisting of n_c clamped nodes and n_p pinned nodes with $n_c = n_p + n_k - 1$, where n_k denotes the number of ends of the elastica at which the inclination

θ is prescribed (i.e., $n_k = 0$, 1, or 2 depending on whether the elastica is pinned-pinned, pinned-clamped, or clamped-clamped). All the segments have boundary conditions consistent with the canonical problem presented in Section 3.2.

Let $s_{[i]}$ denote the arc length coordinate of node i, $i = 1, n$, with $s_{[1]} = 0$ and $s_{[n]} = 1$. The length ℓ_i of segment i, bounded by nodes i and $i+1$ is thus given by $\ell_i = s_{[i+1]} - s_{[i]}$. Denoting by $\theta_i(s)$ the inclination of the elastica along segment i, it is evident that determining the deformed shape of the elastica is equivalent to computing function $\theta_i(s)$ and length ℓ_i for each segment $i = 1, m$. Solution $\theta_i(s)$, $s_{[i]} \leq s \leq s_{[i+1]}$, for each segment can be expressed in terms of four parameters, using the explicit asymptotic expansion of the solution of the canonical problem. As discussed in Section 3.2.3, these four parameters can be chosen as length ℓ_i, inclinations $\theta_i(s_i)$ and $\theta_i(s_{i+1})$, and inclination α_i of the force transmitted by segment i. Solving the constrained elastica problem is thus transformed, with the segmentation technique, into determining the $4m$ parameters that completely define the global solution.

3.3.2 System of Equations

The $4m$ primary unknowns are computed by imposing a series of conditions that reflect the boundary conditions (imposed inclination or curvature at the end nodes, horizontal displacement of force at the first node), continuity of the solution, force equilibrium, and several constraints (imposed length of the elastica, no vertical offset between the two ends of the elastica, constraint on the vertical displacement due to the existence of walls). In particular, if there are n_w nodes in contact with the walls, the nodal reaction forces represent n_w additional secondary unknowns, which are determined by imposing a known displacement at these nodes. Thus, there is a total of $4m + n_w$ unknowns. We present next the $4m + n_w$ equations to be solved for the $4m$ primary and n_w secondary unknowns. These equations can be grouped in 8 categories, as follows.

1. Inclination at the clamped nodes (n_c equations):

$$\mathcal{G}_{[i]}(\theta_{[i]}) = 0, \tag{3.37}$$

   where relation $\mathcal{G}_{[i]}(\theta_{[i]})$ provides either an implicit or an explicit expression for $\theta_{[i]}$, the inclination of the elastica at node i.

2. Continuity of inclination between two segments at an interior node ($n - 2$ equations):

$$\theta_i(s_{[i+1]}) = \theta_{i+1}(s_{[i+1]}), \quad i \in \mathcal{I}_{in} \tag{3.38}$$

   where $\mathcal{I}_{in} = \{2, .., n-1\}$

3. Continuity of curvature between two segments at a clamped interior node ($n_c - n_k$ equations):

$$\theta_i'(s_{[i+1]}) = \theta_{i+1}'(s_{[i+1]}) \tag{3.39}$$

4. Force equilibrium at an interior node ($2n - 4$ equations):

$$\mathcal{R}_i \cos\alpha_i = \mathcal{R}_{i+1} \cos\alpha_{i+1}, \qquad i = 1, m-1 \tag{3.40}$$

$$\mathcal{R}_i \sin\alpha_i = \mathcal{R}_{i+1} \sin\alpha_{i+1} + F_{[i+1]}\delta_{i+1,k} \quad k \in \mathcal{I}_w \tag{3.41}$$

where $F_{[i+1]}$ denotes the vertical reaction force at node $i+1$ in contact with a wall, $\delta_{i,k}$ denotes the Kronecker delta, and $\mathcal{I}_w$ is the index set for the constrained nodes.

5. Imposed vertical displacement at the n_w constrained interior nodes (n_w equations):

$$\sum_{i=1}^{k} \Delta y_i = c, \quad k+1 \in \mathcal{I}_{w^+} \qquad \text{and} \qquad \sum_{i=1}^{k} \Delta y_i = -c, \qquad k+1 \in \mathcal{I}_{w^-}, \tag{3.42}$$

where

$$\Delta y_i = \int_{s_{[i]}}^{s_{[i+1]}} \sin\theta_i(s)\,\mathrm{d}s. \tag{3.43}$$

and $\mathcal{I}_{w^\pm}$ denotes the set containing the index of the nodes in contact with the upper ($+$) and the lower ($-$) walls ($\mathcal{I}_w = \mathcal{I}_{w^-} \cup \mathcal{I}_{w^+}$). Conditions (3.42) provide the additional equations required to solve the vertical reaction force at the n_w constrained nodes.

6. Constraint on the segment lengths (1 equation):

$$\sum_{i=1}^{m} \ell_i = 1. \tag{3.44}$$

for the classical problem and

$$\sum_{i=1}^{m} \ell_i = 1 + \bar{\delta}. \tag{3.45}$$

for the insertion problem

7. Zero vertical offset between the two ends of the elastica (1 equation):

$$\sum_{i=1}^{m} \Delta y_i = 0. \tag{3.46}$$

8. Imposed horizontal force or displacement at the first node (1 equation):

$$\mathcal{R}_1 \cos\theta_{[1]} = \mathcal{Q} \qquad \text{or} \qquad \sum_{i=1}^{m} \Delta x_i = \delta, \tag{3.47}$$

for the classical problem and

$$\mathcal{R}_1 \cos\theta_{[1]} = \mathcal{Q} \qquad \text{or} \qquad \sum_{i=1}^{m} \Delta x_i = 1, \tag{3.48}$$

for the insertion problem, where

$$\Delta x_i = \int_{s_{[i]}}^{s_{[i+1]}} \cos\theta_i(s)\,\mathrm{d}s. \tag{3.49}$$

It can readily be verified that the total number of equations is indeed $4m + n_w$, after noting that $m = 2n_c - n_k$.

3.3.3 Example

Consider the configuration of a pinned-pinned elastica of constant length, illustrated in Fig. 3.3. This configuration is characterized by two symmetric discrete contacts between the elastica and the upper wall and a free standing fold (Roman and Pocheau, 1999; Pocheau and Roman, 2004). In view of the symmetry, only half of the elastica, consisting of 3 segments (12, 23, and 34), needs to be considered. Nodes 1 and 3 are pinned, while nodes 2 and 4 are clamped. The length ℓ_i of the segments is a priori unknown but are constrained by $\sum_{i=1}^{3} \ell_i = 1/2$, noting that $\ell_2 = \ell_3$ on account of symmetry. There is a vertical reaction force at node 2. Assuming a vertical position for node 4 (to replace constraint (3.46)), the horizontal force-displacement relationship at node 1 can in principle be calculated from the system of equations (3.37)-(3.49). Expressions of these equations for this particular example is given below.

Referring to Figure 3.3, the inclinations, relative inclinations and curvatures for the segments can be expressed as follows

$$\theta_1(s) = \psi_1(s) + \alpha_1 \tag{3.50}$$

$$\theta_2(s) = \psi_2(s) \tag{3.51}$$

$$\psi_1(s) = \big(\theta_{[1]} - \alpha_1\big) \cos\sqrt{\mathcal{R}_1^{(0)}}\, s \qquad s \in \big[s_{[1]}, s_{[2]}\big] \tag{3.52}$$

$$\psi_2(s) = \theta_{[3]} \cos\sqrt{\mathcal{R}_2^{(0)}}\,\big(s_{[3]} - s\big) \qquad s \in \big[s_{[2]}, s_{[3]}\big] \tag{3.53}$$

$$\kappa_1(s) = -\left(\theta_{[1]} - \alpha_1\right)\sqrt{\mathcal{R}_1^{(0)}}\sin\sqrt{\mathcal{R}_1^{(0)}}s \qquad s \in \left[s_{[1]}, s_{[2]}\right] \tag{3.54}$$

$$\kappa_2(s) = \theta_{[3]}\sqrt{\mathcal{R}_2^{(0)}}\sin\sqrt{\mathcal{R}_2^{(0)}}\left(s_{[3]} - s\right) \qquad s \in \left[s_{[2]}, s_{[3]}\right] \tag{3.55}$$

where $\mathcal{R}_2^{(0)} = \mathcal{R}_1^{(0)}\cos\alpha_1 = \mathcal{Q}^{(0)}$, $\theta_{[1]} > 0$, $\theta_{[3]} < 0$ are the inclinations at nodes 1, 3 respectively and α_1 is the inclination angle of the resultant force $\mathcal{R}_1^{(0)}$ at node 1.

The system of equations is then given by

$$\mathbf{F}(\boldsymbol{\phi}) = \left\{ \begin{array}{c} \kappa_1(s_{[2]}) - \kappa_2(s_{[2]}) \\ \int_{s_{[1]}}^{s_{[2]}} \theta_1(s)ds - \Delta y_1 \\ \int_{s_{[2]}}^{s_{[3]}} \theta_2(s)ds - \Delta y_2 \\ \sqrt{\mathcal{Q}^{(0)}/\cos\alpha_1} - \arccos\left(\beta_1\right)/\ell_1 \\ \sqrt{\mathcal{Q}^{(0)}} - \pi/2\ell_2 \end{array} \right\} \tag{3.56}$$

with unknown vector $\boldsymbol{\phi}$ (i.e., $\phi_i \geq 0$, $i = 1, 5$) defined as

$$\boldsymbol{\phi} = \left\{ \begin{array}{c} \theta_{[1]} \\ \theta_{[3]} \\ \alpha_1 \\ \ell_1 \\ \mathcal{Q}^{(0)} \end{array} \right\}$$

In the above, $\beta_1 = -\alpha_1/\left(\theta_{[1]} - \alpha_1\right)$, $\Delta y_1 = c$ is the constant clearance between the upper wall and the centerline and $-c \leq \Delta y_2 \leq 0$ is predefined. Length ℓ_2 of the second segment is given by $\ell_2 = 1/4 - \ell_1/2$.

The system of equations (3.56) is solved numerically using the nonlinear least-squares MatLab solver "lsqnonlin". With this solver, convergence of the solution is achieved even with a poor initial guess. If all terms up to the second order (i.e., ε^2) are kept, the second term of the resultant force $\mathcal{R}_1^{(2)}$ can be obtained by (3.34) by setting $\beta = \beta_1$.

For the insertion problem, the total length of the elastica is not known *a priori*. Hence, the second segment $\bar{\ell}_2$ and the constraint (3.48) have to be included in $\boldsymbol{\phi}$ and $\mathbf{F}(\boldsymbol{\phi})$, respectively. Alternatively, the total length of the elastica can be predefined, while the vertical displacement becomes the additional unknown variable.

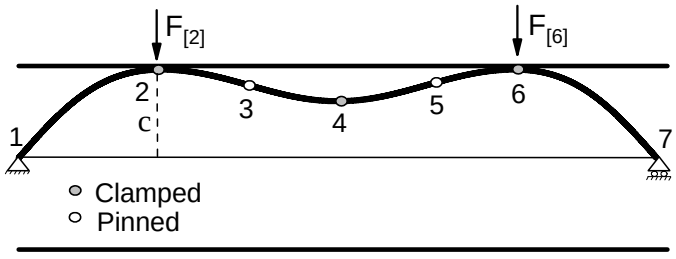

Figure 3.3: Free standing fold

3.4 Validation: Constrained Pinned-Pinned Elastica

Validation of the proposed technique entails demonstrating the effectiveness and accuracy of the geometrical segmentation technique and of the asymptotic solution of the canonical problem. The segmentation technique is validated by computing the post-buckling response of a pinned-pinned elastica constrained by two symmetrically located walls at $y = \pm c$, a classical problem solved by Domokos et al. (1997). Detailed comparison of the asymptotic solution of the canonical problem with the closed-form solution based on elliptic integrals and an asymptotic expansion of this solution is documented in Section 3.2. The possible configurations of the elastica are then described as functions of the buckling mode and the applied load. Each specific configuration is accordingly analyzed by applying the segmentation technique. Lastly, the constrained problem is solved for clearance $c = 0.05$, to enable comparison with published numerical and experimental results of (Domokos et al., 1997).

3.4.1 Validation of canonical problem

The canonical problem, solved in Section 3.2 using a pertubation technique, has also a closed-form solution. However, as stated by Domokos et al. (1997) "The explicit solution involves incomplete elliptic integrals and is awkward to work with, except in a second limiting case when the internal moment at the contact point drops to zero". This statement can be easily confirmed if the analytical solution is adopted to calculate a sequence of equilibrium states of the elastica for force- or displacement-controlled loading conditions for a fixed clearance c. In particular, the problem becomes highly nonlinear when incomplete elliptic integrals are involved. For this reason, the root-finding process, used to construct the whole solution, usually fails, especially if the initial guess is not close to the correct solution. To overcome this numerical difficulty, there are two possible approaches: (1) an approximate solution of the problem by expanding onto a Taylor series the elliptic integrals; and (2) a semi-analytical solution derived from asymptotic

considerations.

In this Section, these approaches are applied and compared with the analytical solution for the the first buckling mode of a pinned-pinned elastica with or without a discrete contact at its midpoint position. The solution of this particular problem does not require a root-finding process.. Based on the segmentation technique, there is a single canonical segment of length $\ell_1 = 0.5$ with boundary conditions $\psi_1(s_{[1]}) = \theta_{[1]} - \alpha_1$, $\psi_1'(s_{[1]}) = 0$ and $\psi_1(s_{[2]}) = \theta_{[2]} - \alpha_1$, where $s_{[1]} = 0$, $s_{[2]} = \ell_1$, $\theta_{[1]} \geq 0$, $\alpha_1 \geq 0$, $\theta_{[1]} \geq 2\alpha_1$ and $\theta_{[2]} = 0$.

The detailed derivation of the analytical solution can be found in Domokos et al. (1997). The results are only summarized here. More specifically, the resultant force $\mathcal{R}_1$ is given by

$$K\left(\bar{k}\right) - F\left(\phi;\bar{k}\right) = \sqrt{\mathcal{R}_1}\ell_1 \tag{3.57}$$

where $\phi = \arcsin\left[\sin\left(\psi(\ell_1)/2\right)/\sin\left(\psi(0)/2\right)\right]$, the cartesian components Δx_1, Δy_1 at the right end of the elastica can be expressed as

$$\Delta x_1 = \int_0^{\ell_1} \cos(\psi_1 + \alpha_1)d\xi, \quad \Delta y_1 = \int_0^{\ell_1} \sin(\psi_1 + \alpha_1)d\xi \tag{3.58}$$

where

$$\int_0^{\ell_1} \cos\psi_1 \mathrm{d}s = \frac{2\left[E(\bar{k}) - E(\phi,\bar{k})\right]}{\sqrt{\mathcal{R}_1}} - \ell_1, \quad \int_0^{\ell_1} \sin\psi_1 \mathrm{d}s = \frac{2\bar{k}}{\sqrt{\mathcal{R}_1}}\cos\phi \tag{3.59}$$

and the compressive axial load becomes $\mathcal{Q} = \mathcal{R}_1\cos\alpha_1$.

As shown in (3.57-3.59), the analytical solution involves incomplete elliptic integrals of first and second kind which can be written as

$$F\left(\phi;\bar{k}\right) = \int_0^{\phi} \frac{d\varphi}{\sqrt{1-\bar{k}^2\sin\varphi}}, \quad E\left(\phi;\bar{k}\right) = \int_0^{\phi} \sqrt{1-\bar{k}^2\sin\varphi}d\varphi$$

where $\bar{k}$ is the modulus of the elliptic integral. If $\phi = \pi/2$, the complete elliptic integrals of first and second kinds are simply obtained as $K(\bar{k}) = F\left(\pi/2;\bar{k}\right)$ and $E(\bar{k}) = E\left(\pi/2;\bar{k}\right)$, respectively. After setting $\chi = \sin\varphi$, a Taylor series expansion of the incomplete elliptic integrals can be derived, leading to

$$F\left(\phi;\bar{k}\right) \approx \phi + \frac{1}{2}\bar{k}^2\int_0^{\phi}\sin^2\varphi d\varphi + \frac{3}{8}\bar{k}^4\int_0^{\phi}\sin^4\varphi d\varphi + ... \tag{3.60}$$

$$E\left(\phi;\bar{k}\right) \approx \phi - \frac{1}{2}\bar{k}^2\int_0^{\phi}\sin^2\varphi d\varphi - \frac{1}{8}\bar{k}^4\int_0^{\phi}\sin^4\varphi d\varphi + ... \tag{3.61}$$

while the complete elliptic integrals become

$$K(\bar{k}) \approx \frac{\pi}{2}\left(1+\frac{1}{4}\bar{k}^2+\frac{9}{64}\bar{k}^4+...\right) \tag{3.62}$$

$$E(\bar{k}) \approx \frac{\pi}{2}\left(1-\frac{1}{4}\bar{k}^2+\frac{3}{64}\bar{k}^4+...\right) \tag{3.63}$$

On the other hand the asymptotic solution of the canonical problem can be found in Section 3.2.2. For convenience, the Taylor series method is called T1, T2, when the first and second order expansions are used, respectively. In a similar way, A1, A2 are the asymptotic solutions of the canonical problem that include the first and second order expansions, respectively. These approaches are compared with the analytical solution for three distinct inclination angles; (1) $\alpha_1 = 0$, (2) $\alpha_1 = 0.1$ and (3) $\alpha_1 = 0.4$. The first case, $\alpha_1 = 0$, corresponds to the unconstrained pinned-pinned elastica. The remaining cases describe configurations of a constrained pinned-pinned elastica with a single discrete contact at the midpoint position. Obviously, for the higher value of inclination angle $\alpha_1 = 0.4$, higher values of clearances $c = \Delta y_1$ are obtained.

When $\theta_{[1]} \approx 2\alpha_1$ or $\psi_{[1]} \approx \alpha_1$, the moment at the discrete contact vanishes, leading to the onset of the continuous contact. In this limited case, the derived axial force coincides with the Euler-buckling load and the asymptotic solutions are identical to the analytical solution, independently of the calculated vertical displacement Δy_1. This coincidence can be easily understood by the fact that the analytical solution only involves complete elliptic integrals, verifying Domokos et al. (1997)'s remark. This conclusion also implies that the comparison of these methods with the analytical solution should be performed by using the relative inclination angle $\psi_{[1]}$ rather than the inclination angle $\theta_{[1]}$. In Figs. 3.4-3.5, the diagrams of the axial force $\mathcal{Q}/\pi^2$, the end-shortening δ_1 and the vertical displacement Δy_1 with respect to $\psi_{[1]}$ for the three distinct clearances are presented.

For the comparison of these approaches with the analytical solution, the relative error with $\max|e| = 0.1$ is used. Based on it, the upper bounds of the relative inclinations $\psi_{[1]} = \theta_{[1]} - \alpha_1$ are obtained for all cases. The results show that the T1 fails even for relatively small displacements (see Figs. 3.4-3.5). Furthermore, the T2 is better for the derivation of the axial force with $\max\psi_{[1]} = 0.8$ when compared to A2 with $\max\psi_{[1]} = 0.6$. Nevertheless, the latter method is more accurate for the derivation of the end-shortening and the vertical displacement with $\max\psi_{[1]} = 1.25$ when compared to the former method with $\max\psi_{[1]} = 0.8$.

This comparison suggests that T2 is the best method for the derivation of the axial force, especially when the elastica is unconstrained and large displacements are present $\psi_{[1]} > 0.6$. However the derivation of a constrained elastica with a fixed clearance requires a root-finding process. The use of T2 is not efficient due to the nonlinear dependence of ϕ on the modulus of the elliptic integral $\bar{k}$, the relative inclination ψ_1 and the inclination angle α_1, and the complex form

of the expansion, which is given by (3.60)-(3.61). For clearance $c \leq 0.2$ (i.e, 1/5 of the total length of the elastica), $\psi_{[1]} \leq 0.6$ and A2 is the most efficient and at the same time accurate enough method for the solution of the constrained problem with fixed clearance. According to Figs. 3.4-3.5, for the same range of clearance, the use of A1 for the derivation of the displacements and the application of A2 for the calculation of the axial force simplifies the solution of the problem, without sacrificing much accuracy.

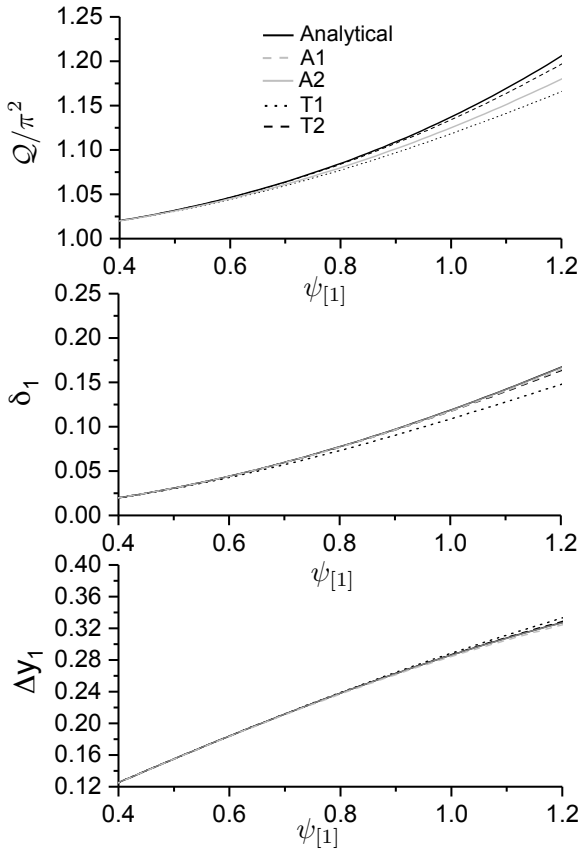

Figure 3.4: Graphs of the axial force $\mathcal{Q}/\pi^2$, the end-shortening δ_1 and the vertical displacement Δy_1 with respect to $\psi_{[1]} = \theta_{[1]}$ for $\alpha_1 = 0$

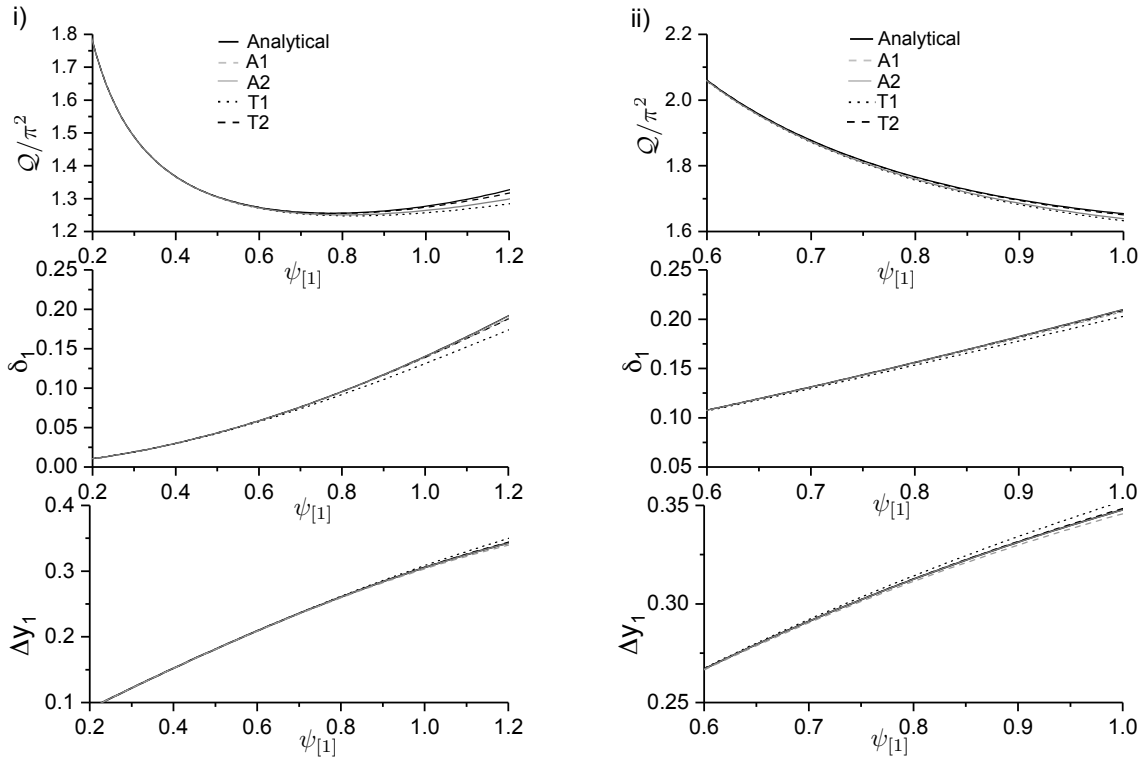

Figure 3.5: Graphs of the axial force $\mathcal{Q}/\pi^2$, the end-shortening δ_1 and the vertical displacement Δy_1 with respect to $\psi_{[1]}$; (i) $\alpha_1 = 0.1$ and (ii) $\alpha_1 = 0.4$

3.4.2 Evolution of Contact Patterns

For an assumed buckling mode, the critical axial force at which stability is lost is given by the classical buckling solution for beam-columns (Timoshenko, 2009). Increasing the axial load beyond the critical value causes continuing deformation of the elastica, which remains initially unconstrained as illustrated in Fig. 3.6i) for the first buckling mode and in Figs 3.7i) and 3.7iv) for higher buckling modes. Eventually the elastica comes in contact with the wall at some discrete points (first contact event), causing the appearance of a reaction force at every contact point $j \in \mathcal{I}_w$. Given the buckling mode, the exact positions of the initial contact points are known, see Figs. 3.6ii, 3.7ii and 3.7v.

At some stage, the direction of the resultant applied force R_i, $i \in \mathcal{I} \setminus \mathcal{I}_w$ at every pinned node $i \in \mathcal{I} \setminus \mathcal{I}_w$ passes from the adjacent contact point $j \in \mathcal{I}_w$ (i.e., $j = i - 1$ and $j = i + 1$ for $i \in \mathcal{I}_{in}$, $j = i + 1$ for the $i = 1$ and $j = i - 1$ for $i = n$). When this happens, the curvature at contact point j vanishes, leading to the onset of a line contact (second contact event), as shown in Figs. 3.6iii and 3.7iii. The contact length increases with continued loading. For the

first buckling mode, this contact pattern persists until secondary buckling occurs (third contact event), as illustrated in Fig. 3.6iv.

Configurations of the elastica characterized by no contact, discrete, and continuous contacts are discussed next. For the calculations, inclination $\theta_{[1]}$ at the elastica fixed end is used as a loading parameter in lieu of δ or $\mathcal{Q}$.

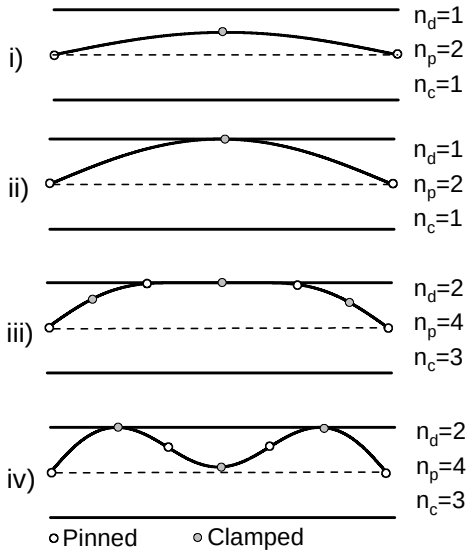

Figure 3.6: First buckling mode of pinned-pinned elastica

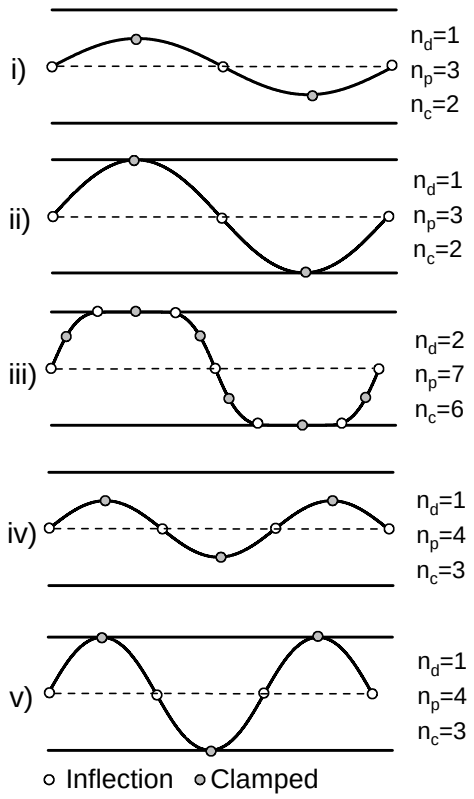

Figure 3.7: Second and third buckling mode of pinned-pinned elastica

3.4.3 Unconstrained elastica

The post-buckling response of an unconstrained elastica is well-known (Love, 2013). However, an approximate solution can be deduced from the asymptotic analysis of the canonical problem described in Section 3.2. In particular, inclination $\theta_1(s)$ of the first segment and horizontal force $\mathcal{R}_1$ of the first segment for the $k-$buckling mode depends on $\theta_{[1]}$ according to

$$\mathcal{R}_1 = (k\pi)^2 \left[1 + \frac{\theta_{[1]}^2}{8}\right] \tag{3.64}$$

$$\theta_1(s) \quad = \quad \theta_{[1]} \left\{ \cos\left[k\pi s\right] + \frac{\theta_{[1]}^2}{192} \left(\cos\left[k\pi s\right] - \cos\left[3k\pi s\right]\right) \right\} \tag{3.65}$$

Because the force transmitted by the unconstrained elastica is uniform, inclination $\theta_i(s)$, $i \in \mathcal{I}_\ell$ of the other segments is easily derived from (3.65) using symmetry and/or antisymmetry

arguments, see Figs. 3.6i, 3.7i and 3.7iv. The above expressions are applicable until the elastica touches one of the horizontal walls.

3.4.4 Discrete contact

Further increasing $\theta_{[1]}$ past the first contact event causes contact force $F_{[j]} > 0$, $j \in \mathcal{I}_w$ to increase. Because of symmetry, the magnitudes of the transverse forces $\mathcal{R}_i \sin\alpha_i$, $i \in \mathcal{I} \setminus \mathcal{I}_w$ are identical and equal to half the contact forces $F_{[j]}$, where $j = i-1$ and $j = i+1$ for $i \in \mathcal{I}_{in}$, $j = i+1$ for $i = 1$ and $j = i-1$ for $i = n$.

The positions of the contact points on the elastica remain unchanged with further loading. Due to symmetry, the solution of a single clamped-pinned segment of length $\ell_i = 1/2k$, $i \in \mathcal{I}_\ell$ is only required for which $\Delta y_i = c$, $i \in \mathcal{I}_\ell$ and $\Delta x_i = (1-\delta)/m$, $i \in \mathcal{I}_\ell$ are satisfied. This contact pattern is present until $\theta_{[i]} = 2\alpha_i$, which leads to the onset of the continuous contact.

3.4.5 Continuous contact

Past the second contact event, the elastica consists of two types of segments: pinned-discrete contact elements and straight elements in continuous contact with the wall. Noting that the moment vanishes at the ends of the continuous contact zones, the original $2k$ pinned-discrete point elements are divided in half by assigning a clamped node at its midpoint and the k straight elements are also divided in half in order to be consistent with the canonical problem. After subdivision, there are thus $m = 6k$ segments.

The solution for the whole elastica is constructed for a given $\theta_{[1]}$, once the solution for one of the $4k$ pinned-clamped segments has been obtained. Due to symmetry, the solution for these segments satisfies

$$\Delta y_i = c/2, \qquad \Delta x_i = (1-\delta-\bar{s})/4k, \quad i \in \mathcal{I} \setminus \mathcal{I}_w$$

where $\bar{s}$ denotes the combined length of the line contact segments.

$$\bar{s} = \sum_{i=1}^{k} \left(s_{[6i-1]} - s_{[6i-3]} \right)$$

Furthermore, forces $\boldsymbol{\mathcal{R}}_i$, $i \in \mathcal{I} \setminus \mathcal{I}_w$ are equal and satisfy $\mathcal{R}_i \sin\alpha_i = F_{[j]}$, where $j = i-1$ and $j = i+1$ for $i \in \mathcal{I}_{in}$, $j = i+1$ for the $i = 1$ and $j = i-1$ for $i = n$. Taking into account that the resultant force $\boldsymbol{\mathcal{R}}_1$ passes through the first contact point (node 3), a geometric relation can be obtained

$$\alpha_1 = \arctan\left(\frac{2kc}{1-\delta-\bar{s}}\right)$$

In the special case of the first buckling mode $k = 1$, this contact pattern is present until secondary buckling (i.e., post-buckling of line contact segment) is reached with $\ell_i \approx 1/4k$, $i = 1, m$.

3.4.6 Numerical Results

The post-buckling response of a pinned-pinned elastica constrained by two symmetrically located rigid walls is calculated for a clearance $c = 0.05$. The response is expressed as relationships between compressive axial force $\mathcal{Q}$ and end displacement δ for various admissible configurations of the elastica, see the bifurcation diagram illustrated in Fig. 3.8. the solution — in particular, the parametric relationships $\mathcal{Q}(\theta_{[1]})$, $\delta(\theta_{[1]})$ — is calculated for different admissible configurations by varying the imposed angle $\theta_{[1]}$.

The asymptotic method with terms up to the second order captures accurately the analytical solution of Domokos et al. (1997); no difference could be detected if both solutions were plotted in the bifurcation diagram of Fig. 3.8. The discrepancy between analytical and the experimental results in Fig. 3.8, is attributed to some initial imperfections of the elastica (Domokos et al., 1997). As the description of the sequence of deformation shapes can be found in (Domokos et al., 1997), only the main results are presented here. In particular, the bifurcation diagram is shown in Fig. 3.8 and the points at the contact pattern change are summarized in Table 6.1.

Points	$\theta_{[1]}$	δ	$\mathcal{Q}/\pi^2$
2	0.1575	0.0062	1.003
3	0.2	0.0075	3.985
4	0.406	0.0155	15.8
7	0.407	0.35	15.8
10	0.48	0.0616	9

Table 3.1: Points of evolution of the contact patterns for the bifurcation diagram for a constrained pinned-pinned elastica with clearance $c = 0.05$

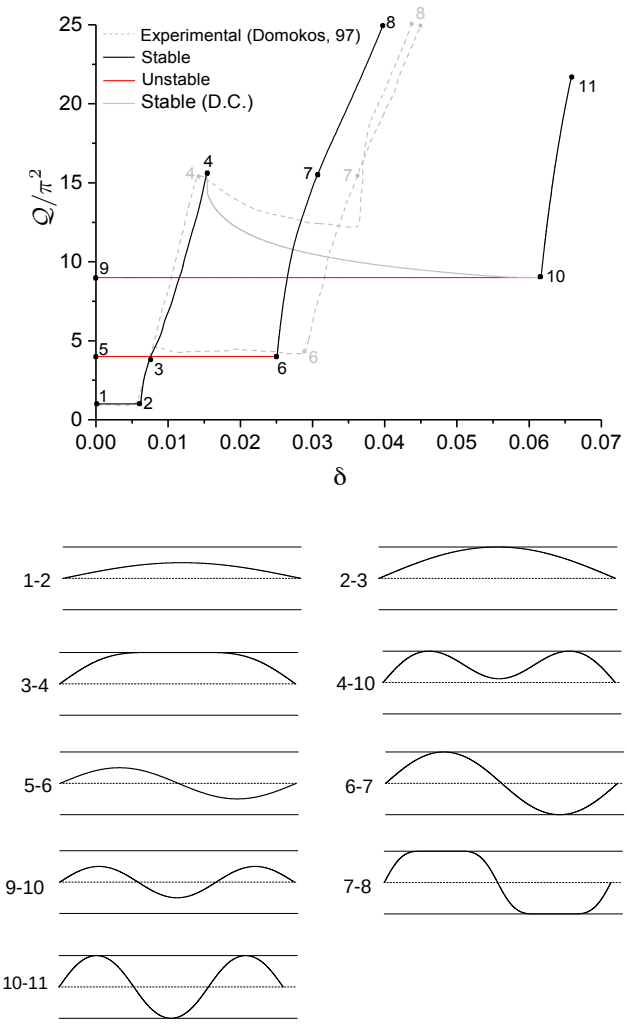

Figure 3.8: Bifurcation diagram for a constrained pinned-pinned elastica with clearance $c = 0.05$

3.5 Stability analysis based on the number of inflection points

The stability of an unconstrained elastica can be determined from the number of inflection points (Sachkov, 2008a; Jin and Bao, 2008, 2014). A somewhat similar geometry-based stability criterion is conjectured to hold for constrained elastica. The criterion depends on the number of the inflection points and on the nature of the contact conditions. Although a formal proof of this conjecture does not exist yet, its predictions are confirmed by results from other studies

(Ro et al., 2010; Manning and Bulman, 2005; Chen et al., 2015).

For the purpose of the stability analysis, the elastica is now sectioned into elements based on the contact positions (Holmes et al., 1999). There are thus two types of elements: (i) the two end-elements — connecting one of the elastica ends to a discrete contact or to the endpoint of a continuous contact; and (ii) the mid-elements — either elements of continuous contacts, or elements in between two discrete contacts. The total number of elements is $m_e^{(d)} = n_w + 1$ for discrete contacts and $m_e^{(l)} = 2n_w/3 + 1$ for continuous contacts.

Continuous and discrete contacts may not coexist in the case of a weightless elastica. Indeed, the contact patterns are consistent with the configurations derived from the (Euler-)buckling modes under consideration (Timoshenko, 2009). Due to the contact constraints, a symmetrical evolution of the configurations is derived for clamped-clamped and pinned-pinned boundary conditions leading to identical types of contact conditions (discrete or line contacts). Even for asymmetrical cases the contact conditions are limited to discrete contacts (e.g., clamped-pinned elastica) since either the deformation shape evolves gradually to a symmetrical configuration with higher number of discrete contacts, or it loses stability at the onset of a continuous contact.

The stability analysis for force-controlled and displacement-controlled boundary conditions have to be investigated separately. For force-controlled conditions the negative slope of a branch (i.e., softening) is a sufficient condition for instability, while for displacement-controlled conditions the softening branches can be either stable or unstable based on the current configuration of the elastica.

The stability criteria can be expressed solely in terms of n_p —the number of inflection points, and m_e — the number of elements. For configurations with discrete contacts, the elastica is unstable if $n_p^{(d)} > m_e^{(d)}$ for force-controlled conditions and $n_p^{(d)} > m_e^{(d)} + 1$ for displacement-controlled conditions. For configurations with continuous contacts, the elastica loses stability if $n_p^{(l)} > 2m_e^{(l)} - 2$ for either force- or displacement-controlled conditions.

The stability of an unconstrained elastica in the post-buckling regime is well-known (Love, 2013)(Bigoni, 2016). Provided that the two end supports are on the axis of the elastica in its unstressed state, the elastica becomes unstable when $n_p^{(u)} > m_e + 1$ (or $n_p^{(u)} > 2$), irrespective of the boundary condition (index (u) is used unconstrained).

3.6 Insertion problem

Here we first investigate the post-buckling responses of a clamped-clamped elastica, considering both cases of constant and variable length and compare the bifurcation diagrams for these two cases. Next we analyze the problem of inserting a clamped-pinned elastica in a conduit and we compare the sequence of equilibrium configurations with results for the insertion of a clamped-clamped elastica. The difference between force- and displacement-controlled conditions is also contrasted for the problems considered.

3.6.1 Clamped-clamped elastica with symmetric walls

The similarities and differences between the post-buckling behavior of a constrained clamped-clamped elastica for a classical and an insertion problem are discussed in details for a clearance $c = 0.05$ (see also (Manning and Bulman, 2005)) and are outlined for $c = 0.1$. The corresponding bifurcation diagrams illustrated in Figs 3.9 and 3.10 are expressed not only in terms of the axial force $\mathcal{Q}$, but also with respect to the internal axial force $\mathcal{R}\cos\alpha$. In this manner the additional effect of the configurational force is clearly demonstrated.

Consider first displacement-controlled conditions. The behavior for the first symmetric buckling mode shares some similarities with the pinned-pinned case examined in Section 3.4.6 (see Fig. 3.8). Due to symmetry the elastica comes into contact with the wall at the midpoint position at configuration $C2$ for the classical problem, and at $C\bar{2}$, $C2'$ for the insertion problem, see Table 3.2 for the characteristics ($\theta_{[2]}$, δ, $\mathcal{Q}/\pi^2$, $\mathcal{R}\cos\alpha/\pi^2$) of the critical configurations at which a change of pattern takes place. (The symbol Ci stands for the configuration of the elastica at Point i of the bifurcation diagram, where i i', $\bar{i}$ denote the corresponding points of the graphs $\mathcal{Q} = \mathcal{R}\cos\alpha$ for the classical problem and $\mathcal{Q}$, $\mathcal{R}\cos\alpha$ for the insertion problem, respectively.)

The following observations can be made from a comparison of the two problems; (1) almost identical values of δ and $\bar{\delta}$, with $\bar{\delta} < \delta$, are obtained at the onset of the first contact and (2) the post-buckling response is consistent with a super-critical bifurcation for the classical problem and sub-critical bifurcation for the insertion problem. The second observation can easily be rationalized by considering the first order term of the asymptotic expansion of the axial force $\mathcal{R}^{(0)}/\pi^2 = 4/\left(1+\bar{\delta}\right)^2$; this term indicates that the internal axial force decreases with increasing length of the elastica and the applied axial force is even lower $\mathcal{Q}^{(0)}/\pi^2 = \left(1-\theta_{[1]}^2\right)\mathcal{R}^{(0)}/\pi^2$ due to the configurational force. In contrast, the first order term in the classical problem is equal to the Euler-buckling load $\mathcal{Q}^{(0)}/\pi^2 = 4$, while the second order term has an additional positive effect, leading to a gradual increase of the axial force with end-shortening δ. Hence, the branches $1-2$ and $\bar{1}-\bar{2}$, or $1'-2'$ have positive (i.e., hardening branch) and negative (i.e., softening branch) slopes, respectively; they are both stable for displacement-controlled conditions.

The contact pattern $2-3$ remains unchanged until $C3$, or $C3 = \mathrm{C}3'$, see Table 3.2. The axial applied and internal forces coincide at Points $\bar{3}$ and $3'$, because the bending moment at the insertion point of the sliding sleeve vanishes, leading to the vanishing of the configurational force. This configuration also corresponds to the vanishing of the moment at the discrete contact. Nevertheless it does not evolve into a continuous contact. In addition the simultaneous change of the moments of both ends is not feasible. Hence, beyond Point 3 the sign of the moment at the right end changes, leading to an asymmetrical configuration with a single discrete contact (see pattern $3-4$). More explanation can be found in Appendix B.

Along Branch $3-4$, $\bar{3}-\bar{4}$, or $3'-4'$, the horizontal load decreases with increasing δ or $\bar{\delta}$ (i.e., softening branch). This branch is present until a second discrete contact occurs at $C4$, $C\bar{4}$, or $C4'$,

where the configuration becomes anti-symmetric with two discrete contacts. To understand the slight difference between Points 4 and $\bar{4}$, the second-root of the first buckling load of a clamped-clamped elastica has to be analyzed. This corresponds to an anti-symmetric unconstrained configuration of the elastica (see shape $8-4$) with initial $C8 = C\bar{8} = C8'$. This branch is unstable. Theoretically, if δ ($\bar{\delta}$) is gradually increased, Point 4 ($\bar{4}$) is eventually reached. As explained above, this clearly shows the super-critical and sub-critical bifurcations and explains the reason behind the difference between the Points 4 and $\bar{4}$. An additional reduction arises from the configurational or Eshelby-like force, which leads to a lower value of the applied force $\mathcal{Q}$ of Point $4'$. Beyond these points, the calculated configuration $4-5$ with two discrete contacts remains unchanged until $C5$, or $C\bar{5} = C5'$. Then an asymmetrical configuration is obtained with shape $5-6$, for similar reasons described above. Past this point, the difference between the classical and the insertion problems starts increasing. See for example the difference between $C6$, $C\bar{6}$ and $C6'$ in Table 3.2, both corresponding to the onset of three discrete contacts.

To complete the presentation, the distinction between the displacement- and force-controlled conditions should be also clarified. For force-controlled conditions, the softening branches $\bar{1}-\bar{2}$, or $1'-2'$ and $3-4$, $\bar{3}-\bar{4}$, or $3'-4'$ and $5-6$, $\bar{5}-\bar{6}$, or $5'-6'$ are unstable. Instead, the solution jumps from Points $\bar{1}$, or $1'$ and 3, $\bar{3}$, or $3'$ and 5, $\bar{5}$, or $5'$ to the branches $\bar{2}-\bar{3}$, or $2'-3'$ and $4-5$, $\bar{4}-\bar{5}$, or $4'-5'$ and $6-7$, $\bar{6}-\bar{7}$, or $6'-7'$. These jumps are indicated by arrows in Fig. 7.2. Upon unloading, the response follows the force-controlled type of sequence of deformations shapes in the opposite way (i.e., from shape $6-7$ to the shape $4-5$ and then $2-3$ until its unconstrained mode).

From the bifurcation diagram, it is shown that the effect of the configurational force becomes significant along the softening branches. This is evident due to the increasing values of the bending moments at the insertion point of the sliding sleeve with increasing displacement, which leads to higher values of the configurational force. On the other hand, the Points $\bar{3}, 3'$ and $\bar{5}, 5'$ coincide, respectively, because the bending moment vanishes at the insertion point, implying that $\mathcal{Q} = \mathcal{R}\cos\alpha$.

We conclude this Section with a few remarks on the case with clearance $c = 0.1$ (see also (Ro et al., 2010)). The sequence of the deformation shapes is identical to the case $c = 0.05$. However, the difference between the bifurcation values of the parameters δ and $\bar{\delta}$ at Points $2-6$ ($\bar{2}-\bar{6}$, or $2'-6'$) increases, especially for large displacements. The bifurcation diagrams of the constrained elastica for both problems are given in Fig. 5.11, while the particulars of the solution ($\theta_{[2]}$, δ, $\mathcal{Q}/\pi^2$, $\mathcal{R}\cos\alpha$) at the bifurcation points $2-6$ ($\bar{2}-\bar{6}$, or $2'-6'$) are summarized in Table 7.1.

Points	Classical problem			Insertion problem			
	$\theta_{[2]}$	δ	$\mathcal{Q}/\pi^2 = \mathcal{R}\cos\alpha/\pi^2$	$\theta_{[2]}$	δ	$\mathcal{R}\cos\alpha/\pi^2$	$\mathcal{Q}/\pi^2$
$2, \bar{2}, 2'$	0.16	0.0062	4.01	0.1565	0.00615	3.96	3.91
$3, \bar{3}, 3'$	0.2	0.0075	15.90	0.2	0.0074	15.30	15.3
$4, \bar{4}, 4'$	0.26	0.026	8.30	0.253	0.02564	7.85	7.45
$5, \bar{5}, 5'$	0.29	0.034	33.00	0.29	0.033	32.80	32.8
$6, \bar{6}, 6'$	0.367	0.0606	16.35	0.347	0.0571	14.67	13.24
$8, \bar{8}, 8'$	0	0	8.18	0	0	8.18	8.18

Table 3.2: Points of evolution of the contact patterns for the bifurcation diagram for a constrained clamped-clamped elastica with clearance $c = 0.05$

Points	Classical problem			Insertion problem			
	$\theta_{[2]}$	δ	$\mathcal{Q}/\pi^2 = \mathcal{R}\cos\alpha\ /\pi^2$	$\theta_{[2]}$	δ	$\mathcal{R}\cos\alpha\ /\pi^2$	$\mathcal{Q}/\pi^2$
$2, \bar{2}, 2'$	0.318	0.025	4.05	0.311	0.025	3.86	3.67
$3, \bar{3}, 3'$	0.407	0.030	15.78	0.394	0.030	14.86	14.86
$4, \bar{4}, 4'$	0.536	0.113	8.50	0.484	0.100	6.97	5.72
$5, \bar{5}, 5'$	0.560	0.190	27.80	0.517	0.152	24.03	24.03
$6, \bar{6}, 6'$	0.790	0.296	17.60	0.628	0.219	11.46	8.00

Table 3.3: Points of evolution of the contact patterns for the bifurcation diagram for a constrained clamped-clamped elastica with clearance $c = 0.1$

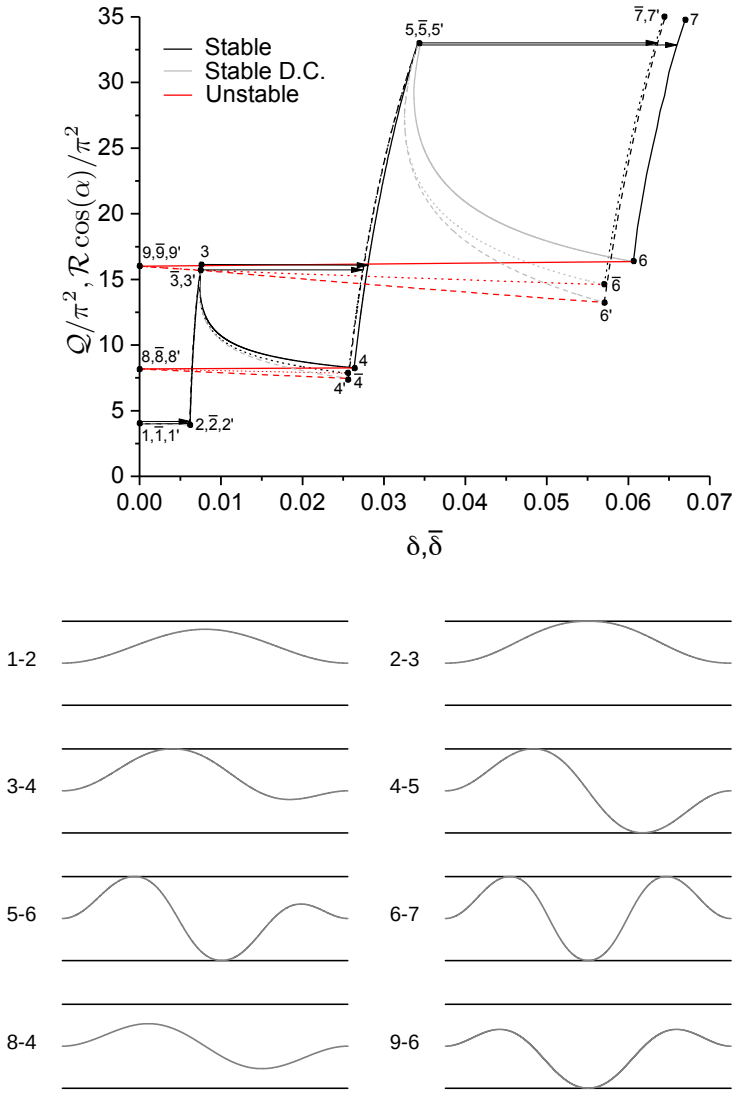

Figure 3.9: Bifurcation diagram for a constrained clamped-clamped elastica with clearance $c = 0.05$; (1) classical stability problem (dashed line) and (2) insertion stability problem with dashed line for the applied load $\mathcal{Q}$ and dotted line for the axial force $\mathcal{R}\cos\alpha$.

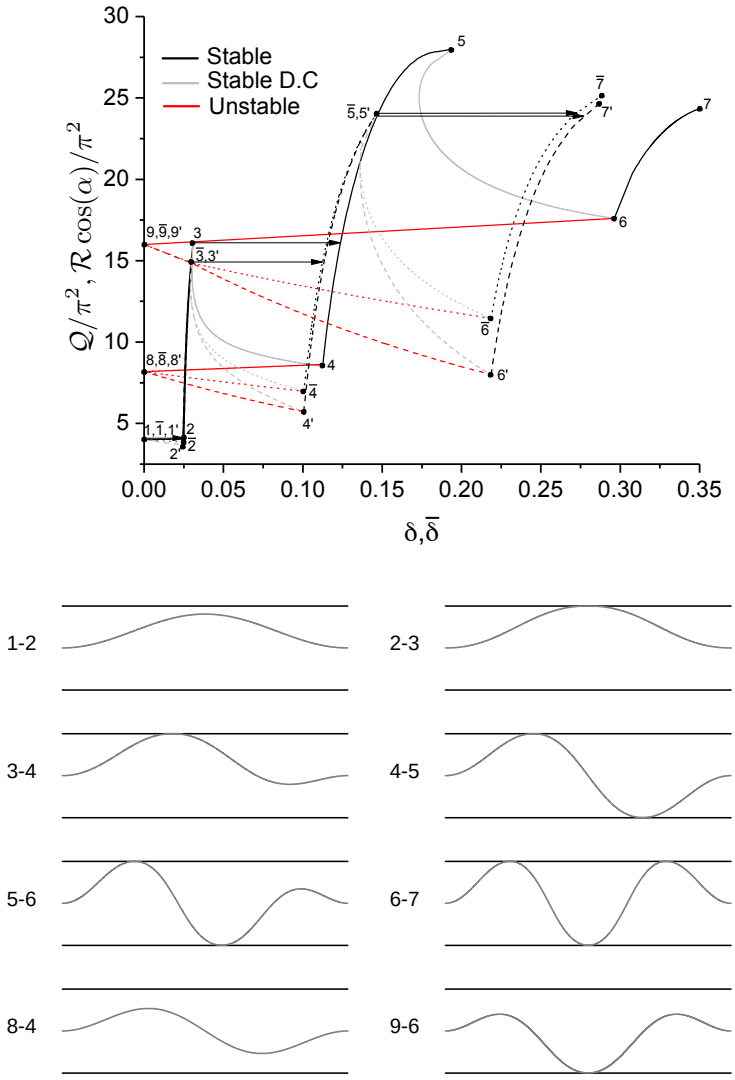

Figure 3.10: Bifurcation diagram for a constrained clamped-clamped elastica with clearance $c = 0.1$; (1) classical stability problem (solid line) and (2) insertion stability problem with dashed line for the applied load $\mathcal{Q}$ and dotted line for the axial force $\mathcal{R}\cos\alpha$.

3.6.2 Clamped-pinned elastica with symmetric walls

Here we analyze the post-buckling behavior of a clamped-pinned inserted elastica and compare it with the response of a clamped-clamped inserted elastica presented above. For both cases, clearance $c = 0.05$.

Initially, the elastica deflects according to the first buckling mode of a clamped-pinned elastica. As the elastica is gradually inserted in the conduit, a discrete contact appears at $C2$ or $C\bar{2}$, as shown in Table 5.3.2. This contact pattern remains unchanged until the moment at the discrete contact vanishes at $C3$ or $C\bar{3}$. Beyond this point, a change of the sign of the moment occurs leading to the asymmetrical deformation shape $3-4$. This softening branch gradually evolves, until a second discrete contact with the opposite wall is achieved at $C4$ or $C\bar{4}$. This new deformation shape $4-5$ evolves until the moment vanishes at both discrete contacts at $C5$ or $C\bar{5}$. In a similar manner, a new asymmetrical configuration $5-6$ is then obtained. Along this branch, the axial force decreases and a third discrete contact appears at the midpoint position at $C6$ or $C\bar{6}$ with a symmetrical shape $6-7$. For force-controlled conditions, all softening branches (i.e., $1-2$, $\bar{1}-\bar{2}$ $3-4$, $\bar{3}-\bar{4}$ $5-6$, $\bar{5}-\bar{6}$) are unstable. Hence, at points $1, \bar{1}, 3, \bar{3}, 5, \bar{5}$ the evolution of the deformation shapes is shown by the arrows in Fig. 5.8.

Points	Insertion problem		
	$\theta_{[1]}$	δ	$\mathcal{Q}/\pi^2$
2	0.2	0.0064	2.03
3	0.3	0.0085	8.93
4	0.36	0.0254	6.35
5	0.495	0.0329	23.84
6	0.505	0.0563	12.63

Table 3.4: Points of evolution of the contact patterns for the bifurcation diagram of a constrained clamped-pinned elastica with clearance $c = 0.05$

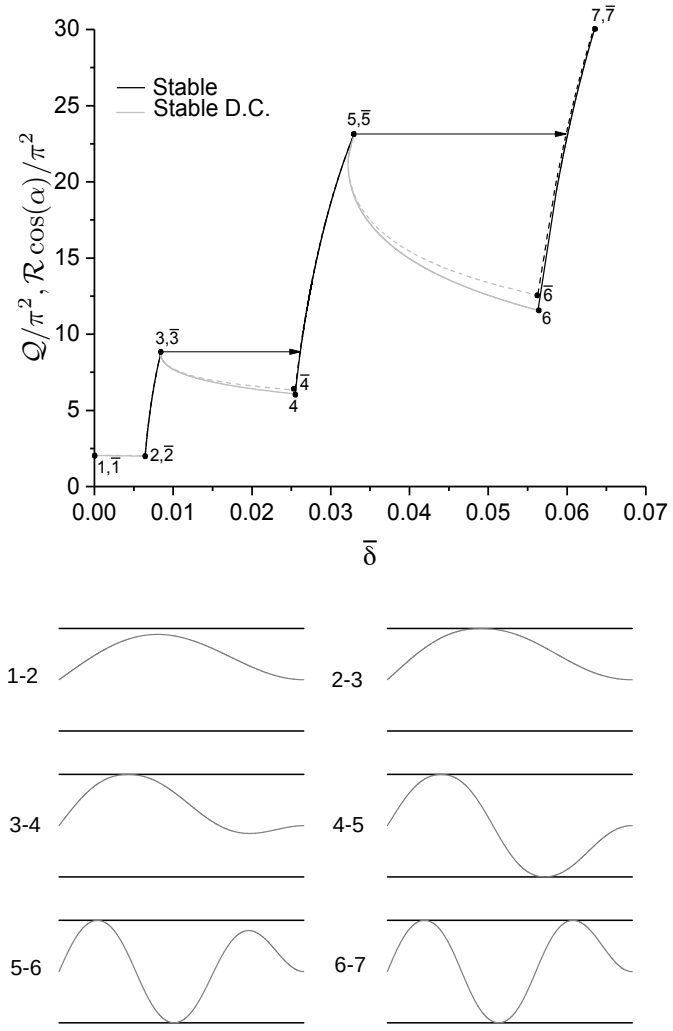

Figure 3.11: Bifurcation diagram for a constrained clamped-pinned elastica with clearance $\bar{c} = 0.05$; solid line for the applied load $\mathcal{Q}$ and dashed line for the axial force $\mathcal{R}\cos\alpha$

3.7 Conclusions

This Chapter has introduced a method that enables accurate and rapid determination of the different equilibrium states of a constrained elastica of constant or variable length. The method hinges on a segmentation of the elastica that defines sub-problems, each consistent with a single canonical problem, and on a closed-form asymptotic solution of the canonical problem.

The equilibrium solution of the elastica is then constructed by assembling the solutions of the subproblems while satisfying various continuity and constraints requirements. The complete solution requires solving a nonlinear system of equations. The principle of minimum energy is applied to determine the optimal sequence of equilibrium configurations associated with monotonic loading of the elastica under either force- or displacement-control (see Appendix B). In addition a simple geometry-based criterion to assess the stability of an equilibrium has been conjectured. The criterion is based on the number of inflection points and on the nature of the contact. A formal proof of this conjecture remains to be done, however.

The asymptotic solution of the canonical problem is compared with the analytical solution and another asymptotic method, both based on the elliptic integrals. The proposed asymptotic solution is shown to be the most efficient and is accurate enough to compute the post-buckling response of constrained elastica for clearances $c \leq 0.25$. The proposed segmentation method is then validated by computing the constrained response of pinned-pinned elastica. The solution is shown to be in full agreement with previously reported numerical results (Domokos et al., 1997).

The method has then been applied to the solution of several classical and insertion problems. The two classes of problems are first compared for a particular constrained buckling problem of a clamped-clamped elastica. Their main difference is the development of a configurational force at the insertion point of the sliding sleeve, which is not present in the classical problem. This leads to an applied axial load lower than the internal axial force. Even though this distinction is present, the analysis shows that the derived solutions are almost identical for small displacements and clearances. Discrepancy appears for large displacements, because the difference between the end-shortening for the classical problem and the change of the length of the elastica for the insertion problem becomes significant. Factors such as the boundary and loading conditions have also been investigated.

Chapter 4

Optimal Control

The application of the calculus of variations in the stability analysis of elastic structures subjected to unilateral constraints is questionable. The main source of the problem is the assumption of the 1-norm (i.e., assumption of piecewise-smooth functions) when nonsmooth conditions are present. This issue is resolved by applying an optimal control method, as explained in Section 4.1.

The equivalence between the calculus of variations and the optimal control is first shown by summarizing the derivation of Berkovitz (1961). We then provide a detailed description of the optimal control theory with pure-state constraints, including some preliminary studies on the derivation of the second-order sufficient conditions for optimality (Malanowski et al., 2004; Hermant, 2009b). Numerical methods for solving general optimal control problems are also presented, with the main focus on the direct methods.

The content of the chapter is not original. It is a compilation of materials from (Berkovitz, 1961, 1962; Bonnans and Hermant, 2008; Betts, 1998, 2010; Bryson, 2016; Berkovitz and Medhin, 2012; Bryson et al., 1963; Bryson and Denham, 1964; Hartl et al., 1995; Hermant, 2009b,a; Elnagar et al., 1995; Ross, 2015; von Stryk, 1993; Wachter and Biegler, 2005; Biegler and Zavala, 2009; Kameswaran and Biegler, 2007; Barclay et al., 1998; Gill et al., 2002; Liberzon, 2012; Mesterton-Gibbons, 2009; Nocedal, 2006; Waltz et al., 2005; Byrd et al., 2006; Goldfarb, 1970; G. Fasano, 2012; Bulirsch and Stoer, 2010; Goh and Teo, 1988; Kraft, 1985; Malanowski et al., 2004; Maurer and Pickenhain, 1995; Maurer and Oberle, 2002). To make the text more readable, quotation marks on specific sentences copied from papers were not used as well as attribution to the corresponding sources. This chapter was included to provide background material on the methodology used to solve the constrained buckling problems described in Chapters 5-7, where the interface ICLOCS (Falugi P. and van Wyk, 2010) connected with the NLP software IPOPT (Biegler and Zavala, 2009; Wachter and Biegler, 2005) is used.

4.1 From calculus of variations to optimal control

A classical calculus of variations problem is an equivalent optimal control problem even if inequality constraints are present. It is shown below that the necessary conditions for a calculus of variations problem can also be translated into necessary conditions for the optimal control if some supplementary conditions are included (Berkovitz, 1961, 1962). It is also shown that the Pontryagin's Minimum Principle is a direct translation of the usual Weierstrass condition.

The main distinction between calculus of variations and optimal control is the choice of the norm in the derivation of the local optimality. In particular, on the space of $\mathcal{C}^1$ curves $x : [a, b] \to \mathbb{R}$, there are two candidates for the norm

$$\|x\|_0 = \max_{a \le s \le b} |x(s)| \tag{4.1}$$

$$\|x\|_1 = \max_{a \le s \le b} |x(s)| + \max_{a \le s \le b} |x'(s)| \tag{4.2}$$

where (4.1) is the 0-norm $\|x\|_0$ and (4.2) is 1- norm $\|x\|_1$.

When the 0-norm or the 1-norm is assumed the extremal of the corresponding functional is called strong or weak extremal, respectively. In the field of calculus of variations, the 1-norm is adopted. This means that piecewise-smooth functions are assumed in order to derive the first and second variation of a functional. This restriction is relaxed in the optimal control theory where the 0-norm is assumed, which implies that piecewise-continuous functions are also allowed.

In Section 4.1.1, we show the equivalence between the calculus of variations and the optimal control under the presence of unilateral constraints. The theorem of Pontryagin's Minimum Principle is accordingly deduced.

4.1.1 Analysis

A general nonlinear optimal control problem $\mathcal{P}$ with mixed - pure state constraints (Ross, 2015) is given by

$$\begin{cases} \text{Minimize} \quad \mathcal{J}\left[\mathbf{x}(\cdot), \mathbf{u}(\cdot), s\right] = \int_0^{s_\ell} \mathcal{L}\left(\mathbf{x}(s), \mathbf{u}(s)\right) ds \\ \text{subject to} \\ \qquad\qquad \mathbf{x}' = \mathbf{f}(\mathbf{x}(s), \mathbf{u}(s)) \\ \qquad\qquad \mathbf{h}(\mathbf{x}(s), \mathbf{u}(s)) \le 0 \\ \qquad\qquad \boldsymbol{\phi}\left(\mathbf{x}(0), \mathbf{x}(s_\ell)\right) = 0 \end{cases} \tag{4.3}$$

which involves the derivation of the control and state spaces $\{\mathbf{x}(\cdot), \mathbf{u}(\cdot)\}$, where $\mathbf{x}(\cdot) \in \mathbb{R}^{N_x}$ are piecewise-smooth functions and $\mathbf{u}(\cdot) \in \mathbb{R}^{N_u}$ are piecewise-continuous functions. In the system of equations (4.3), $\mathcal{L} : \mathbb{R}^{N_x} \times \mathbb{R}^{N_u} \to \mathbb{R}$ is the Lagrangian, or the running cost, $\mathbf{f} : \mathbb{R}^{N_x} \times \mathbb{R}^{N_u} \to \mathbb{R}^{N_x}$ is the spatial dynamics, $\boldsymbol{\phi} : \mathbb{R}^{N_x} \times \mathbb{R}^{N_x} \to \mathbb{R}^{N_\phi}$ are the boundary conditions,

and $\mathbf{h} :\in \mathbb{R}^{N_h}$ are mixed-pure state constraints. We assume that all functions are k-times continuously differentiable C^k with respect to their arguments ($k \geq 2$) and the dynamics f is Lipschitz continuous.

The functional $\mathcal{J}[\mathbf{x}(\cdot), \mathbf{u}(\cdot), s]$ is of Lagrangian form since it only includes a Lagrangian, or running cost. Other forms of the functional $\mathcal{J}[\mathbf{x}(\cdot), \mathbf{u}(\cdot), s]$ are also possible (Liberzon, 2012). In particular, the functional $\mathcal{J}[\mathbf{x}(\cdot), \mathbf{u}(\cdot), s]$ is of Bolza form, when it involves both a running cost and an endpoint cost, while it is of Mayer form, when it includes only an endpoint cost (Ross, 2015). A problem can be easily transformed from one to another form if it is necessary.

When an isoperimetric constraint is also present

$$\int_0^s \varphi(\sigma, x, u) d\sigma \leq c \tag{4.4}$$

a new state variable is included with associated spatial derivative $x' = \varphi(s, x, u)$, initial condition $x(0) = x_o$ and constraint $x(s) \leq c$.

A classical optimal control problem can be transformed to a calculus of variations problem if we replace the control variables $\mathbf{u}(\cdot) \in \mathbb{R}^{N_u}$ by $\mathbf{y}'(\cdot) \in \mathbb{R}^{N_u}$ and assign the associated spatial derivative $\mathbf{y}'(s) = \mathbf{u}(s)$ with initial conditions $\mathbf{y}(0) = 0$. If inequality constraints are also present, they can be transformed to equality constraints by adding slack variables. In this manner the optimal control problem $\mathcal{P}$ becomes a new problem $\mathcal{P}_c$ in the calculus of variations;

$$\begin{cases} \text{Minimize} & \mathcal{J}[\mathbf{x}(\cdot), \mathbf{y}'(\cdot), s] = \int_0^{s_\ell} \mathcal{L}(\mathbf{x}(s), \mathbf{u}(s)) \, ds \\ \text{subject to} & \\ & \mathbf{f}(\mathbf{x}(s), \mathbf{y}'(s)) - \mathbf{x}' = 0 \\ & \mathbf{h}(\mathbf{x}(s), \mathbf{y}'(s)) + \boldsymbol{\xi}'^2 = 0 \\ & \boldsymbol{\phi}(\mathbf{x}(0), \mathbf{x}(s_\ell), \mathbf{y}(0), \mathbf{y}(s_\ell), \boldsymbol{\xi}(0), \boldsymbol{\xi}(s_\ell)) = 0 \end{cases} \tag{4.5}$$

where $\boldsymbol{\xi} \in \mathbb{R}^{N_h}$ is the slack variable and the boundary conditions $\boldsymbol{\phi}(\mathbf{x}(0), \mathbf{x}(s_\ell), \mathbf{y}(0), \mathbf{y}(s_\ell), \boldsymbol{\xi}(0), \boldsymbol{\xi}(s_\ell)) = 0$ are given by

$$\begin{aligned} \mathbf{x}(0) = \mathbf{x}_o, \quad \mathbf{y}(0) = 0, \quad \boldsymbol{\xi}(0) = 0 \\ \mathbf{x}(s_\ell) = \mathbf{x}_\ell, \quad \mathbf{y}(s_\ell) = \mathbf{y}_\ell, \quad \boldsymbol{\xi}(s_\ell) = \boldsymbol{\xi}_\ell \end{aligned} \tag{4.6}$$

The augmented Lagrangian can be expressed as

$$\bar{\mathcal{L}}(t, \mathbf{x}, \mathbf{y}, \mathbf{x}', \mathbf{y}', \boldsymbol{\xi}', \boldsymbol{\lambda}, \boldsymbol{\mu}) = \mathcal{L} + \boldsymbol{\lambda}(\mathbf{f} - \mathbf{x}') + \boldsymbol{\mu}\left(\mathbf{h} + \boldsymbol{\xi}'^2\right) \tag{4.7}$$

where $\boldsymbol{\lambda}(s) \in \mathbb{R}^{N_x}$ and $\boldsymbol{\mu}(s) \in \mathbb{R}^{N_h}$ are the Lagrange multipliers of the equality constraints $\mathbf{f}(\mathbf{x}(s), \mathbf{y}'(s)) - \mathbf{x}' = 0$ and $\mathbf{h}(\mathbf{x}(s), \mathbf{y}'(s)) + \boldsymbol{\xi}'^2 = 0$, respectively.

Let us denote the extremal variables by the symbol " $*$ ". More specifically, the optimal

control is given by $\mathbf{u}^* = \mathbf{y}^{'*}(s)$, while the arc $\mathcal{Z}$ is defined by $\{\mathbf{x}^*(s), \mathbf{y}^*(s), \boldsymbol{\xi}^*(s)\}$, where

$$\left(\boldsymbol{\xi}^{*'}\right)^2 = -\mathbf{h}\left(s, \mathbf{x}^*, y*'\right), \quad \boldsymbol{\xi}^*(0) = 0 \tag{4.8}$$

furnishes a minimum for the problem $\mathcal{P}_c$.

Assuming a 1-norm (4.2), we can consider the family of trial curves

$$\begin{aligned} y(s) &= y^*(s) + \varepsilon\eta_y(s) \\ x(s) &= x^*(s) + \varepsilon\eta_x(s) \\ \xi(s) &= \xi^*(s) + \varepsilon\eta_\xi(s) \end{aligned} \tag{4.9}$$

where $\varepsilon \ll 1$ is a positive parameter and η_x, η_y, η_ξ are arbitrary admissible functions that satisfy the boundary conditions (4.6). The Euler-Lagrange equations along $\mathcal{Z}$ are then derived separately for the variables $\{\mathbf{x}(s), \mathbf{y}(s), \boldsymbol{\xi}(s)\}$

$$\frac{d\bar{\mathcal{L}}_{\mathbf{x}'}}{ds} = \bar{\mathcal{L}}_{\mathbf{x}}, \quad \frac{d\bar{\mathcal{L}}_{\mathbf{y}'}}{ds} = \bar{\mathcal{L}}_{\mathbf{y}}, \quad \frac{d\bar{\mathcal{L}}_{\boldsymbol{\xi}'}}{ds} = \bar{\mathcal{L}}_{\boldsymbol{\xi}} \tag{4.10}$$

If $\left\{\mathbf{x}^{'*}(s), \mathbf{y}^{'*}(s), \boldsymbol{\xi}^{'*}(s)\right\}$ are not continuous everywhere along $\mathcal{Z}$, additional requirements should be satisfied. In particular, the du Bois-Reymond equation is derived by the vanishing first variation of the functional

$$\bar{\mathcal{L}}_{\mathbf{x}'} = \int_0^{s_\ell} \bar{\mathcal{L}}_{\mathbf{x}} ds + C_x \tag{4.11}$$

where C_x is some arbitrary constant (Mesterton-Gibbons, 2009).

Let us suppose that there is at least one $s_c \in (0, s_\ell)$ at which $\mathbf{x}^{'*}$ is discontinuous. For the sake of definiteness, suppose that the left- and right-hand limits of $\mathbf{x}^{'*}$ at the corner s_c are given by $\omega_1 = \mathbf{x}^{'*}(s_c^-) = \lim_{s \to s_c^-} \mathbf{x}^{'*}(s)$ and $\omega_2 = \mathbf{x}^{'*}(s_c^+) = \lim_{s \to s_c^+} \mathbf{x}^{'*}(s)$ with $\omega_1 \neq \omega_2$. Now, even though the integrand on the right-hand side of the du Bois-Reymond equation (4.11) is discontinuous at the corner s_c, the integral itself is continuous. Hence, the right-hand side of (4.11) must be continuous at s_c, which implies the continuity of the "momentum"

$$\bar{\mathcal{L}}_{\mathbf{x}'}\left(s_c, \mathbf{x}^*\left(s_c\right), \omega_1\right) = \bar{\mathcal{L}}_{\mathbf{x}'}\left(s_c, \mathbf{x}^*\left(s_c\right), \omega_2\right) \tag{4.12}$$

This is the so-called first Weierstrass-Erdmann corner condition. The consequence is that any broken extremal must be consistent with the Euler-Lagrange equation, except at corners where (4.12) should be satisfied.

In addition we can assume that the other variables $\mathbf{y}^{'*}(s)$, $\boldsymbol{\xi}^{'*}(s)$ are also discontinuous at the same position s_c with left- and right-hand limits $\varphi_1 = \mathbf{y}^{'*}(s_c^-)$, $\varphi_2 = \mathbf{y}^{'*}(s_c^+)$, $\chi_1 = \xi^{'*}(s_c^-)$ and $\chi_2 = \xi^{'*}(s_c^+)$, respectively. Taking into account (4.10) and considering that $\bar{\mathcal{L}}_{\mathbf{y}} = \bar{\mathcal{L}}_{\boldsymbol{\xi}} = 0$,

the momenta $\bar{\mathcal{L}}_{\mathbf{y}'}$ and $\bar{\mathcal{L}}_{\xi'}$ are constant values. This implies that the continuity of $\bar{\mathcal{L}}_{\mathbf{y}'}$ and $\bar{\mathcal{L}}_{\xi'}$ is trivially satisfied everywhere.

To derive the second Weierstrass-Erdmann corner condition, we assume two distinct classes of trial curves with a predefined corner point s_c. The first trial curve $x^{(1)}(s)$ can be expressed as follows

$$x^{(1)}(s) = \begin{cases} x^*(s) & \text{if} \quad 0 \leq s \leq s_c \\ x^*(s) + \omega_1(s - s_c) & \text{if} \quad s_c \leq s \leq s_c + \varepsilon \\ x^*(s) + \frac{\{x^*(s_c)+\omega_1\varepsilon - x^*(s_c+\varepsilon)\}(s_\ell - x)}{(s_\ell - s_c - \varepsilon)} & \text{if} \quad s_c + \varepsilon < s \leq s_\ell \end{cases} \tag{4.13}$$

where $0 \leq \varepsilon < s_\ell - s_c$, while the second trial curve $x^{(2)}(s)$ is

$$x^{(2)}(s) = \begin{cases} x^*(s) + \frac{\{x^*(s_c) - \omega_2\varepsilon - x^*(s_c-\varepsilon)\}x}{(s_c - \varepsilon)} & \text{if} \quad 0 \leq s \leq s_c - \varepsilon \\ x^*(s) - \omega_2(s_c - s) & \text{if} \quad s_c - \varepsilon \leq s \leq s_c \\ x^*(s) & \text{if} \quad s_c < s \leq s_\ell \end{cases} \tag{4.14}$$

where $0 \leq \varepsilon < s_c - s_o$. Similar functions can be expressed for $y(s)$ and $\xi(s)$.

Considering the augmented functional $\bar{\mathcal{J}}^{(1)} = \int_0^{s_\ell} \bar{\mathcal{L}} ds$, the minimization of the first variation $\bar{\mathcal{J}}'^{(1)}(0) \geq 0$ is first deduced by imposing (4.13). The augmented functional can be accordingly decomposed as

$$\bar{\mathcal{J}}^{(1)}(\varepsilon) = \bar{\mathcal{J}}_1 + \bar{\mathcal{J}}_2(\varepsilon) + \bar{\mathcal{J}}_3(\varepsilon)$$

where $\bar{\mathcal{J}}_1 = \int_0^{s_c} \bar{\mathcal{L}} ds$, $\bar{\mathcal{J}}_2(\varepsilon) = \int_{s_c}^{s_c+\varepsilon} \bar{\mathcal{L}} ds$ and $\bar{\mathcal{J}}_3(\varepsilon) = \int_{s_c+\varepsilon}^{s_\ell} \bar{\mathcal{L}} ds$. This leads to $\bar{\mathcal{J}}_1'(0) = 0$ and

$$\bar{\mathcal{J}}_2'(0) = \bar{\mathcal{L}}(s_c, \mathbf{x}^*(\mathrm{s_c}), \mathbf{y}^*(s_c), \boldsymbol{\xi}^*(s_c), \boldsymbol{\omega}_1, \boldsymbol{\varphi}_1, \boldsymbol{\chi}_1) \tag{4.15}$$

$$\begin{aligned} \bar{\mathcal{J}}_3'(0) = &-\bar{\mathcal{L}}(s_c, \mathbf{x}^*(\mathrm{s_c}), \mathbf{y}^*(s_c), \boldsymbol{\xi}^*(s_c), \boldsymbol{\omega}_2, \boldsymbol{\varphi}_2, \boldsymbol{\chi}_2) - (\omega_1 - \omega_2)\bar{\mathcal{L}}_{\mathbf{x}'}(s_c, \mathbf{x}^*(s_c), \omega_1) \\ &- (\varphi_1 - \varphi_2)\bar{\mathcal{L}}_{\mathbf{y}'}(s_c, \mathbf{y}^*(s_c), \varphi_1) - (\chi_1 - \chi_2)\bar{\mathcal{L}}_{\xi'}(s_c, \boldsymbol{\xi}^*(s_c), \chi_1) \end{aligned} \tag{4.16}$$

The same derivation is repeated by applying the second trial curve (4.14) and taking into account the continuity of the momenta (4.12), which gives $\bar{\mathcal{J}}^{(2)\prime}(0) = -\bar{\mathcal{J}}^{(1)}(0) \geq 0$. This means that $\bar{\mathcal{J}}^{(2)\prime}(0) = -\bar{\mathcal{J}}^{(1)}(0) = 0$. This provides the second Weierstrass-Erdmann corner condition at the corner point s_c, namely the continuity of $\bar{\mathcal{L}} - \mathbf{x}'\bar{\mathcal{L}}_{\mathbf{x}'} - \mathbf{y}'\bar{\mathcal{L}}_{\mathbf{y}'} - \xi'\bar{\mathcal{L}}_{\xi'}$ at any corner point.

So far, we considered a weak variation of the involved variables. If we relax this restriction and assume the 0-norm (4.1), a new trial curve $x = x(s, \varepsilon)$ should be predefined with the

following structure (Mesterton-Gibbons, 2009)

$$x(s,\varepsilon)=\begin{cases} x^*(s) & \text{if} \quad 0\le s\le s_c \\ x^*(s)+\omega(s-s_c) & \text{if} \quad s_c\le s\le s_c+\varepsilon \\ x^*(s)+\frac{\{x^*(s_c)+\omega\varepsilon-x^*(s_c+\varepsilon)\}(s_g-x)}{(s_g-s_c-\varepsilon)} & \text{if} \quad s_c+\varepsilon<s\le s_g \\ x^*(s) & \text{if} \quad s_g\le s\le s_\ell \end{cases} \tag{4.17}$$

where s_c is not a corner, ω may be any real number and $0\le\varepsilon<s_g-s_c<s_\ell-s_c$. This is a strong variation since the trial function fails to satisfy $\lim\limits_{\varepsilon\to0^+}\left|x_s(s,\varepsilon)-x^{'*}(s)\right|=0$ for all $s\in[0,s_\ell]$. Based on the trial function (4.17) and assuming similar expressions for the other variables, the augmented functional can be divided into four terms $\bar{\mathcal{J}}(\varepsilon)=\bar{\mathcal{J}}_1+\bar{\mathcal{J}}_2(\varepsilon)+\bar{\mathcal{J}}_3(\varepsilon)+\bar{\mathcal{J}}_4$ where $\bar{\mathcal{J}}_2(\varepsilon)=\int_{s_c}^{s_c+\varepsilon}\bar{\mathcal{L}}ds$ and $\bar{\mathcal{J}}_3(\varepsilon)=\int_{s_c+\varepsilon}^{s_g}\bar{\mathcal{L}}ds$. The first variation of the augmented sub-functionals yields to (4.15) and (4.16) if we replace $\{\omega_1,\varphi_1,\chi_1\}$ by $\{\omega,\varphi,\chi\}$ and $\{\omega_2,\varphi_2,\chi_2\}$ by $\left\{\mathbf{x}^{*'},\mathbf{y}^{*'},\boldsymbol{\xi}^{*'}\right\}$. In this way, we get the Weierstrass $\mathcal{E}$ function

$$\mathcal{E}(s,\mathbf{x}^*,\mathbf{y}^*,\boldsymbol{\xi}^*,\boldsymbol{\omega},\boldsymbol{\varphi},\boldsymbol{\chi},\mathbf{x}^{*'},\mathbf{y}^{*'},\boldsymbol{\xi}^{*'},\boldsymbol{\lambda},\boldsymbol{\mu})\ge0 \tag{4.18}$$

where

$$\begin{aligned}\mathcal{E}=&\bar{\mathcal{L}}(s,\mathbf{x}^*,\mathbf{y}^*,\boldsymbol{\xi}^*,\boldsymbol{\omega},\boldsymbol{\varphi},\boldsymbol{\chi})-\bar{\mathcal{L}}\left(s,\mathbf{x}^*,\mathbf{y}^*,\boldsymbol{\xi}^*,\mathbf{x}^{*'},\mathbf{y}^{*'},\boldsymbol{\xi}^{*'}\right)\\&-(\boldsymbol{\omega}-\mathbf{x}^{*'})\bar{\mathcal{L}}_{\mathbf{x}'}-(\boldsymbol{\varphi}-\mathbf{y}^{*'})\bar{\mathcal{L}}_{\mathbf{y}'}-(\boldsymbol{\chi}-\boldsymbol{\xi}^{*'})\bar{\mathcal{L}}_{\boldsymbol{\xi}'}\end{aligned} \tag{4.19}$$

with the functions $\bar{\mathcal{L}}_{x'}$, $\bar{\mathcal{L}}_{y'}$ and $\bar{\mathcal{L}}_{\xi'}$ being evaluated at $(s,\mathbf{x}^*,\mathbf{y}^*,\boldsymbol{\xi}^*,\mathbf{x}^{*'},\mathbf{y}^{*'},\boldsymbol{\xi}^{*'})$. This condition (4.18) is the so-called Weierstrass necessary condition.

We can now examine the terminal conditions $\boldsymbol{\phi}(\mathbf{x}(0),\mathbf{x}(s_\ell),\mathbf{y}(0),\mathbf{y}(s_\ell),\boldsymbol{\xi}(0),\boldsymbol{\xi}(s_\ell))=0$. Assuming strong variations for the trial curves we get $x=x(s,\varepsilon)$ with $x^*(s)=x(s,0)$, $\eta_x(s)=x_\varepsilon(s,0)$ and $x'=x_s(s,\varepsilon)$. Then the terminal conditions are obtained $s_\ell=s_\ell(\varepsilon)$, $\mathbf{x}_\ell(\varepsilon)=\mathbf{x}_\ell(s_\ell(\varepsilon),\varepsilon)$, $\mathbf{y}_\ell(\varepsilon)=\mathbf{y}_\ell(s_\ell(\varepsilon),\varepsilon)$ and $\boldsymbol{\xi}_\ell(\varepsilon)=\boldsymbol{\xi}_\ell(s_\ell(\varepsilon),\varepsilon)$. The vanishing first variation leads to

$$\left(\bar{\mathcal{L}}-\mathbf{x}'\bar{\mathcal{L}}_{x'}-\mathbf{y}'\bar{\mathcal{L}}_{y'}-\boldsymbol{\xi}'\bar{\mathcal{L}}_{\xi'}\right)s_{\ell\varepsilon}+\bar{\mathcal{L}}_{\mathbf{x}'}\mathbf{x}_{\ell\varepsilon}+\bar{\mathcal{L}}_{y'}\mathbf{y}_{\ell\varepsilon}+\bar{\mathcal{L}}_{\xi'}\boldsymbol{\xi}_{\ell\varepsilon}+E_\varepsilon=0 \tag{4.20}$$

where the subscript ε denotes partial derivative with respect to ε. Because the terms are in general $\mathbf{y}_{\ell\varepsilon}\neq\mathbf{0}$, $\boldsymbol{\xi}_{\ell\varepsilon}\neq\mathbf{0}$, the momenta are given by $\bar{\mathcal{L}}_{y'}=0$ and $\bar{\mathcal{L}}_{\xi'}=0$ and are constant everywhere. Using $\bar{\mathcal{L}}_{\xi'}=0$, we get $\boldsymbol{\mu}\mathbf{h}=0$, while the other Euler-Lagrange equations (4.10) become

$$\frac{\partial\mathcal{L}}{\partial\mathbf{y}'}+\boldsymbol{\lambda}\frac{\partial\mathbf{f}}{\partial\mathbf{y}'}+\mu\frac{\partial\mathbf{h}}{\partial\mathbf{y}'}=0 \tag{4.21}$$

$$-\boldsymbol{\lambda}'=\frac{\partial\mathcal{L}}{\partial\mathbf{x}}+\boldsymbol{\lambda}\frac{\partial\mathbf{f}}{\partial\mathbf{x}}+\mu\frac{\partial\mathbf{h}}{\partial\mathbf{x}} \tag{4.22}$$

A final necessary condition is the Clebsch-Legendre condition. Before we derive this condition, three additional constraint conditions are necessary. First, if $N_h > N_u$, then at most N_u components of $\mathbf{h}(\mathbf{x}(s), \mathbf{u}(s))$ can vanish. Second, the Jacobian $\partial h^i/\partial u^j$ where i ranges over those indices such that $h^i = 0$ and $j = \{1, 2, ..., N_u\}$ has maximum rank. Lastly, we assume that the equations $\mathbf{f}(\mathbf{x}(s), \mathbf{y}'(s)) - \mathbf{x}' = 0$ and $\mathbf{h}(\mathbf{x}(s), \mathbf{y}'(s)) + \boldsymbol{\xi}'^2 = 0$ are independent; that is the matrix

$$\begin{bmatrix} \mathbf{f}_{\mathbf{y}'} & -\mathbf{I} & \mathbf{0} \\ \mathbf{h}_{\mathbf{y}'} & \mathbf{0} & 2\boldsymbol{\Xi}' \end{bmatrix} \tag{4.23}$$

has rank $(N_x + N_h)$ along $\mathcal{Z}$ where $\mathbf{I}$ is the N_x-dimensional identity matrix and $2\Xi'$ is an $N_h \times N_h$ with entries $2\left(\xi^i\right)'$ on the diagonal. This is the so-called full rank condition (Berkovitz, 1961, 1962).

Then for every vector $(\boldsymbol{\pi}, \boldsymbol{\rho}, \boldsymbol{\kappa}) \neq 0$ with $\boldsymbol{\pi} \in \mathbb{R}^{N_x}$, $\boldsymbol{\rho} \in \mathbb{R}^{N_u}$ and $\boldsymbol{\kappa} \in \mathbb{R}^{N_h}$, a unique solution of the linear system of equations can be obtained by the full-rank condition (4.23)

$$\begin{cases} \mathbf{f}_{\mathbf{y}'}\boldsymbol{\rho} - \mathbf{I}\boldsymbol{\pi} = \mathbf{0} \\ \mathbf{h}_{\mathbf{y}'}\boldsymbol{\rho} + 2\boldsymbol{\Xi}'\boldsymbol{\kappa} = \mathbf{0} \end{cases} \tag{4.24}$$

if the following inequality holds

$$\boldsymbol{\pi}\bar{\mathcal{L}}_{x'x'}\boldsymbol{\pi} + \boldsymbol{\rho}\bar{\mathcal{L}}_{y'y'}\boldsymbol{\rho} + 2\boldsymbol{\kappa}\boldsymbol{\mu}\boldsymbol{\kappa} \geq 0 \tag{4.25}$$

Since $\bar{\mathcal{L}}_{x'x'} = 0$, (4.25) becomes $\boldsymbol{\rho}\bar{\mathcal{L}}_{y'y'}\boldsymbol{\rho} + 2\boldsymbol{\kappa}\boldsymbol{\mu}\boldsymbol{\kappa} \geq 0$. If $h^i < 0$, then by $\mu^i h^i = 0$ we get $\mu^i = 0$. On the other hand, If $h^i = 0$ at this point, $\mu^i \geq 0$ in order to satisfy (4.25). This gives the complementarity condition due to the inequality constraint

$$\mu_i = \begin{cases} = 0 & if \quad g_i < 0 \\ \geq 0 & if \quad g_i = 0 \end{cases} \tag{4.26}$$

Based on the assumption of maximum rank of the matrix $\partial h/\partial y'$ for the closed constraints $h^i = 0$, the solution of the (4.24) implies the vanishing vector $\boldsymbol{\kappa} \in \mathbb{R}^{N_h}$. Hence, the final form of the Clebsch-Legendre condition becomes

$$\boldsymbol{\rho}\bar{\mathcal{L}}_{y'y'}\boldsymbol{\rho} \geq 0 \tag{4.27}$$

where the vector $\boldsymbol{\rho}$ satisfies

$$\sum_{i=1}^{N_u} \frac{\partial h^i}{\partial y^{j'}}\rho^j = 0, \quad i = \left\{1, 2, ..., N_h^{'}\right\} \tag{4.28}$$

with $N_h^{'} \leq N_h$ the dimension of the closed constraints $h^i = 0$ for $\forall i \in N_h^{'}$.

To make a clear connection with a classical optimal control problem, the above derivation should be expressed in terms of a new function, the Hamiltonian. Based on a Legendre transformation (i.e., $\mathcal{L} = H - \boldsymbol{\lambda}\mathbf{x}'$), we can introduce the simple Hamiltonian

$$H(t, \mathbf{x}, \mathbf{y}', \boldsymbol{\lambda}) = \mathcal{L}(t, \mathbf{x}, \mathbf{y}') + \boldsymbol{\lambda}\mathbf{f}\left(t, \mathbf{x}, \mathbf{y}'\right) \tag{4.29}$$

The augmented Lagrangian (4.7) can be then reformulated in terms of the Hamiltonian (4.29)

$$\bar{\mathcal{L}} = H - \boldsymbol{\lambda}\mathbf{x}' + \boldsymbol{\mu}\left(\mathbf{h} + \boldsymbol{\xi}'^2\right) \tag{4.30}$$

Along the arc $\mathcal{Z}$ defined by $\{\mathbf{x}^*(s), \mathbf{y}^*(s), \boldsymbol{\xi}^*(s)\}$ and combining (4.30) with (4.21-4.22), the following system of equations is obtained

$$\begin{cases} \mathbf{x}'(t) = H_{\boldsymbol{\lambda}} \\ \boldsymbol{\lambda}' = -\left(H_{\mathbf{x}} + \boldsymbol{\mu}\mathbf{h}_{\mathbf{x}}\right) \\ H_{\mathbf{y}'} + \boldsymbol{\mu}\mathbf{h}_{\mathbf{y}'} = 0 \\ \mu^i h^i, \quad \boldsymbol{\mu}^i \geq 0 \end{cases} \tag{4.31}$$

Since $\bar{\mathcal{L}}_{y'}$ and $\bar{\mathcal{L}}_{\xi'}$ vanish along $\mathcal{Z}$, the continuity of $\bar{\mathcal{L}} - \mathbf{x}'\bar{\mathcal{L}}_{\mathbf{x}'} - \mathbf{y}'\bar{\mathcal{L}}_{\mathbf{y}'} - \xi'\bar{\mathcal{L}}_{\xi'}$ becomes $\bar{\mathcal{L}} - \mathbf{x}'\bar{\mathcal{L}}_{\mathbf{x}'} = H$, which implies continuity of the simple Hamiltonian at corner points. In addition the transversality condition (4.20) is given by

$$Hs_{\ell\varepsilon} + \lambda\mathbf{x}_{\ell\varepsilon} + E_{\varepsilon} = 0 \tag{4.32}$$

while the Weierstrass's necessary condition (4.19) reads

$$H(t, \mathbf{x}^*, \boldsymbol{\varphi}, \boldsymbol{\lambda}) \geq H(t, \mathbf{x}^*, \mathbf{y}^{*'}, \boldsymbol{\lambda}) \tag{4.33}$$

which can be translated as minimization of the Hamiltonian with respect to the control variable $\mathbf{y}' = \mathbf{u}$ along $\mathcal{Z}$ where $\boldsymbol{\mu}\mathbf{h} = 0$.

Finally, the Clebsch-Legendre condition is simply given by

$$\boldsymbol{\rho}\left(\left(H + \boldsymbol{\mu}\mathbf{h}\right)_{y'y'}\right)\boldsymbol{\rho} \geq 0 \tag{4.34}$$

for any solution vector $\boldsymbol{\rho}$ of the system (4.28).

Replacing $\mathbf{y}'$ by $\mathbf{u}$, the above derivation is completely equivalent to the Pontryagin's Minimum Principle applied on the original problem $\mathcal{P}$ which is summarized below.

Pontryagin's Minimum Principle

Let $\{\mathbf{x}^*(\cdot), \mathbf{u}^*(\cdot)\}$ be an optimal pair of problem $\mathcal{P}$ such that the full-rank condition holds for $\{s, x^*(s), u\}$. Then there exist right-continuous vector functions, $\boldsymbol{\lambda}(\cdot) \in [0, s_\ell] \to \mathbb{R}^{N_x}$ and right continuous covectors, $\boldsymbol{\mu}(\cdot) \in [0, s_\ell] \to \mathbb{R}^{N_g}$ such that $(\boldsymbol{\lambda}, \boldsymbol{\mu}) \neq \mathbf{0}$ for every s (i.e., nontriviality condition), the optimality conditions (4.31) and (4.33) hold on $[0, s_\ell]$ and the transversality conditions (4.32) are satisfied at $s = 0$ and $s = s_\ell$.

4.2 Optimal control method

Optimal control is usually encountered in different research areas, such as mechanical and aerospace engineering (Bryson, 2016; Paiva and Fontes, 2015) with the main focus on the controllability, or the optimization of a dynamical system. Quite recently, Liberzon (2012); O'Reilly and Peters (2012); Sachkov (2008a) introduced the optimal control concept in a different context, such as the stability analysis of a mechanical system. In particular, Liberzon (2012) gives a precise introduction in calculus of variation and optimal control and explains their connection through concrete examples, while O'Reilly and Peters (2012); Sachkov (2008a) analyze the stability behavior of elastic rods by applying optimal control.

Inspired by Liberzon (2012) and Maurer and Mittelmann (1991), we apply the optimal control method for the analysis of a constrained buckling problem (see Chapters 5, 6 and 7). In particular, in the following Section, we describe a general optimal control problem with unilateral constraints. Multiple studies regarding the optimal control that includes (mixed-state and pure-state) constraints can be found in literature (Maurer and Pickenhain, 1995; Malanowski, 1997; Maurer and Malanowski, 1998; Augustin and Maurer, 2001; Malanowski and Maurer, 2001; Maurer and Oberle, 2002; Malanowski et al., 2004; Bryson, 2016; Berkovitz and Medhin, 2012). Nevertheless, our attention is placed on pure-state constraints because of the nature of the unilateral constraints present in the constrained buckling problem. The derivation of the conditions that constitute the minimum Pontryagin's principle are then provided while the preliminary studies in the derivation of second-order optimality conditions are also discussed.

4.2.1 Optimal control theory

Inspired by Liberzon (2012), we demonstrate an optimal control problem with pure-state constraints (i.e., functions of the state variables) of order $q > 1$ (Ross, 2015). The functional to be optimized is the potential energy of the mechanical system, which is the Lagrangian of the problem. The dynamics involves spatial derivatives rather than temporal derivatives. Based on the above assumptions, our main concern is the computation of the state and control spaces $\{\mathbf{x}(\cdot), \mathbf{u}(\cdot)\}$ composed by piecewise-smooth and piecewise-continuous functions respectively, which solve the following optimal control problem $\mathcal{P}$

$$\begin{cases} \text{Minimize} \quad \mathcal{J}\left[\mathbf{x}(\cdot),\mathbf{u}(\cdot)\right] = \int_0^\ell \mathcal{L}\left(\mathbf{x}(s),\mathbf{u}(s)\right) ds \\ \text{subject to} \\ \qquad\qquad \mathbf{x}' = \mathbf{f}(\mathbf{x}(s),\mathbf{u}(s)) \\ \qquad\qquad \boldsymbol{\phi}\left(\mathbf{x}(0),\mathbf{x}(\ell)\right) \leq 0 \\ \qquad\qquad \mathbf{g}(\mathbf{x}(s)) \leq 0 \end{cases} \tag{4.35}$$

where s is the arclength defined on the interval $\mathcal{I} = [0, \ell]$, $\mathbf{x} \in \mathbb{R}^{N_x}$ is the state vector, $\mathbf{u} \in \mathbb{R}^{N_u}$ is the control vector, $\mathcal{L} : \mathbb{R}^{N_x} \times \mathbb{R}^{N_u} \to \mathbb{R}$ is the Lagrangian, or the running cost, $\mathbf{f} : \mathbb{R}^{N_x} \times \mathbb{R}^{N_u} \to \mathbb{R}^{N_x}$ represents the spatial dynamics, $\boldsymbol{\phi} : \mathbb{R}^{N_x} \times \mathbb{R}^{N_x} \to \mathbb{R}^{N_\phi}$ characterize the boundary conditions, or events, and $\mathbf{g} :\in \mathbb{R}^{N_g}$ characterize the pure-state constraints. We assume that all functions are k-times continuously differentiable C^k with respect to their arguments ($k \geq 2$), and the dynamics $\mathbf{f}$ is Lipschitz continuous.

The objective of the study is not only to derive a feasible pair $\{\mathbf{x}(\cdot),\mathbf{u}(\cdot)\}$ that satisfies the problem $\mathcal{P}$ but also to minimize globally the functional $\mathcal{J}\left[\mathbf{x}(\cdot),\mathbf{u}(\cdot),s\right]$. In this case, the feasible pair $\{\mathbf{x}(\cdot),\mathbf{u}(\cdot)\}$ is called the optimal pair, denoted by $\{\mathbf{x}^*(\cdot),\mathbf{u}^*(\cdot)\}$. The optimal pair can be derived by applying the Pontryagin's minimum principle (for more details see (Hartl et al., 1995; Bonnans and Hermant, 2007b, 2009; Hermant, 2009b,a)).

Due to the presence of pure-state constraints, special care in the derivation of the Pontryagin's minimum principle is required. Hence, we start with some necessary definitions for the pure-state constraints and then we complete our analysis with the presentation of the Pontryagin's minimum principle for problem $\mathcal{P}$. The contact and regularity conditions for second-order pure-state constraints, which are involved in our problem, are also included.

4.2.2 Preliminaries on the pure-state constraints

The order of a pure-state constraint provides us with information about the nature and evolution of the contact patterns. Based on it, we are also aware of the continuity properties of the adjoint variables.

The order of a pure-state constraint is derived if we differentiate the pure state constraint with respect to arclength as many times as required until it depends explicitly on the control variable. If we denote $g(\mathbf{x}(s)) =: g^0$, the $i-th$ order (i.e., $i \geq 1$) can be written as

$$\begin{aligned} g^i\left(\mathbf{x},\mathbf{u}\right) &= \frac{dg^{i-1}\left(\mathbf{x},\mathbf{u}\right)}{ds} = \partial_{\mathbf{x}} g^{i-1}(\mathbf{x},\mathbf{u})^\top \mathbf{x}' \\ &= \partial_{\mathbf{x}} g^{i-1}(\mathbf{x},\mathbf{u})^\top \mathbf{f}(\mathbf{x},\mathbf{u}) \end{aligned} \tag{4.36}$$

If the order of the pure state constraint is q, it means that

$$\partial_{\mathbf{u}} g^i\left(\mathbf{x},\mathbf{u}\right) = 0 \quad \text{for} \quad 0 \leq i \leq q-1 \qquad \text{and} \qquad \partial_{\mathbf{u}} g^q\left(\mathbf{x},\mathbf{u}\right) \neq 0 \tag{4.37}$$

Let us denote $0 \leq \zeta_1 < \zeta_2 \leq \ell$. An interval (ζ_1, ζ_2) is an unconstrained segment (or interior arc) if $\mathbf{g}(\mathbf{x}(s)) < 0$ and it is a continuous segment (or boundary arc) if $\mathbf{g}(\mathbf{x}(s)) = 0$ for $s \in [\zeta_1, \zeta_2]$. In the latter case, we denote $\zeta_{en} \equiv \zeta_1$ and $\zeta_{ex} \equiv \zeta_2$ the entry and exit points, respectively. On the other hand, a discrete contact ζ_c at the endpoint of an unconstrained segment can be met if $\mathbf{g}(\mathbf{x}(\zeta_c)) = 0$ holds. Entry, exit, and contact points are called junction points (Bonnans and Hermant, 2007b).

Let us consider the maximal interval $\mathcal{I} = [0, \ell]$. Suppose that there is a finite set of junction points denoted by $\mathcal{Z} = \mathcal{Z}_{en} \cup \mathcal{Z}_{ex} \cup \mathcal{Z}_c$, where $\mathcal{Z}_{en} = \left\{\zeta_{en}^1, \zeta_{en}^2, .., \zeta_{en}^{N_\ell}\right\}$, $\mathcal{Z}_{ex} = \left\{\zeta_{ex}^1, \zeta_{ex}^2, .., \zeta_{ex}^{N_\ell}\right\}$ and $\mathcal{Z}_c = \left\{\zeta_c^1, \zeta_c^2, .., \zeta_c^{N_c}\right\}$. The pairs of $\zeta_{en}^j, \zeta_{ex}^j$ with $\zeta_{en}^j \in \mathcal{Z}_{en}$,$\zeta_{ex}^j \in \mathcal{Z}_{ex}$ for $j = \{1, 2, .., N_\ell\}$ define the union of continuous segments $\mathcal{I}_\ell \subseteq \mathcal{I} = \cup_{j=1}^{N_\ell} \left[\zeta_{en}^j, \zeta_{ex}^j\right]$.

Pontryagin's minimum principle

Before we formulate the necessary conditions of Pontryagin's minimum principle, we introduce a new function, the Hamiltonian function (Gelfand, 2000) which is derived by applying a Legendre transformation of the Lagrangian function $\mathcal{L}$. More precisely, the Hamiltonian is given by

$$H(\boldsymbol{\lambda}, \mathbf{x}, \mathbf{u}) = \mathcal{L}(\mathbf{x}, \mathbf{u}) + \boldsymbol{\lambda}^\top \mathbf{f}(\mathbf{x}, \mathbf{u}) \tag{4.38}$$

Taking into account the presence of the pure-state constraints $\mathbf{g}(\mathbf{x}(s))$, the simple Hamiltonian $H(\boldsymbol{\lambda}, \mathbf{x}, \mathbf{u})$ is replaced by the augmented Hamiltonian

$$\bar{H}(\boldsymbol{\mu}, \boldsymbol{\lambda}, \mathbf{x}, \mathbf{u}) = H(\boldsymbol{\lambda}, \mathbf{x}, \mathbf{u}) + \boldsymbol{\mu}^\top \mathbf{g}(\mathbf{x}) \tag{4.39}$$

where $\boldsymbol{\mu} \in \mathbb{R}^{N_g}$ is the vector of Lagrange multipliers that satisfies the complementarity condition

$$\mu_i = \begin{cases} = 0 & if \quad g_i(\mathbf{x}_o, \mathbf{x}_f) < 0 \\ \geq 0 & if \quad g_i(\mathbf{x}_o, \mathbf{x}_f) = 0 \end{cases}, \quad i \in N_g, \tag{4.40}$$

also denoted as $\boldsymbol{\mu} \perp \mathbf{g}$.

The necessary conditions for global optimality, which constitute the Pontryagin's minimum principle (Hartl et al., 1995), involve the following properties: (1) the minimization of the Hamiltonian with respect to the control which should be consistent with the control space; (2) the canonical, or adjoint equations of the augmented Hamiltonian; and (3) the transversality conditions (i.e., satisfaction of the boundary conditions).

Since only pure-state constraints are present and there are no constraint functions with respect to the control, the control space is simply $\mathbf{u} \in \mathbb{R}^{N_u}$. The Hamiltonian minimization condition (HMC) is then derived in terms of the simple Hamiltonian as far as HMC does not

violate the complementarity condition (4.40);

$$\partial_{\mathbf{u}}\bar{H} = \partial_{\mathbf{u}}H = 0 \quad \text{with } \boldsymbol{\mu}\perp\mathbf{g} \tag{4.41}$$

The second necessary condition involves the adjoint, or canonical equations, which are derived by the augmented Hamiltonian $\bar{H}$

$$\begin{aligned} -\boldsymbol{\lambda}' &= \partial\bar{H}/\partial\mathbf{x} \\ &= \partial H/\partial\mathbf{x} + (\partial\mathbf{g}/\partial\mathbf{x})^{\top}\boldsymbol{\mu} \quad \boldsymbol{\mu}\perp\mathbf{g} \end{aligned} \tag{4.42}$$

and

$$\mathbf{x}' = \partial\bar{H}/\partial\boldsymbol{\lambda} = \mathbf{f}(\mathbf{x}(s),\mathbf{u}(s)) \tag{4.43}$$

Based on the complementarity condition (4.40), we get a non-vanishing value of the corresponding covector $\mu_i \neq 0$ at a closed contact $\zeta \in \mathcal{Z}$, where $g_i(\mathbf{x}(\zeta)) = 0$. Considering that there is a finite number of contact points, a finite number of non-vanishing elements of $\boldsymbol{\mu}(s)$ is also present. This implies that $\boldsymbol{\mu}(s)$ are piecewise-continuous vector functions.

If we assume that the vectors $\boldsymbol{\lambda}, \boldsymbol{\mu}$ are right-continuous vector functions, the adjoint variables can be written as a Lebesgue-Stieltjes integral in the following way

$$\begin{aligned} \boldsymbol{\lambda}(\ell^{+}) - \boldsymbol{\lambda}(0^{+}) &= -\int_{(0,\ell]} (\partial\mathbf{g}/\partial\mathbf{x})^{\top}\boldsymbol{\mu}ds \\ &= \int_{(0,\ell]} (\partial\mathbf{g}/\partial\mathbf{x})^{\top} d\tilde{\boldsymbol{\mu}} \end{aligned} \tag{4.44}$$

where $\tilde{\boldsymbol{\mu}}$ is a function of bounded variation, which can be written as the sum of two functions; (1) an absolutely continuous function $\tilde{\boldsymbol{\mu}}^{(1)}$ and (2) a singular function $\tilde{\boldsymbol{\mu}}^{(2)}$ and $\boldsymbol{\mu}(s) = -\dot{\tilde{\boldsymbol{\mu}}}$ for every s for which $\dot{\tilde{\boldsymbol{\mu}}}$ exists (Hartl et al., 1995). Based on this decomposition, the integral at the right side of (4.44) can be evaluated as follows

$$\begin{aligned} \int_{(0,\ell]} (\partial\mathbf{g}/\partial\mathbf{x})^{\top} d\tilde{\boldsymbol{\mu}} &= \int_{0}^{\ell} (\partial\mathbf{g}/\partial\mathbf{x})^{\top}\dot{\tilde{\boldsymbol{\mu}}}^{(1)}ds + \int_{(0,\ell]} (\partial\mathbf{g}/\partial\mathbf{x})^{\top} d\tilde{\boldsymbol{\mu}}^{(2)} \\ &= \int_{0}^{\ell} (\partial\mathbf{g}/\partial\mathbf{x})^{\top}\dot{\tilde{\boldsymbol{\mu}}}^{(1)}ds + \sum_{\zeta_i\in(0,\ell]} (\partial\mathbf{g}/\partial\mathbf{x})^{\top}\left[\tilde{\boldsymbol{\mu}}(\zeta_i^{+}) - \tilde{\boldsymbol{\mu}}(\zeta_i^{-})\right] \end{aligned}$$

while a single jump condition at a discrete contact ζ is given by

$$\begin{aligned} \boldsymbol{\lambda}(\zeta^{-}) - \boldsymbol{\lambda}(\zeta^{+}) &= \left(\frac{\partial\mathbf{g}}{\partial\mathbf{x}}\right)\Big|_{\mathbf{x}(\zeta)} \left[\tilde{\boldsymbol{\mu}}(\zeta^{-}) - \tilde{\boldsymbol{\mu}}(\zeta^{+})\right] \\ &= \left(\frac{\partial\mathbf{g}}{\partial\mathbf{x}}\right)\Big|_{\mathbf{x}(\zeta)} \boldsymbol{\eta}(\zeta) \end{aligned} \tag{4.45}$$

This implies that an adjoint variable λ_i (associated with the state variable x_i) with $i \in N_x$ is a piecewise absolutely continuous function, if at least one pure-state constraint g_j with $j \in N_g$ is a function of the state variable x_i and is closed at least in one junction point. Otherwise, in the absence of the state constraints, the adjoint variable is an absolutely continuous function.

To complete the necessary conditions of the Pontryagin minimum principle, we need to satisfy the existing boundary conditions. Let us denote by $\boldsymbol{\nu} \in \mathbb{R}^{N_\phi}$ the Lagrange multipliers, or covectors of the boundary conditions $\boldsymbol{\phi}(\mathbf{x}(0), \mathbf{x}(\ell)) \leq 0$ which satisfy the complementarity condition $\boldsymbol{\nu} \perp \boldsymbol{\phi}$ and the associated scalar function $\Phi = \boldsymbol{\nu}^\top \boldsymbol{\phi}(\mathbf{x}(0), \mathbf{x}(\ell))$. Based on it, the transversality conditions can be written as

$$\boldsymbol{\lambda}(0) = -\frac{\partial \Phi}{\partial \mathbf{x}_o}, \quad \boldsymbol{\lambda}(\ell) = \frac{\partial \Phi}{\partial \mathbf{x}_\ell} \tag{4.46}$$

where $\boldsymbol{\nu} \perp \boldsymbol{\phi}$ is always satisfied.

In the optimal control problem $\mathcal{P}$, the Hamiltonian and the pure-state constraints are not explicitly dependent on the arc-length. This implies that the augmented Hamiltonian is constant (an integral of motion $d\bar{H}/ds = 0$), which is an important property of our system (Goldstein et al., 2002).

The canonical equations (4.43-4.43) together with the transversality conditions (4.46) constitute a two-point boundary value problem, while the minimization of the Hamiltonian with respect to the control (4.41) forms an algebraic system. This means that an optimal control problem that satisfies the first-order optimality conditions involves a differential-algebraic system of equations.

Minimum Pontryagin's principle - Theorem

Let $\{\mathbf{x}^*(\cdot), \mathbf{u}^*(\cdot)\}$ be an optimal pair of problem $\mathcal{P}$. Then, there exist a right-continuous vector functions $\boldsymbol{\lambda}(\cdot) \in [0, \ell] \to \mathbb{R}^{N_x}$, $\boldsymbol{\mu}(\cdot) \in [0, \ell] \to \mathbb{R}^{N_g}$ and $\boldsymbol{\nu} \in \mathbb{R}^{N_\phi}$ associated with the boundary conditions $\boldsymbol{\phi} : \mathbb{R}^{N_x} \times \mathbb{R}^{N_x} \to \mathbb{R}^{N_\phi}$ such that $(\boldsymbol{\lambda}, \boldsymbol{\mu}(\ell) - \boldsymbol{\mu}(0), \boldsymbol{\nu}) \neq \mathbf{0}$ for every $s \in \mathcal{I}$ (i.e., nontriviality condition), the optimality conditions (4.41)-(4.44) hold almost everywhere on $[0, \ell]$ and the transversality conditions (4.46) are satisfied at the extremities. In addition, for any junction point $\zeta \in \mathcal{Z}$, the jump condition should also hold (4.45).

Contact and regularity conditions for second-order state constraints

In case of a scalar control variable and a scalar pure state constraint of order q, Bonnans and Hermant (2007b) provide a result (Proposition 2.5) based on (Jacobson et al., 1971), which explains the regularity conditions of the control variable at the junction points depending on the order of the state constraint. Our focus is the second-order pure-state constraint $q = 2$. If the trajectory $\{u(s), \mathbf{x}(s)\}$ is a regular Pontryagin extremal, then u and its $q-2$ first derivatives

are continuous at $\zeta \in \mathcal{Z}$. The only special case is when the contact point ζ_c first appears without the presence of a jump (i.e., $\eta = 0$), where u and its q first derivatives remain continuous at $\zeta \in \mathcal{Z}_c$. In addition Hartl et al. (1995) categorizes the types of contact conditions, depending on the order of a pure state constraint. For $q = 2$, a point contact occurs first, which is gradually transformed to a continuous contact.

Second-order optimality conditions

The general solution of an optimal control problem involves the satisfaction of the minimum Pontryagin's principle. By minimizing the Hamiltonian with respect to the control variable and deriving the canonical equations of the augmented Hamiltonian, we arrive at a differential-algebraic system (DAE). This system can be solved by a shooting method. The stability of an optimal control problem is typically investigated by the shooting structure of the problem (Malanowski et al., 2004; Bonnans and Hermant, 2007b).

For an unconstrained, or a control-constrained optimal control problem, the shooting method can be easily applied. In this case, the shooting structure (e.g., Jacobian) can be directly derived for the unconstrained case, while when mixed-pure state constraints are present, the shooting method can be applied once the structure of active constraints is known (Bulirsch and Stoer, 2010; Betts, 2010). Nevertheless for state-constrained optimal control problems, the shooting structure cannot be easily obtained, especially if the order of a pure-state constraint is of high order $q > 2$. The existence of set-valued functions of the adjoint variables and point and/or continuous contacts makes the optimal control problem very challenging.

The first attempt to establish necessary conditions for an optimal control problem with pure state constraints is attributed to (Bryson et al., 1963; Bryson and Denham, 1964). In particular, Jacobson et al. (1971) presented the first results on the regularity of the multipliers and on contact conditions, which are associated with the order of the involved pure-state constraints. More analyticaly, this result shows that the spatial derivative of the control is continuous until an order relative to the order of the constraint and the nature of the contact conditions (continuous or point contact), as also explained in Section 4.2.2 for a pure-state constraint of order $q = 2$. This analysis of the junction conditions was considered the starting point in the derivation of second-order sufficient conditions. Various versions of Pontryagin's principle with state constraints were summarized by (Hartl et al., 1995).

Second-order sufficient conditions for first-order state constraints were first obtained by Malanowski (1995) using the implicit function theorem, which were later modified by Malanowski (1997) taking into account only the strictly active constraints. Then Malanowski et al. (2004); Malanowski and Maurer (2001) derived sensitivity results by applying the implicit function theorem to the shooting mapping for a parametric optimal control problem with first-order and

higher-order pure-state constraints, where the following assumptions hold; (1) the reference solution has a regular structure with a finite number of boundary subintervals and contact points and (2) strict complementarity conditions are satisfied. They realized that if the order of the pure-state constraint is $q \geq 2$, the derived solution can become sensitive due to the potential variation of entry contact points. Based on (Malanowski and Maurer, 2001; Malanowski et al., 2004) numerical examples can be found in (Augustin and Maurer, 2001). From this analysis it became even more apparent that additional contact conditions are required for a constrained stability analysis.

Inspired by Jacobson et al. (1971), Bonnans and Hermant (2007b) investigated an optimal control problem with a scalar pure-state constraint and established conditions for well-posedness of the shooting equations. In particular, Bonnans and Hermant (2007b) showed that the shooting algorithm is well-posed (i.e., invertible Jacobian) iff the no-gap second-order sufficient optimality condition holds. As explained in (Bonnans and Hermant, 2007a), a no-gap condition holds, when the only change between necessary and sufficient second-order optimality conditions is between a strict and non strict inequality, respectively. Bonnans and Hermant (2007a) provided additional contact conditions that should be satisfied for this purpose. The extension of it to the optimal control problem with a vector-valued state constraint of arbitrary orders can be found in (Bonnans and Hermant, 2009).

4.3 Numerical techniques for solving an optimal control problem

Numerical methods that solve an optimal control problem are presented herein (Bryson, 2016; Berkovitz and Medhin, 2012; Kornienko et al., 2014; Paiva and Fontes, 2015). These involve two different approaches; (1) the indirect and (2) the direct methods. An indirect method attempts to solve the optimal control necessary conditions. Based on Pontryagin's minimum principle, the differential-algebraic system (DAE) is obtained, which is solved by applying a shooting, or a collocation method. On the other hand, in a direct method, the optimality conditions are only indirectly obtained. Discretization of the control and/or the state variables is initially applied and the problem is then formed as a nonlinear optimization problem (NLP) subjected to (mixed-state and/or pure-state) constraints. More precisely, a direct method involves three main steps; (1) the transcription of the optimal control problem using a collocation method, (2) the solution of the derived nonlinear programming sub-problem (NLP) by applying a NLP solver (Nocedal, 2006) and (3) repetition of (1)-(2) until convergence of the problem. The derived solution is then used to check if the necessary conditions, the minimization conditions and the canonical equations are all satisfied.

Essentially, the indirect methods are more accurate than the direct methods as the solution

is based on the optimality conditions. Nevertheless the direct methods are preferable, because several numerical difficulties arise when an indirect method is applied. The necessary conditions of optimality involve a differential-algebraic system, namely the algebraic system by the minimization of the Hamiltonian with respect to the control and the first order ODE with respect the state and adjoint variables. To derive the solution, the partial derivatives of the Hamiltonian $\nabla_x H$, $\nabla_u H$ should be obtained which are usually computationally difficult, especially when the problem is complex and high dimensional (Betts, 2010). Another difficutly arises in the solution of the algebraic equation $\nabla_u H = 0$, as its derivation depends on the condition number of the matrix $\nabla_{uu} H$. Only if $\nabla_{uu} H$ is non-singular and specifically positive to get minimization of the Hamiltonian with respect to the control, a unique solution of the control variables can be obtained.

Even if the Hamiltonian is convex with respect to the control $\nabla_{uu} H > 0$, the solution of the system of the first order ODE with respect to the state and adjoint variables is non-trivial. This system together with the boundary and transversality conditions forms a two-point boundary value problem. To achieve its solution an initial guess of the involved variables is required. A classical shooting method is very sensitive to any noise, which is usually produced by an erroneous initial guess of the adjoint variables. Even with a reasonable guess of the adjoint variables, the numerical solution of the adjoint equations can be very ill-conditioned, as explained in detail by Betts (2010). Another numerical issue is met in optimal control problems with pure-state constraints. In fact, if the number, position and sequence of constrained/unconstrained subarcs are unknown, then its solution is infeasible.

The direct method is presented in detail in the following Section. The presentation involves (1) the application of a direct collocation method and (2) the numerical methods that are applied for solving a nonlinear optimization problem (NLP). Computational details, such as the exploitation of sparsity in the NLP, or the methodology in the computation of derivatives of the objective and constraint functions are omitted, see, for instance, (Jorge Nocedal, 2006; Bryson, 2016; Betts, 2010).

4.3.1 Direct collocation methods

An optimal control problem can be solved by two distinct classes of direct methods; (1) the simple, or multiple shooting method and (2) the collocation method. The direct shooting method shares several similarities with the numerical difficulties that arises in an indirect shooting method, such as the solution of the involved initial value problem. This is not the case in a direct collocation method. The initial value problem is avoided as the differential equations are approximated by collocation. Even though the discrete approximation of the variables can lead to a highly dimensional problem, the sparsity pattern, both in the Hessian matrix of the Lagrangian function and in the Jacobian matrix of the constraint functions does not make the

final form of the problem computationally cumbersome.

For these reasons, a direct collocation method is preferable. In particular, in a direct collocation method, the state and/or control of the original optimal control problem are approximated in some appropriate manner. In the case where only the control is approximated, the method is called a control parameterization method (Goh and Teo, 1988). When both the state and control are approximated, the method is called a state and control parameterization method (von Stryk, 1993). In either case, the optimal control problem is converted into a minimization problem of an algebraic equation subjected to finite-dimensional equality and inequality constraints. In other words, the collocation method is the bridge between an optimal control problem that involves continuous functions and an NLP that consists of a finite set of variables. This stage is called transcription process (Kraft, 1985).

Direct collocation methods involve the discretization of the differential equations using for instance, trapezoidal, Hermite–Simpson, or pseudospectral approximations (Elnagar et al., 1995; Betts, 1998, 2010). Consider a fixed interval $[s_o, s_f]$ which is divided by N equally-sized subintervals with the following intermediate nodes

$$s_o < s_1 \leq ... \leq s_N = s_f \tag{4.47}$$

In this manner, we derive the segments $[s_k, s_{k+1}]$ with $k = \{0, 1, ...N-1\}$. Based on this subdivision, the control variables $\mathbf{u} \in \mathbb{R}^{N_u}$ are usually chosen as piecewise linear interpolating functions between $\mathbf{u}(s_k)$ and $\mathbf{u}(s_{k+1})$ (von Stryk, 1993);

$$\bar{\mathbf{u}}(t) \approx \mathbf{u}(s_k) + \frac{s - s_k}{s_{k+1} - s_k} \left(\mathbf{u}\left(s_{k+1}\right) - \mathbf{u}\left(s_k\right)\right), \quad s \in [s_k, s_{k+1}] \tag{4.48}$$

and the state variables $\mathbf{x} \in \mathbb{R}^{N_x}$ are approximated by applying a M- degree piecewise polynomial

$$\bar{\mathbf{x}}(s) \approx \sum_{m=0}^{M} a_m^{(k)} \left(s - s_k\right)^m, \quad s \in [s_k, s_{k+1}] \tag{4.49}$$

where the coefficients $a_m^{(k)}$ are the $M+1$ polynomial coefficients for the interval $[s_k, s_{k+1}]$. These polynomial coefficients are computed by equating the continuous function of the state variable to its corresponding polynomial approximation at the endpoints of the interval, that is

$$\bar{\mathbf{x}}(s_k) = \mathbf{x}(s_k), \quad \bar{\mathbf{x}}(s_{k+1}) = \mathbf{x}(s_{k+1}) \tag{4.50}$$

and by matching the spatial derivatives $\mathbf{x}'(s) = \mathbf{f}(\mathbf{x}, \mathbf{u}, s)$ with $s \in [s_o, s_f]$ in a similar manner;

$$\frac{d\bar{\mathbf{x}}(s_k)}{ds} = \mathbf{f}\left(\mathbf{x}\left(s_k\right), \mathbf{u}(s_k), s\right), \quad \frac{d\bar{\mathbf{x}}(s_{k+1})}{ds} = \mathbf{f}\left(\mathbf{x}\left(s_{k+1}\right), \mathbf{u}(s_{k+1}), s\right) \tag{4.51}$$

Equations (4.50) and (4.51) constitute the (Lobatto) collocation conditions.

For instance, the trapezoidal method (see G. Fasano (2012)) is based on a quadratic interpolation polynomial. Hence, (4.49) can be written as

$$\bar{\mathbf{x}}(s) = a_o^{(k)} + a_1^{(k)}\,(s - s_k) + a_2^{(k)}\,(s - s_k)^2 \tag{4.52}$$

Computing (4.52) at node s_k, we get $\bar{\mathbf{x}}(s_k) = \mathbf{x}(s_k) = a_o^{(k)}$. The other polynomial coefficients are deduced by the spatial derivatives at s_k and s_{k+1}, as

$$\frac{d\bar{\mathbf{x}}(s_k)}{ds} = \mathbf{f}(\mathbf{x}\,(s_k)\,, \mathbf{u}(s_k), s) = \mathbf{f}_k = a_1^{(k)} \tag{4.53}$$

$$\frac{d\bar{\mathbf{x}}(s_{k+1})}{ds} = \mathbf{f}(\mathbf{x}\,(s_{k+1})\,, \mathbf{u}(s_{k+1}), s) = \mathbf{f}_{k+1} = a_1^{(k)} + 2a_2^{(k)}\,(s - s_k) \tag{4.54}$$

Substituting (4.53), (4.54) into (4.50) and using $\bar{\mathbf{x}}(s_k) = \mathbf{x}(s_k) = a_o^{(k)}$, we get

$$\bar{\mathbf{x}}(s) = \bar{\mathbf{x}}(s_k) + \mathbf{f}_k(s - s_k) + \frac{1}{2}\frac{(\mathbf{f}_{k+1} - \mathbf{f}_k)}{(s_{k+1} - s_k)}\,(s - s_k)^2 \tag{4.55}$$

which at node s_{k+1} leads to

$$\bar{\mathbf{x}}(s_{k+1}) = \mathbf{x}(s_k) + \frac{1}{2}\,(\mathbf{f}_{k+1} + \mathbf{f}_k)\,(s_{k+1} - s_k) \tag{4.56}$$

while the spatial derivative is simply written as

$$\frac{d\bar{\mathbf{x}}(s_k)}{ds} = \mathbf{f}_k + \frac{(\mathbf{f}_{k+1} - \mathbf{f}_k)}{(s_{k+1} - s_k)}\,(s - s_k) \tag{4.57}$$

Since $\bar{\mathbf{x}}(s_{k+1}) = \mathbf{x}\,(s_{k+1})$, the defect constraint $\zeta\,(s_k)$ at node s_k is finally derived

$$\zeta\,(s_k) = \mathbf{x}\,(s_{k+1}) - \mathbf{x}(s_k) - \frac{1}{2}\,(\mathbf{f}_{k+1} + \mathbf{f}_k)\,(s_{k+1} - s_k) \tag{4.58}$$

and considering the nodes $j = \{0, 1, ...N - 1\}$, a vector of defect constraints with dimension $N_x N$ is obtained.

In a similar way, other (Lobatto) collocation methods, such as the Hermite-Simpson method with a cubic interpolating polynomial can be also adopted. Nevertheless the matching of the spatial derivatives can be also applied at different nodes rather than at the endpoints of the interval. In fact, in a Gauss mathod, the collocation conditions are imposed somewhere in the interior of the interval, while in a Radau method at most one of the endpoints s_k, or s_{k+1} is a collocation point (Betts, 2010, 1998).

Quite recently, the standard collocation methods were extended to orthogonal, or speudospectral methods. Even though the mathematics around the orthogonal collocation methods was established by (Reddien, 1979), only recently they gained a lot of interest. There are several classses of methods; (1) the Legendre pseudospectral method (Elnagar et al., 1995), (2) the Radau orthogonal collocation method (Kameswaran and Biegler, 2007), (3) the Chebyshev pseudospectral method (Vlassenbroeck and Dooren, 1988), and (4) the Gauss pseudospectral method (Benson et al., 2006). Comparison of the orthogonal, or pseudospectral collocation methods can be found in (Huntington and Rao, 2008).

The main difference between an orthogonal and a standard collocation method is the way the collocation points are chosen. Specifically, in an orthogonal collocation method, the collocation points are not predefined as in the standard collocation methods. Instead, they are indirectly derived by the roots of an orthogonal polynomial. In this manner, we can compute a more accurate quadrature approximation of an integral when compared to a standard collocation method. A comprehensive description of speudospectral, or orthogonal collocation methods can be found in (Elnagar et al., 1995).

Applying a standard, or a speudospectral collocation method, we can transform an optimal control problem to a finite-dimensional minimization problem with inequality constraints

$$\begin{cases} \text{Minimize} & \mathcal{J}(\mathbf{y}) \\ \text{subject to} & \\ & \mathbf{Z}(\mathbf{y}) \leq 0 \\ & \mathbf{E}(\mathbf{y}) \leq 0 \\ & \mathbf{G}(\mathbf{y}) \leq 0 \end{cases} \tag{4.59}$$

where $\mathbf{y} \in \mathbb{R}^{N_y}$ with $N_y = (N+1)(N_x+N_u)$ is the vector, which represents the values of the state and control variables at the nodes of the interval $[s_o, s_f]$, $\mathbf{Z} : \mathbb{R}^{N_y} \to \mathbb{R}^{N_\zeta}$ with $N_\zeta = N_x N$ is the vector of the defect constraints and $\mathbf{E} : \mathbb{R}^{N_y} \to \mathbb{R}^{(N+1)N_g}$, $\mathbf{G} : \mathbb{R}^{N_y} \to \mathbb{R}^{(N+1)N_g}$ are the discrete representations of the endpoints cost and the equality/inequality constraints, respectively. This is a classical inequality-constrained nonlinear programming problem (NLP), which can be solved by applying a NLP solver, such as IPOPT (Wachter and Biegler, 2005; Biegler and Zavala, 2009), SNOPT (Barclay et al., 1998; Gill et al., 2002), and KNITRO (Byrd et al., 2003, 2006). A short description of these solvers is shown below.

4.3.2 The NLP problem

A nonlinear optimization problem (NLP) is a minimization problem of a nonlinear objective function $f : \mathbb{R}^n \to \mathbb{R}$ with respect to $\mathbf{x} \in \mathbb{R}^n$ under the presence of bilateral (equality) and

unilateral (inequality) constraints $\mathbf{g} : \mathbb{R}^n \to \mathbb{R}^m$ with $m \leq n$, which can be written as

$$\begin{aligned} \min_{x \in \mathbb{R}^n} \quad & f(\mathbf{x}) \\ \textit{subject to} \quad & g_i(\mathbf{x}) = 0, \qquad i \in \mathcal{I}_\mathcal{E} \\ & g_i(\mathbf{x}) \geq 0, \qquad i \in \mathcal{I}_\mathcal{I} \end{aligned} \tag{4.60}$$

where $\mathcal{I}_\mathcal{E}$,$\mathcal{I}_\mathcal{I}$ are the index sets for the equality and inequality constraints, respectively.

There are various techniques that can be applied to solve (4.60). If the constraints are linear and the objective function is quadratic, the optimization problem is called quadratic (QP). A linear equality, or inequality constraint can be formulated as $\mathbf{Ax} = \mathbf{b}$, or $\mathbf{Ax} \geq \mathbf{b}$, where $\mathbf{A}$ is an $m \times n$ matrix and $\mathbf{b} \in \mathbb{R}^m$. A quadratic objective function is given by $f(\mathbf{x}) = \mathbf{x}^\top \mathbf{Hx}/2 + \mathbf{x}^\top \mathbf{c}$, where $\mathbf{c} \in \mathbb{R}^n$ is a vector and $\mathbf{H}$ is a $n \times n$ matrix which is called the Hessian matrix. If the Hessian matrix is positive (semi)-definite, the quadratic problem is called convex and its solution is simpler than a non-convex program, where several stationary points and local minima can be present. In particular, if the Hessian matrix is positive (semi)-definite and the KKT conditions are satisfied, then a unique global solution is always derived.

Alternative methodologies for the solution of the constrained optimization problem (4.60) are also available, especially when the objective function is not quadratic. These methodologies have a common motivation; to replace the constrained optimization problem by a single function that includes the objective function with an additional term for every constraint function, leading to an unconstrained optimization problem (Jorge Nocedal, 2006). These approaches are the penalty and augmented Lagrangian methods. For example, the exact penalty function is given by

$$f(x) + \mu \sum_{i \in \mathcal{I}_\mathcal{E}} |g_i(x)| + \mu \sum_{i \in \mathcal{I}_\mathcal{I}} [g_i(x)]^- \tag{4.61}$$

where $[g_i(x)]^- = \max\{0, -g_i(x)\}$. On the other hand, the augmented Lagrangian function $\mathcal{L}_\mathcal{A}(x, \lambda, \mu)$ is a combination of the quadratic penalty function and the Lagrangian function. For instance, for an equality-constrained problem, it can be written as

$$\mathcal{L}_\mathcal{A}(x, \lambda, \mu) = f(x) - \sum_{i \in \mathcal{I}_\mathcal{E}} \lambda_i g_i(x) + \frac{\mu}{2} \sum_{i \in \mathcal{I}_\mathcal{E}} g_i^2(x) \tag{4.62}$$

where the first two terms constitute the Lagrangian function $\mathcal{L}(\boldsymbol{x}, \boldsymbol{\lambda})$ and $\boldsymbol{\lambda} \in \mathbb{R}^m$ is the Lagrange multiplier vector, associated with the equality constraints $\mathbf{g} : \mathbb{R}^n \to \mathbb{R}^m$.

Nevertheless when the constraints are nonlinear, the optimization problem is highly dimensional, or nonconvex issues are present, alternative approaches are applied, such as sequential quadratic programming (SQP) (or active-set) and interior-point (or barrier) methods. These approaches are currently considered the most powerful numerical techniques for large-scale nonlinear inequality-constrained programming.

One main difference between the SQP approach and the interior point methods is the procedure that is adopted to consider the inequality constraints. SQP algorithm initiates by making a guess of the optimal active set $\mathcal{I}_{\mathcal{A}}$, which contains only the strictly active constraints $g_i(x) = 0$. This implies that the optimal active set is a subset of the involved inequality constraints $\mathcal{I}_{\mathcal{A}} \subseteq \mathcal{I}_{\mathcal{I}}$. The corresponding optimization problem is solved by utilizing only equality constraints and ignoring the rest of the inactive constraints. As the problem then iterates, an update of the active set is required in order to satisfy the KKT conditions. The appropriate choice of the initial active set and its accurate update in later stages constitute a very challenging problem in nonlinear optimization that is called "combinatorial" difficulty of inequality constrained problems (Nocedal, 2006).

A different methodology is followed by interior-point (or barrier) methods as all equality-inequality constraints are included. In particular, the problem is solved in a manner that it stays inside the feasible region defined by the constraints, which is achieved by applying a barrier function. As the optimal solution is approached, the effect of the barrier function is gradually diminished such that an accurate result is obtained. Hence, the interior-point method is superior to SQP approach in this aspect, because the combinatorial issues of nonlinear programming are avoided. In this method, however, the whole set of constraints is hold even if a subset of these inequality constraints does not probably affect the result of the problem, leading to higher dimension of the optimization program and accordingly affecting the computational cost.

Nevertheless numerical tests show that interior-point methods are usually faster than active-set SQP methods on large problems, particularly when the number of free variables is also large (Nocedal, 2006). On the other hand, the opposite holds if the number of active constraints is nearly as large as the number of variables, implying a small number of free variables. In this particular case, SQP method can be faster and more robust when compared to the interior-point method, especially if the latter is badly scaled.

Before the presentation of the two methodologies some complementary material is included. This involves the classical Newton method of an equality-constrained optimization problem, traditionally applied for the solution of subproblems of both approaches. A short illustration of the merit and filter functions is also included, which are applied to decide whether an iteration step is acceptable, or further improvement is required.

Newton method

In practice, the inequality-constrained problem (4.60) is always transformed to an equality-contrained problem of the form;

$$\begin{aligned} \min_{x \in \mathbb{R}^n} \quad & f(\mathbf{x}) \\ \text{subject to} \quad & \mathbf{g}(\mathbf{x}) = 0 \end{aligned} \tag{4.63}$$

by adopting two distinct methodologies; (i) the whole set of inequality constraints is transformed into equality constraints using slack variables, or (ii) the active set is only included, which involves, by definition, only closed constraints. An additional necessary condition is essential for inequality-constrained problem, namely the non-negative value of their correspondent Lagrange multipliers. More specifically, for an inactive inequality constraint $g_i > 0$ a zero value of Lagrange multiplier $\lambda_i = 0$ is implied, while for an active constraint $g_i = 0$ a positive Lagrange multiplier is expected $\lambda_i > 0$. This is the well-known complementarity condition $g_i \lambda_i = 0$.

The Lagrangian function of the problem is $\mathcal{L}(\mathbf{x}, \boldsymbol{\mu}) = f(\mathbf{x}) - \boldsymbol{\lambda}^\top \mathbf{g}(\mathbf{x})$, where $\boldsymbol{\lambda} \in \mathbb{R}^m$ are the Lagrange multipliers. Let us denote as $\mathcal{G}(\mathbf{x})$ the Jacobian matrix of the constraints

$$\mathcal{G}(\mathbf{x})^\top = [\nabla g_1(\mathbf{x}), \nabla g_2(\mathbf{x}), ..., \nabla g_m(\mathbf{x})] \tag{4.64}$$

where $g_i(\mathbf{x})$ is the ith component of the constraint vector $\mathbf{g}(\mathbf{x})$. The first-order optimality (KKT) conditions can be written as a $(n+m)$-system of equations

$$\mathcal{F}(\mathbf{x}, \boldsymbol{\mu}) = \begin{bmatrix} \nabla f(\mathbf{x}) - \mathcal{G}(\mathbf{x})^\top \boldsymbol{\lambda} \\ \mathbf{g}(\mathbf{x}) \end{bmatrix} = \mathbf{0} \tag{4.65}$$

with unknowns $\mathbf{x} \in \mathbb{R}^n$ and $\boldsymbol{\lambda} \in \mathbb{R}^m$.

Let us now describe the most classical methodology to solve (4.63) for a single step k. Deriving the Jacobian of the system, the Newton's method from a known pair of (x_k, μ_k) of the k-step can be expressed as

$$\begin{bmatrix} \nabla^2_{\mathbf{xx}} \mathcal{L}_k & -\mathcal{G}_k^\top \\ \mathcal{G}_k & 0 \end{bmatrix} \begin{Bmatrix} \triangle \mathbf{x}_k \\ \triangle \boldsymbol{\mu}_k \end{Bmatrix} = - \begin{Bmatrix} \nabla f_k - \mathcal{G}_k^\top \boldsymbol{\lambda}_k \\ \mathbf{g}_k(\mathbf{x}) \end{Bmatrix} \tag{4.66}$$

where $f(x_k) = f_k$, $\mathbf{x}_{k+1} = \mathbf{x}_k + \triangle \mathbf{x}_k$ and $\boldsymbol{\lambda}_{k+1} = \boldsymbol{\lambda}_k + \triangle \boldsymbol{\lambda}_k$. The matrix on the left side of (4.66) is called the Karush–Kuhn–Tucker (KKT) matrix. To derive a unique solution for a Newton step, the condition number of the Karush-Kuhn-Tucker (KKT) matrix is crucial. In fact, the non-singularity of this matrix quarantees the uniqueness of the solution. This can be achieved if the Jacobian $\mathcal{G}(\mathbf{x})$ has full row rank, which implies linear independence constraint qualification (LICQ) and the Hessian matrix $\mathbf{H} = \nabla^2_{\mathbf{xx}} \mathcal{L}(\mathbf{x}, \boldsymbol{\mu})$ is positive definite $\mathbf{v}^\top \nabla^2_{\mathbf{xx}} \mathcal{L}(\mathbf{x}, \boldsymbol{\mu}) \mathbf{v} > 0$ in the tangent space of the constraints, defined by $\mathcal{G}(\mathbf{x})\mathbf{v} = 0$. In case, however, the Hessian $\nabla^2_{\mathbf{xx}} \mathcal{L}_k$ is not positive definite, or the active-set is not properly defined, numerical issues can be met. Multiple numerical techniques can be applied in these cases, such as a quasi-Newton method when for instance a large matrix is involved and its inverse is computationally cumbersome. There are two widely used quasi-Newton techniques; (i) the BFGS method, where a rank-two positive secand update is assumed (Fletcher, 1970; Goldfarb, 1970; Shanno, 1970) and (ii) the SR1 method, where a symmetric rank-one is applied. Even though a recursive update is easier

to implement, the correspondent quasi-Newton method exhibits a superlinear convergence when compared to the classical Newton method, which provides a quadratic convergence. This implies that a larger number of iterations are usually required in the case of a quasi-Newton method.

After the completion of a single step, some additional criteria are required in order to ensure the acceptance of the step, or to improve the size of it. These criteria are described in the following Section.

Criteria for step size control and acceptance/rejection

Let us suppose that a Newton step is applied, as explained in Section 4.3.2. If the value of the objective function is reduced, or increased at the end of the step while the violation of the unilateral constraints is increased, or decreased, respectively, it is not easy to decide if this step is acceptable. In other words, the main goal is to find the best methodology to achieve a simultaneous reduction of the objective function and the violation of the constraints at every single Newton step. To this point, methods for correcting deficiencies of Newton's methods are available, which are called "globalization strategies". In particular, to solve this issue, merit functions and/or filter methods are typically applied.

In merit functions, the cost function and the constraints are combined into a single minimization problem. For instance, a merit function is simply given by

$$\phi_1(x;\mu) = f(x) + \mu \sum_{i \in \mathcal{I}_\mathcal{E}} |g_i(x)| + \mu \sum_{i \in \mathcal{I}_\mathcal{I}} |g_i(x)|^- \tag{4.67}$$

where μ is a positive penalty parameter. The particular merit function (4.67) is called ℓ_1 penalty function, which is not differentiable because of the presence of inequality constraints. Nevertheless the choice of an appropriate value of the penalty parameter μ is a difficult task. Instead, a filter technique can be applied, where the minimization of the cost function and the set of the constraints are applied seperately. In particular, a measure of infeasibility is defined

$$h(x) = \sum_{i \in \mathcal{I}_\mathcal{E}} |g_i(x)| + \sum_{i \in \mathcal{I}_\mathcal{I}} [g_i(x)]^- \tag{4.68}$$

which includes only the constraints. For every step, a new pair of $\left\{ \min_x f(x), \min_x h(x) \right\}$ is derived. The list of these pairs constitutes the so-called filter. If the current pair is not dominated by any other pair in the filter, the particular step is accepted.

Some algorithms based on merit functions, or filters may fail to converge rapidly because they reject steps that make good progress toward a solution. This undesirable phenomenon is typically called the Maratos effect (Nocedal, 2006). To eliminate this effect second-order correction steps (SOC) can be applied, which lead to a fast local convergence (Wachter and Biegler, 2005). We can also use a merit function, such as Fletcher's augmented Lagrangian

function, which does not suffer from the Maratos effect (Ulbrich, 2003).

These merit and/or filter methods are applied in combination with a line-search method, or a trust-region method. More specifically, in line search methods, the magnitude of the step is adjusted by applying criteria defined by a merit, or a filter method. In trust-region methods, a merit, or filter method aims to determine whether the step is accepted, or rejected and if the trust-region radius should be adjusted. This also implies that in trust-region methods, a simultaneous correction of the magnitude and the direction of a step can be applied. The choice of the approach is based on the problem under consideration.

In a line-search method, the size of a step $\triangle \mathbf{x}_k$ is derived by the following expression

$$\alpha_k^{\max} = \max \{\alpha \in (0,1] : x_k + \alpha \triangle \mathbf{x}_k \geq (1-\tau)\, x_k\} \tag{4.69}$$

with $\tau \in (0,1)$ (a typical value of τ is 0.995). (4.69) is the maximum length that satisfies a sufficient decrease of a merit function, or ensuring acceptability of a filter at the end of a step $\triangle \mathbf{x}_k$. The new iterate is then defined as

$$x_{k+1} = x_k + \alpha_k^{\max} \triangle \mathbf{x}_k \tag{4.70}$$

If the Hessian $\nabla^2_{\mathbf{xx}} \mathcal{L}_k$ is not necessarily positive definite and Jacobian singularities $\mathcal{G}_k$ are possibly present, a trust-region method is a better choice. In this case, a trust-region constraint is included which can be written as

$$\| \triangle \mathbf{x}_k \| \leq \Delta_k \tag{4.71}$$

and indicates that every step $\triangle \mathbf{x}_k$ should lie inside the trust region, defined by the circle of radius Δ_k. The trust-region constraint (4.71) is an additional constraint of the problem with its associated Lagrange multiplier τ, also called Levenberg parameter (Levenberg, 1944). The classical methodology is to assign a constant radius Δ_k and update the Levenberg parameter τ such that $\| \triangle \mathbf{x}_k \| = \Delta_k$. Nevertheless the choice of the value of Δ_k is under question. If the assigned value of Δ_k is not appropriate, the solution can be remarkably affected. This numerical issue is eliminated by using a merit, or a filter method, as mentioned above and explained in detail in (Bonnans, 2006; Nocedal, 2006).

Active-set or SQP approach

One approach to solve (4.60) for a single step $\triangle \mathbf{x}_k$ is the sequential quadratic programming method (SQP), or active-set method, which can be written in the following form

$$\begin{array}{ll} \min\limits_{\triangle \mathbf{x}_k \in \mathbb{R}^n} & f_k + \nabla f_k^\top \triangle \mathbf{x}_k + (\triangle \mathbf{x}_k)^\top \nabla^2_{\mathbf{xx}} \mathcal{L}_k \triangle \mathbf{x}_k / 2 \\ \text{subject to} & g_k^i + \mathcal{G}_k^i \triangle \mathbf{x}_k = 0, \qquad i \in \mathcal{I}_\mathcal{E} \\ & g_k^i + \mathcal{G}_k^i \triangle \mathbf{x}_k \geq 0, \qquad i \in \mathcal{I}_\mathcal{I} \end{array} \tag{4.72}$$

This formulation is obtained by applying a linear approximation of the equality/inequality constraints $\mathbf{g}(\mathbf{x})$ (4.72b),c)) and a quadratic approximation of the cost function, or a pure quadratic approximation of the Lagrangian function $\mathcal{L}_k$ if equality constraints are only included.

There are two main procedures for solving (4.72), the inequality-constrained QP (IQP) approach and the equality-constrained (EQP) QP method. In the former case, there is an initial guess of the active set of the inequality constraints, which remains unchanged during iteration. For this active set, a Newton method is then applied. The second approach selects a subset of constraints at each iteration to be the so-called working set $\mathcal{I}_\mathcal{W}$, and solves only equality-constrained subproblems of (4.72), where the constraints in the working sets are imposed as equalities and all other constraints are ignored.

A possible difficulty with SQP methods is that the linearizations (4.72) of the nonlinear constraints may lead to an infeasible subproblem. To overcome this difficulty, the nonlinear optimization program can be formulated as a ℓ_1 penalty program

$$\begin{array}{ll} \min\limits_{x \in \mathbb{R}^n} & f(\mathbf{x}) + \mu \sum\limits_{i \in \mathcal{I}_\mathcal{E}} (r_i + s_i) + \mu \sum\limits_{i \in \mathcal{I}_\mathcal{E}} t_i \\ \text{subject to} & g_i = r_i - s_i, \qquad i \in \mathcal{I}_\mathcal{E} \\ & g_i \geq -t_i, \qquad i \in \mathcal{I}_\mathcal{I} \\ & \mathbf{r}, \mathbf{s}, \mathbf{t} \geq 0 \end{array} \tag{4.73}$$

where $\mathbf{r}, \mathbf{s}, \mathbf{t}$ are slack variables that allow relaxation of the inequality constraints and μ is a penalty parameter with necessarily positive value. The quadratic subproblem (4.72) associated with (4.73) is always feasible. This formulation is used by Barclay et al. (1998); Gill et al. (2002) in the SNOPT software package.

Another alternative methodology, the so-called sequential linear-quadratic programming (SLQP) method has been proposed by Byrd et al. (2003, 2006) in KNITRO package, where a two-step procedure is suggested. In particular, a linear program (LP) is first solved to calculate the working set $\mathcal{I}_\mathcal{W}$, which consists of the active inequality-equality constraints. This linear program (LP) includes the linear approximation of the main problem (i.e., the Hessian $\nabla^2_{\mathbf{xx}} \mathcal{L}_k$ is not included) and a trust-region constraint (4.71) is applied for improving the magnitude and the direction of the first iteration step. For the derived working set $\mathcal{I}_\mathcal{W}$, the EQP associated problem of (4.73) is then solved with a new trust-region constraint (4.71).

SQP methods often use a merit function in combination with a line search, or a trust region method to decide whether a trial step should be accepted. A variety of merit functions have

been used in SQP methods, such as nonsmooth penalty functions and augmented Lagrangians.

Interior point methods

The interior-point method, or barrier method is formulated in a different manner. The nonlinear inequality-constrained optimization problem (4.60) is transformed to the following equality-constrained optimization problem

$$\begin{array}{lll} \min\limits_{x\in\mathbb{R}^n} & f(\mathbf{x}) & \\ \textit{subject to} & g_i(\mathbf{x}) = 0 & i \in \mathcal{I}_{\mathcal{E}} \\ & g_i(\mathbf{x}) - s_i = 0 & i \in \mathcal{I}_{\mathcal{I}} \\ & \mathbf{s} \geq 0 & \end{array} \tag{4.74}$$

where $\mathbf{s} \in \mathbb{R}^{\mathcal{I}}$ is a vector of slack variables. If an inequality of the form $g(\mathbf{x}) < 0$ is included, (4.74c) becomes $g(\mathbf{x}) + s = 0$ with $s \geq 0$.

Interior-point methods can be seen as continuation methods, or as barrier methods. In a continuation (or homotopy) method, a perturbed KKT condition is derived, which can be written as

$$\begin{array}{c} \nabla f(\mathbf{x}) - \mathcal{G}_{\mathcal{E}}^{\top}(\mathbf{x})\,\mathbf{y} - \mathcal{G}_{\mathcal{I}}^{\top}(\mathbf{x})\,\mathbf{z} = \mathbf{0} \\ \mathbf{S}\mathbf{z} - \mu\mathbf{e} = \mathbf{0} \\ \mathbf{g}_{\mathcal{E}}(\mathbf{x}) = \mathbf{0} \\ \mathbf{g}_{\mathcal{I}}(\mathbf{x}) - \mathbf{s} = \mathbf{0} \\ \mathbf{s} \geq \mathbf{0}, \quad \mathbf{z} \geq \mathbf{0} \end{array} \tag{4.75}$$

with $\nu \geq 0$ and $\mathbf{g}_{\mathcal{E}}(\mathbf{x}), \mathbf{g}_{\mathcal{I}}(\mathbf{x})$ are the equality and inequality constraints with associated Jacobians $\mathcal{G}_{\mathcal{E}}(\mathbf{x}), \mathcal{G}_{\mathcal{I}}(\mathbf{x})$ and Lagrange multipliers $\mathbf{y}, \mathbf{z}$, respectively. We define S and Z to be the diagonal matrices whose diagonal entries are given by the vectors $\mathbf{s}$ and $\mathbf{z}$, respectively, and let $e = (1, 1, ..., 1)^{\top}$ (Jorge Nocedal, 2006; Nocedal, 2006). For a fixed value of μ a Newton method is applied, which in this case is called a primal-dual system. The homotopy approach consists of solving (4.75) for a sequence of positive parameters $\{\mu_j\}$ until it converges to zero, while maintaining $\mathbf{s}, \mathbf{z} > \mathbf{0}$. If $\mu = 0$ is reached, the KKT conditions are derived. Furthermore, by requiring the iterates to decrease a merit function (or to be acceptable to a filter), the iteration can possibly converge to a minimizer, not simply a KKT point (Bonnans, 2006; Nocedal, 2006).

The second derivation of interior-point methods associates (4.74) with a barrier function

$$\begin{array}{lll} \min\limits_{x\in\mathbb{R}^n} & f(\mathbf{x}) - \mu \sum\limits_{i=1}^{m} \log s_i & \\ \textit{subject to} & g_i(\mathbf{x}) = 0 & i \in \mathcal{I}_{\mathcal{E}} \\ & g_i(\mathbf{x}) - s_i = 0 & i \in \mathcal{I}_{\mathcal{I}} \end{array} \tag{4.76}$$

where μ is a positive parameter and $\log(\cdot)$ denotes the natural logarithm function. The barrier function $\log s_i$ is very large when $s_i \to 0$ and consequently it can be viewed as a "barrier" in the minimization process. Problem (4.76) does not include the additional constraint $\mathbf{s} \geq \mathbf{0}$ that is required in (4.74). The barrier approach consists of finding successive solutions of the problem (4.76) for a sequence of positive barrier parameters μ_j until the KKT conditions are satisfied (i.e., $\mu_j \to 0$), as above.

Specifically, the derivation of (4.76) can be translated as follows; the logarithmic barrier function is given by

$$\varphi_\mu(x) = f(\mathbf{x}) - \mu \sum_{i=1}^{m} \log(g_i(x))$$

subjected to the perturbed complementarity condition (perturbed KKT system)

$$g_i(x)\lambda_i = \mu \tag{4.77}$$

where μ is the barrier, or homotopy parameter. The gradient of barrier function is then derived, as follows

$$\nabla\varphi_\mu(x) = \nabla f(\mathbf{x}) - \mu \sum_{i=1}^{m} \frac{\nabla g_i(x)}{g_i(x)} \tag{4.78}$$

If we substitute (4.77) into (4.78), we get

$$\nabla\varphi_\mu(x) = \nabla f(\mathbf{x}) - \lambda \nabla \mathbf{g}(x) = 0 \tag{4.79}$$

which means that the gradient of $f(x)$ should lie in the subspace, spanned by the gradient of the unilateral constraint. This system of primal-dual equations (4.79) subject to (4.77) is repeatedly solved until the convergence of the problem (i.e., $\mu = 0$).

Wachter and Biegler (2005); Biegler and Zavala (2009) have suggested an interior-point software package, IPOPT that includes a line-seach method in combination with a filter method and second-order corrections for a faster convergence of the above barrier problem. This is the NLP solver, applied in the current study. On the other hand, alternative software packages are also available such as KNITRO, which is a barrier method with a line search, or a trust-region algorithm, see (Chen et al., 2014; Waltz et al., 2005).

Chapter 5

Optimization-based stability analysis of constrained weightless elastica

5.1 Introduction

The stability problem of a constrained elastic structure is widely encountered in engineering and medical applications. In particular, the constrained buckling of the drill-pipes is a crucial issue in oil drilling operations (Gao and Miska, 2009b,a; Wicks et al., 2008; Miller, 2014; Gao and Huang, 2015; Huang et al., 2015; Sun et al., 2015). To solve the constrained buckling problem simplified analyses based on a spectral decomposition method are typically used (Wicks et al., 2008; Gao and Huang, 2015; Gao and Miska, 2009a). Similar applications can be found in the insertion of a guidewire, or a catheter into blood vessels (Duriez et al., 2006; Li et al., 2011b; Tang et al., 2012; Lenoir et al., 2006). In the latter case, the focus is placed on an accurate real-time simulation rather than a stability analysis.

While the buckling of a slender object is a classical topic (Love, 2013; Bigoni, 2016; Wang et al., 2004; Wang, 1997), the constrained stability problem has not been investigated extensively. Two distinct classes of problems can be found: (i) the constrained buckling problem of an elastic structure of constant length with a movable end (classical stability problem) (Domokos et al., 1997; Holmes et al., 1999) and (ii) the stability problem of an elastica of variable length inside a conduit (insertion stability problem) (Denoel and Detournay, 2011; Huynen et al., 2016; Lu and Chen, 2008).

Maurer (1979) was the first to derive the buckling response of a nonlinear beam under the presence of unilateral constraints by applying an optimal control method. Nevertheless Maurer

and Mittelmann (1991)'s innovative idea remained almost unknown for several years and only recently O'Reilly and Peters (2012) and Sachkov (2008a) revisited the optimal control concept for the buckling analysis of elastic rods, limited only to unconstrained conditions.

Inspired by Maurer (1979) and Liberzon (2012), we extend this idea to the stability problem of thin elastic structures constrained by rigid obstacles. Instead of using the calculus of variations, the optimal control method is applied. The direct method is adopted for the solution of the constrained stability problem. In particular, the interface ICLOCS (Falugi P. and van Wyk, 2010), which is connected with a interior-point filter line-search algorithm IPOPT (Biegler and Zavala, 2009; Wachter and Biegler, 2005), is used. Details can be found in Chapter 4.

The optimal control problem consists of formulating the potential energy of the elastica subject to the spatial derivatives of the state variables (i.e., spatial dynamics of the system) and the inequality constraints. The state variables involve the cartesian coordinates of the elastica and the Euler angles. The evolution of the cartesian coordinates in space is derived by applying the inextensibility-unshearability constraints, while the spatial derivatives of the Euler angles are the control variables of the problem. Lastly, the unilateral constraints represent the presence of rigid longitudinal obstacles. These unilateral constraints are imposed by predefining lower and upper bounds on the corresponding state variables and are particularly second-order pure-state constraints. As explained in detail in (Maurer and Mittelmann, 1991; Malanowski and Maurer, 2001; Bonnans and Hermant, 2009; Hartl et al., 1995; Bryson et al., 1963; Bryson and Denham, 1964; Jacobson et al., 1971), the existence of a second order pure state constraint leads to set-valued functions of the adjoint equations. This discontinuity is physically understood due to the presence of pointwise contact forces, whenever the elastica comes in contact with the wall. A more detailed analysis of an optimal control problem with other types of constraints can be found in (Bryson, 2016; Berkovitz and Medhin, 2012; Ross, 2015).

At the beginning of the Chapter, the classical stability problem is analyzed. From the governing equations of the problem we show step-by-step the equivalence of a classical calculus of variations problem to an optimal control problem, including a concrete example. The corresponding optimal control formulation for the insertion stability problem is also briefly presented. These two classes of stability problems are investigated by varying several factors, such as the clearances of the walls, the boundary and loading conditions. The method is shown to reproduce numerical results published in the literature for a planar elastica of either constant or variable length, for any combination of boundary conditions and different types of longitudinal obstacles (Domokos et al., 1997; Manning and Bulman, 2005; Ro et al., 2010; Fang et al., 2013).

In the final Section, we complete our study with the investigation of the constrained stability of a spatial elastica, or Kirchhoff rod. Initially, the optimal control problem of a spatial elastica is formulated and its optimality conditions are demonstrated. Validation of the optimal control formulation is performed for contact-free conditions. A particular example of a clamped-clamped spatial elastica constrained by a cylindrical wall is then solved and its derivation is compared

with published results (Fang et al., 2013).

5.2 Stability of constrained planar elastica

The optimal control problem is formulated to study the stability of a planar elastica of constant length constrained by two rigid horizontal walls (classical stability problem). This particular problem for force-controlled conditions is described below. The methodology of optimal control is clarified and its equivalence to a calculus of variation problem is described. A representative example is also included.

5.2.1 Description of the problem

A weightless planar elastica of constant length L and uniform bending rigidity EI is considered. The left end of the elastica is fixed while the right end is free to move horizontally. Its initial configuration is stress-free (i.e., straight elastica). The supports of the elastica are either clamped at zero inclination, or pinned. The planar elastica is constrained by symmetrically, or non-symmetrically located horizontal longitudinal obstacles of clearances C_u, C_l, where u, l hold for the upper and lower walls, respectively. The concern of this study is the post-buckling behavior of the elastica under the action of an axial compressive force Q at the right end. This action leads to shortening of the distance between the two supports. The derived displacement is denoted by Δ. This is the so-called classical stability problem for force-controlled conditions.

The problem is described in a system of coordinates (X, Y) with associated inclination angle $\Theta(S)$ about the X-axis. More specifically, we define a system of coordinates (X, Y) with origin at the left end of the elastica, see Figure 5.1. We also introduce the arc-length coordinate S with its origin $S = 0$ at $X = 0$ and $Y = 0$. In its initial configuration, the elastica is straight implying that $\Theta(S) = 0$, $0 \leq S \leq L$. Due to the inextensibity and unshearability constraints, its deformed configuration $\hat{X}(S)$, $\hat{Y}(S)$ is fully defined by the function $\Theta(S)$ and the origin of the system. In view of the imposed boundary conditions, the additional condition of the cartesian coordinate $\hat{Y}(L) = 0$ should be also satisfied. The end-shortening is expressed as $\Delta = L - \hat{X}(L)$ and the rigid horizontal longitudinal obstacles are formulated mathematically by imposing the unilateral constraints $C_l \leq \hat{Y}(S) \leq C_u, \quad 0 < S < L$.

Figure 5.1 illustrates a particular configuration of a clamped-clamped elastica with two discrete contacts at P_1 and P_2. The internal force $R(S)$ with its inclination $\alpha(S)$ about the X-axis is also shown. The relation between the applied force Q and the internal force $R(S)$ is simply given by $Q = R\cos\alpha = R_x$. The horizontal force is uniform since the effect of the friction is neglected, while the shear force $R_y = R\sin\alpha$ is piecewise uniform as it is discontinuous at contact points.

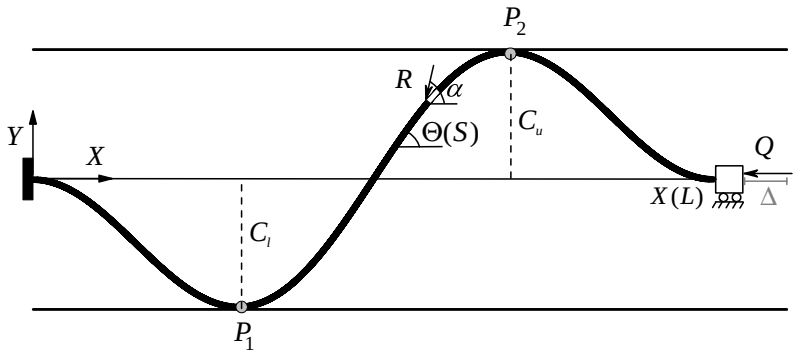

Figure 5.1: Description of the classical stability problem for a clamped-clamped elastica

Scaling of the problem follows from adopting L as length scale and EI/L^2 as force scale

$$s = \frac{S}{L}, \quad x = \frac{X}{L}, \quad y = \frac{Y}{L}, \quad c_{u,l} = \frac{C_{u,l}}{L}, \quad \delta = \frac{\Delta}{L}, \quad \mathcal{R} = \frac{RL^2}{EI}, \quad \mathcal{Q} = \frac{QL^2}{EI} \tag{5.1}$$

The cartesian coordinates of the elastica $\hat{x}(s)$, $\hat{y}(s)$ are derived by $\theta(s)$ through integration

$$\hat{x}(s) = \int_0^s \cos\theta \mathrm{d}\xi, \qquad \hat{y}(s) = \int_0^s \sin\theta \mathrm{d}\xi \tag{5.2}$$

taking into account the boundary conditions $\hat{x}(0) = \hat{y}(0) = 0$. At the right end $\hat{x}(1) = 1 - \delta$ and $\hat{y}(1) = 0$, while the unilateral constraints are given by $c_l \leq \hat{y}(s) \leq c_u, \quad 0 < s < 1$.

The dimensionless form of the potential energy of the elastica can be written as follows

$$\Pi = \frac{1}{2}\int_0^1 \theta'^2(s)ds - \mathcal{Q}(1 - \int_0^1 \cos\theta(s)ds) \tag{5.3}$$

where $\frac{1}{2}\int_0^1 \theta'^2(s)ds$ is the elastic bending energy of the elastica and $\mathcal{Q}(1 - \int_0^1 \cos\theta(s)ds)$ is the external work of the axial compressive force $\mathcal{Q}$ under the presence of the equality and inequality constraints

$$\begin{gathered} \int_0^s \sin\theta d\zeta - c_u \leq 0 \\ -\int_0^s \sin\theta d\zeta + c_l \leq 0 \\ \int_0^1 \sin\theta ds = 0 \end{gathered} \tag{5.4}$$

and the boundary conditions which are $\theta(0) = \theta(1) = 0$, $\theta'(0) = \theta'(1) = 0$ for clamped-clamped and pinned-pinned boundary conditions, respectively.

The equation governing of the extremal solution is accordingly derived by vanishing the first variation of the potential energy subject to the constraints and the boundary conditions. The derivation of an extremal solution is based on the choice of the norm. There are different

candidates of this norm. In calculus of variations, the 1-norm is traditionally assumed

$$\|\chi\|_1 = \max_{0\leq s\leq 1} |\chi(s)| + \max_{0\leq s\leq 1} |\chi'(s)| \tag{5.5}$$

where $\chi : [0,1] \to \mathbb{R}$ is some curve. If we denote by * the extremal values, closeness (or boundness) in the sense of the 1-norm implies that not only χ is close enough to its extremal solution χ^*, but also its derivative. Using this norm, by definition, a weak (local) extremal solution is obtained (Mesterton-Gibbons, 2009). In our case, considering that $\mathcal{Q} = \mathcal{R}\cos\alpha$ and the fact that the Lagrange multiplier associated with the equality constraint is the shear force $\mathcal{R}\sin\alpha$, the governing equation of the elastica (i.e., Euler-Lagrange equation) is derived

$$\frac{d^2\theta}{ds^2} + \mathcal{R}\cos\alpha\sin\theta - \mathcal{R}\sin\alpha\cos\theta = 0 \tag{5.6}$$

for the unconstrained case. When the inequality constraints (5.4i)-ii)) are also present, pointwise shear forces (i.e., associated Lagrange multipliers) are developed, modifying accordingly the governing equation of the elastica (i.e., non-uniform resultant force $\mathcal{R}$ and inclination angle α but the product $\mathcal{R}\cos\alpha$ is always equal to the applied force $\mathcal{Q}$ as friction is neglected).

The solution of a particular configuration of the elastica with a known contact pattern can be derived analytically, or numerically (Domokos et al., 1997; Holmes et al., 1999). The elastica is divided into segments with respect to the contact points and every segment is solved separately. The complete solution is then constructed by assembling the solution for each segment. This involves the enforcement of the continuity conditions, namely identical moment, or curvature and horizontal force at the common extremities of the segments (at the contact points). To derive the stability of these equilibrium configurations, a second (weak) variation of the functional is required. Nevertheless this derivation involves some mathematical difficulties when unilateral constraints are present due to the assumption of a 1-norm (see Chapter 2). This restriction of the 1-norm is relaxed in an optimal control formulation, where a different norm is considered to be more suitable. In particular, the 0-norm is assumed

$$\|\chi\|_0 = \max_{0\leq s\leq 1} |\chi(s)| \tag{5.7}$$

for a curve $\chi : [0,1] \to \mathbb{R}$. Closeness in the sense of the 0-norm means that only χ should be close enough to its extremal solution χ^*. This implies that the variable χ can be piecewise continuous.

With the 0-norm (5.7), by definition, a strong (local) extremal of a functional is obtained (Mesterton-Gibbons, 2009). The difference between a weak and a strong (local) extremal solution is that in the latter case, the Weierstrass necessary condition should be additionally satisfied,

as explained by Liberzon (2012). This means that we do not only derive an equilibrium configuration, but an equilibrium state that is also consistent with the Weierstrass necessary condition. A detailed analysis of the equivalence between an optimal control formulation and a calculus of variation problem with unilateral constraints can be found in Chapter 4.

Let us now construct the optimal control formulation for the particular stability problem. To do so, we need to choose the state and control variables of the problem in an appropriate manner. The functional J coincides with the potential energy of the elastica (7.4). One state variable is clearly the inclination angle $\theta(s)$. The integral (isoperimetric) constraints are also accounted for by adding the cartesian coordinate $y(s) = \int_0^s \sin\theta d\zeta$ with associated spatial derivative $y'(s) = \sin\theta$, as a state variable. Hence, the problem involves two state variables, the inclination angle $\theta(s)$ and the cartesian coordinate $y(s)$ and one control variable, the curvature of the elastica $u(s) = \theta'(s)$. The minimum continuity requirements for these funcrions are: C^0 for $\theta'(s)$ and hence C^1, C^2 for $\theta(s)$ and $y(s)$, respectively. After making these substitutions, we arrive at the following optimal control problem for force-controlled conditions

$$\left\{\begin{array}{ll} \textit{Minimize} & J\left[\mathbf{x}(\cdot), u(\cdot), s\right] = \frac{1}{2}\int_0^1 u^2(s)ds - \mathcal{Q}(1 - \int_0^1 \cos\theta(s)ds) \\ \textit{subject to} & \\ & y'(s) = \sin\theta(s) \\ & \theta'(s) = u(s) \\ & y(0) = y(1) = \theta(0) = \theta(1) = 0 \qquad \textit{clamped B.C. or} \\ & y(0) = y(1) = \theta'(0) = \theta'(1) = 0 \qquad \textit{pinned B.C} \\ & y(s) - c_u \leq 0 \\ & -y(s) + c_l \leq 0 \end{array}\right. \tag{5.8}$$

where the state and control variables are given by

$$\mathbf{x} = \left\{\begin{array}{c} y \\ \theta \end{array}\right\} \in \mathbb{R}^2, \quad u = \theta' \in \mathbb{R} \tag{5.9}$$

The pure-state constraints read

$$\mathbf{g}(y) = \left\{\begin{array}{c} y - c_u \\ -y + c_l \end{array}\right\} \leq \mathbf{0} \tag{5.10}$$

The first and second spatial derivatives of (5.10) are given by

$$\mathbf{g}^1(y) = \left\{\begin{array}{c} \sin\theta \\ -\sin\theta \end{array}\right\} \qquad \mathbf{g}^2(y,u) = \left\{\begin{array}{c} u\cos\theta \\ -u\cos\theta \end{array}\right\} \tag{5.11}$$

where $\mathbf{g}^1_u(y) = 0$ and $\mathbf{g}^2_u(y,u) = \{\cos\theta, -\cos\theta\}^\top$ at contact points which implies that the pure

state constraints (5.10) are of second order.

The normal Hamiltonian is given by

$$H(\boldsymbol{\lambda}, \mathbf{x}, u) = \frac{1}{2}u^2(s) + \mathcal{Q}\left(\cos\theta(s) - 1\right) + \lambda_y \sin\theta(s) + \lambda_\theta u(s) \tag{5.12}$$

where $\boldsymbol{\lambda} = \{\lambda_y, \lambda_\theta\} \in \mathbb{R}^2$ are the covectors, or costate variables of the dynamics $\mathbf{f} = \{\sin\theta, u\} \in \mathbb{R}^2$. The set of the boundary conditions are described by the scalar function

$$\Phi = \nu_1 y(0) + \nu_2 y(1) + \nu_3 \theta(0) + \nu_4 \theta(1) \tag{5.13}$$

for clamped-clamped boundary conditions and

$$\Phi = \nu_1 y(0) + \nu_2 y(1) + \nu_3 \theta'(0) + \nu_4 \theta'(1) \tag{5.14}$$

for pinned-pinned boundary conditions, where $\boldsymbol{\nu}$ is the associated covector, or the vector of Lagrange multipliers which satisfy the complementarity condition for the corresponding arguments.

The Lagrangian of the Hamiltonian, or augmented Hamiltonian is given by

$$\bar{H}\left(\boldsymbol{\mu}, \boldsymbol{\lambda}, \mathbf{x}, u\right) = H(\boldsymbol{\lambda}, \mathbf{x}, u) + \mu_1\left(y(s) - c_u\right) + \mu_2\left(-y(s) - c_l\right) \tag{5.15}$$

where

$$\mu_i = \begin{cases} = 0 & if \quad g_i\left(\mathbf{x}_o, \mathbf{x}_f\right) < 0 \\ \geq 0 & if \quad g_i\left(\mathbf{x}_o, \mathbf{x}_f\right) = 0 \end{cases} \tag{5.16}$$

The minimization of the Hamiltonian in terms of the control variable gives

$$\frac{\partial \bar{H}}{\partial u} = \frac{\partial H}{\partial u} = 0 \Rightarrow u + \lambda_\theta = 0 \tag{5.17}$$

which leads to the optimal control variable $\hat{u} = -\lambda_\theta$. Using this result, we can eliminate the control variable from (5.12) in order to get the lower, or minimized Hamiltonian $\mathcal{H}$, which depends only on the state and costate variables

$$\mathcal{H} = \mathcal{Q}\left(\cos\theta - 1\right) + \lambda_y \sin\theta - \frac{1}{2}\lambda_\theta^2 \tag{5.18}$$

This remains constant for every $s \in [0, 1]$, since it does not depend explicitly on s. The same also holds for the augmented Hamiltonian (6.41).

The adjoint equations are given by

$$-\lambda_y^{'} = \frac{\partial \bar{H}}{\partial y} = \begin{cases} 0 & \text{if} \quad \mathbf{g} < \mathbf{0} \\ \mu_1 & \text{if} \quad y(\zeta_c) = c_u \\ -\mu_2 & \text{if} \quad y(\zeta_c) = -c_l \end{cases} \tag{5.19}$$

$$-\lambda_\theta^{'} = \frac{\partial \bar{H}}{\partial \theta} = -\mathcal{Q}\sin\theta + \lambda_y \cos\theta \tag{5.20}$$

where ζ_c denotes the position of a discrete contact (i.e., closed contact). The initial and terminal transversality conditions are $\lambda_y(0) = -\nu_1$, $\lambda_\theta(0) = -\nu_3$ and $\lambda_y(1) = \nu_2$, $\lambda_\theta(1) = \nu_4$ for clamped-clamped boundary conditions, respectively. In a similar manner the same expressions can be derived for pinned-pinned boundary conditions.

For the unconstrained case $\lambda_y(s) = -\nu_1 = \nu_2$. This means that a uniform lateral, or shear force is present. If we denote α the inclination angle of the resultant force $\mathcal{R}$ with respect to the x-axis, then $\mathcal{Q} = \mathcal{R}\cos\alpha$, $\lambda_y = \mathcal{R}_y = \mathcal{R}\sin\alpha$ and (5.20) becomes $\lambda_\theta^{'} = \mathcal{R}\sin(\theta - \alpha)$. If we substitute $\lambda_\theta = -\hat{u} = -\theta'$, we get

$$\theta'' + \mathcal{R}\sin(\theta - \alpha) = 0 \tag{5.21}$$

with boundary conditions $\theta(0) = \theta(1) = 0$ for a clamped elastica. Equation (6.45) is identical to (5.6), derived by applying the calculus of variations. Nevertheless, in optimal control, the assumption of the 0-norm introduces the additional requirement of the Weierstrass necessary condition. This condition is equivalent to the minimization of Hamiltonian with respect to the control variable, the curvature of the elastica. For instance, for a predefined axial compressive force $\mathcal{Q}$ (i.e., force-controlled conditions), the internal force and the inclination angle are both unknown except of their product, $\mathcal{Q} = \mathcal{R}\cos\alpha$. Hence, we may derive more than one equilibrium state that satisfy (6.45). The equilibrium state with the mimimum Hamiltonian energy with respect to the control variable is the optimal solution (i.e., stable solution).

Let us now assume that we have a single contact point ζ_c where $y(\zeta_c) = c_u$ is satisfied. In this case, the shear force is $\lambda_y(s) = -\nu_1$, for $s \in [0, \zeta_c)$, $\lambda_y(\zeta_c^-) - \lambda_y(\zeta_c^+) = \eta_1$ (i.e., $\eta_1 = \int_{\zeta_c-\varepsilon}^{\zeta_c+\varepsilon} \mu_1 ds$) at the contact point ζ_c and $\lambda_y(s) = -\nu_1 - \eta_1 = \nu_2$, for $s \in (\zeta_c, 1]$. On the other hand, $\lambda_\theta(\zeta_c^-) - \lambda_\theta(\zeta_c^+) = 0$ since the pure state constraint is independent of θ. This also means that $\lambda_\theta = -\hat{u} = -\theta'$ is continuous. However $-\lambda_\theta^{'} = -\hat{u}'$ is discontinuous at the contact points (5.20), because it depends on the shear force $\lambda_y(s)$. When a continuous contact is present the only difference is the vanishing control variable $u(\zeta) = 0$ for $\zeta \in [\zeta_{en}, \zeta_{ex}]$, where ζ_{en} and ζ_{ex} denote the entry and exit points of a continuous contact.

For force-controlled conditions, a predefined value of the axial compressive force is assigned. Then the displacements are obtained by the solution of the optimization problem, while the adjoint variables are calculated indirectly by the adjoint equations (5.19)-(5.20).

Illustrative example with an elastica of constant length

To clarify the application of the optimal control method to solve a constrained buckling problem, a simple example is presented. Let us consider a planar elastica of constant length, which is constrained by two symmetrically located walls with clearances $c_u = -c_l = 0.05$. Pinned-pinned boundary conditions are assumed and the elastica is initially unstressed. Force-controlled conditions are applied.

Following the mathematical derivation of Section 5.2.1, the initial and terminal transversality conditions are $\lambda_y(0) = -\nu_1$, $\lambda_\theta(0) = 0$ and $\lambda_y(1) = \nu_2$, $\lambda_\theta(1) = 0$ for pinned-pinned boundary conditions, respectively. Taking into account the canonical equations (5.19)-(5.20), $\lambda_y(s) = -\nu_1 = \nu_2$ for the unconstrained case. Using additionally the minimization of the Hamiltonian with respect to the control variable $\lambda_\theta = -\hat{u} = -\theta'$, we arrive at equation $\theta'' + \mathcal{R}\sin\theta = 0$ with boundary conditions $\theta'(0) = \theta'(1) = 0$.

Instead, if there is a contact point ζ_c, $y(\zeta_c) = c_u$ is satisfied and the shear force becomes discontinuous. In particular, $\lambda_y(s) = -\nu_1$, for $s \in [0, \zeta_c)$, $\lambda_y(\zeta_c^-) - \lambda_y(\zeta_c^+) = \eta_1$ and $\lambda_y(s) = \nu_2 = -\nu_1 - \eta_1$, for $s \in (\zeta_c, 1]$. Due to symmetry $\eta_1 = 2\nu_1$. When a continuous contact is present the control variable $u(\zeta)$ vanishes for $\zeta \in [\zeta_{en}, \zeta_{ex}]$ and the shear force becomes $\lambda_y(s) = -\nu_1$, for $s \in [0, \zeta_c)$, $\lambda_y(\zeta_{en}^-) - \lambda_y(\zeta_{en}^+) = \eta_1$, $\lambda_y(\zeta_{ex}^-) - \lambda_y(\zeta_{ex}^+) = \eta_2$ and $\lambda_y(s) = \nu_2 = -\nu_1 - \eta_1 - \eta_2$, for $s \in (\zeta_c, 1]$ with $\eta_1 = \eta_2 = \nu_1$.

For symmetrical reasons only half of the elastica has to be solved. If the elastica is in contact with the wall, we solve $\theta'' + \mathcal{R}\sin(\theta - \alpha) = 0$ with boundary conditions $\theta'(0) = \theta'(1/2) = 0$, or $\theta'(0) = \theta'(\zeta_{en}) = 0$ for a discrete, or a continuous contact at ζ_{en}, respectively.

Let us now analyze the post-buckling behavior of the pinned-pinned elastica, as derived by the optimal control problem. The elastica remains straight until an axial compressive force of $\mathcal{Q}/\pi^2 = 1$ is applied which corresponds to the first buckling load of a pinned-pinned elastica with deformed shape $(1-2)$, as shown in Figure 7.2. In this case the elastica is unconstrained until C2 ($\mathcal{Q}/\pi^2 = 1.03$, $\delta = 0.0062$) where a discrete contact at the midpoint position $s = 0.5$ occurs. Beyond C2 the position of the contact point remains unchanged with increasing axial compressive force while a contact force also appears with increasing magnitude. When C3 ($\mathcal{Q}/\pi^2 = 3.98$, $\delta = 0.0075$) is reached, the moment, or the curvature at the discrete contact vanishes leading to the onset of a continuous contact. Then the length of the continuous contact starts increasing with maximum value of $\ell_c = 0.498 \approx 0.5$ at C4 ($\mathcal{Q}/\pi^2 = 15.85 \approx 16$, $\delta = 0.0154$). At C4, the values $\ell_c = 0.5$ and $\mathcal{Q}/\pi^2 = 16$ imply that the continuous segment buckles according to the first buckling mode of a clamped-clamped elastica (i.e., the Euler buckling load $4\pi^2/\ell_c^2$ is overcome under further loading).

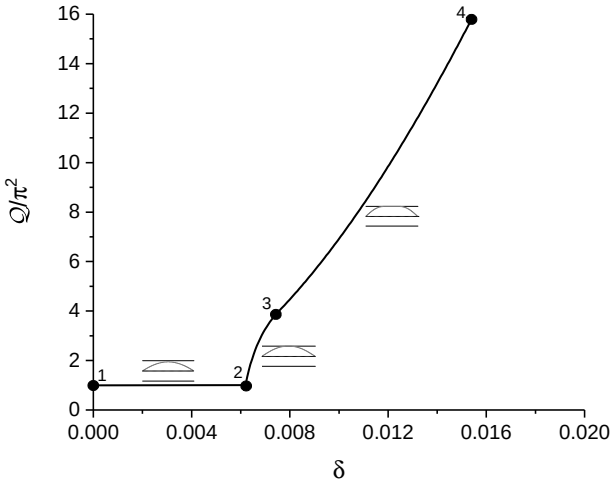

Figure 5.2: Bifurcation diagram for a constrained pinned-pinned elastica of constant length with clearances $c_u = -c_l = 0.05$

The inclination α of the internal force $\mathcal{R}(0)$, the inclination angle $\theta(0)$ and the angle $\beta = \arctan\left[c_u/x\left(\zeta_{en}\right)\right]$ are also shown in Figure 5.3 after the onset of the discrete contact. From these angles some notable conclusions are deduced, which have clear geometrical interpretation, as also explained by (Domokos et al., 1997). Beyond C2 the inclination α increases from zero with $\alpha < \beta$ to $\alpha = \beta = 0.1$ at C3. This means that at $C3$ the internal force $\mathcal{R}(0)$ passes through the position of the discrete contact, implying therefore a vanishing bending moment at that point. Past $C3$, $\alpha = \beta$ or in other words the curvature at the entry point ζ_{en} remains equal to zero until $C4$, where $\alpha = \beta = 0.2$. On the other hand, the inclination angle at $s = 0$ is $\theta(0) > 2\alpha$ along the branch $2 - 3$ and $\theta(0) = 2\alpha$ when the deformation shape $3 - 4$ initiates. In summary, there are two geometrical restrictions; $\alpha \leq \beta$ and $\alpha \leq \theta(0)/2$.

The new deformation shape after C4 is not derived herein since the scope of this Section is to briefly describe the optimal control method. Further analysis of this particular example can be found in (Manning and Bulman, 2005; Domokos et al., 1997).

The benefit of the assumption of strong variation of a functional, which is incorporated in the optimal control formulation, is not obvious through this particular example. Nevertheless its advantage becomes evident in Section 5.3.

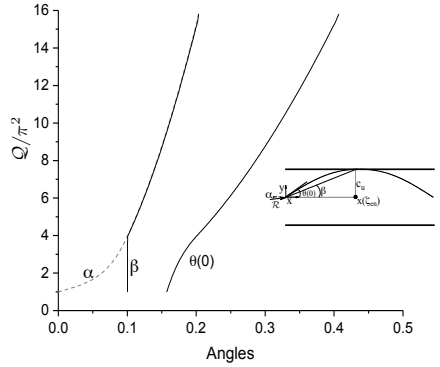

Figure 5.3: Axial compressive force $\mathcal{Q}/\pi^2$ with respect to the angles; (i)α, (ii) β and (iii) $\theta(0)$ for a discrete contact

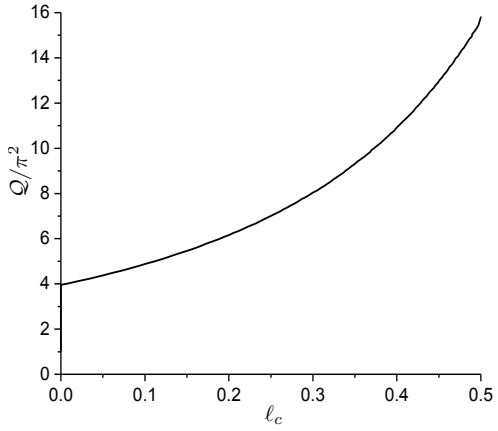

Figure 5.4: Axial compressive force $\mathcal{Q}/\pi^2$ with respect to the length of the continuous contact ℓ_c

5.2.2 Displacement controlled with fixed length or variable length

The constrained stability problem of the planar elastica for force-controlled conditions is explained in detail in Section 5.2. If we assume displacement-controlled conditions, the external work of the axial compressive force $\mathcal{Q}$ is removed from the potential energy of the planar elastica since the value of the applied force is unknown. Instead, the distance between the two supports should be predefined. To impose a specific value of the coordinate $x(1)$, or end-shortening δ, a new state variable $x(s)$ with its associated spatial derivative $x'(s) = \cos\theta(s)$ is added with boundary conditions $x(0) = 0$ and $x(1) = 1 - \delta$. Hence, the nonlinear optimal control problem

$\mathcal{P}_\delta$ of the constrained planar elastica for displacement-controlled conditions is formulated as follows

$$\begin{cases} \textit{Minimize} & J\left[\mathbf{x}(\cdot),\mathbf{u}(\cdot),s\right]=\frac{1}{2}\int_0^1 u^2(s)ds \\ \textit{subject to} & \\ & y'(s)=\sin\theta(s) \\ & x'(s)=\cos\theta(s) \\ & \theta'(s)=u(s) \\ & y(0)=y(1)=x(0)=\theta(0)=\theta(1)=0 \qquad \textit{clamped B.C. or} \\ & y(0)=y(1)=x(0)=\theta'(0)=\theta'(1)=0 \qquad \textit{pinned B.C} \\ & x(1)=1-\delta \\ & y-c_u\leq 0 \\ & -y-c_l\leq 0 \end{cases} \tag{5.22}$$

where y is the vertical displacement, x is the horizontal displacement, θ is the inclination angle, δ is the imposed end-shortening and c_u, c_l are the clearances of the upper and lower horizontal walls, respectively. The adjoint equations can be derived in a similar manner to the force-controlled problem. Nevertheless the axial compressive force $\mathcal{Q}$ is computed here by the corresponding adjoint variable λ_x of the additional state variable $x(s)$ with $\lambda_x'=0$. Similarly to the force-controlled problem, the graph of the axial compressive force $\mathcal{Q}/\pi^2$ is also derived in terms of the end-shortening δ.

Another constrained buckling problem can be also solved using a similar set-up. In particular, we consider that the elastica is clamped or pinned at the left end, while it is inserted through a fixed frictionless device that functions as a clamped end at the right end. Hence, the arc-length of the elastica varies while the distance between the fixed end of the elastica and the point of insertion is constant. This is the insertion stability problem, which can be described by the new optimal control problem $\bar{\mathcal{P}}_\delta$

$$\begin{cases} \textit{Minimize} & J\left[\mathbf{x}(\cdot),\mathbf{u}(\cdot),s\right]=\frac{1}{2}\int_0^{1+\bar{\delta}} u^2(s)ds \\ \textit{subject to} & \\ & y'(s)=\sin\theta(s) \\ & x'(s)=\cos\theta(s) \\ & \theta'(s)=u(s) \\ & y(0)=y(1+\bar{\delta})=x(0)=\theta(1+\bar{\delta})=0 \\ & \theta(0)=0 \quad \text{or} \quad \theta'(0)=0 \\ & x(1+\bar{\delta})=1 \\ & y-c_u\leq 0 \\ & -y-c_l\leq 0 \end{cases} \tag{5.23}$$

where $\bar{\delta}$ is the change of the inserted length. For the solution of the above problem, a predefined value of the arc-length is assigned, while the horizontal position is always $x(1+\bar{\delta})=1$. The solution is similar to the classical stability problem for displacement-controlled conditions. However the solution of this problem provides the internal axial force $\mathcal{R}\cos\alpha$ rather than the applied force $\mathcal{Q}$. As explained in Chapter 3, the applied axial force $\mathcal{Q}$ is accordingly obtained by $\mathcal{Q}=\mathcal{R}\cos\alpha-P$, where $P=\theta'(1+\bar{\delta})^2/2$ is a configurational or Eshelby-like force generated at the insertion point of the sliding sleeve. In addition the graph of the axial compressive force $\mathcal{Q}/\pi^2$ and the internal axial force $\mathcal{R}\cos\alpha$ is computed in terms of the change of the arc-length $\bar{\delta}$ rather than the end-shortening δ that is used above.

5.3 Bifurcation diagrams of planar elastica

Here we apply the optimal control method for several cases. Initially we verify the use of the optimal control in the derivation of the post-buckling behavior of an unconstrained elastica with pinned-pinned boundary conditions. The complete solution of this problem has been first obtained by (Kuznetsov and Levyakov, 2002) and it is compared with the optimal control formulation.

Next the constrained stability problem is investigated. Three distinct examples are presented. The first example involves the classical stability problem of an elastica with clamped-clamped boundary conditions, which is constrained by two symmetrically located walls with clearances $c_u=-c_l=0.05$. Force-controlled and displacement-controlled conditions are imposed separately and their effect in the post-buckling response of the elastica is investigated.

Then we investigate the insertion stability problem, where the length of the elastica varies while the horizontal distance between the two supports is fixed. The particular constrained problem has been first performed by (Ro et al., 2010) for clearances $c_u=-c_l=0.1$. In this case the bifurcation diagram is expressed in terms of the change of the arc-length $\bar{\delta}$ instead of the end-shortening that is used above.

Finally we examine the effect of the boundary conditions and the asymmetrical location of the walls. In particular, we investigate the post-buckling behavior of a pinned-pinned elastica of constant length constrained by two asymmetrically located rigid walls with clearances $c_u=0.125$ and $c_l=0$. The same problems have been first solved by (Ro et al., 2010; Manning and Bulman, 2005; Domokos et al., 1997) and they are used for comparison.

5.3.1 Verification example

The post-buckling behavior of an unconstrained pinned-pinned elastica of constant length is investigated assuming that the left support is fixed at $x(0)=0$ while the right end is free to move along the x-axis. The bifurcation diagram is given in Figure 5.5. The sequence of the

configurations of the elastica is also illustrated. The minimized Hamiltonian (i..e, mimimized total energy) initially increases with increasing applied horizontal force, or end-shortening until it reaches a plateau with $\mathcal{Q}/\pi^2 = 2.18$. At this point the two supports come in contact meaning that the end-shortening is $\delta = 0$. Beyond this point the solution is unstable. For force-controlled conditions, the solution jumps to C4 with $\delta = 2$ (see Figure 5.5), while for displacement-controlled conditions, it moves to C2′ with tensile load $\mathcal{Q}/\pi^2 = -2.18$ which is obtained by a 180 rotation of the previous configuration. For the same absolute value of forces, a configuration under the action of the tensile force can be derived by the corresponding configuration under the action of the compressive load if we add to the latter inclinations angles an angle of π. In two-dimensional space, we cannot recognize the difference between the configurations. This solution is in agreement with the solution by (Kuznetsov and Levyakov, 2002), who derived the same problem using a semi-analytical solution of a Sturm-Liouville boundary value problem.

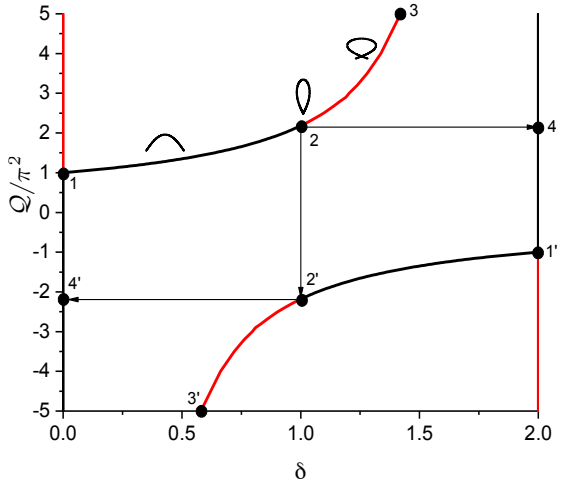

Figure 5.5: Bifurcation diagram for a pinned-pinned elastica of constant length

5.3.2 Clamped-clamped elastica with symmetrically located walls

The post-buckling behavior of a clamped-clamped elastica constrained by two symmetrically located walls is now studied. The classical and insertion stability problems are examined separately. The results are compared with previous works (Manning and Bulman, 2005; Ro et al., 2010).

Classical problem

A clamped-clamped elastica is constrained by two symmetrically located walls with clearances $c_u = -c_l = 0.05$. The elastica is of constant length (classical stability problem) and both force- and displacement-controlled conditions are applied which are considered.

For displacement-controlled conditions, the elastica is initially unconstrained and its deformation shape $(1-2)$ corresponds to the minimum root of the first buckling mode of a clamped-clamped elastica, as shown in Figure 5.6. With further increase of δ, the elastica comes in contact with the wall at its midpoint position $s = 0.5$ at $C2$ for symmetrical reasons. When the horizontal force reaches 3, the moment vanishes at the discrete contact. Past this point there are three distinct possibilities; (i) onset of a continuous contact, (ii) simultaneous change of the sign of moments at both end supports and (iii) change of the sign of moment at the one end. The third case is optimal, which leads to the asymmetrical deformation shape $(3-4)$. Along this branch the axial force starts decreasing until a second contact point on the opposite wall appears at 4. Accordingly the axial force increases gradually until 5. Beyond this point a new change of sign of the moment at the one end appears, leading to a new asymmetrical deformation shape $(5-6)$ with decreasing applied load. This branch evolves until a third contact point develops at 6. Due to symmetry the second contact point is located at $s = 0.5$ and the other contact points are symmetrically located at the opposite walls.

The adjoint functions for representative values of δ are also presented in Figure 5.7 for displacement-controlled conditions. Due to the absence of any external pressure, the nature of the boundary conditions and the symmetrical location of the walls, the functions of the adjoint variables and accordingly the cartesian coordinates of the elastica can be also reversed, or changed in sign without affecting the bifurcation diagram.

In the case of a force-controlled problem, the elastica deforms in an identical manner at the initial stage, see deformation shapes $(1-2)$ and $(2-3)$. Nevertheless past C3 the asymmetrical deformation shape $(3-4)$ is unstable as the axial compressive force decreases (i.e., the branch is softening). Instead the configuration jumps to the branch $(4-5)$ with two symmetrically located contact points to the opposite walls. For the same reason, it jumps to the deformation shape $(6-7)$ beyond C5, as shown in Figure 5.6. The bifurcation diagram is shown in Figure 5.6 and the points of evolutions of the contact patterns are summarized in Table 5.3.2.

Points of evolution of the contact patterns for the bifurcation diagram for a constrained clamped-clamped planar elastica with clearances $c_u = -c_l = 0.05$

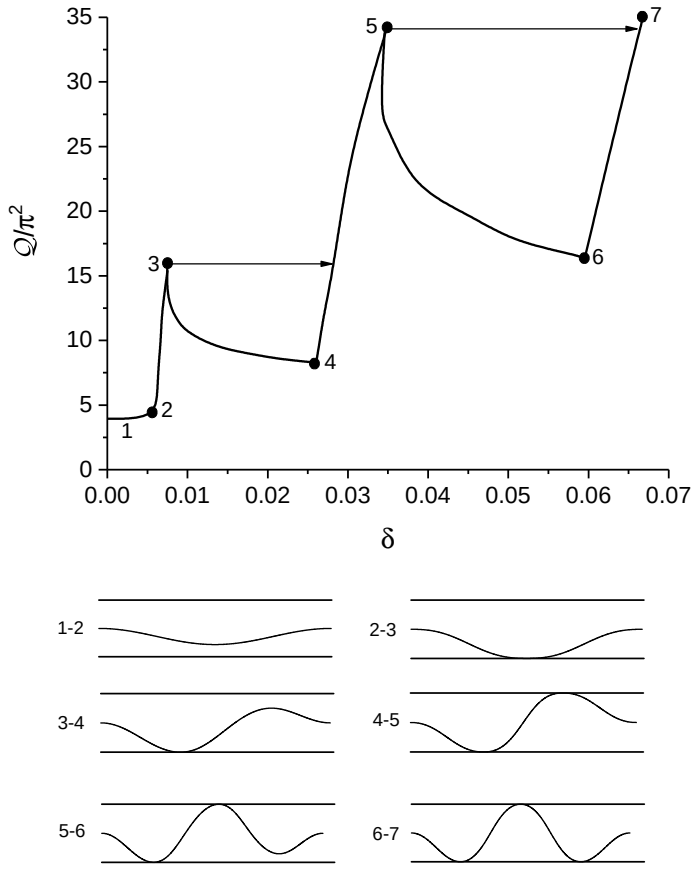

Figure 5.6: Bifurcation diagram for a constrained clamped-clamped elastica of constant length with clearances $c_u = -c_l = 0.05$

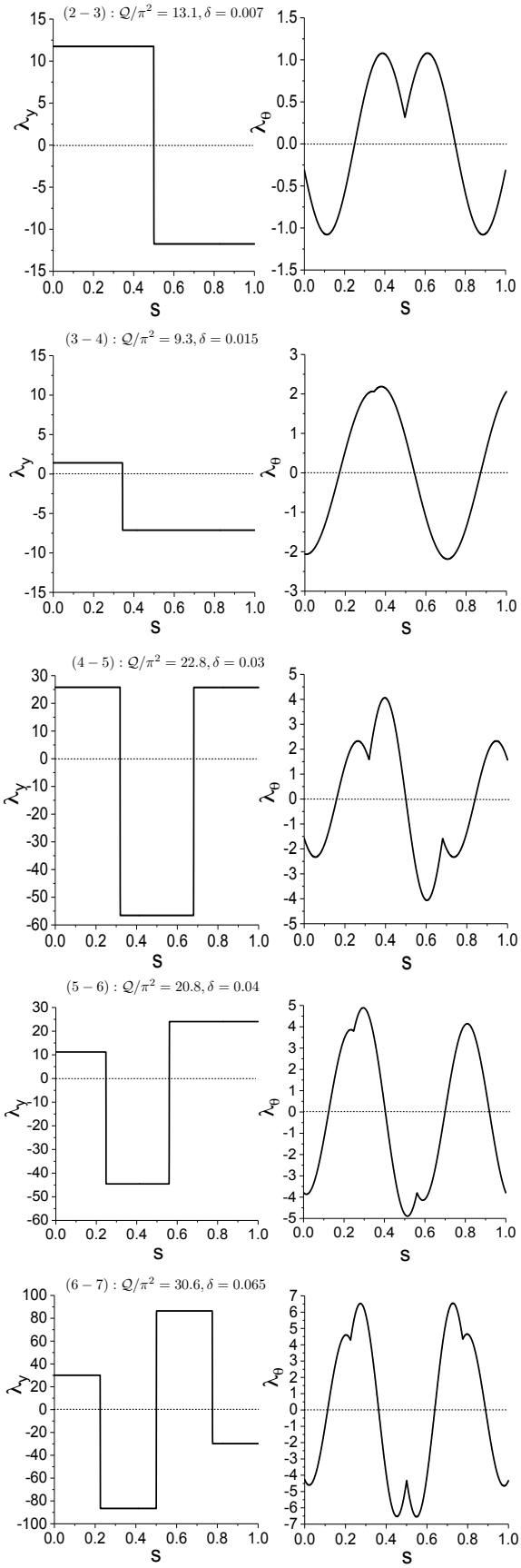
$(2-3): \mathcal{Q}/\pi^2 = 13.1, \delta = 0.007$
λ_y
λ_θ
s
$(3-4): \mathcal{Q}/\pi^2 = 9.3, \delta = 0.015$
λ_y
λ_θ
s
$(4-5): \mathcal{Q}/\pi^2 = 22.8, \delta = 0.03$
λ_y
λ_θ
s
$(5-6): \mathcal{Q}/\pi^2 = 20.8, \delta = 0.04$
λ_y
λ_θ
s
$(6-7): \mathcal{Q}/\pi^2 = 30.6, \delta = 0.065$
λ_y
λ_θ
s

Insertion problem

The post-buckling behavior of a clamped-clamped elastica of variable length constrained by symmetrically located walls with $c_u = -c_l = 0.1$ is investigated. In this case the horizontal distance between the two supports is assumed to be fixed $x(1+\bar{\delta}) - x(0) = 1$ while the arc-length gradually increases. The same problem has been solved by applying the geometry-based technique in Chapter 3. In Figure 5.8, the applied and internal axial forces are illustrated with respect to the change of the length of the elastica. The applied axial force is lower than the internal axial force as a configurational or Eshelby-like force is generated at the insertion point of the sliding sleeve. More details about the development of the Eshelby-like force can be found in Chapter 3.

One main difference between the constrained elastica of constant length and variable length is the initial post-buckling behavior of the elastica in its unconstrained condition. In the former case the value of the horizontal applied force increases (i.e., super-critical bifurcation), while in the latter case the opposite behavior is observed (i.e., sub-critical bifurcation). However the sequence of the contact patterns is exactly the same compared with the case of a displacement-controlled problem of a constrained elastica of constant length. The value of the horizontal force at $C3$ is approximately the same as in the previous example for a change of arc-length $\bar{\delta} = 0.029$. The decrease of the horizontal force occurs until $C4$. Beyond $C4$ two contact points are present until $C5$. Then the deformation shape becomes asymmetrical until $C6$, where three contact points appear. The subsequent deformation shapes are shown in Figure 5.8 and the corresponding points of evolution of the contact patterns are summarized in Table 6.1.

Points	Insertion problem			
	$\theta_{[2]}$	δ	$\mathcal{R}\cos\alpha\ /\pi^2$	$\mathcal{Q}/\pi^2$
$2, \bar{2}$	0.311	0.025	3.86	3.67
$3, \bar{3}$	0.394	0.030	14.86	14.86
$4, \bar{4}$	0.484	0.100	6.97	5.72
$5, \bar{5}$	0.517	0.152	24.03	24.03
$6, \bar{6}$	0.628	0.219	11.46	8.00

Table 5.1: Points of evolution of the contact patterns for the bifurcation diagram for a constrained clamped-clamped elastica with clearance $c_u = -c_l = 0.1$

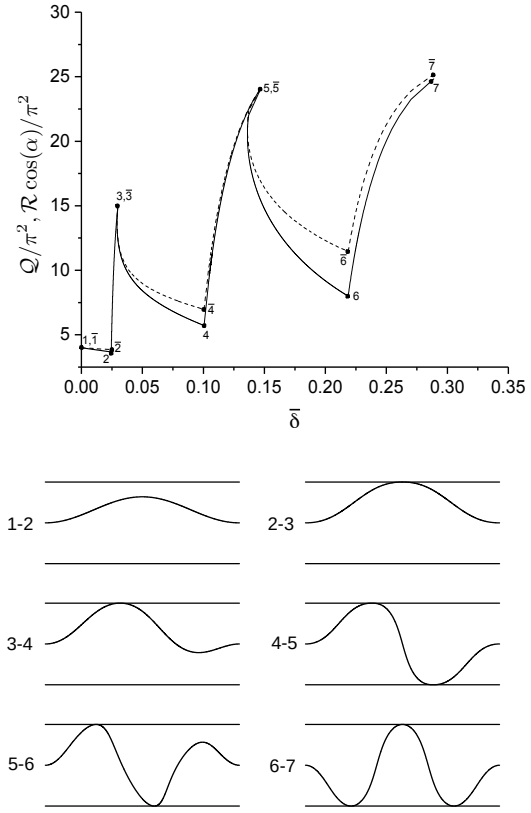

Figure 5.8: Bifurcation diagram for a constrained clamped-clamped elastica with clearance $c_u = -c_l = 0.1$; solid line for the applied load $\mathcal{Q}$ and dashed line for the axial load $\mathcal{R}\cos\alpha$.

5.3.3 Pinned-pinned elastica constrained by asymmetrically located walls

A pinned-pinned elastica of constant length is constrained by two asymmetrically located rigid walls with clearances $c_u = 0.125$ and $c_l = 0$. The problem is solved for both force-controlled and displacement-controlled conditions.

Initially, the elastica is unconstrained and its configuration $(1-2)$ is consistent with the first buckling mode of a pinned-pinned elastica with axial force $\mathcal{Q}/\pi^2 = 1$, see Figure 5.9. Due to symmetry the elastica comes in contact with the upper wall at $s = 0.5$ corresponding to C2. This discrete contact remains unchanged until C3, where the moment at the contact point vanishes. This leads to the onset of the continuous contact with deformation shape $(3-4)$, which is a stable configuration in the case of a pinned-pinned elastica. The length of the continuous contact increases until C4. Past this point the continuous segment buckles as the

first buckling mode of a clamped-clamped elastica forming a free-standing fold, see deformation shape $(4-5)$. This branch is stable for displacement-controlled conditions, while it is unstable for force-controlled conditions, because a decrease of the load is observed. Hence for displacement-controlled conditions the axial force decreases until a new discrete contact is met at $s = 0.5$ with the lower wall at C5. This yields to the new symmetrical configuration $(5-6)$. On the other hand, for force-controlled conditions, beyond C3 the elastica jumps directly to the branch $(5-6)$.

The whole sequence of the contact patterns is illustrated in Figure 5.9 and the points of evolution of the contact patterns are summarized in Table 7.1. The same problem has been also solved by (Domokos et al., 1997) and it is in full agreement with the current solution.

Points of evolution of the contact patterns for the bifurcation diagram for a constrained pinned-pinned planar elastica with clearances $c_u = 0.125$ and $c_l = 0$

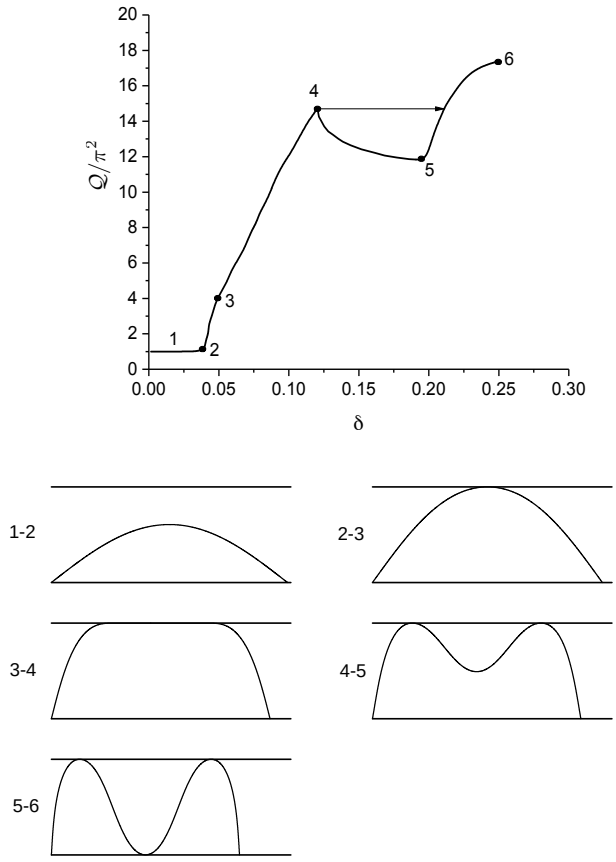

Figure 5.9: Bifurcation diagram for a constrained pinned-pinned elastica of constant length with clearances $c_u = 0.125$ and $c_l = 0$

5.4 Stability of constrained spatial elastica

Now we examine the post-buckling behavior of a spatial elastica of constant length (classical stability problem) constrained by a cylindrical wall. A short description of the geometrical characteristics and the potential (strain) energy of an isotropic inextensible-unshearable elastic rod, the so-called Kirchhoff rod or spatial elastica, is first provided. Based on the Kirchhoff rod model we construct the new form of the optimal control problem for displacement-controlled conditions. Validation of the formulation is then achieved by solving a well-known stability problem of an unconstrained spatial elastica with clamped-clamped boundary conditions and for a material parameter $\gamma = 5/7$ which is the ratio of the shear to the bending moduli (Maddocks, 1984; Majumdar et al., 2012; Goyal et al., 2005; Majumdar and Goriely, 2013). Keeping the same

material parameter γ and assuming the same boundary conditions, the post-buckling response of a spatial elastica constrained by a wall with clearance $c = 0.1$ is solved and the results are compared with similar results obtained by (Fang et al., 2013; Chen and Fang, 2013).

5.4.1 Kirchhoff rod model

A Kirchhoff rod is a special case of a Cosserat rod, which is inextensible and unshearable. As Bernoulli law (i.e., the cross section remains plane and rigid) is applicable in this case, this problem can be formulated as a one dimensional continuum (Weiss, 2002).

The Kirchhoff rod is parametrized by s the arc-length paramater with $s \in [0, L]$. Its initial configuration is unstressed. Then the configuration of the rod is described by its centerline $\mathbf{r}$(s) and the orthonormal director basis $\{\mathbf{d}_1, \mathbf{d}_2, \mathbf{d}_3\}$. The director basis is related to the reference configuration $\{\mathbf{e}_1, \mathbf{e}_2, \mathbf{e}_3\}$ by a rotation matrix $\mathfrak{D}(s)$

$$\mathbf{d}_i(s) = \mathfrak{D}(\mathrm{s})\mathbf{e}_i \tag{5.24}$$

and satisfies the following property

$$\mathbf{d}_1(s) = \mathbf{d}_2(s) \times \mathbf{d}_3(s) \tag{5.25}$$

(5.25) indicates that $\mathbf{d}_1(s)$ is orthogonal to the cross-section plane defined by $\{\mathbf{d}_2(s), \mathbf{d}_3(s)\}$.

The director basis $\{\mathbf{d}_1, \mathbf{d}_2, \mathbf{d}_3\}$ changes smoothly with respect to the reference configuration $\{\mathbf{e}_1, \mathbf{e}_2, \mathbf{e}_3\}$. This change is described by the following kinematic relation

$$\partial_s \mathbf{d}_k = \boldsymbol{\kappa} \times \mathbf{d}_k \tag{5.26}$$

where $\boldsymbol{\kappa} = \{\kappa_1, \kappa_2, \kappa_3\}$ is called Darboux vector (or strain vector) which involves the twist (κ_1) and the bending (κ_2, κ_3) of the rod about the three directors.

Considering that the Kirchhoff rod is inextensible and unshearable, the kinematics of the centerline is given by

$$\partial_s \mathbf{r} = \mathbf{v} = \mathbf{d}_1 \tag{5.27}$$

where $\mathbf{v}$ is a vector-valued function whose components along the three directors $\mathbf{v} = v_i d_i = \{v_1, v_2, v_3\}$ describe the extension $v_1 = 1$ and the shear $v_2 = v_3 = 0$ of the rod.

The resulting strain energy of an isotropic Kirchhoff rod becomes

$$\mathcal{U} = \frac{1}{2} \int_0^L GJ\kappa_1^2(s) + EI \left(\kappa_2^2(s) + \kappa_3^2(s)\right) ds \tag{5.28}$$

where $I = \pi\alpha^4/4$ is the second moment of area and $J = \pi\alpha^4/2$ is the polar moment of area for a cylindrical rod of uniform radius α.

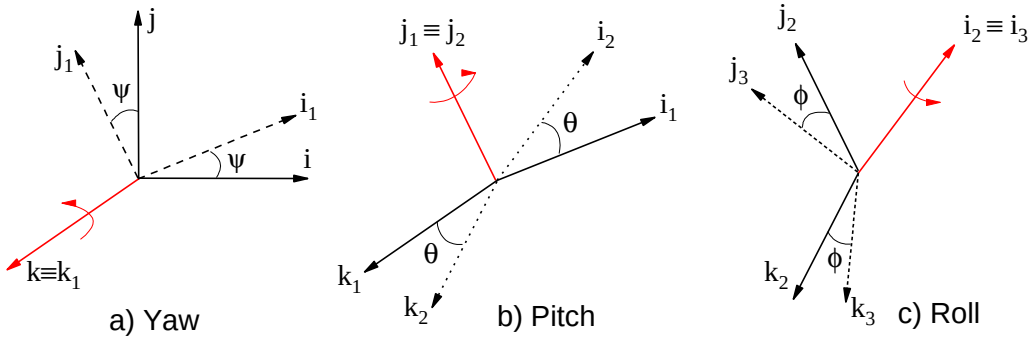

Figure 5.10: Method $3-2-1$ of Euler angles

To derive the components of the Darboux vector, we need to define the rotation matrix $\mathfrak{D}(s)$ which is described by a set of Euler angles $\{\theta(s), \phi(s), \psi(s)\}$ with respect to the reference configuration $\{\mathbf{e}_1, \mathbf{e}_2, \mathbf{e}_3\}$. Let us denote that $\mathbf{i} = \mathbf{e}_1$, $\mathbf{j} = \mathbf{e}_2$ and $\mathbf{k} = \mathbf{e}_3$. In this study, the three Euler angles are obtained applying the method $(3-2-1)$ (Atanackovic, 1997), which yields to the simplest possible form of the director axis $\mathbf{d}_1$, as shown in Figure 5.10. In fact, we first apply a rotation ψ around $\mathbf{k}$ (i.e., yaw) which leads to $\left\{\mathbf{i}^{(1)}, \mathbf{j}^{(1)}, \mathbf{k}^{(1)}\right\}$ coordinate system. A new rotation θ around $\mathbf{j}^{(1)}$ (i.e., pitch) is then imposed which gives the $\left\{\mathbf{i}^{(2)}, \mathbf{j}^{(2)}, \mathbf{k}^{(2)}\right\}$ coordinate system. A third rotation ϕ around $\mathbf{i}^{(2)}$ (i.e., roll) finally gives the $\left\{\mathbf{i}^{(3)}, \mathbf{j}^{(3)}, \mathbf{k}^{(3)}\right\}$ coordinate system which coincides with the director axes $\{\mathbf{d}_1, \mathbf{d}_2, \mathbf{d}_3\}$. This sequence of rotation matrices can be expressed as follows

$$\mathcal{D}_x = \begin{bmatrix} 1 & 0 & 0 \\ 0 & \cos\phi & \sin\phi \\ 0 & -\sin\phi & \cos\phi \end{bmatrix}, \quad \mathcal{D}_y = \begin{bmatrix} \cos\theta & 0 & -\sin\theta \\ 0 & 1 & 0 \\ \sin\theta & 0 & \cos\theta \end{bmatrix}, \quad \mathcal{D}_z = \begin{bmatrix} \cos\psi & \sin\psi & 0 \\ -\sin\psi & \cos\psi & 0 \\ 0 & 0 & 1 \end{bmatrix} \tag{5.29}$$

leading to the total rotation matrix $\mathfrak{D} = \mathcal{D}_x\mathcal{D}_y\mathcal{D}_z$. Based on (5.24) the director axes $\mathbf{d}_1, \mathbf{d}_2, \mathbf{d}_3$ become

$$\mathbf{d}_1 = \cos\theta\cos\psi\mathbf{i} + \cos\theta\sin\psi\mathbf{j} - \sin\theta\mathbf{k} \tag{5.30}$$

$$\begin{aligned} \mathbf{d}_2 = &\left(\sin\theta\sin\phi\cos\psi - \cos\phi\sin\psi\right)\mathbf{i} \\ &+ \left(\sin\theta\sin\phi\sin\psi + \cos\phi\cos\psi\right)\mathbf{j} \\ &+ \sin\phi\cos\theta\mathbf{k} \end{aligned} \tag{5.31}$$

$$\mathbf{d}_3 = \left(\sin\theta\cos\phi\cos\psi + \sin\phi\sin\psi\right)\mathbf{i}$$

$$+ (\sin\theta\cos\phi\sin\psi - \sin\phi\cos\psi)\,\mathbf{j}$$
$$+ \cos\phi\cos\theta\mathbf{k} \tag{5.32}$$

and applying the method $(3-2-1)$ the Darboux vector $\boldsymbol{\kappa}$ can be described as follows

$$\boldsymbol{\kappa} = \psi'\mathbf{k} + \theta'\mathbf{j}^{(1)} + \phi'\mathbf{i}^{(3)} \tag{5.33}$$

where the $\mathbf{j}^{(1)} = \mathbf{j}^{(2)}$,$\mathbf{k}$ axes can be expressed about the director axes as $\mathbf{j}^{(1)} = \cos\phi\mathbf{d}_2 - \sin\phi\mathbf{d}_3$ and $\mathbf{k} = -\sin\theta\mathbf{d}_1 + \sin\phi\cos\theta\mathbf{d}_2 + \cos\phi\cos\theta\mathbf{d}_3$, respectively while $\mathbf{i}^{(2)} \equiv \mathbf{d}_1$. This leads to

$$\begin{aligned} \kappa_1 &= \phi' - \psi'\sin\theta \\ \kappa_2 &= \psi'\sin\phi\cos\theta + \theta'\cos\phi \\ \kappa_3 &= \psi'\cos\phi\cos\theta - \theta'\sin\phi \end{aligned} \tag{5.34}$$

where $\kappa_1 = \tau$ is the torsion, κ_2 and κ_3 are the curvatures about the director axes.

5.4.2 Optimal control

The optimal control formulation of a spatial elastica constrained by a cylindrical wall is derived herein. The potential energy of the spatial elastica is given by (5.28) and involves the torsion and bending curvatures (7.5). Adopting L as length scale and EI/L^2 as force scale (see also (7.2)), the strain energy becomes

$$\mathcal{U} = \frac{1}{2}\int_0^1 \left(\kappa_2^2(s) + \kappa_3^2(s)\right) ds + \frac{\gamma}{2}\int_0^1 \kappa_1^2(s) ds \tag{5.35}$$

where $\gamma = GJ/EI$ is the ratio of shear to bending moduli. Taking into account the director axes (5.30-5.32) and considering that $\partial_s\mathbf{r} = \mathbf{d}_1$(5.27), the inextensibility-unshearability constraints can be written as follows

$$\begin{aligned} x' &= \cos\theta\cos\psi \\ y' &= \cos\theta\sin\psi \\ z' &= -\sin\theta \end{aligned} \tag{5.36}$$

where $\{x, y, z\}$ are the cartesian coordinates of the Kirchhoff rod. If we consider a cylindrical wall of clearance c, the unilateral constraint can be expressed with respect to the cartesian coordinates $\{y, z\}$;

$$y^2(s) + z^2(s) \leq c^2 \tag{5.37}$$

For displacement-controlled conditions we predefine the boundary condition $x(1) = 1-\delta$ where δ is the end-shortening and the optimal control problem for clamped-clamped boundary conditions

takes the following form

$$\begin{cases} \text{Minimize} \quad J\left[\mathbf{x}(\cdot),\mathbf{u}(\cdot)\right] = \frac{1}{2}\int_0^1 \left(\kappa_2^2(s)+\kappa_3^2(s)\right) ds + \frac{\gamma}{2}\int_0^1 \kappa_1^2(s) ds \\ \text{subject to} \\ \qquad\qquad x' = \cos\theta(s)\cos\psi(s) \\ \qquad\qquad y' = \cos\theta(s)\sin\psi(s) \\ \qquad\qquad z' = -\sin\theta(s) \\ \qquad\qquad \psi' = u_1 \\ \qquad\qquad \theta' = u_2 \\ \qquad\qquad \phi' = u_3 \\ \qquad x(0) = y(0) = z(0) = y(1) = z(1) = 0 \\ \qquad \psi(0) = \psi(1) = \theta(0) = \theta(1) = \phi(0) = \phi(1) = 0 \\ \qquad\qquad y^2(s) + z^2(s) \leq c^2 \end{cases} \tag{5.38}$$

where the state variables are the cartesian coordinates $\{x, y, z\}$ of the elastica and the Euler angles $\{\psi, \theta, \phi\}$ and the control variables are the spatial derivatives of the Euler angles $\{\psi', \theta', \phi'\}$ while the rotational strains become

$$\kappa_1 = u_3 - u_1 \sin\theta \tag{5.39}$$

$$\kappa_2 = u_1 \sin\phi\cos\theta + u_2\cos\phi \tag{5.40}$$

$$\kappa_3 = u_1 \cos\phi\cos\theta - u_2\sin\phi \tag{5.41}$$

Substituting (5.39-5.41) into the potential energy of the spatial elastica (5.35), the final form of the functional is obtained

$$J\left[\mathbf{x}(\cdot),\mathbf{u}(\cdot)\right] = \frac{1}{2}\int_0^1 \left(u_1^2\cos^2\theta + u_2^2\right) ds + \frac{\gamma}{2}\int_0^1 \left(u_3 - u_1\sin\theta\right)^2 ds \tag{5.42}$$

The normal, or simple Hamiltonian can be then expressed as follows

$$\begin{aligned} H(\boldsymbol{\lambda},\mathbf{x},\mathbf{u}) = {} & \frac{1}{2}\left(u_1^2\cos^2\theta + u_2^2\right) + \frac{\gamma}{2}\left(u_3 - u_1\sin\theta\right)^2 \\ & + \lambda_x\cos\theta\cos\psi + \lambda_y\cos\theta\sin\psi + \\ & - \lambda_z\sin\theta + \lambda_\psi u_1 + \lambda_\theta u_2 + \lambda_\phi u_3 \end{aligned}$$

and the augmented Hamiltonian is given by

$$\bar{H}\left(\boldsymbol{\mu},\boldsymbol{\lambda},\mathbf{x},\mathbf{u}\right) = H(\boldsymbol{\lambda},\mathbf{x},\mathbf{u}) + \mu\left(\mathrm{y}^2(s) + \mathrm{z}^2(s) - \mathrm{c}^2\right) \tag{5.43}$$

where $\mu \dagger g$ is always satisfied. Based on the assigned boundary conditions the scalar function Φ is described as follows

$$\begin{aligned}\Phi = &\nu_1 x(0) + \nu_2 x(1) + \nu_3 y(0) + \nu_4 y(1) + \nu_5 z(0) + \nu_6 z(1) \\ &+ \nu_7 \psi(0) + \nu_8 \psi(1) + \nu_9 \theta(0) + \nu_{10} \theta(1) + \nu_{11} \phi(0) + \nu_{12} \phi(1)\end{aligned} \tag{5.44}$$

The minimization of the Hamiltonian with respect to the control variables gives

$$\bar{H}_{\mathbf{u}} = \left\{ \begin{array}{c} u_1 \left(\cos^2\theta + \gamma \sin^2\theta\right) - \gamma u_3 \sin\theta + \lambda_\psi \\ u_2 + \lambda_\theta \\ \gamma \left(u_3 - u_1 \sin\theta\right) + \lambda_\phi \end{array} \right\} = \mathbf{0}$$

which leads to the optimal control variables $\hat{u}_1 = -\left(\lambda_\psi + \lambda_\phi \sin\theta\right) / \cos^2\theta$, $\hat{u}_2 = -\lambda_\theta$, $\hat{u}_3 = -\left(\lambda_\psi + \lambda_\phi \sin\theta\right) \sin\theta / \cos^2\theta - \lambda_\phi / \gamma$. The adjoint equations derived by $\bar{H}$ are written as follows

$$-\lambda_x^{'} = \frac{\partial \bar{H}}{\partial x} = 0 \tag{5.45}$$

$$-\lambda_y^{'} = \frac{\partial \bar{H}}{\partial y} = \left\{ \begin{array}{cc} 0 \quad \text{if} & \text{unconstrained} \\ \mu_c \sin\beta \quad \text{if} & y_c^2 + z_c^2 = c^2 \end{array} \right. \tag{5.46}$$

$$-\lambda_z^{'} = \frac{\partial \bar{H}}{\partial z} = \left\{ \begin{array}{cc} 0 \quad \text{if} & \text{unconstrained} \\ \mu_c \cos\beta \quad \text{if} & y_c^2 + z_c^2 = c^2 \end{array} \right. \tag{5.47}$$

$$-\lambda_\psi^{'} = \frac{\partial \bar{H}}{\partial \psi} = \cos\theta \left(-\lambda_x \sin\psi + \lambda_y \cos\psi\right) \tag{5.48}$$

$$\begin{aligned}-\lambda_\theta^{'} = \frac{\partial \bar{H}}{\partial \theta} = &\frac{(\gamma - 1)}{2} u_1^2 \sin 2\theta - \gamma u_1 u_3 \cos\theta \\ &- \sin\theta \left(\lambda_x \cos\psi + \lambda_y \sin\psi\right) - \lambda_z \cos\theta\end{aligned} \tag{5.49}$$

$$-\lambda_\phi^{'} = \frac{\partial \bar{H}}{\partial \phi} = 0 \tag{5.50}$$

where $y_c = c \sin\beta$, $z_c = c \cos\beta$ and $\mu_c = 2c\mu$. The adjoint variables have a clear physical meaning. In particular, λ_x, $\{\lambda_y, \lambda_z\}$ and $\{\lambda_\psi, \lambda_\theta, \lambda_\phi\}$ provide the axial compressive force, the shear forces and the moments (twisting and bending), respectively.

The initial and terminal transversality conditions are given by $\lambda_x(0) = -\nu_1$, $\lambda_y(0) = -\nu_3$,$\lambda_z(0) = -\nu_5$, $\lambda_\psi(0) = -\nu_7$, $\lambda_\theta(0) = -\nu_9$, $\lambda_\phi(0) = -\nu_{11}$, $\lambda_x(1) = \nu_2$, $\lambda_y(1) = \nu_4$, $\lambda_z(1) = \nu_6$, $\lambda_\psi(1) = \nu_8$, $\lambda_\theta(1) = \nu_{10}$ and $\lambda_\phi(1) = \nu_{12}$. Using the equations of the adjoint variables, $\lambda_x(s) = \nu_2 = -\nu_1$ and $\lambda_\phi(s) = \nu_{12} = -\nu_{11}$.

Taking into account $\hat{u}_3 - \hat{u}_1 \sin\theta = -\lambda_\phi/\gamma$ and $\lambda'_\phi = 0$

$$\frac{d}{ds}\left(\hat{u}_3 - \hat{u}_1 \sin\theta\right) = 0 \Rightarrow \kappa'_1 = 0$$

which implies that the torsion κ_1 is uniform for an isotropic cylindrical rod independently of the loading conditions.

For displacement-controlled conditions the axial compressive force $\mathcal{Q}$ is indirectly derived by the adjoint variable λ_x. Instead, if we apply force-controlled conditions, the external work $\mathcal{Q}\int_0^1 \cos\theta(s)\cos\psi(s)ds$ with predefined axial compressive force $\mathcal{Q}$ is included in the functional (5.42) while the end-shortening δ is indirectly calculated by the solution of the problem. In the current study displacement-controlled conditions are only assumed.

5.4.3 Results

The stability behavior of an unconstrained spatial elastica is initially studied in order to validate the optimal control formulation for the spatial case . More specifically, we investigate the post-buckling behavior of the clamped-clamped spatial elastica for a ratio of shear to bending moduli $\gamma = 5/7$. Its analytical description is not included here, as it can be found in Chapter 2.

The classical constrained stability problem is then analyzed. A particular example is solved and compared with Fang et al. (2013).

Constrained clamped-clamped spatial elastica

Next we investigate a clamped-clamped spatial elastica constrained by a cylindrical wall of radius $c = 0.1$ and $\gamma = 5/7$. The same problem has been solved by (Chen and Fang, 2013). The elastica is initial unstressed (i.e., straight elastica) and δ is gradually increased.

The elastica remains straight until it reaches a load of $4\pi^2$, which is consistent with the first symmetrical buckling mode of a planar clamped-clamped elastica. The elastica does not touch the wall until C2, where a point contact with the midpoint position of the elastica is met. This is a planar deformation shape and it remains unchanged until C3, where an out-of plane deformation initiates with the same contact condition. Very rapidly the discrete contact becomes a continuous contact at C4 whose length slightly increases until C5. Past this point, the continuous contact splits into two point contacts symmetrically located left and right from the midpoint position $s = 0.5$. At C6 the point contact at midpoint position appears again, which implies a three-contact-point deformation shape. Then the contact point at $s = 0.5$ becomes a continuous, or line contact at C7. The line contact gradually increases until the point-line-point deformation becomes a single continuous contact at C8. This reaches a maximum horizontal force $\mathcal{Q}/\pi^2 = 12.03$ with end-shortening $\delta = 0.239$. Accordingly a reduction of the horizontal load is observed. At C9 the single continuous contact is splitted into three continuous contacts.

As the horizontal force continues to decrease, the two continuous contacts next to the midpoint position $s = 0.5$ become discrete contacts at C10). Hence, a point-line-point deformation shape is obtained. The midpoint continuous contact also becomes a point contact leading to a point-point-point deformation shape at C11, which remains until C12.

As shown in Figure 5.11, the bifurcation diagram is identical to previous work performed by Fang et al. (2013). Nevertheless there are two minor differences. The first difference is that we derive the deformation shape $(4-5)$ with a continuous contact while Fang et al. (2013) jumps from the deformation shape $(3-4)$ directly to $(5-6)$ without the presence of a continuous contact. The second difference is around the plateau. Using optimal control the deformation shape $(8-9)$ starts before the plateau, while Fang et al. (2013) derives the same contact pattern after the peak. The rest of the deformation shapes and their sequence are identical. The deformation shapes for distinct values of end-shortening δ are summarized in Figure 5.12.

Classical Problem											
Points	2	3	4	5	6	7	8	9	10	11	12
δ	0.025	0.0261	0.048	0.057	0.15	0.155	0.22	0.34	0.36	0.4	0.7
$\mathcal{Q}/\pi^2$	4.05	8.02	8.068	8.123	10.8	10.93	11.95	9.647	8.73	7.038	4.01

Table 5.2: Points of evolution of the contact patterns for the bifurcation diagram for a constrained clamped-clamped spatial elastica with clearance $c = 0.1$

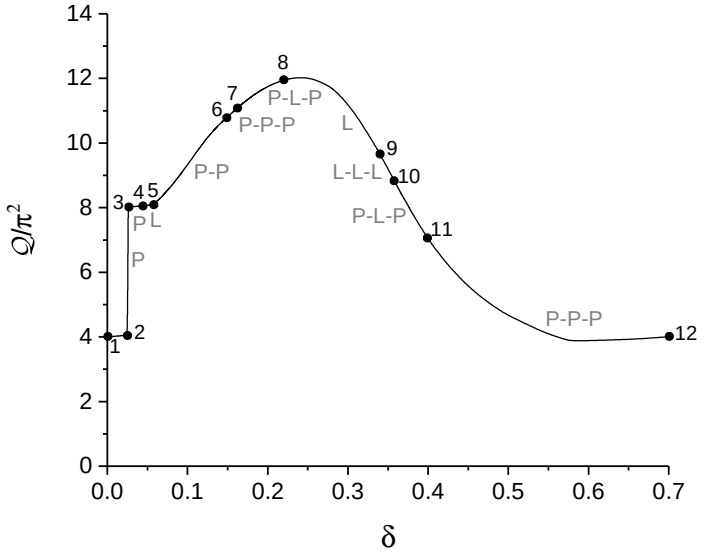

Figure 5.11: Bifurcation diagram for a constrained clamped-clamped elastica of constant length with clearance $c = 0.1$

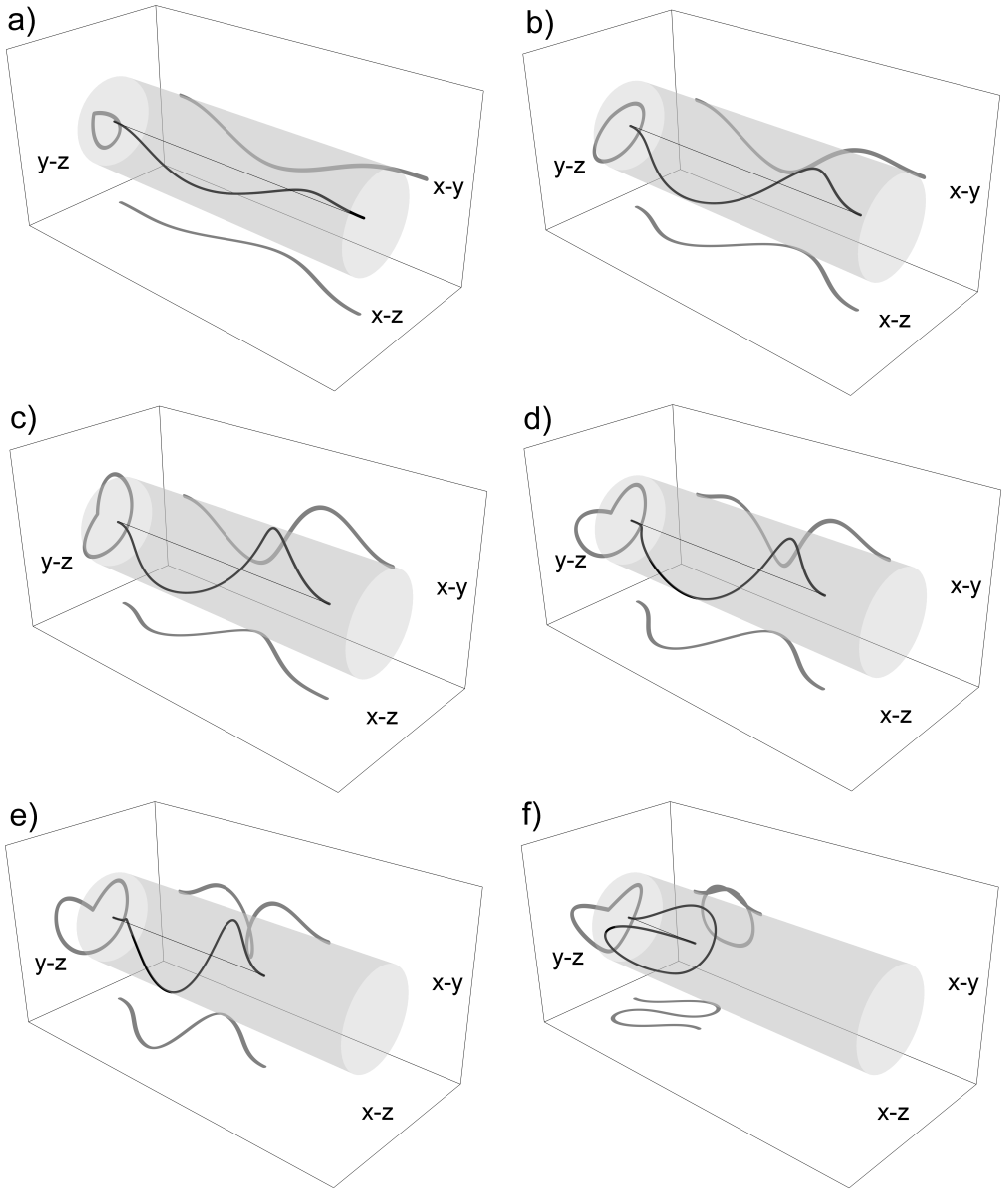

Figure 5.12: Deformation shapes; a) Spatial one point ($\mathcal{Q} = 8.05\pi^2$, $\delta = 0.04$, $\kappa_1 = 0.21$), b) Point-point ($\mathcal{Q} = 9.33\pi^2$, $\delta = 0.1$, $\kappa_1 = 0.64$), c) Point-line-point ($\mathcal{Q} = 11.04\pi^2$, $\delta = 0.16$, $\kappa_1 = 1.21$), d) Line contact ($\mathcal{Q} = 11.95\pi^2$, $\delta = 0.22$, $\kappa_1 = 1.8$) , e) Point-line-point contact ($\mathcal{Q} = 8.31\pi^2$, $\delta = 0.37$, $\kappa_1 = 3.37$) and f) Point-point-point contact ($\mathcal{Q} = 3.95\pi^2$, $\delta = 0.7$, $\kappa_1 = 4.2$)

5.5 Conclusions

From this study it is evident that the optimal control is an efficient tool for the stability analysis of elastic rods in the presence of unilateral constraints. Further analysis could also include second-order optimality conditions. This would require three distinct steps; (i) derivation of the solution adopting a direct method, (ii) use of this solution to define properly an initial guess of the involved variables such that an indirect shooting method can be easily derived for further accuracy and (iii) application of a sensitivity analysis of the shooting mapping which can provide the second-order optimality conditions through the solution of the Riccati equations, as explained in detail in (Malanowski and Maurer, 2001; Maurer and Oberle, 2002). Even though we do not examine the second-order optimality conditions, the assumption of strong variations in the derivation of the first-order optimality conditions, which includes the Weierstrass necessary condition, is sufficient to derive properly the bifurcation diagrams for all conditions without difficulty.

Chapter 6

Optimization-based stability analysis of constrained heavy elastica

The constrained buckling problem of a planar elastica with a non-negligible self-weight, also known as a heavy elastica (Wang, 1984b), is analyzed here. Its buckling response differs remarkably from the buckling problem of a weightless elastica, especially if unilateral constraints are also present, thus special attention is placed to this effect.

The Chapter consists of three parts; (1) the loop tests, (2) the buckling response of a heavy elastica lying on a rigid horizontal or inclined foundation and (3) the buckling behavior of a heavy elastica constrained by two rigid horizontal walls. The first part includes a short review of the available loop tests, which are widely used in the manufacturing of thin elastic sheets for measuring their material properties (see (Plaut, 2015)). In the second part, a step-by-step derivation of the buckling problem is provided, including the effect of the friction. The same problem is then solved by applying an optimal control method. A similar formulation is then suggested for the analysis of the constrained buckling problem with two-sided foundations. Several factors are investigated, such as the effect of the boundary and loading conditions and the clearance of the walls.

6.1 Loop tests

The folding of slender elastic objects with a negligible self-weight is important in manufacturing of papers and textiles (Lloyd et al., 1978; Mahadevan and Keller, 1999). A long thin sheet can be considered inextensible and unshearable. Hence, a simple model of a planar weightless elastica

is a good approximation for the response of slender objects, which undergo only planar bending. Based on the governing equation of the elastica and considering as length scale $l_b = (EI/V)^{1/2}$, where EI is the bending stiffness of the elastica and V is the vertical load, (Wang, 1981a) derived similarity solutions for three distinct cases; (1) the elastica is compressed by two parallel approaching plates, (2) it is folded by two symmetric rollers moving to the right, or (3) it is folded between a moving roller and a flat plane, as shown in Figure 6.1. The dimensionless quantities α, β, ℓ_f denote the width, height and fold length of the elastica, respectively and are given by

$$\begin{cases} \alpha = \sqrt{2}, \quad \beta = 1.69443, \quad \ell_f = 1.85407, & Case\ 1 \\ \alpha = 2.67181, \quad \beta = 1.28591, \quad \ell_f = 3.14844, & Case\ 2 \\ \alpha = 2.70745, \quad \beta = 1.34972, \quad \ell_f = 5.26292, & Case\ 3 \end{cases}$$

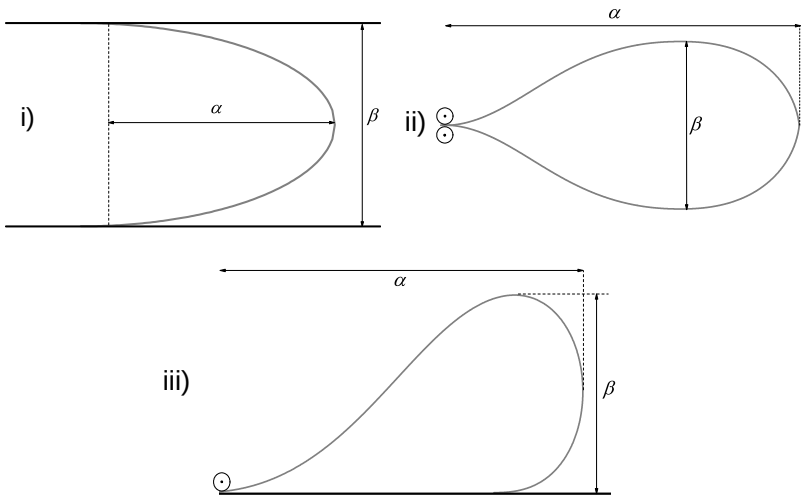

Figure 6.1: Folds of elastica i) Case 1, ii) Case 2 and iii) Case 3

If the weight effect is essential, the length scale $l_b = (EI/V)^{1/2}$ is replaced by $l_g = (EI/w)^{1/3}$, where w is the weight per unit length. The length scale l_g, also called bending length, is a measure of the ratio of its flexural rigidity to its weight. Similarly to the case 3 (see 6.1 iii)), Stuart (1966) proposed a loop test that consists in laying down on a horizontal surface a sufficiently long strip with length ℓ ($\ell \geq 5l_g$) in the form of a loop. In that instance, the dimensionless quantities α, β, ℓ_f are given by

$$\alpha = 3.24324, \quad \beta = 0.9066, \quad \ell_f = 4.6833 \tag{6.1}$$

This experimental test, called "free-standing fold" (Plaut, 2015), is widely used to measure the Young modulus E of "heavy" strips. In particular, for a given weight per unit length w and considering the known geometry of the invariant loop (6.1), Young modulus E can be indirectly computed.

The invariance of the loop can be also verified by solving the following optimal control problem

$$\begin{cases} \underset{u(s)}{minimize} & J = \frac{1}{2}\int_0^\ell u^2(s)ds + \int_0^\ell y(s)ds \\ subject\ to & \\ & y'(s) = \sin\theta(s) \\ & x'(s) = \cos\theta(s) \\ & \theta'(s) = u(s) \\ & y(0) = 0, \quad \theta(0) = -\pi/2 \\ & y(\ell) = -c, \quad \theta(\ell) = -\pi, \quad \theta'(\ell) = 0 \\ & -y(s) - c \leq 0 \end{cases} \tag{6.2}$$

where the functional J consists of the bending energy of the elastica and the gravitational potential energy, x, y are the cartesian coordinates, θ is the inclination angle with respect to the x-axis, u is the control variable, $\ell > \ell_f = 4.6833$ is the total length and c is the clearance, which should be small enough such that a contact with the wall is feasible. Assigning any appropriate combination of ℓ, c, the invariant loop with geometrical characteristics, given by (6.1), is obtained. More details for the optimal control formulation can be found in Chapters 4 and 5.

Alternative experimental tests can be also applied for the derivation of the bending stiffness of thin elastic sheets, such as the heart loop, the standing wrinkle and the clamped fold. More details can be found in (Lloyd et al., 1978; Plaut, 2015; Mahadevan and Keller, 1999).

6.2 Heavy elastica on a horizontal foundation

The buckling behavior of a slender elastic object with a non-negligible self-weight, which is constrained by one-sided foundation, is a problem widely encountered in a variety of applications. For instance, the upheaval buckling problem of a heavy elastic sheet from a rigid foundation and/or rigid walls gained a lot of interest in oil drilling operations and rail tracks (Maltby and Calladine, 1995a,b; Chen and Lin, 2013; Wicks et al., 2008; Miller et al., 2015). Other applications involve the textile fabric and wrinkling of papers during handling operations (Hunt and Blackmore, 1997; Kopp et al., 2000; Lloyd et al., 1978; Jae Ho Jung et al., 2004).

The first major contribution in the buckling problem of a heavy elastic sheet from a flat rigid horizontal substrate is attributed to (Wang, 1981b, 1984a). Wang (1986) applied a simple model of a planar elastica to analyze its buckling response under the action of a compressive

force. Based on the length of the elastica, Wang (1984b) proposed two definitions in accordance with its buckling behavior; (1) the elastica is called "short" if the buckled sheet does not touch the rigid foundation, except at its extremities and (2) the elastica is called "long" if a localized "ruck" is formed, while the rest (also, called flat-lying section) remains in contact with the rigid foundation. These definitions are quite universal nowadays (Domokos et al., 2003; Santillan et al., 2006; Chen and Lin, 2013; Vella et al., 2009; Kolinski et al., 2009).

The main focus, however, was placed on the buckling response of the "long" heavy elastica lying on a horizontal foundation. More specifically, Domokos et al. (2003) solved this buckling problem numerically by using a global search algorithm and compared the theoretical results with experimental observations. The main conclusion is that as the uplift of the formed ruck increases, its symmetrical shape gradually transforms into an asymmetric configuration. This transition point is the "symmetry-breaking bifurcation" and occurs before a self-contact is established. The same result was also deduced by Chen and Lin (2013). In particular, Chen and Lin (2013) used an Eulerian description of the problem, taking into account the variation of the contact points during vibration, and accordingly applied a shooting method from which natural values of the lowest frequencies imply a stable equilibrium state. A similar methodology was followed by Santillan et al. (2006), who studied the buckling behavior of heavy elastic strips resting on an inclined rigid foundation.

Quite recently, the motion of the localized ruck along a horizontal substrate was also investigated. The major results that arise from experimental observations (see Vella et al. (2009)) are the steady speed and the steady shape of the ruck, except at initial and final stages of the experiments. Vella et al. (2009) also noticed that the velocity of the travelling ruck is not uniquely dependent on its shape. This observation is in full aggreement with the numerical analysis by Santillan et al. (2006); Chen and Lin (2013), who calculated a zero fundamental frequency that implies that the ruck can translate at any velocity. For an inclined substrate, Kolinski et al. (2009) also observed the same phenomenon (i.e., steady motion) and found that velocity increases as we increase the slope of the foundation.

Another important factor is the friction between the "heavy" elastica and the rigid substrate. Comninou (1978) was the first who discovered that a rug can be moved from one place on the floor to another by pulling along one of its edges until friction is overcome and simply making it slip. These ruck modes in polymer surfaces were first discovered by Schallamach (1971) and are called Schallamach waves (Barquins, 1985). Viswanathan et al. (2015) showed that Schallamach waves are qualitatively similar to dislocations and carpet rucks, even though three different length scales (nm,microns and m) are present and the corresponding materials have unrelated structural properties.

To understand the effect of friction, Vella et al. (2009) then performed experiments by simply shifting the one end of the strip vertically, then moving it rapidly downwards and keeping this end fixed afterwards, while the rest is resting on the frictional substrate. In this manner, a ruck is

generated from the "fixed" end that moves towards the free end. The experimental results showed that the slipping of the flat-lying section causes the ruck height to reduce and consequently a ruck velocity to increase as the free end is gradually approached. A further characteristic of the slipping ruck behaviour was identified by O'Keefe and Gooch (2015). When the elastic strip is sufficiently long, the ruck was observed to reduce to a certain "residual" height with a constant "residual" speed. This condition remains unchanged until reaching the free end.

Even though this buckling problem has been extensively studied, its physics is not completely understood yet. In particular, there are two main issues; (1) why theory predicts an infinite compressive force for the formation of the ruck and (2) what is the dissipation mechanism in the motion of the ruck, the rolling or the sliding friction. The first paradox was recently investigated by Lee et al. (2015), who suggested that the reason behind this unorthodox result is the assumption of inextensibility. Relaxing this property, a finite value of the compressive horizontal force can be derived. The second issue is still unclear. For instance, as we mention above, Vella et al. (2009) and O'Keefe (2015) take only into account the effect of a sliding friction, while Kolinski et al. (2009) believes that the rolling friction is dominant in the case of an inclined substrate.

6.2.1 "Long" heavy elastica on a horizontal foundation

The main focus of the current study is the response of a long heavy elastic strip on a horizontal frictional foundation under the action of compressive loads. An analytical description of the static problem is first presented. The dynamics of the localized ruck is then analyzed. Based on Vella et al. (2009); O'Keefe and Gooch (2015), the dissipation mechanism, arising from the effect of friction, is also explained.

Static analysis

Let us consider a heavy elastica of length L resting on a horizontal rigid foundation under the action of a pair of equal and opposite compressive forces. If the elastica is considered to be "long" in the sense of Wang (1984b), its buckling is accompanied by a formation of a ruck of length $L_r \ll L$, while the rest remains in contact with the rigid foundation, as shown in Figure 6.2 a).

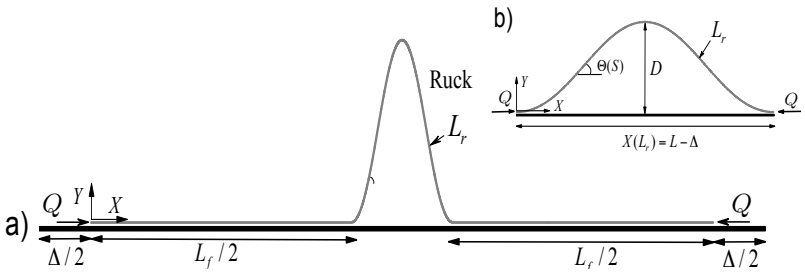

Figure 6.2: Problem description a) heavy elastica of length L, b) ruck formation of length L_r

The potential energy of the "heavy" elastica can be expressed as follows

$$\Pi = \int_0^L \left\{ \frac{1}{2} EI \left(\frac{d\Theta(S)}{dS} \right)^2 + wY(S) + Q\left(\cos\Theta(S) - 1\right) \right\} dS \tag{6.3}$$

where E is the Young modulus, I is the moment of inertia, $\Theta(S)$ is the inclination angle, w is the weight per length of the elastica and Q is the applied horizontal force. The energy functional involves the bending energy, the gravitational potential energy and the external work of the applied force Q, respectively.

By vanishing the first variation of the functional (6.3), the governing equation of the elastica is obtained $EId^2\Theta/dS^2 + Q\sin\Theta - w\left(L/2 - S\right)\cos\Theta = 0$. The elastica is then divided into the buckled shape, also called ruck, with length $L_r \ll L$ and the flat-lying segment of length $L_f = L - L_r$. The solution of the unstressed section is trivial, thus the problem is reduced to the analysis of the ruck. In particular, due to symmetry the left-half part of the ruck is only analyzed, as shown in Figure 6.2 b).

Scaling of the problem follows from adopting $l_g = \left(EI/w\right)^{1/3}$ as length scale, $f_g = EI/\ell_g^2 = \left(EIw^2\right)^{1/3}$ as force scale and $m_g = EI/\ell_g = \left(\left[EI\right]^2 w\right)^{1/3}$ as moment scale (i.e., weight based scaling law (WSL)) Wang (1981b)

$$s = \frac{S}{l_g}, \quad x = \frac{X}{l_g}, \quad \ell = \frac{L}{l_g}, \quad y = \frac{Y}{l_g}, \quad d = \frac{D}{l_g}, \quad \delta = \frac{\Delta}{l_g} \quad , \mathcal{Q} = \frac{Q}{f_g}$$

which leads to the governing equation of the ruck

$$\frac{d^2\theta}{ds^2} + \mathcal{Q}\sin\theta - \left(\frac{\ell_r}{2} - s\right)\cos\theta = 0 \tag{6.4}$$

with boundary conditions $\theta(0) = \theta'(0) = \theta\left(\ell_r/2\right) = 0$.

If we assume small displacements and apply the boundary conditions, we get $\tan\left(\ell_r\sqrt{\mathcal{Q}}/2\right) = \ell_r\sqrt{\mathcal{Q}}/2$ with minimum root $\ell_r\sqrt{\mathcal{Q}}/2 = \alpha$ where $\alpha = 4.49341$.

Nevertheless, the product form of $\ell_r\sqrt{\mathcal{Q}}$ makes the explicit solution of the parameters (e.g., the end-shortening δ) a difficult task. Instead, an intermediate scaling is imposed to overcome this complexity. Starting from the original equation of the ruck and assuming a length scale $l_f = (EI/Q)^{1/2}$ (i.e., force based scaling law (FSL)), the equation of the ruck becomes

$$\frac{d^2\theta}{d\bar{s}^2} + \sin\theta - \varepsilon\left(\frac{\bar{\ell}_r}{2} - \bar{s}\right)\cos\theta = 0 \tag{6.5}$$

where $\bar{\ell}_r = L_r/l_f$ is the length of the ruck. For small displacements $\theta \ll 1$, which also implies $\sin\theta = \theta - \theta^3/6$ and $\cos\theta = 1 - \theta^2/2$, (6.5), shows that the parameter $\varepsilon = w\left(EI/Q^3\right)^{1/2}$ is necessarily small. Based on this assumption, an asymptotic analysis can be applied with expansion $\theta = \varepsilon\vartheta(\bar{s}) + \mathcal{O}(\varepsilon^2)$, which is substituted into (6.5) to get the first-order term

$$\mathcal{O}(\varepsilon): \quad \frac{d^2\vartheta}{ds^2} + \vartheta = \left(\frac{\bar{\ell}_r}{2} - \bar{s}\right) \tag{6.6}$$

with boundary conditions $\vartheta(0) = \vartheta'(0) = \vartheta\left(\bar{\ell}_r/2\right) = 0$. Its solution is $\vartheta(\bar{s}) = \sin\bar{s} - \bar{\ell}_r\cos s\bar{/}2 + \bar{\ell}_r/2 - \bar{s}$, where $\bar{\ell}_r = 2\alpha$ and $\alpha = 4.49341$.

The cartesian parametrization of the elastica $\bar{x}(\bar{s}) = X(S)/l_f$, $\bar{y}(\bar{s}) = Y(S)/l_f$ is derived by applying the inextensibility-unshearability conditions

$$\bar{x}(\bar{s}) = \int_0^{\bar{s}} \cos\theta \mathrm{d}\xi, \qquad \bar{y}(\bar{s}) = \int_0^{\bar{s}} \sin\theta \mathrm{d}\xi \tag{6.7}$$

Taking into account the asymptotic expansion of the inclination θ, consistent expansions of the cartesian components are assumed $\bar{x}(\bar{s}) = \bar{s} - \varepsilon^2\zeta(\bar{s})$, $\bar{y}(\bar{s}) = \varepsilon\eta(\bar{s})$ with $d\eta(\bar{s})/d\bar{s} = \vartheta(\bar{s})$ and $d\zeta(\bar{s})/d\bar{s} = \vartheta^2(\bar{s})/2$. Considering that $\bar{x}(0) = \eta(0) = 0$ and $\bar{y}(0) = \zeta(0) = 0$, we get

$$\eta(\bar{s}) = 1 - \cos\bar{s} - \bar{s}\sin\bar{s} + \bar{s}\frac{\bar{\ell}_r}{2} - \frac{\bar{s}^2}{2} \tag{6.8}$$

$$\begin{aligned}\zeta(\bar{s}) = -\frac{1}{2}\Bigg\{ &\frac{\bar{\ell}_r}{4}\cos 2\bar{s} + \frac{1}{4}\left(\frac{\bar{\ell}_r^2}{4} - 1\right)\sin 2\bar{s} + \bar{\ell}_r\bar{s}\sin\bar{s} + 2\bar{s}\cos\bar{s} \\ &-2\left(\frac{\bar{\ell}_r^2}{4} + 1\right)\sin\bar{s} + \bar{s}^2\left(\frac{\bar{s}}{3} - \frac{\bar{\ell}_r}{2}\right) + \frac{1}{2}\left(\frac{3\bar{\ell}_r^2}{4} + 1\right)\bar{s} - \frac{\bar{\ell}_r}{4}\Bigg\}\end{aligned} \tag{6.9}$$

Using the values $\zeta\left(\bar{\ell}_r/2\right) = 37.80215$ and $\eta\left(\bar{\ell}_r/2\right) = 15.6987$, we can evaluate the involved parameters, namely the maximum vertical component d, the end-shortening δ, the length of the deformed segment ℓ_r and the maximum bending moment m. In particular, we combine the two distinct scaling laws to express all terms with respect to the horizontal force $\mathcal{Q}$, or the end-shortening $\delta = 2\varepsilon^2\zeta\left(\bar{\ell}_r/2\right) l_f/l_g = 75.6043\mathcal{Q}^{-7/2}\mathcal{Q} = 3.441\delta^{2/7}$

$$d = Y(L_r/2)l_g^{-1} = \varepsilon\eta\left(\bar{\ell}_r/2\right)l_f l_g^{-1} = 15.6987\mathcal{Q}^{-2}, \quad \text{or} \quad d = 1.326\delta^{4/7} \tag{6.10}$$

$$\ell_r = L_r l_g^{-1} = \bar{\ell}_r l_f l_g^{-1} = 2\alpha\mathcal{Q}^{-1/2}, \quad \text{or} \quad \ell_r = 4.844\delta^{1/7} \tag{6.11}$$

$$m = EI\varepsilon m_g^{-1} l_f^{-1} \frac{d\vartheta\left(\bar{\ell}_r/2\right)}{d\bar{s}} = -5.6033\mathcal{Q}^{-1}, \quad \text{or} \quad m = -1.6284\delta^{2/7} \tag{6.12}$$

The equations (6.10)-(6.12) are then used to calculate the energy terms included in (6.3). Taking into account the energy scale $l_g f_g$, the bending energy of the ruck is given by

$$\mathcal{U}_b = \frac{2}{l_g f_g}\left[\int_0^{L_r/2} \frac{1}{2} EI \left(\frac{d\theta(S)}{dS}\right)^2 dS\right] \simeq \alpha \int_0^{\bar{\ell}_r/2} \left(\frac{d\vartheta(\bar{s})}{d\bar{s}}\right)^2 d\bar{s} \tag{6.13}$$

where $\alpha = EI\varepsilon^2/l_f l_g f_g = 3.441^{-5/2}\delta^{5/7}$ and $\int_0^{\bar{\ell}_r/2}\left(d\vartheta(\bar{s})/d\bar{s}\right)^2 d\bar{s} = 45.065$, leading to $\mathcal{U}_b = 2.06\delta^{5/7}$. The gravitational potential energy is similarly obtained

$$\mathcal{U}_w = \frac{2}{l_g f_g}\left[\int_0^{L_r/2} wY(S)dS\right] \simeq 2\beta \int_0^{\bar{\ell}_r/2} \eta\left(\bar{s}\right) d\bar{s} \tag{6.14}$$

where $\beta = wl_f^2\varepsilon/l_g f_g = 3.441^{-5/2}\delta^{5/7}$ and $\int_0^{\bar{\ell}_r/2}\eta\left(\bar{s}\right)d\bar{s} = 30.242$, which gives $\mathcal{U}_w = 2.75\delta^{5/7}$. The external work of the horizontal force can be approximated by substituting $\mathcal{Q} = 3.441\delta^{-2/7}$ and evaluating the integral with respect to the change of the end-shortening $\mathcal{W}_\mathcal{R} = \int 3.441\delta^{-2/7}d\delta = 4.82\delta^{5/7}$ (O'Keefe and Gooch, 2015). We can easily verify that $\mathcal{W}_\mathcal{R} = \mathcal{U}_b + \mathcal{U}_w$.

Dynamics

When the motion of the "dynamic" ruck is analyzed, the translational and rotational kinetic energies should be also included, which in dimensionless form (i.e, WSL scaling law) become

$$\mathcal{E}_k = \frac{1}{2}\int_0^{\ell_r}\left(\dot{x}^2 + \dot{y}^2\right)ds + \frac{1}{2}\alpha\int_0^{\ell_r}\dot{\theta}^2 ds \tag{6.15}$$

where $\alpha = gl_g/(E/\rho)$ and $t_g = (l_g/g)^{1/2}$ is the time scale. However the velocity of the elastica is much slower than the speed of the sound $\alpha \ll 1$. This implies that the rotational kinetic energy is negliglible when compared to the translational kinetic energy and therefore it is omitted (Dichmann et al., 1996; Dichmann and Maddocks, 2000).

By vanishing the first variation of the total energy functional (6.13-6.15), the governing equations of the ruck are given by

$$\frac{\partial\bar{\mathcal{R}}_x}{\partial s} = \frac{\partial^2 x}{\partial t^2}, \qquad \frac{\partial\bar{\mathcal{R}}_y}{\partial s} = \frac{\partial^2 y}{\partial t^2} \tag{6.16}$$

$$\frac{\partial^2\theta}{\partial s^2} = \bar{\mathcal{R}}_x \sin\theta - \bar{\mathcal{R}}_y \cos\theta \tag{6.17}$$

where (6.16), (6.17) are the force and moment balances and $\bar{\mathcal{R}}_x$, $\bar{\mathcal{R}}_y$ are the dimensionless horizontal and vertical components, respectively.

Nevertheless, Vella et al. (2009) deduced by experiments that the ruck moves at a constant speed and its shape remains almost identical, except at the early and final stages of its dynamical motion. Hence, Vella et al. (2009) proposed to transform the PDE system (6.16-6.17) to an ODE, assuming steady motion. More specifically, Vella et al. (2009) introduced a new variable $\eta \equiv s - v_r t$ where v_r is the constant speed of the ruck which leads to $\bar{\mathcal{R}}_x(s,t) \equiv -\left(\mathcal{Q} + v_r^2\right)$, $\bar{\mathcal{R}}_y(s,t) \equiv \left(\bar{\ell}_r/2 - \eta\right)$ and a single equation for $\theta(s,t) = \bar{\theta}(\eta)$:

$$\frac{\partial^2\bar{\theta}}{\partial\eta^2} = -\left(\mathcal{Q} + v_r^2\right)\sin\bar{\theta} + \left(\frac{\ell_r}{2} - \eta\right)\cos\bar{\theta} \tag{6.18}$$

which is the same with the governing equation of the "static" ruck (6.4) if we replace the "static" horizontal force $\mathcal{Q}$ by the "effective" term $\mathcal{Q}+v_r^2$ and modify the boundary conditions by imposing the change of variables. This similarity also implies that the shapes of a steadily moving ruck and a static ruck (see Section 6.2.1) are identical for a given δ if small displacements are assumed.

Inspired by Vella et al. (2009), O'Keefe and Gooch (2015) suggested a simple procedure to evaluate the kinetic energy of the ruck. The ruck can be divided into n identical elements of length $\ell_e = \ell_r/n$, which are moving with constant speed v_r. For given length ℓ_e and speed v_r, the time step dt is then derived by $dt = \ell_e/v_r$. In this manner, the horizontal displacement of the ruck at the time step dt is exactly equal to the length of the element ℓ_e.

To clarify the procedure, we assume that the ruck is divided into 8 elements (see Figure 6.3). Since the motion is under constant speed, the number and the length of the elements remain unchanged. At time t the first and the last nodes [1], [9] which are in contact with the rigid foundation are replaced by the nodes [2], [10] at time $t + dt$.

Let us now follow the path of a specific node for a steadily moving ruck. For instance, the displacement of the node [7] is denoted as $u_{[7]}$ in Figure 6.3. Considering that the horizontal motion is prescribed by the constant speed v_r and the horizontal displacement is equal to the length of the element $\ell_e = \ell_7$, we can approximately evaluate the displacement of the node [7] $u_{[7]}^2 = 2\ell_7^2\left(1 - \cos\theta_7\right)$ by applying the law of cosines for the corresponding triangle, as shown in Figure 6.3.

Hence, in general if the set of nodes is $\mathcal{I}_t = \{[1], ..., [n+1]\}$ for n elements at time t, the new set of nodes at time $t + dt$ becomes $\mathcal{I}_{t+dt} = \{[2], ..., [n+2]\}$. In addition, the displacement of a node $[i]$ can be approximated as $u_{[i]}^2 = 2\ell_i^2\left(1 - \cos\theta_i\right)$. If we assume that the velocity of a node $[i]$ is given by $v_{[i]} \approx u_{[i]}/dt$, which defines the speed of the element i, the kinetic energy

can be approximated as follows

$$\mathcal{E}_k = \frac{1}{2}\sum_{i=1}^{n} v_{[i]}^2 = \frac{1}{2}\sum_{i=1}^{n}\left(\frac{u_{[i]}}{dt}\right)^2 = \\ = \left(\frac{\ell_e}{dt}\right)^2 \sum_{i=1}^{n}(1-\cos\theta_i) = v_r^2\delta \tag{6.19}$$

where for the first node $u_{[1]} = 0$. Consequently the total energy of the ruck can be expressed in terms of the end-shortening and the speed of the ruck as follows

$$\mathcal{E} = \mathcal{U}_b + \mathcal{U}_w + \mathcal{E}_k = 4.82\delta^{5/7} + v_r^2\delta \tag{6.20}$$

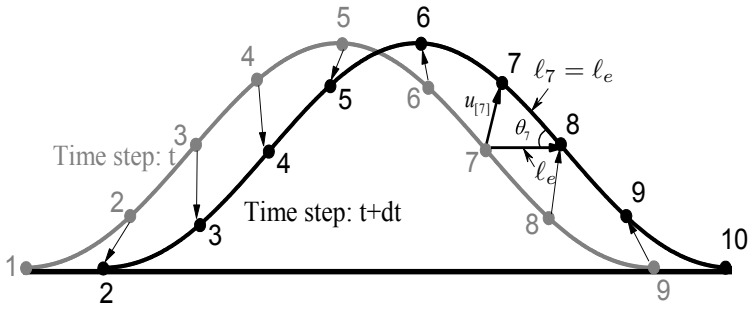

Figure 6.3: Steady motion

Effect of friction

The frictional effect between the elastica and the rigid foundation on the motion of the ruck is investigated in the following Section. We consider that the left end of the elastica is fixed, while the right end is free to move. Following the experiments we can define the initial condition of the ruck by predefing its shape based on a given end-shortening δ and assigning an initial "steady" velocity of the ruck v_r^s.

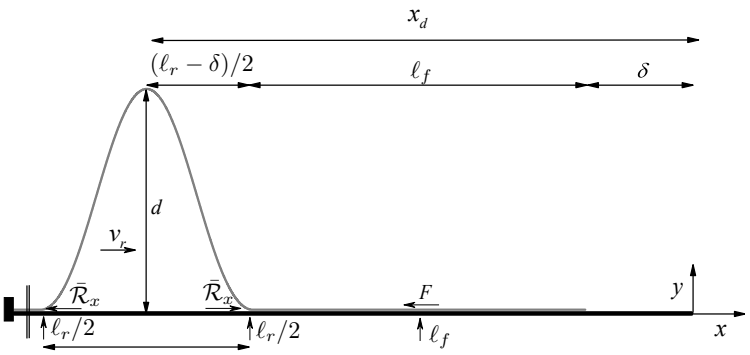

Figure 6.4: Problem description

Let us now define a system of coordinates (x, y) with origin at the right extremity of the elastica in its unstressed state, as shown in Figure 6.4. We denote as x_d the coordinate of the x-position of the ruck of the maximum height d and F the frictional force between the elastica and its foundation, which is derived by integration of the corresponding length of elastica (Lee et al., 2015).

Based on experimental observations (O'Keefe and Gooch, 2015; Vella et al., 2009), the ruck is initially moving with constant velocity v_r and its shape remains unchanged until the onset of slipping. In particular, we can assume that the shape of the traveling ruck is identical to the static case of the ruck for a given end-shortening δ, while the "dynamic" horizontal force can be approximated as follows

$$\bar{\mathcal{R}}_x = \mathcal{Q} - v_r^2 = 3.441\delta^{-2/7} - v_r^2 \tag{6.21}$$

where v_r is the speed of the ruck. More details for the derivation of (6.21) can be found in Sections (6.2.1-6.2.1).

On the other hand, the friction force can be approximated as follows

$$F = \left(\ell_f + \frac{\ell_r}{2}\right)\mu = \left(-x_d - \frac{\delta}{2}\right)\mu$$

where μ is the friction coefficient. If the friction force F is larger than the applied horizontal force $F > \bar{\mathcal{R}}_x$, the flat-lying segments does not move and the end-shortening remains unchanged. At this stage, the shape of the ruck does not change and its speed $v_r = v_r^s$. This condition is called sticking behavior. The slipping process initiates when the friction force between the flat-lying segment and the rigid foundation becomes lower than the "dynamic" horizontal force.

Past the "slipping point", the flat-lying segment starts accelerating. This leads to a gradual reduction of the end-shortening δ, which affects the "static" horizontal force $\mathcal{Q} = 3.441\delta^{-2/7}$ and the shape of the ruck. More specifically, the height of the ruck starts decreasing, while the ruck

is moving with higher speed (Vella et al., 2009). The latter effect can be explained as follows; since a ruck of lower height d has less potential energy and requires less kinetic energy to travel at its current velocity, the excess energy is transferred to the kinetic energy of the "reduced" ruck, which starts accelerating (O'Keefe, 2015). Eventhough the velocity of the ruck increases and a steady motion is not present, we can assume that (6.21) continues to be valid with updated values of horizontal force and speed (O'Keefe, 2015). This approximation is considered to be consistent with experimental results, which show that the shape of the ruck remains almost symmetrical, implying uniform motion of the reduced ruck.

Nevertheless, this gradual increase of the velocity of the ruck may lead to the vanishing value of the horizontal force $\bar{\mathcal{R}}_x$ when $v_r = (3.441)^{1/2}\,\delta^{-1/7}$. This is called "self-sustaining" velocity v_s. Past this point, the "dynamic" horizontal force $\bar{\mathcal{R}}_x$ becomes tensile. Eventhough the force $\bar{\mathcal{R}}_x$ opposes the motion of the flat-lying segment, it continues moving because of its inertia with a resultant force equal to the sum of the "dynamic" horizontal and the friction forces. This causes the flat-lying section to reduce in velocity and cease slipping. At this stage, the ruck attains a constant height, which is called residual condition with a "residual" velocity v_r^r. This final condition is only met when the length of the heavy elastica is sufficiently long.

The whole slipping process is presented in Figure 6.5. A simple algorithm following this approximate mathematical process can be found in O'Keefe (2015).

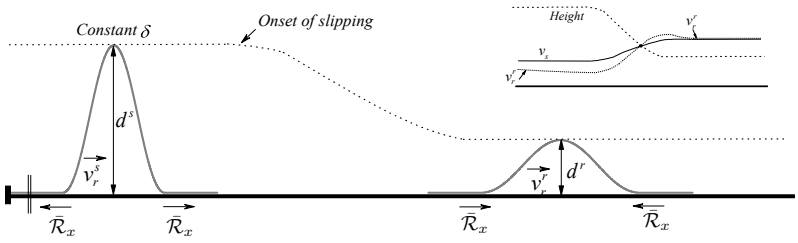

Figure 6.5: Slipping process

6.2.2 "Short" heavy elastica on a horizontal foundation

When the heavy elastica is short in the sense of Wang 1984b, the elastica is not in contact with the horizontal wall except at its extremities. The governing equation of the elastica is given by $EId^2\theta/dS^2 + Q\sin\theta - W\,(L/2 - S)\cos\theta = 0$ with boundary conditions $\theta(0) = 0$ and $\theta(L/2) = 0$. Scaling of this problem follows from adopting $l_b = L$ as length scale and $f_b = EI/L^2$ as force scale (i.e., bending based scaling law (BSL)), which leads to

$$\frac{d^2\theta}{ds^2} + \mathcal{Q}\sin\theta - w\left(\frac{1}{2} - s\right)\cos\theta = 0 \tag{6.22}$$

Assuming small displacements $\theta \ll 1$ we can deduce from (6.22) that the dimensionless weight w is necessarily small. Considering $w = \varepsilon^3$, an asymptotic analysis is applied with expansions for both the axial load $\mathcal{Q} = \mathcal{Q}_o + \varepsilon\mathcal{Q}_1 + \varepsilon^2\mathcal{Q}_2$ and the inclination angle $\theta = \varepsilon\vartheta_o + \varepsilon^2\vartheta_1 + \varepsilon^3\vartheta_2$, respectively. If we also expand $\sin\theta = \theta - \theta^3/6$ and $\cos\theta = 1 - \theta^2/2$, (6.22) is reformulated with boundary conditions $\theta(0) = 0$ and $\theta(1/2) = 0$. Accordingly, the first three order terms can be obtained

$$\mathcal{O}(\varepsilon): \quad \frac{d^2\vartheta_o}{ds^2} + \mathcal{Q}_o\vartheta_o = 0 \tag{6.23}$$

$$\mathcal{O}(\varepsilon^2): \quad \frac{d^2\vartheta_1}{ds^2} + \mathcal{Q}_o\vartheta_1 = -\mathcal{Q}_1\vartheta_o \tag{6.24}$$

$$\mathcal{O}(\varepsilon^3): \quad \frac{d^2\vartheta_2}{ds^2} + \mathcal{Q}_o\vartheta_2 = -\mathcal{Q}_1\vartheta_o - \mathcal{Q}_1\vartheta_1 + \frac{\mathcal{Q}_o\vartheta_o^3}{6} + \left(\frac{1}{2} - s\right) \tag{6.25}$$

The first order solution $\vartheta_o(s)$ is given by $\vartheta_o(s) = \Theta\sin\left(\sqrt{\mathcal{Q}_o}s\right)$ with $\mathcal{Q}_o = 4\pi^2$ and Θ the inclination angle at the inflection point at $s = 1/4$. The next order solution $\vartheta_1(s)$ can be expressed as follows

$$\vartheta_1(s) = -\frac{\mathcal{Q}_1\bar{\Theta}}{2\sqrt{\mathcal{Q}_o}}s\sin\left(\sqrt{\mathcal{Q}_o}s\right) \tag{6.26}$$

which satisfies the boundary conditions only when $\mathcal{Q}_1 = 0$. Hence, $\vartheta_1(s) = 0$. Lastly, the terms $\vartheta_2(s)$ and $\mathcal{Q}_2$ are given by

$$\vartheta_2(s) = \frac{1-2s}{2\mathcal{Q}_o} + \frac{1}{4\mathcal{Q}_o}\left(\frac{\mathcal{Q}_o\Theta^3}{8} - \mathcal{Q}_2\Theta\right)(1-2s)\cos\sqrt{\mathcal{Q}_o}s + \frac{\Theta^3}{192}\sin 3\sqrt{\mathcal{Q}_o}s \tag{6.27}$$

and $\mathcal{Q}_2 = \mathcal{Q}_o\Theta^2/8 + \mathcal{Q}_o^{-1/2}\Theta^{-1}$. For the critical buckling load, we seek the minimum of equation $d\mathcal{Q}_2/d\Theta = 0$ that leads to $\mathcal{Q}_2 = 3\cdot 2^{-5/3}$. Hence, the final expression of the horizontal force becomes $\mathcal{Q} = 4\pi^2 + 3\cdot 2^{-5/3}w^{2/3}$.

The vertical and horizontal coordinates are derived by the inextensibility constraints as $dx/ds = \cos\theta$, $dy/ds = \sin\theta$. Taking into account the expansions of the trigonometric identities, we deduce that their asymptotic expansions are given by $x \approx x_o + \varepsilon^2 x_1$ and $y \approx \varepsilon y_o$ where $x_o(s) = s$, $x_1(s) = \Theta^2\left(s - \sin 2\sqrt{\mathcal{Q}_o}s/2\sqrt{\mathcal{Q}_o}\right)/4$ and $y_o(s) = \Theta\left(1 - \sin\sqrt{\mathcal{Q}_o}s\right)/\sqrt{\mathcal{Q}_o}$. The vertical displacement at $s(1/2)$, the horizontal coordinate $x(1)$ and the end-shortening δ are then approximated as $y(1/2) = \Theta\pi^{-1}w^{1/3}$, $x(1) = 1 - \left(\Theta^2/4\right)w^{2/3}$ and $\delta = \left(\Theta^2/4\right)w^{2/3}$, respectively. In a similar manner, the bending moment $d\theta/ds$ can be easily evaluated.

6.2.3 Optimal control formulation

The buckling response of a heavy elastica constrained by a rigid horizontal, or inclined foundation is analyzed by applying the optimal control method. Utilizing a bending based scaling law (BSL)), the nonlinear optimal control problem $\mathcal{P}$ for clamped-clamped boundary conditions can

be expressed as follows

$$\begin{cases} Minimize \quad J = \frac{1}{2}\int_0^1 u^2(s)ds + \int_0^1 w\left[y(s)\cos\beta + x(s)\sin\beta\right]ds \\ subject\ to \\ \qquad\qquad y'(s) = \sin\theta(s) \\ \qquad\qquad x'(s) = \cos\theta(s) \\ \qquad\qquad \theta'(s) = u(s) \\ \qquad x(0) = y(0) = y(1) = \theta(0) = \theta(1) = 0 \\ \qquad\qquad x(1) = 1 - \delta \\ \qquad\qquad -y(s) \leq 0 \end{cases} \tag{6.28}$$

where β is the inclination of the foundation, θ is the inclination angle with respect to the x-axis and x, y are the cartesian coordinates. The pure-state constraints is $g(y) = y$ with first and second time derivatives given by $g^1(\theta) = -\sin\theta$ and $g^2(y,u) = -u\cos\theta$. This implies that the pure state constraint is of second-order. In the case of a closed contact, we have $g_u^1(y) = 0$ and $g_u^2(y,u) = -\cos\theta$.

Based on the optimal control problem $\mathcal{P}$, the simple Hamiltonian is given by

$$H(\boldsymbol{\lambda}, \mathbf{X}, \mathbf{u}) = \frac{1}{2}u^2(s) + w\left(y(s)\cos\beta + x(s)\sin\beta\right) + \lambda_x\cos\theta + \lambda_y\sin\theta + \lambda_\theta u \tag{6.29}$$

where $\boldsymbol{\lambda} = \{\lambda_y, \lambda_\theta\} \in \mathbb{R}^2$ are the covectors of the dynamics $\mathbf{f} = \{\sin\theta, u\} \in \mathbb{R}^2$. The set of the boundary conditions is described by the scalar function

$$\Phi = \nu_1 y(0) + \nu_2 y(1) + \nu_3\theta(0) + \nu_4\theta(1) + \nu_5 x(0) + \nu_6 x(1) \tag{6.30}$$

for clamped-clamped boundary conditions.

The Lagrangian of the Hamiltonian, or the augmented Hamiltonian additionally includes the pure-state constraint, namely $\bar{H}\left(\boldsymbol{\mu}, \boldsymbol{\lambda}, \mathbf{X}, \mathbf{u}\right) = H(\boldsymbol{\lambda}, \mathbf{X}, \mathbf{u}) + \mu\left(-y(s)\right)$, where the complementarity condition $\boldsymbol{\mu}\perp\mathbf{g}$ is satisfied. The minimization of the augmented Hamiltonian with respect to the control variable is then expressed as

$$\frac{\partial\bar{H}}{\partial u} = \frac{\partial H}{\partial u} = 0 \Rightarrow u + \lambda_\theta = 0 \tag{6.31}$$

Eliminating the control variable in (6.30), the lower Hamiltonian is derived

$$\mathcal{H} = w\left(y(s)\cos\beta + x(s)\sin\beta\right) + \lambda_y\sin\theta - \frac{1}{2}\lambda_\theta^2 + \mu\left(-y(s)\right)$$

which is constant since it does not depend explicitly on s.

The adjoint equations are given by

$$-\lambda_x' = \frac{\partial \bar{H}}{\partial x} = w \sin\beta \tag{6.32}$$

$$-\lambda_y' = \frac{\partial \bar{H}}{\partial y} = \begin{cases} w\cos\beta & \text{if} \quad \text{unconstrained} \\ w\cos\beta - \mu & \text{if} \quad y(\tau_c) = 0 \end{cases} \tag{6.33}$$

$$-\lambda_\theta' = \frac{\partial \bar{H}}{\partial \theta} = -\lambda_x \sin\theta + \lambda_y \cos\theta \tag{6.34}$$

with initial and terminal transversality conditions $\lambda_x(0) = -\nu_5$, $\lambda_y(0) = -\nu_1$, $\lambda_\theta(0) = -\nu_3$ and $\lambda_y(1) = \nu_2$, $\lambda_\theta(1) = \nu_4$, $\lambda_x(1) = \nu_6$. Based on (6.32), the horizontal force is a linear function $\lambda_x(s) = -\nu_5 - w\sin\beta$ and satisfies the terminal condition $\lambda_x(1) = \nu_6$. A similar expression for the shear force is derived $\lambda_y(s) = -\nu_1 - w\cos\beta s$ if the unconstrained case is investigated. In this particular case, if we consider (6.34) and make use of (6.31), we get

$$\theta'' = -\lambda_x \sin\theta + \lambda_y \cos\theta \tag{6.35}$$

with boundary conditions $\theta(0) = \theta(1) = 0$ for a clamped elastica.

Let us now assume that we have a single contact point ζ_c, where $y(\zeta_c) = 0$ is satisfied. In this case, the shear force is $\lambda_y(s) = -\nu_1 - w\cos\beta s$, for $s \in [0, \zeta_c)$, $\lambda_y(\zeta_c^-) - \lambda_y(\zeta_c^+) = \eta$ (i.e., $\eta_1 = \int_{\zeta_c-\varepsilon}^{\zeta_c+\varepsilon} \mu_1 ds$) at the contact point ζ_c which leads to $\lambda_y(s) = -\nu_1 - w\cos\beta s - \eta_1 = \nu_2$, for $s \in (\zeta_c, 1]$. On the other hand, $\lambda_\theta(\tau_c^-) - \lambda_\theta(\tau_c^+) = 0$, because the pure state constraint is independent of θ. This also implies that $\lambda_\theta = -u = -\theta'$ is continuous while its spatial derivative $-\lambda_\theta' = -u'$ is discontinuous at the contact points (6.34) since it depends on the discontinuous shear force $\lambda_y(s)$. In the case of a continuous segment, the only difference is the vanishing control variable $u(\zeta) = 0$ for $\zeta \in [\zeta_{en}, \zeta_{ex}]$, where ζ_{en} and ζ_{ex} denote the entry and exit points of a continuous contact.

Results

Based on the optimal control formulation, we investigate the post-buckling behavior of a heavy elastica with different values of self-weight w and different foundation gradients β. To establish the correctness of the model we first analyze the well-known post-buckling response of a heavy elastica on a horizontal foundation $\beta = 0$ (Wang, 1984b; Domokos et al., 2003; Santillan et al., 2006; Chen and Lin, 2013).

In this class of problem, displacement-controlled conditions are assumed. Load-controlled conditions cannot be applied, because the load initially decreases until a minimum value and then starts increasing, as shown in Figure 6.6 a). The bifurcation graph illustrates the evolution of the "buckling" load $\mathcal{Q}$, derived indirectly by the adjoint variable λ_x, with respect to the

end-shortening δ for distinct values of self-weight w. From Figure 6.6 a), the branch of zero self-weight w can be considered as an "envelope" since all other branches of non-zero values of self-weight w approach asymptotically this line. Figure 6.6 b) indicates that the height of the localized ruck attains a maximum value $h \sim 0.4$ for a weightless elastica, which slightly decreases as the self-weight increases.

Let us now investigate the transition behavior from a symmetric to an asymmetric configuration, also known as the symmetry breaking bifurcation, which was first observed by Domokos et al. (2003). In Figure 6.7, we indicate this transition condition by a solid line (above the solid line, asymmetric configurations are obtained). The graph also shows that the transition occurs at a lower value of end-shortening δ as the self-weight of the elastica increases. Based on this analysis, Domokos et al.' conclusion is confirmed, which states that the symmetry-breaking bifurcation occurs before a self-contact is established. Nevertheless, this result is valid only if the self-weight is $w \geq 130$. For a self-weight $w < 130$, the buckling behavior of the elastica is similar to a weightless elastica, where only a self-contact can occur (no development of an asymmetric configuration).

The corresponding bifurcation diagrams for different foundation gradients β are similar to Figure 6.6. A representative example (i.e., self-weight $w = 200$ and foundation gradient $\beta = \pi/3$) is only shown in Figure 6.8.

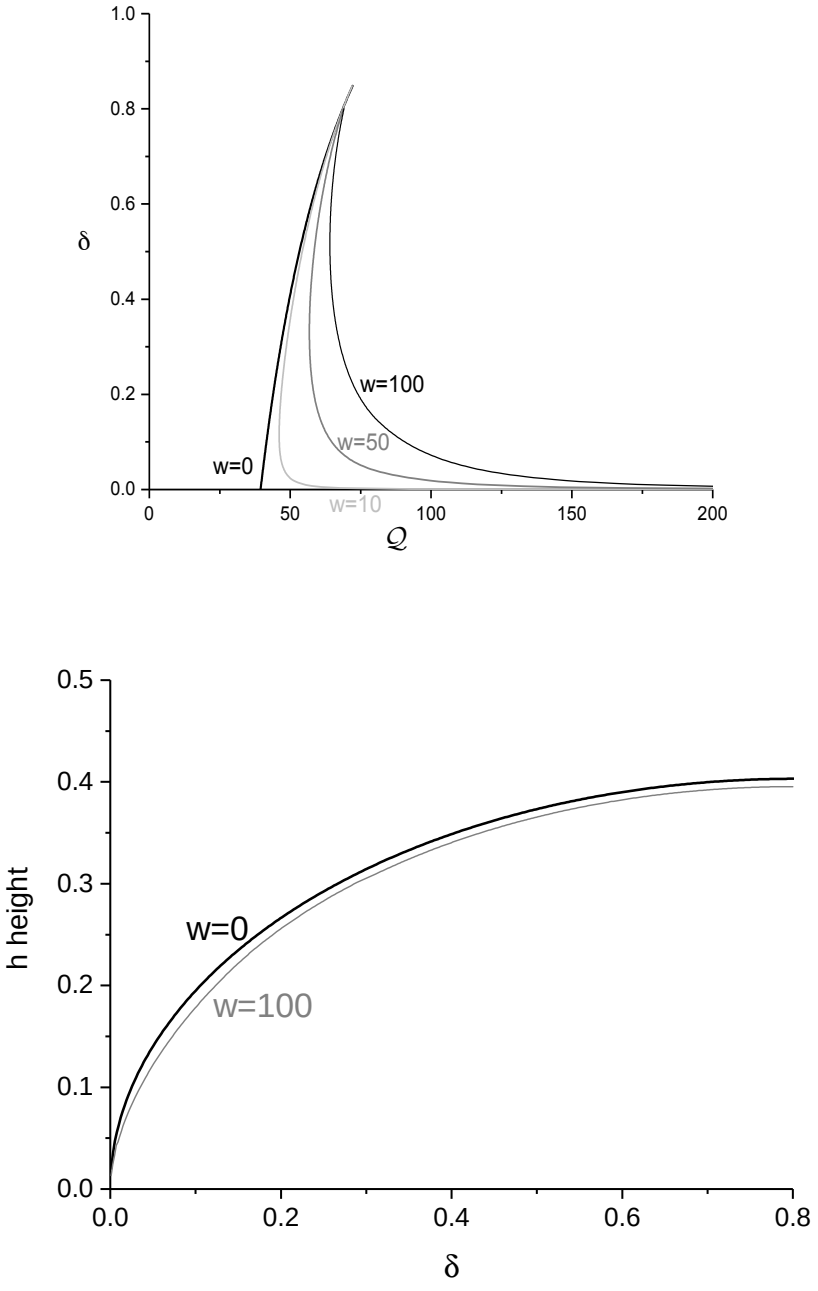

Figure 6.6: a) Bifurcation diagram for a clamped-clamped elastica for different values of self-weight w with one-sided horizontal foundation and b) height of the formed ruck for two distinct values of self-weight $w = 0, 100$

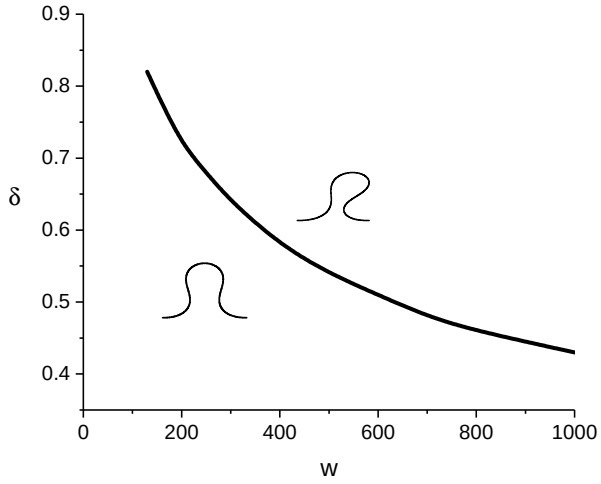

Figure 6.7: "Symmetry-breaking bifurcation" for a horizontal foundation

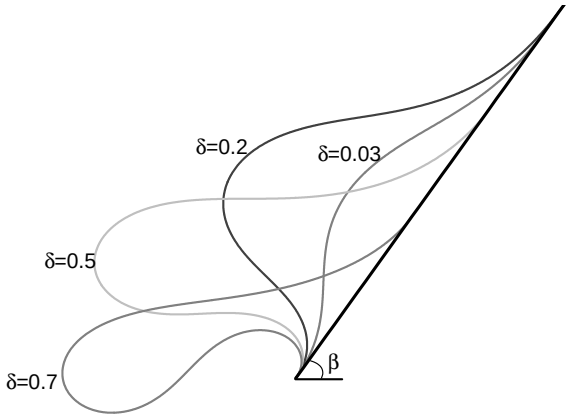

Figure 6.8: Deformation shapes for different values of end-shortening δ for self-weight $w = 200$ and foundation slope $\beta = \pi/3$

6.3 Heavy elastica constrained by rigid horizontal walls

In the following Section, the buckling problem of a heavy elastic sheet with one-sided foundation is extended to the stability analysis of a heavy elastica constrained by two rigid symmetrically, or asymmetrically located walls, as shown in Figure 6.9.

Applying a bending-based scaling law (BSL), a planar unit-length elastica with a self-weight w is considered. The left end of the elastica is fixed, while the right end is constrained to move horizontally. The extremities of the elastica are either clamped at zero inclination or pinned, i.e., free to rotate.

We define a system of coordinates (x, y) with origin at the left end of the elastica and with the x-axis pointing towards the elastica right end. To describe a deformation shape of the elastica, we introduce the arc-length coordinate s with its origin $s = 0$ at $x = 0$ and $y = 0$, and the local inclination angle $\theta(s)$ of the elastica with respect to the x-axis. Applying the inextensibility-unshearability constraints, its deformed configuration $x(s), y(s)$ is fully defined by the function $\theta(s)$ and the fixed end at $s = 0$. The unilateral constraints associated with the presence of the two walls is represented by the inequality condition $-c_l \leq y(s) \leq c_u$ where c_l, c_u are the clearances of the lower and upper walls, respectively.

The initial configuration of the elastica depends on its self-weight w and the clearance c_l of the lower wall. In particular, if the clearance c_l is zero, the elastica rests on the lower wall and its initial buckling behavior is identical to the case of a "long" heavy elastica with one-sided foundation, see Section 6.2.1. On the other hand, if the lower wall is located at $y = -c_l$ with $c_l \neq 0$, two distinct cases are obtained; the elastica is in static equilibrium due to its self-weight either without, or with a point/continuous contact with the lower wall. In the former case, the initial response of the heavy elastica is similar to the post-buckling behavior of a weightless elastica with initial imperfection, while in the latter case the effect of the weight is dominant at the initial state.

We seek to determine the (post)-buckling behavior of the elastica in response to the application of a displacement $\delta = 1 - x(1)$ at the right end that tends to shorten the distance between the two ends. Let us ignore the tensile load, present at the initial state of the elastica. In other words, we restrict our attention to the evolution of the compressive load $\mathcal{Q}$. Hence, for a vanishing compressive load (starting point of our study), the end-shortening δ is always non-zero when the self-weight is non-negligible.

The same problem can be also slightly modified in order to solve the constrained buckling problem of a heavy elastica of variable length, which is the "insertion problem". In this particular problem, the distance between the supports remains constant, while the length $1 + \bar{\delta}$ of the inserted elastica gradually increases. In its initial state, we assume that the length of the elastica L is identical to the horizontal distance between the supports, meaning that a tensile load is present when the self-weight is non-negligible. Hence, the same bending scaling law (BSL) can be also applied here. If we ignore the tensile force, obtained at the initial state, the presence of a compressive load $\mathcal{Q}$ implies that the inserted length is always $1 + \bar{\delta} > 1$ for a non-negligible self-weight w of the elastica. The evolution of the compressive load $\mathcal{Q}$ with respect to the change of the inserted length $\bar{\delta}$ is our main concern below.

Using optimal control, the formulation of the classical problem is first presented. A detailed

analysis for the insertion problem is omitted due to its similarity. Then we illustrate some representative results for the buckling problem of the elastica constrained by two rigid walls with clearances $c_l = 0$ and $c_r > 0$ (see Figure 6.9a)). The same analysis is then performed for symmetrically located walls (see Figure 6.9b)). To illustrate the effect of the weight in the buckling behavior of the constrained elastica, the above examples are calculated for both a weightless and a heavy elastica. The effects of the boundary conditions and the clearances of the walls are also investigated in combination with the presence of the self-weight w.

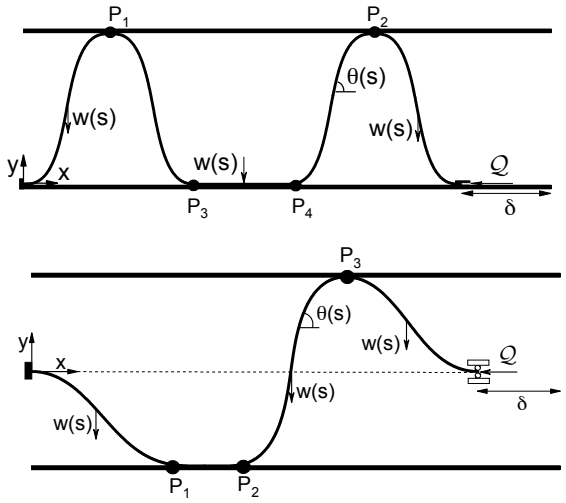

Figure 6.9: Buckling problem of elastica constrained by a) asymmetrically and b) symmetrically located rigid walls

6.3.1 Optimal control formulation of constrained heavy elastica

The constrained buckling problem of a heavy elastica is solved by applying the optimal control method. In particular, in Section 6.3.1, the classical problem is first demonstrated for clamped-clamped boundary conditions. The framework is generic in order to demonstrate the theoretical aspects of the problem. The optimal control formulation for the insertion problem is also presented in Section 6.3.1.

Classical problem

A constant length elastica is constrained by two rigid horizontal walls. A bending-based length scale (BSL) is applied with length scale, the length of the elastica. Accordingly, the nonlinear optimal control problem $\mathcal{P}$ for displacement-controlled conditions can be expressed as

$$\begin{cases} Minimize & J = \frac{1}{2}\int_0^1 u^2(s)ds + \int_0^1 wy(s)ds \\ subject\ to & \\ & y'(s) = \sin\theta(s) \\ & x'(s) = \cos\theta(s) \\ & \theta'(s) = u(s) \\ & x(0) = y(0) = y(1) = \theta(0) = \theta(1) = 0 \\ & x(1) = 1 - \delta \\ & y(s) - c_u \leq 0 \\ & -y(s) + c_l \leq 0 \end{cases} \tag{6.36}$$

where θ is the inclination angle with respect to the x-axis, x, y are the cartesian coordinates, δ is the end-shortening and c_u, c_l are the clearances of the upper and lower horizontal walls, respectively. Clamped-clamped boundary conditions are assumed in (6.36). The pure-state constraints read

$$\mathbf{g}(y) = \left\{ \begin{array}{c} y - c_u \\ -y + c_l \end{array} \right\} :\in \mathbb{R}^{N_2} \tag{6.37}$$

The first and second time derivatives of (6.37) are given by

$$\mathbf{g}^1(\theta) = \left\{ \begin{array}{c} \sin\theta \\ -\sin\theta \end{array} \right\} \qquad \mathbf{g}^2(y,u) = \left\{ \begin{array}{c} u\cos\theta \\ -u\cos\theta \end{array} \right\} \tag{6.38}$$

where $\mathbf{g}_u^1(y) = 0$ and $\mathbf{g}_u^2(y,u) = \{\cos\theta, -\cos\theta\}^\top$ at contact points, or continuous contacts, which implies that the pure state constraints (6.37) are of second-order.

The simple Hamiltonian is given by

$$H(\boldsymbol{\lambda}, \mathbf{X}, \mathbf{u}) = \frac{1}{2}u^2(s) + wy(s) + \lambda_x \cos\theta + \lambda_y \sin\theta + \lambda_\theta u \tag{6.39}$$

where $\boldsymbol{\lambda} = \{\lambda_y, \lambda_\theta\} \in \mathbb{R}^2$ are the covectors of the dynamics $\mathbf{f} = \{\sin\theta, u\} \in \mathbb{R}^2$. The boundary conditions are described by the following scalar function

$$\Phi = \nu_1 y(0) + \nu_2 y(1) + \nu_3 \theta(0) + \nu_4 \theta(1) + \nu_5 x(0) + \nu_6 x(1) \tag{6.40}$$

for clamped-clamped boundary conditions.

The augmented Hamiltonian also includes the inequality constraints

$$\bar{H}\left(\boldsymbol{\mu}, \boldsymbol{\lambda}, \mathbf{X}, \mathbf{u}\right) = H(\boldsymbol{\lambda}, \mathbf{X}, \mathbf{u}) + \mu_1\left(y(s) - c_u\right) + \mu_2\left(-y(s) - c_l\right) \tag{6.41}$$

where the complementarity condition $\boldsymbol{\mu} \perp \mathbf{g}$ should be satisfied.

The minimization of the augmented Hamiltonian with respect to the control variable leads

to $u = -\lambda_\theta$. Eliminating the control variable in (6.40), the lower Hamiltonian is then derived

$$\mathcal{H} = wy(s) + \lambda_y \sin\theta - \frac{1}{2}\lambda_\theta^2 + \mu_1 \left(y(s) - c_u\right) + \mu_2 \left(-y(s) + c_l\right)$$

which remains constant for every $s \in [0,1]$ as it does not depend explicitly on s. Accordingly, the adjoint equations are obtained

$$-\lambda_x' = \frac{\partial \bar{H}}{\partial x} = 0 \tag{6.42}$$

$$-\lambda_y' = \frac{\partial \bar{H}}{\partial y} = \begin{cases} w & \text{if} \quad \text{unconstrained} \\ w + \mu_1 & \text{if} \quad y(\tau_c) = c_u \\ w - \mu_2 & \text{if} \quad y(\tau_c) = -c_l \end{cases} \tag{6.43}$$

$$-\lambda_\theta' = \frac{\partial \bar{H}}{\partial \theta} = -\lambda_x \sin\theta + \lambda_y \cos\theta \tag{6.44}$$

with initial and terminal transversality conditions $\lambda_x(0) = -\nu_5$, $\lambda_y(0) = -\nu_1$, $\lambda_\theta(0) = -\nu_3$ and $\lambda_y(1) = \nu_2$, $\lambda_\theta(1) = \nu_4$, $\lambda_x(1) = \nu_6$. Based on (6.42), the horizontal force is uniform, meaning that $\lambda_x(s) = -\nu_5 = \nu_6$ and it is equal to the applied load $\mathcal{Q}$.

For the unconstrained case the shear force is a linear function $\lambda_y(s) = -\nu_1 - ws$, which satisfies at the right end $\lambda_y(1) = -\nu_1 - w = v_2$. If we consider (6.44) and make use of $u = -\lambda_\theta$, we get

$$\theta'' = -\lambda_x \sin\theta + \lambda_y \cos\theta \tag{6.45}$$

with boundary conditions $\theta(0) = \theta(1) = 0$.

Let us now assume that we have a single contact point ζ_c (i.e., $y(\zeta_c) = c_u$). In this case, the shear force is $\lambda_y(s) = -\nu_1 - ws$, for $s \in [0, \zeta_c)$, $\lambda_y\left(\zeta_c^-\right) - \lambda_y\left(\zeta_c^+\right) = \eta_1$ (i.e., $\eta_1 = \int_{\zeta_c-\varepsilon}^{\zeta_c+\varepsilon} \mu_1 ds$) at the contact point ζ_c which leads to $\lambda_y(s) = -\nu_1 - ws - \eta_1 = \nu_2$, for $s \in (\zeta_c, 1]$. On the other hand, $\lambda_\theta\left(\zeta_c^-\right) - \lambda_\theta\left(\zeta_c^+\right) = 0$ as the pure state constraint is independent of θ. This implies that the curvature, or the bending moment$\lambda_\theta = -u = -\theta'$ is continuous. However $-\lambda_\theta' = -u'$ is discontinuous at the contact points (6.44) since it depends on the shear force $\lambda_y(s)$. In the case of a continuous segment, the only difference is the vanishing control variable $u(\zeta) = 0$ for $\zeta \in [\zeta_{en}, \zeta_{ex}]$.

The numerical procedure of the constrained optimization problem is not described here. A detailed description can be found in Chapter 4. Nevertheless, the effect of the loading conditions is shortly explained. For displacement-controlled conditions, a predefined value of the end-shortening δ is assigned, while the applied force $\mathcal{Q}$ is derived indirectly by the covector λ_x. The same problem can be also formulated for force-controlled conditions if we include the external work of an imposed applied load $\mathcal{Q}$ in the energy functional J. In this case, the end-shortening δ becomes the unknown variable, which is computed by the solution of the problem. However

force-controlled conditions are not considered here.

Insertion problem

The nonlinear optimal control problem $\bar{\mathcal{P}}$ of the insertion problem becomes

$$\begin{cases} \textit{Minimize} & J = \frac{1}{2}\int_0^{1+\bar{\delta}} u^2(\bar{s})d\bar{s} + \int_0^{1+\bar{\delta}} wy(s)d\bar{s} \\ \textit{subject to} & \\ & y'(s) = \sin\theta(s) \\ & x'(s) = \cos\theta(s) \\ & \theta'(s) = u(s) \\ & x(0) = y(0) = y(1+\bar{\delta}) = \theta(0) = \theta(1+\bar{\delta})) = 0 \\ & x(1+\bar{\delta})) = 1 \\ & y - c_u \leq 0 \\ & -y - c_l \leq 0 \end{cases} \tag{6.46}$$

for clamped-clamped boundary conditions. Further analysis is not included since it is identical to the "classical problem", see Section 6.3.1.

6.3.2 Results

The buckling response of a heavy elastica with a self-weight w constrained by two rigid horizontal walls is analyzed by applying an optimal control method. Several effects, such as the clearance, the boundary conditions and the value of the self-weight are analyzed.

Asymmetric walls

The post-buckling behavior of a constant length elastica constrained by two asymmetrically located walls with clearances $c_l = 0$ and $c_u = 0.1$ is investigated. To understand the effect of the self-weight, two distinct values are applied, namely $w = 0$ and $w = 100$, as shown in Figures 6.10 and 6.11.

The initial response of the constrained weightless elastica is not comparable with the case of the heavy elastica. In particular, the weightless elastica remains in its unstressed configuration with $\delta = 0$ on the rigid foundation until it reaches the first (symmetrical) buckling mode of clamped-clamped elastica with applied force $\mathcal{Q}/\pi^2 = 4$. A nearly straight line is then followed until it comes in contact with the upper wall at the midpoint position at C2. Past C2, an abrupt growth of the stiffness $\mathcal{Q}/\delta$ is detected due to the remarkable increase of the horizontal force $\mathcal{Q}$ when compared to the slight progression of the end-shortening δ. Accordingly C3 corresponds to the vanishing of the moment at the discrete contact. This leads to the onset of the continuous contact.

Even though the contact pattern $3-4$ of a clamped-clamped elastica constrained by two symmetrically located walls is unstable, this is not the case when the lower wall has a clearance $c_l = 0$. This implies that, the lower wall functions as an additional stabilization to the clamped supports. The length of this continuous contact gradually increases until the initiation of a secondary buckling at C4. Past C4, a free-standing fold is formed with configuration $4-5$ (see (Pocheau and Roman, 2004; Roman and Pocheau, 1999)). The maximum height of this segment progressively increases until a new discrete contact is detected at C5 with a symmetrical configuration $5-6$. This new discrete contact turns gradually into a continuous contact at C6. In a similar manner, a new secondary buckling occurs at C7, which is a new form of a free-standing fold with shape $7-8$. At C8, a new discrete contact occurs, leading to the symmetrical configuration $8-9$.

The buckling behavior of the heavy elastica with self-weight $w = 100$ is entirely different at the initial stage. The heavy elastica remains unstressed on the rigid horizontal wall and an infinite horizontal force is required for the formation of a ruck, as explained in Section 6.2.1. The height of this ruck gradually increases and the horizontal force initially decreases with increasing the end-shortening. If the upper wall is not present, the horizontal force reaches a minimum value and then starts increasing, while the height of the ruck reaches a plateau (maximum value). If the value of the maximum height is lower than the clearance of the upper wall, a discrete contact at the midpoint position is met, which is also the case in this example at C2. Comparing with the weightless elastica, which is not in contact with the lower wall except at its end-points (see shape $2-3$ in Figure 6.10), a small part of the heavy elastica, the ruck, is unconstrained (see shape $2-3$ in Figure 6.11). Nevertheless, the length of the constrained ruck increases, while a formation of a continuous contact is not possible. Instead, the flat-lying segment buckles as the first buckling mode of a clamped-clamped elastica, leading to a second ruck at C3. This leads to the asymmetrical shape $3-4$ with a softening response. When the new ruck comes in contact with the upper wall, a symmetrical shape $4-5$ appears at C4. Beyond C4, the sequence of the equilibrium configurations is identical to the weightless elastica. However the values of R_x, δ are dissimilar (see Table 6.1).

a) Weightless Elastica			b) Elastica with self-weight $w = 100$		
Points	δ	$\mathcal{Q}/\pi^2$	Points	δ	$\mathcal{Q}/\pi^2$
2	0.0251	4.05	2	0.035	12.54
3	0.033	18.05	3	0.055	39.82
4	0.047	33.96	4	0.106	19.10
5	0.105	16.92	5	0.131	54.62
6	0.139	62.65	6	0.182	85.55
7	0.171	81.16	7	0.269	46.66
8	0.266	41.71			

Table 6.1: Points of evolution of the contact patterns for the bifurcation diagram for a constrained clamped-clamped elastica with self-weight $w = 0, 100$ and clearances $c_l = 0$ and $c_u = 0.1$ for the classical problem

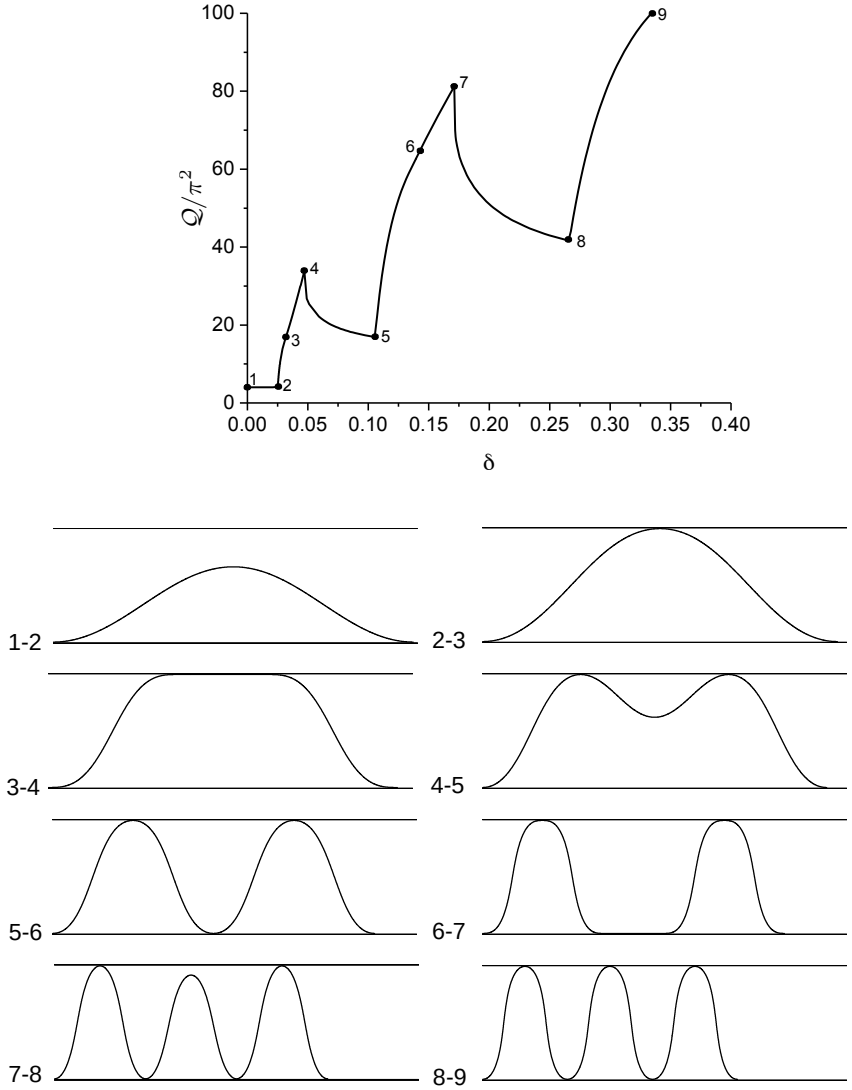

Figure 6.10: Bifurcation diagram for a constrained clamped-clamped elastica with self-weight $w = 0$ and clearances $c_l = 0$ and $c_u = 0.1$ for the classical problem

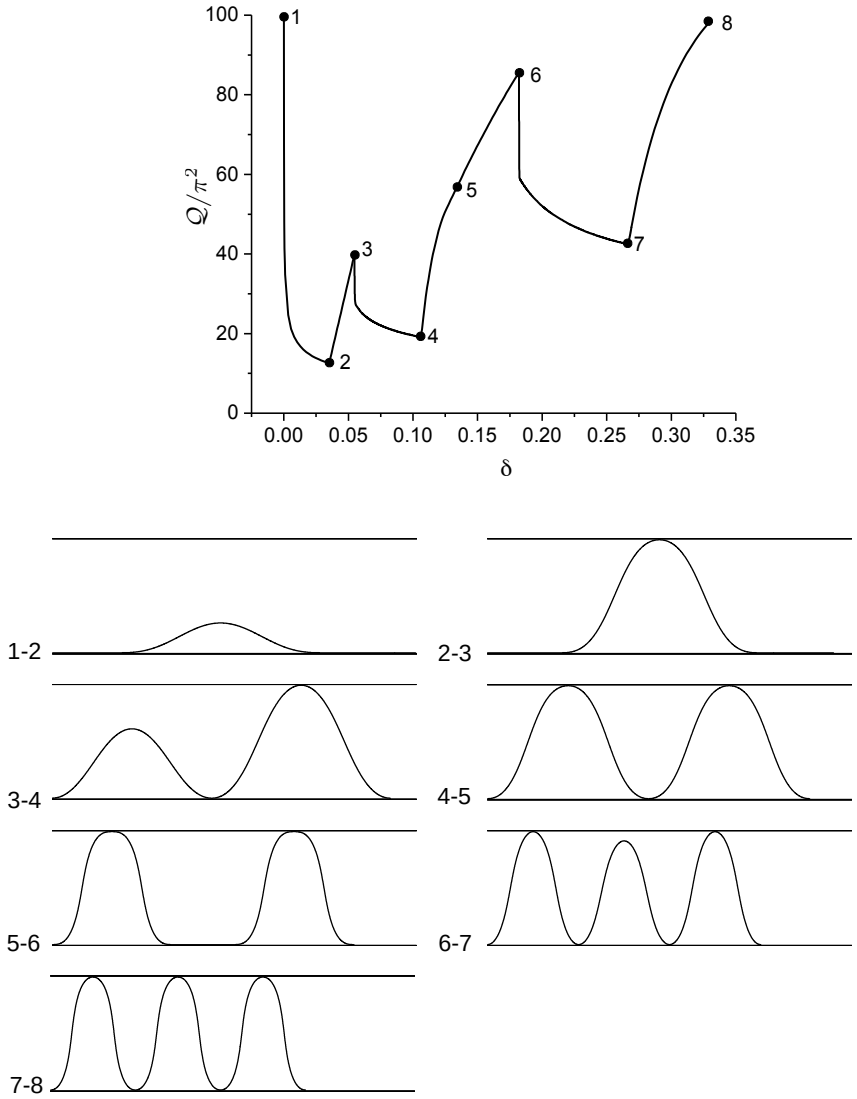

Figure 6.11: Bifurcation diagram for a constrained clamped-clamped elastica with self-weight $w = 100$ and clearances $c_l = 0$ and $c_u = 0.1$ for the classical problem

The same problem is also solved as an insertion problem considering an elastica of variable length $1 + \bar{\delta}$ with constant distance between the supports $\bar{x}(1 + \bar{\delta}) = 1$ (see Section 6.3.1). The bifurcation diagrams of the applied force $\mathcal{Q}/\pi^2$ with respect to the change of the length of the elastica $\bar{\delta}$ for $w = 0, 100$ are shown in Figures 6.12 and 6.13, respectively. One main difference is that the post-buckling behavior of the weightless elastica buckles α via a sub-critical bifurcation $\mathcal{Q}/\pi^2 < 4$ rather than a subcritical bifurcation $\mathcal{Q}/\pi^2 > 4$, which is the case in the classical

problem. Nevertheless, the sequence of the contact patterns and the complete diagram are similar to the case of the classical problem. The transition points, where the contact patterns evolve are summarized in Table 6.2, while the corresponding contact patterns are shown in Figures 6.12 and 6.13.

Points	$w = 0$			$w = 100$		
	$\bar{\delta}$	$\mathcal{R}_x/\pi^2$	$\mathcal{Q}/\pi^2$	$\bar{\delta}$	$\mathcal{R}_x/\pi^2$	$\mathcal{Q}/\pi^2$
2	0.021	3.88	3.68	0.035	12.64	12.64
3	0.031	16.14	16.14	0.049	32.04	32.04
4	0.044	29.9	29.9	0.095	16.74	15.05
5	0.095	14.04	11.68	0.111	41.26	41.26
6	0.12	51.22	51.22	0.144	63.24	63.24
7	0.14	64.3	64.3	0.206	28.52	20.31
8	0.204	27.33	18.35	0.233	68.52	68.02

Table 6.2: Transition points of contact patterns for $w = 0, 100$ consistent with Figures 6.12 and 6.13

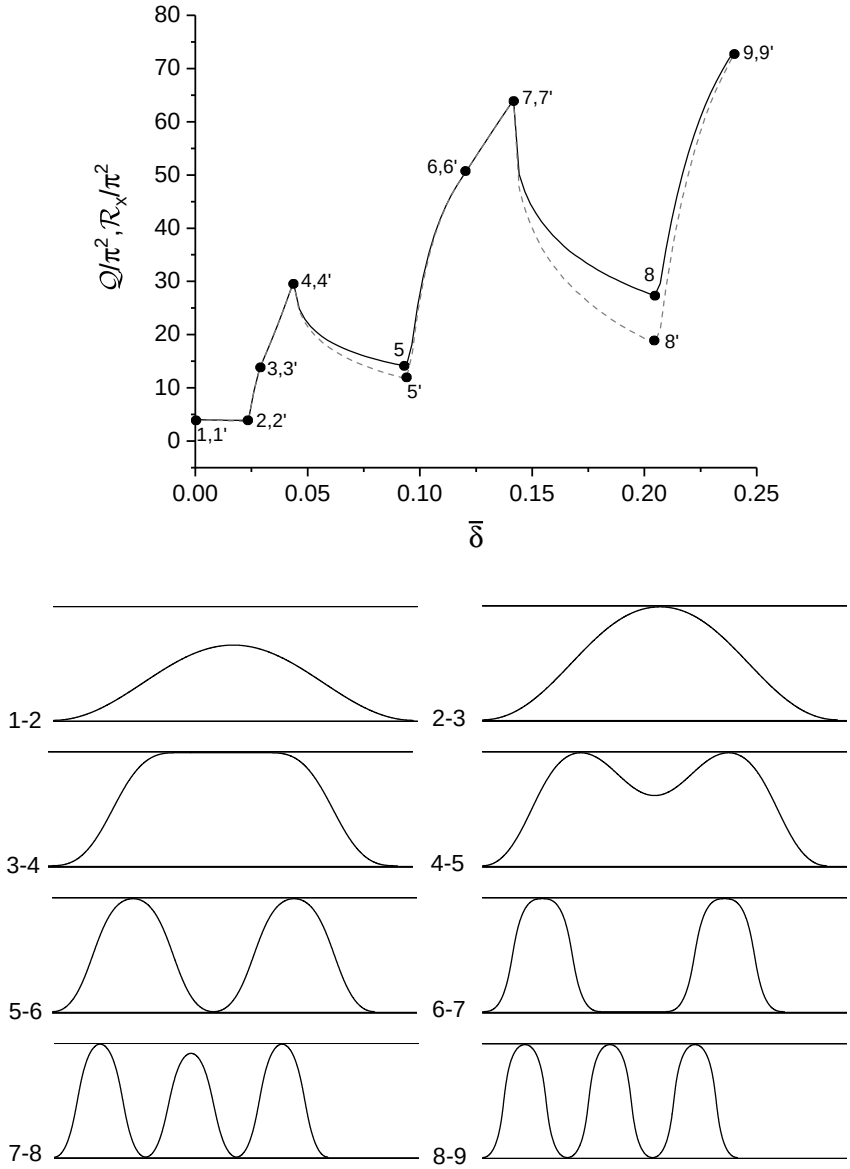

Figure 6.12: Bifurcation diagram for a constrained clamped-clamped elastica with self-weight $w = 0$ and clearances $c_l = 0$ and $c_u = 0.1$ for the insertion problem; (i) solid line denotes the evolution of the internal horizontal force $\mathcal{R}_x/\pi^2$ and (ii) dashed line denotes the evolution of the applied load $\mathcal{Q}/\pi^2$

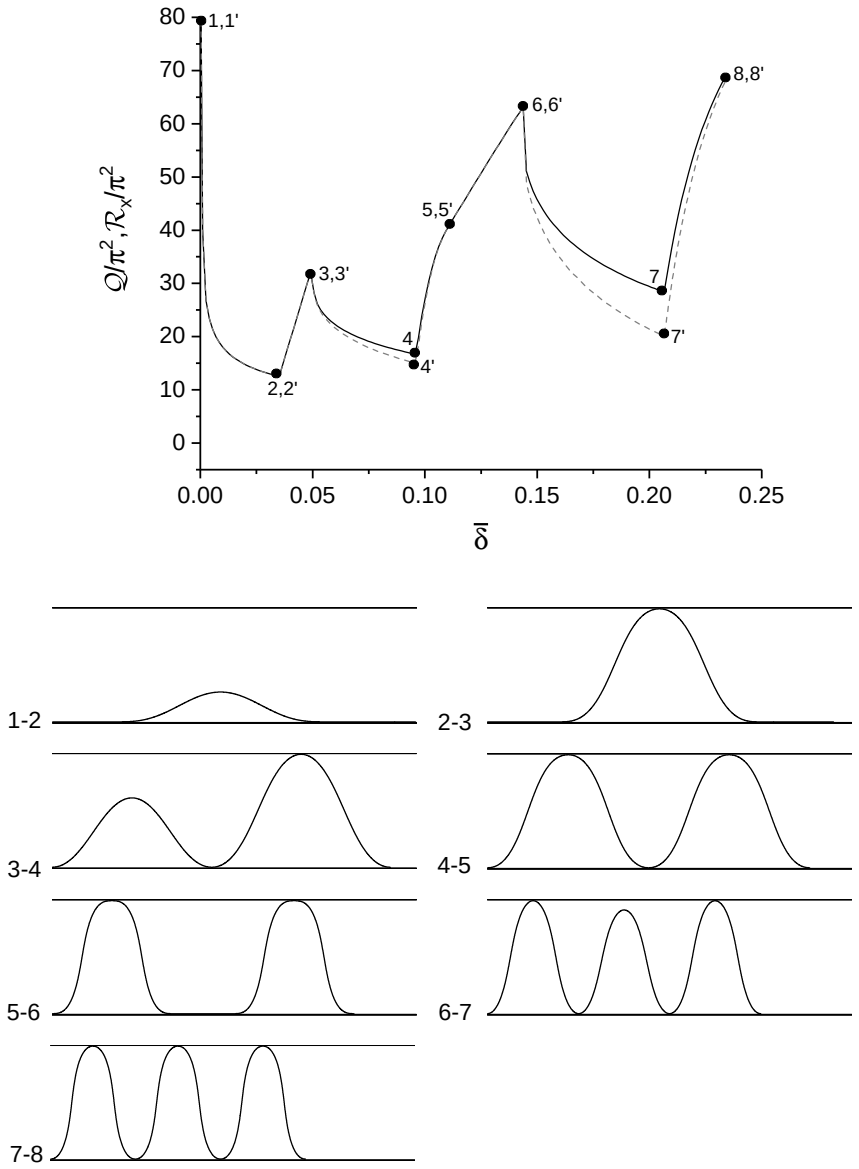

Figure 6.13: Bifurcation diagram for a constrained clamped-clamped elastica with self-weight $w = 100$ and clearances $c_l = 0$ and $c_u = 0.1$ for the insertion problem; (i) solid line denotes the evolution of the internal horizontal force $\mathcal{R}_x/\pi^2$ and (ii) dashed line denotes the evolution of the applied load $\mathcal{Q}/\pi^2$

Symmetrical walls

The post-buckling behavior of the constrained clamped-clamped elastica constrained by symmetrically located walls with clearance $c_u = c_l = 0.1$ is investigated. Two disitinct values of self-weight $w = 0$ and $w = 100$ are examined, as shown in Figure 6.14.

In the case of a weightless elastica, the equilibrium configurations with negative y coordinate (see Figure 6.14) can be also replaced by the same contact patterns with positive sign without affecting the bifurcation diagram. For instance, the branch $7 - 8$ can be described either by the shape $7' - 8'$, or $7'' - 8''$. This symmetry is broken whenever the self-weight is $w \neq 0$. In particular, the branches $7' - 8'$ and $7'' - 8''$ for a heavy elastica with self-weight $w = 100$ are entirely different responses (see Figure 6.14), while the branch $7 - 8$ of the weightless elastica lies approximately in the middle of them.

Let us now analyze the behavior of the weightless elastica in more detail. For low values of end-shortening δ, the first buckling mode of a clamped-clamped elastica is obtained without any contact. Due to symmetry the elastica comes in contact with the wall at the midpoint position at C2. The position of the discrete contact remains unchanged until C4, which corresponds to the vanishing of the moment at the discrete contact. Nevertheless, it does not continue to a continuous contact, while a simultaneous change of the sign of the moments of both ends is also not feasible. Hence, beyond point 4, the sign of the moment changes only at one end, leading to the asymmetrical configuration $4 - 5$ with one discrete contact. Along Branch $4 - 5$, the horizontal load decreases with increasing δ (i.e., softening branch) until it reaches C5. Past C5, a symmetrical configuration $5 - 7$ with two discrete contacts is obtained. At C7, the bending moments at the discrete contacts vanish simultaneously for symmetrical reasons. Beyond this point, a new softening branch $7-8$ is detected until a third discrete contact occurs at C8. Lastly, past this point we get a symmetrical configuration $8 - 9$ with increasing horizontal force as the end-shortening further increases.

a) Weightless Elastica		
Points	δ	$\mathcal{Q}/\pi^2$
2	0.0251	4.051
4	0.0305	15.51
5	0.113	8.84
7	0.171	27.4
8	0.295	17.95

b) Elastica with $w = 100$		
Points	δ	$\mathcal{Q}/\pi^2$
3	0.0268	0
4	0.0519	36.7
5	0.11831	12.28
6	0.14	21.4
$7''$	0.19	27.33
$8''$	0.29	16.78

Table 6.3: Points of evolution of the contact patterns of the bifurcation diagram for a constrained clamped-clamped elastica with self-weights $w = 0, 100$ and clearances $c_l = c_u = 0.1$

In the case of a heavy elastica with self-weight $w = 100$, the initial configuration of the elastica is modified. More specifically, at C1, the weight effect is dominant and a symmetrical

configuration $3-4$ with a continuous contact is detected. Increasing the end-shortening δ, the length of the continuous contact and the horizontal force $\mathcal{Q}$ gradually increases. At C4, an asymmetrical configuration $4-5$ with a softening response is derived with one discrete contact. When a second discrete contact occurs at C5, a symmetrical symmetrical configuration $5-6$ is obtained. At C6, the discrete contact with the lower wall turns into a continuous contact. This deformation shape remains until C7", where a softening branch $7''-8''$ is obtained. If we further increase the end-shortening δ, a symmetrical configuration with three discrete contacts is obtained starting at C8". The branches $7'-8'$ and $8'-9'$ are also stable branches but their minimized energy cost is higher than the corresponding branches $7''-8''$ and $8''-9''$, respectively. Hence, in diplacement-controlled loading conditions, the branches $7''-8''$ and $8''-9''$ are the most favorable.

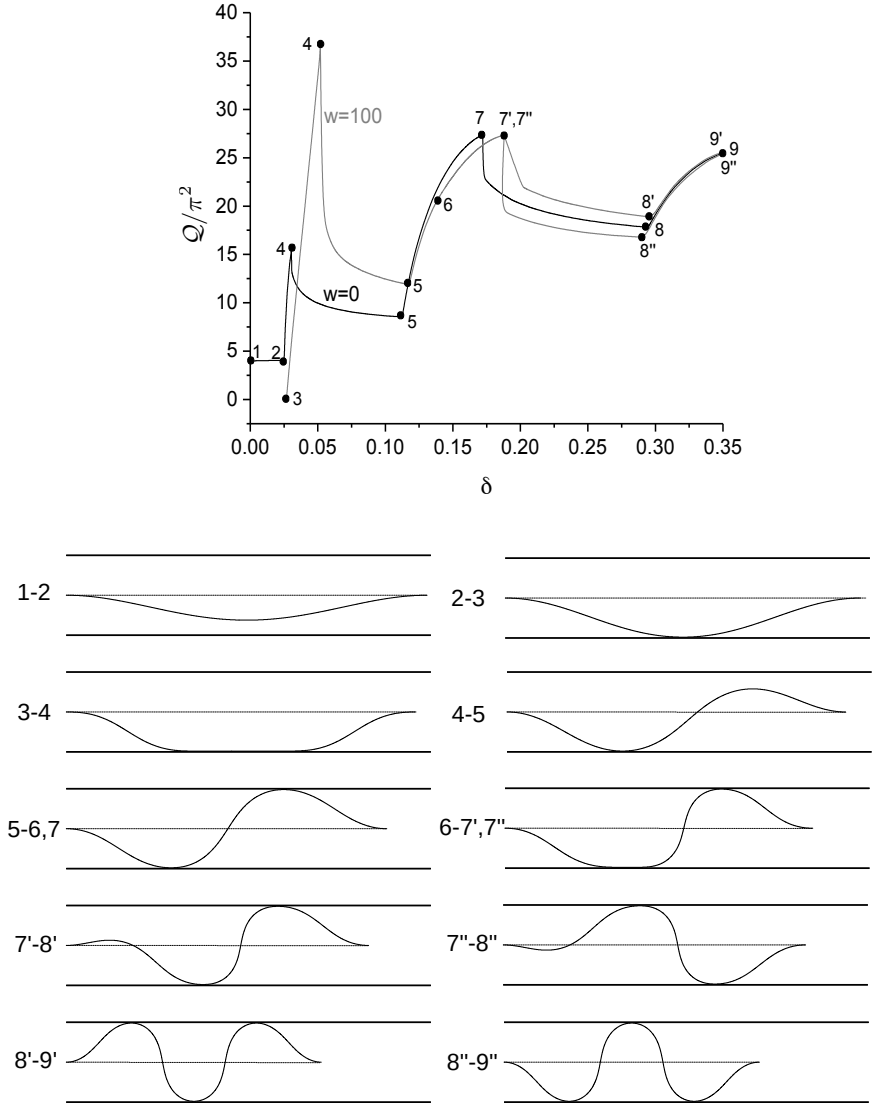

Figure 6.14: Bifurcation diagram for a constrained clamped-clamped elastica with self-weights $w = 0, 100$ and clearances $c_l = c_u = 0.1$

Let us now investigate the effect of the self-weight, keeping the same clearance $c_u = c_l = 0.1$ and assigning a self-weight $w = 10$. As shown in Figure 6.15, the sequence of the contact patterns remains unchanged except at the initial stage. In particular, the effect of the self-weight is not dominant, while a clear post-buckling behavior is also not possible. The initial response is similar to a post-buckling behavior of a weightless elastica with initial imperfection.

The effect of the clearance of the symmetrically located walls is also examined. Keeping a constant value of self-weight $w = 10$, a lower value of clearance $c_u = c_l = 0.05$ is assigned. Comparing Figures 6.16 and 6.15, we can observe that the sequence of contact patterns is identical. Nevertheless, for lower value of clearance, higher values of applied load $\mathcal{Q}$ and lower values of end-shortening δ are obtained. This implies that the stiffness $\mathcal{Q}/\delta$ of all branches is steeper in this example.

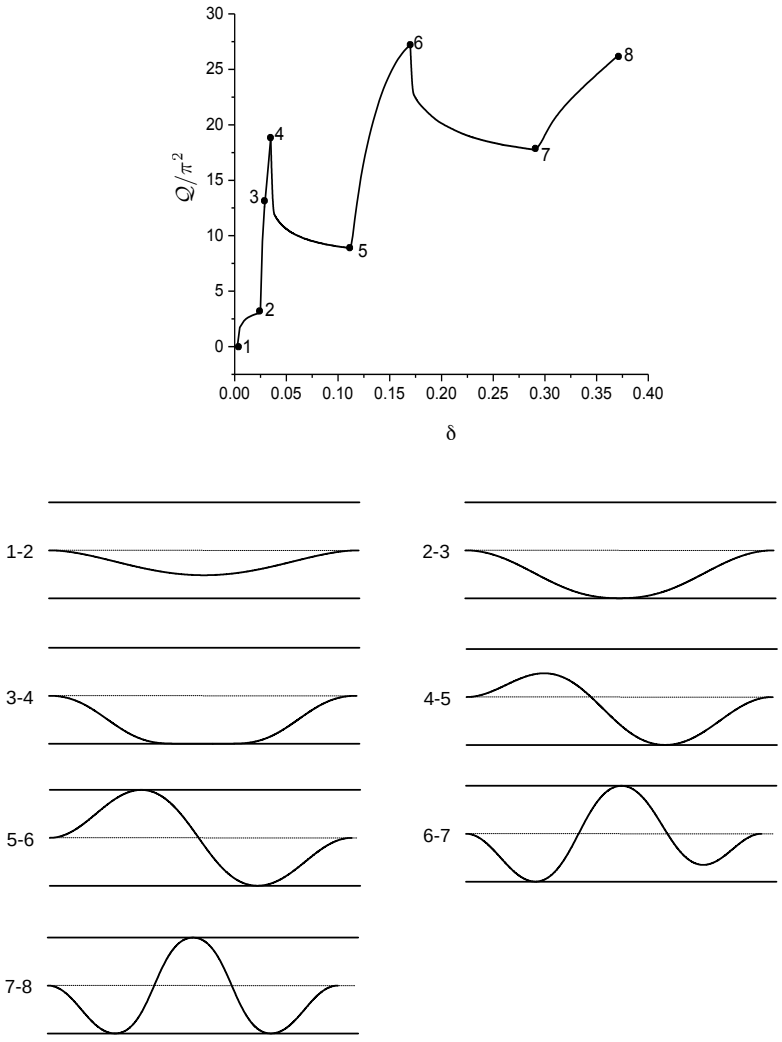

Figure 6.15: Bifurcation diagram for a constrained clamped-clamped elastica with self-weight $w = 10$ and clearances $c_l = c_u = 0.1$

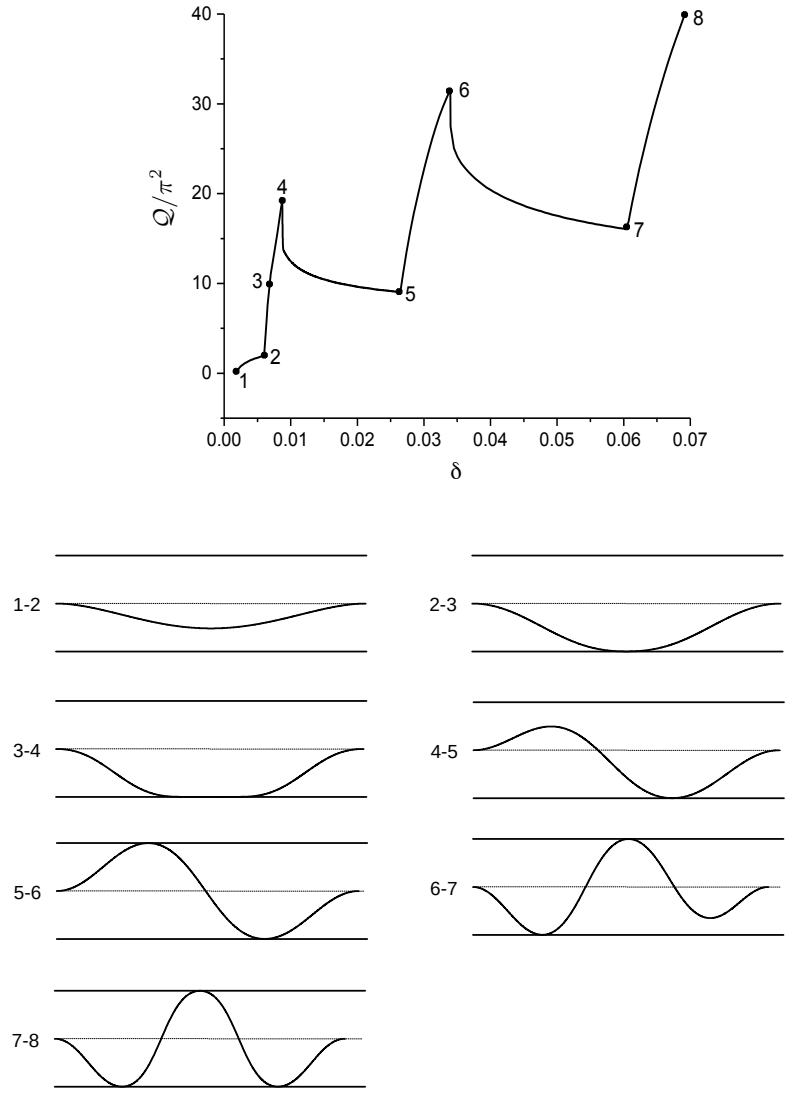

Figure 6.16: Bifurcation diagram for a constrained clamped-clamped elastica with self-weight $w = 10$ clearances $c_l = c_u = 0.05$

Now, we investigate the effect of the boundary conditions in the buckling response of a constrained heavy elastica. Consider a pinned-pinned elastica with self-weight $w = 10$ constrained by symmetrically located walls with clearances $c_l = c_u = 0.05$. If we compare Figure 6.16 with Figure 6.17, an entirely different sequence of contact patterns is observed. Even though the initial configuration of a clamped-clamped elastica is unconstrained, this is not the case in a

pinned-pinned elastica. Its initial deformation shape is consistent with the first buckling mode of a pinned-pinned elastica with a discrete contact at the midpoint. Increasing the end-shortening, the discrete contact gradually becomes a continuous contact. The length of the continuous contact then increases until it buckles as the first buckling mode of a clamped elastica at C3. Beyond this point, a free standing fold is obtained with a softening response. When C4 is reached, a new discrete contact with the upper wall at the midpoint is detected. This shape $4-5$ remains unchanged until one of the discrete contacts with the lower wall turn into a continuous contact. Similarly, the subsequent configurations of the elastica are obtained, as shown in Figure 6.17. From this example, we can observe that, for the same range of end-shortening δ, the number of discrete contacts is higher here when compared to the clamped-clamped elastica. This also leads to higher values of applied force $\mathcal{Q}$.

Elastica with $w = 10$		
Points	δ	$\mathcal{Q}/\pi^2$
3	0.017	17.9
4	0.025	5
6	0.096	55.7

Table 6.4: Points of evolution of the contact patterns of the bifurcation diagram for a constrained pinned-pinned elastica with self-weights $w = 10$ and clearances $c_l = c_u = 0.05$

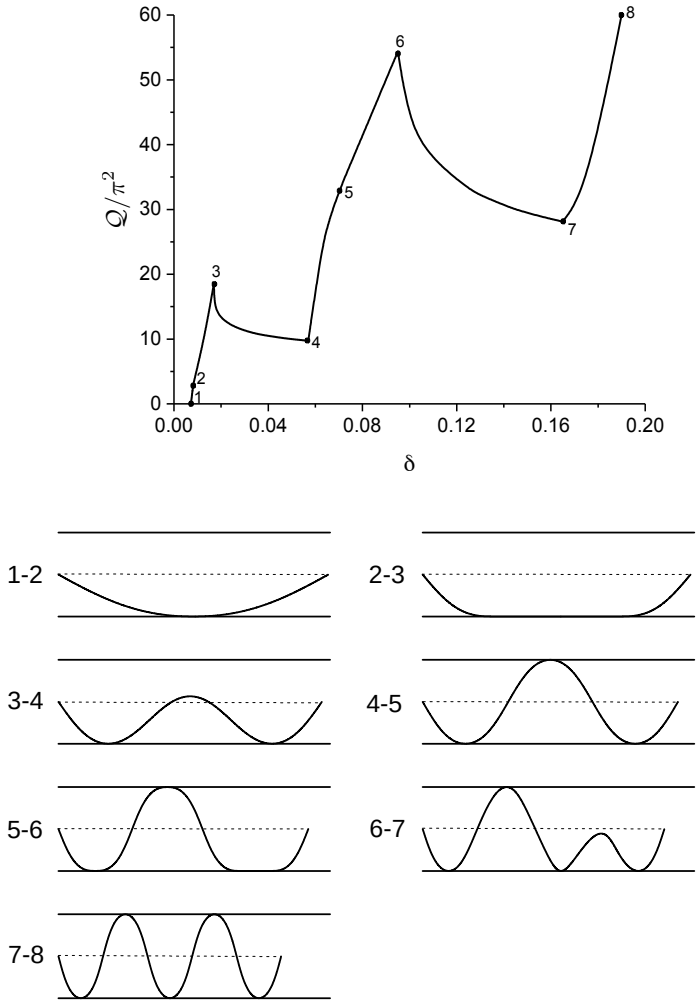

Figure 6.17: Bifurcation diagram for a constrained pinned-pinned elastica with self-weight $w = 10$ and clearance $c_l = c_u = 0.05$

6.3.3 Summary

The effect of the self-weight w in the buckling response of the elastica constrained by rigid walls is investigated in this Chapter. A short review of previous studies on the loop tests and the buckling problem of a heavy elastica lying on a horizontal foundation is included. The latter problem is then solved by applying optimal control. In this manner, we first confirm the validity of the optimal control method. The "symmetry breaking bifurcation" is also investigated and the

results are shown to be in agreement with Domokos et al. (2003)' analysis. The same problem is also investigated for inclined foundations.

Extension of the one-sided foundation to two-sided foundations is then provided. By applying an optimal control method, two distinct classes of problems are analyzed; (1) the classical buckling problem and (ii) the insertion buckling problem. In the first class of problems, the elastica is of constant length and the right end is free to move towards the fixed left end under displacement-controlled conditions. On the other hand, in the second class of problems, the heavy elastica is of variable length while the distance of the two supports is unchanged.

The buckling response of the heavy elastica constrained by two asymmetrically located walls with $c_l = 0$ is first analyzed. At the initial state, the response of the elastica is identical to the case of an elastica resting on a horizontal foundation. Nevertheless, the additional constraint of the upper wall leads to a different sequence of deformation shapes if a sufficient development of the end-shortening δ for the classical problem, or the inserted length of the elastica $1 + \bar{\delta}$ for the insertion problem occurs.

The buckling analysis of the heavy elastica constrained by two symmetrically located walls is then analyzed. If we assign different values of self-weight w for the same clearance and boundary conditions, the derived bifurcation diagrams are similar, except at the initial state, where three distinct cases are met; (i) if the elastica is weightless, a classical post-buckling response is observed, (ii) if the self-weight w is relatively small, a post-buckling behavior of a weightless-like elastica with initial imperfection is detected and (iii) if the self-weight w is sufficiently large, an initial configuration with a discrete, or a continuous contact is met. Several other effects, such as the clearances and the boundary conditions are also investigated. All results are compared with the buckling response of a weightless elastica in order to clearly illustrate the effect of the self-weight.

Chapter 7

Insertion problem of spatial elastica

7.1 Introduction

The aim of the Chapter is the study of the constrained buckling problem of a variable-length spatial elastica. The main focus is placed on the derivation of the configurational or Eshelby-like force, which is generated at the insertion point of the sliding sleeve (see (Bigoni et al., 2015) for the planar case). The reason behind the development of this configuration force is two fold; (1) the change of the length of the elastica as it is gradually inserted inside the conduit and (2) the isoperimetric constraint of a fixed distance between the extremities of the inserted elastica. This effect leads to a reduction of the applied axial force at the point of insertion.

Based on the calculus of variations, we first calculate the configuration force. Then, a representative example is solved by applying the optimal control method. The effect of the configurational force is used to compute the applied force.

7.2 Derivation of Eshelby-like force

A weightless spatial (isotropic) elastica of total length $\bar{L}_t$ of uniform bending EI and torsional GJ rigidity is constrained by a cylindrical wall of clearance C and it is initially unstressed. The elastica is clamped, or pinned at the left end and it is inserted through a fixed frictionless sliding sleeve that functions as a clamped end (see Figure 7.1). Hence, the distance L between the fixed end of the elastica and the insertion point is constant, while the inserted length $\bar{L}$ of the elastica varies (i.e., inserted length increment $\bar{\Delta} = \bar{L} - L$). We seek to analyze the post-buckling response of the spatial elastica under the action of a compressive load Q.

A system of coordinates (X, Y, Z) is defined with origin at the left extremity of the elastica and with the X-axis pointing towards the elastica right end. A cylindrical wall with clearance

C with respect to the centerline is also present, which can be described by $Y^2 + Z^2 = C^2$.

We introduce the arc-length coordinate S with its origin $S = 0$ at $X = 0$, $Y = 0$, $Z = 0$, while three Euler angles $\Theta(S), \Psi(S), \Phi(S)$ are used to define the rotation matrix with respect to the reference configuration (see Chapter 5 for a detailed derivation). In view of the inextensibity and unshearability constraints characterizing the elastica, its deformed configuration $\hat{X}(S)$, $\hat{Y}(S)$, $\hat{Z}(S)$ is fully defined by

$$\begin{aligned} \hat{X}' &= \cos\Theta\cos\Psi \\ \hat{Y}' &= \cos\Theta\sin\Psi \\ \hat{Z}' &= -\sin\Theta \end{aligned} \tag{7.1}$$

with boundary conditions $\hat{X}(0) = \hat{Y}(0) = \hat{Z}(0) = 0$, while $\hat{Y}(\bar{L}) = \hat{Z}(\bar{L}) = 0$ and $\hat{X}(\bar{L}) = L$ in accordance with the imposed boundary condition $\bar{\Delta} = \bar{L} - X(\bar{L})$. The unilateral constraint associated with the presence of the cylindrical wall is characterized by the inequality condition $\hat{Y}^2(S) + \hat{Z}^2(S) \leq C^2$ with $S \in [0, \bar{L}]$.

The internal force transmitted by the elastica is denoted by $R(S)$ with components R_x, R_y, R_z along the corresponding axes. The functions R_y and R_z become piecewise uniform whenever there is a discrete or a continuous contact with the cylindrical wall. In addition the applied compressive force Q does not coincide with the axial force R_x. More specifically, at the insertion point, a configurational force is generated, which leads to a reduced value of the applied load Q when compared to the axial force. This effect was first verified by Bosi et al. (2015) for the insertion problem of an unconstrained planar elastica. Here, we derive this effect for the spatial elastica by applying the calculus of variations.

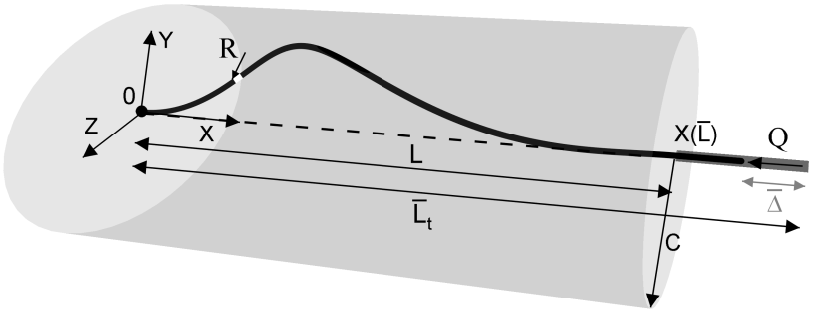

Figure 7.1: A spatial elastica constrained by a cylindrical wall with clearance C located with respect to the centerline with the left end fixed, while the elastica is gradually inserted through a fixed frictionless sleeve at the right end.

7.2.1 Governing equations of spatial elastica

Scaling of this problem follows from adopting L as length scale and EI/L^2 as force scale

$$s = \frac{S}{L}, \quad x = \frac{X}{L}, \quad y = \frac{Y}{L}, \quad z = \frac{Z}{L}, \quad \bar{\delta} = \frac{\bar{\Delta}}{L}, \quad c = \frac{C}{L}, \quad \mathcal{R} = \frac{RL^2}{EI}, \quad \mathcal{Q} = \frac{QL^2}{EI} \tag{7.2}$$

where $\bar{\delta}$ is the change of inserted length of the elastica. The inserted length is denoted by $\rho = 1 + \bar{\delta}$ and the total length of the elastica is $\rho_t \geq \rho$.

The cartesian parametrization of the elastica, $\hat{x}(s)$, $\hat{y}(s)$, $\hat{z}(s)$ is derived by applying the inextensibility and unshearability constraints (7.1)

$$\begin{aligned} \hat{x}(s) &= \textstyle\int_0^s \cos\theta \cos\psi ds \\ \hat{y}(s) &= \textstyle\int_0^s \cos\theta \sin\psi ds \\ \hat{z}(s) &= -\textstyle\int_0^s \sin\theta \end{aligned} \tag{7.3}$$

where the boundary conditions $\hat{x}(0) = \hat{y}(0) = \hat{z}(0) = 0$ and the Euler angles $\{\psi, \theta, \phi\}$ have been taken into account.

7.2.2 The calculus of variations

The potential energy of the spatial elastica (see Chapter 5) can be expressed as

$$\Pi = \mathcal{U}_s - \mathcal{W}_\mathcal{Q} = \frac{1}{2}\int_0^\rho \left(\kappa_2^2(s) + \kappa_3^2(s)\right) ds + \frac{\alpha}{2}\int_0^\rho \kappa_1^2(s) ds - \mathcal{Q}\left(\rho_t - \int_0^{\rho_t} \cos\theta\cos\psi ds\right) \tag{7.4}$$

where $\mathcal{U}_s$ is the elastic strain energy, $\mathcal{W}_\mathcal{Q}$ is the external work of the axial compressive load $\mathcal{Q}$, α is the ratio of torsional to bending moduli, $\kappa_1 = \tau$ is the torsion, κ_2 and κ_3 are the curvatures about the director axes

$$\begin{aligned} \kappa_1 &= \phi' - \psi'\sin\theta \\ \kappa_2 &= \psi'\sin\phi\cos\theta + \theta'\cos\phi \\ \kappa_3 &= \psi'\cos\phi\cos\theta - \theta'\sin\phi \end{aligned} \tag{7.5}$$

and $\mathcal{Q}\left(\rho_t - \int_0^{\rho_t}\cos\theta\cos\psi ds\right)$ is the external work of the axial compressive force $\mathcal{Q}$ under the presence of the equality and inequality constraints

$$\begin{gathered} \left(\textstyle\int_0^s \cos\theta\sin\psi d\xi\right)^2 + \left(\textstyle\int_0^s -\sin\theta d\xi\right)^2 - c^2 \leq 0, \quad s \in [0, \rho] \\ \textstyle\int_0^\rho \cos\theta\cos\psi ds = 1 \\ \textstyle\int_0^\rho \cos\theta\sin\psi ds = 0 \\ \textstyle\int_0^\rho -\sin\theta ds = 0 \end{gathered} \tag{7.6}$$

and the boundary conditions, which are $\psi(0) = \psi(\rho) = \theta(0) = \theta(\rho) = \phi(0) = \phi(\rho) = 0$ for clamped-clamped boundary conditions. If displacement-controlled conditions are assumed, the applied force $\mathcal{Q}$ becomes the unknown Lagrange multiplier associated with the imposed bilateral constraint $\rho_t - \int_0^{\rho_t} \cos\theta \cos\psi ds = \bar{\delta}$.

Let us investigate an equilibrium configuration of the constrained elastica with a single discrete contact at a position $s = \ell_1$. In a similar manner, the derivation can be accordingly extended to a multiple number of contact points. Based on this assumption, the potential energy can be expressed as

$$\begin{aligned}\Pi &= \mathcal{U}_s + \mathcal{U}_i - \mathcal{W}_{\mathcal{Q}} - \mathcal{W}_F \\ &= \frac{1}{2}\int_0^{\rho} \left(\psi'^2 \cos^2\theta + \theta'^2\right) ds + \frac{\gamma}{2}\int_0^{\rho} \left(\phi' - \psi' \sin\theta\right)^2 ds - \mathcal{Q}\left(\rho_t - \int_0^{\rho_t} \cos\theta\cos\psi ds\right) \\ &- \lambda_x \left(1 - \int_0^{\rho} \cos\theta\cos\psi ds\right) + \lambda_y \int_0^{\rho} \cos\theta \sin\psi ds + \lambda_z \int_0^{\rho} -\sin\theta ds \\ &+ F\left[\left(\int_0^{\ell_l} \cos\theta\sin\psi d\xi\right)^2 + \left(\int_0^{\ell_l} -\sin\theta d\xi\right)^2 - c^2\right] \end{aligned} \tag{7.7}$$

where $\mathcal{U}_i$ is the energy produced by the isoperimetric constraints (7.6)ii)-iv) with associated Lagrange multipliers λ_x, λ_y, λ_z and $\mathcal{W}_F$ is the external work produced by a closed unilateral constraint (7.6)i) at $s = \ell_l$ with associated Lagrange multiplier F and ℓ_l is the length of the segment from the origin (i.e., $s = 0$) to the discrete contact.

To derive the first variation of the potential energy, variations of the involved variables are assumed

$$\begin{aligned}\theta(s,\varepsilon) &= \hat{\theta}(s) + \varepsilon\eta(s) \\ \psi(s,\varepsilon) &= \hat{\psi}(s) + \varepsilon\zeta(s) \\ \phi(s,\varepsilon) &= \hat{\phi}(s) + \varepsilon\chi(s)\end{aligned} \tag{7.8}$$

$$\begin{aligned}\rho(\varepsilon) &= \hat{\rho} + \varepsilon\gamma \\ \ell_l(\varepsilon) &= \hat{\ell}_l + \varepsilon\gamma_l\end{aligned} \tag{7.9}$$

where $\hat{\theta}(s)$, $\hat{\psi}(s)$, $\hat{\phi}(s)$,$\hat{\rho}$, $\hat{\ell}_l$ are the extremal values and $\eta(s)$, $\zeta(s)$, $\chi(s)$, γ , γ_l are their corresponding variations, while $\varepsilon \ll 1$ is a positive parameter. Based on these variations and taking into account the boundary conditions $\theta(\rho) = \hat{\theta}(\hat{\rho}) = 0$, $\psi(\rho) = \hat{\psi}(\hat{\rho}) = 0$, $\phi(\rho) = \hat{\phi}(\hat{\rho}) = 0$ and $\theta(\ell_l) = \hat{\theta}\left(\hat{\ell}_l\right) = 0$, $\psi(\ell_l) = \hat{\psi}\left(\hat{\ell}_l\right) = 0$, $\phi(\ell_l) = \hat{\phi}\left(\hat{\ell}_l\right) = 0$, the following compatibility equations are obtained;

$$\begin{aligned}\gamma\hat{\theta}'(\hat{\rho}) + \eta(\hat{\rho}) &= 0 \\ \gamma\hat{\psi}'(\hat{\rho}) + \zeta(\hat{\rho}) &= 0 \\ \gamma\hat{\phi}'(\hat{\rho}) + \chi(\hat{\rho}) &= 0\end{aligned} \tag{7.10}$$

$$\begin{aligned}\gamma\hat{\theta}'(\hat{\ell}_l)+\eta(\hat{\ell}_l)&=0\\ \gamma\hat{\psi}'(\hat{\ell}_l)+\zeta(\hat{\ell}_l)&=0\\ \gamma\hat{\phi}'(\hat{\ell}_l)+\chi(\hat{\ell}_l)&=0\end{aligned}\tag{7.11}$$

The first variation of the potential energy is then deduced by applying the following derivation

$$\delta\Pi(\theta,\theta^{'},\psi,\psi^{'},\phi,\phi^{'})=_{\varepsilon\to 0}\left|\frac{\mathrm{d}\Pi}{\mathrm{d}\varepsilon}\right.=\delta\mathcal{U}_s+\delta\mathcal{U}_i-\delta\mathcal{W}_{\mathcal{Q}}-\delta\mathcal{W}_F\tag{7.12}$$

which leads to

$$\begin{aligned}\delta\mathcal{U}_s=&\int_0^{\hat{\rho}}\left(\hat{\psi}'\zeta'\cos^2\hat{\theta}-\left(\hat{\psi}'^2\sin 2\hat{\theta}/2\right)\eta+\hat{\theta}'\eta'\right)ds\\&+\alpha\int_0^{\hat{\rho}}\left(\hat{\phi}'\chi'+\hat{\psi}'\zeta'\sin^2\hat{\theta}+\left(\hat{\psi}'^2\sin 2\hat{\theta}/2\right)\eta\right)ds\\&-\alpha\int_0^{\hat{\rho}}\left(\sin\hat{\theta}\left(\hat{\psi}'\chi'+\hat{\phi}'\zeta'\right)+\hat{\phi}'\hat{\psi}'\cos\hat{\theta}\eta\right)ds\\&+\frac{\gamma}{2}\left(\hat{\psi}'^2(\hat{\rho})\cos^2\hat{\theta}(\hat{\rho})+\hat{\theta}'^2(\hat{\rho})\right)\\&+\frac{\alpha\gamma}{2}\left(\hat{\phi}'^2(\hat{\rho})+\hat{\psi}'^2(\hat{\rho})\sin^2\hat{\theta}(\hat{\rho})-2\hat{\phi}'(\hat{\rho})\hat{\psi}'(\hat{\rho})\sin\hat{\theta}(\hat{\rho})\right)\end{aligned}\tag{7.13}$$

$$\begin{aligned}\delta\mathcal{U}_i=&-\lambda_x\left(\int_0^{\hat{\rho}}\sin\hat{\theta}\cos\hat{\psi}\eta ds+\int_0^{\hat{\rho}}\cos\hat{\theta}\sin\hat{\psi}\zeta ds\right)+\gamma\lambda_x\cos\hat{\theta}(\hat{\rho})\cos\hat{\psi}(\hat{\rho})\\&+\lambda_y\left(-\int_0^{\hat{\rho}}\sin\hat{\theta}\sin\hat{\psi}\eta ds+\int_0^{\hat{\rho}}\cos\theta\cos\hat{\psi}\zeta ds\right)+\gamma\lambda_y\cos\hat{\theta}(\hat{\rho})\sin\hat{\psi}(\hat{\rho})\\&+\lambda_z\int_0^{\hat{\rho}}-\cos\hat{\theta}\eta ds-\gamma\lambda_z\sin\hat{\theta}(\hat{\rho})\end{aligned}\tag{7.14}$$

$$\delta\mathcal{W}_{\mathcal{Q}}=\mathcal{Q}\left(\int_0^{\hat{\rho}}\sin\hat{\theta}\cos\hat{\psi}\eta ds+\int_0^{\hat{\rho}}\cos\hat{\theta}\sin\hat{\psi}\zeta ds\right)\tag{7.15}$$

$$\begin{aligned}\delta\mathcal{W}_F=&-2F\left(\int_0^{\hat{\ell}_l}\cos\hat{\theta}\sin\hat{\psi}d\xi\right)\left[-\int_0^{\hat{\ell}_l}\sin\hat{\theta}\sin\hat{\psi}\eta ds+\int_0^{\hat{\ell}_l}\cos\theta\cos\hat{\psi}\zeta ds+\gamma_l\cos\hat{\theta}\left(\hat{\ell}_l\right)\sin\hat{\psi}\left(\hat{\ell}_l\right)\right]\\&-2F\left(\int_0^{\hat{\ell}_l}-\sin\hat{\theta}d\xi\right)\left[\int_0^{\hat{\ell}_l}-\cos\hat{\theta}\eta ds-\gamma_l\sin\hat{\theta}\left(\hat{\ell}_l\right)\right]\end{aligned}\tag{7.16}$$

All terms in (7.13) that involve $\eta'(s)$, $\zeta'(s)$, $\chi'(s)$, are transformed to $\eta(s)$, $\zeta(s)$, $\chi(s)$ by applying integration by parts in combination with the compatibility equations (7.10). In this manner, we

arrive at the final form

$$\begin{aligned}\delta\Pi = &\int_0^{\hat{\rho}} \left[-\hat{\theta}'' + \hat{\psi}'^2 \sin 2\hat{\theta}\,(\alpha-1)/2 - \hat{\phi}'\hat{\psi}'\cos\hat{\theta} - (\mathcal{Q}+\lambda_x)\sin\hat{\theta}\cos\hat{\psi}\right]\eta ds \\ &+ \int_0^{\hat{\rho}} \left[\left(-\lambda_y + F_y H\left(s-\hat{\ell}_l\right)\right)\sin\hat{\theta}\sin\hat{\psi} + \left(-\lambda_z + F_z H\left(s-\hat{\ell}_l\right)\right)\cos\hat{\theta}\right]\eta ds \\ &+ \int_0^{\hat{\rho}} \left[-\hat{\psi}''\left(\cos^2\hat{\theta} + \alpha\sin^2\hat{\theta}\right) + \hat{\psi}'\sin 2\hat{\theta}\,(1-\alpha) + \alpha\left(\hat{\phi}''\sin\hat{\theta} + \hat{\phi}'\cos\hat{\theta}\right)\right]\zeta ds \\ &+ \int_0^{\hat{\rho}} \left[-(\mathcal{Q}+\lambda_x)\cos\hat{\theta}\sin\hat{\psi} + \left(\lambda_y - F_y H\left(s-\hat{\ell}_l\right)\right)\cos\hat{\theta}\cos\hat{\psi}\right]\zeta ds \\ &+ \alpha\int_0^{\hat{\rho}} \left[\hat{\psi}''\sin\hat{\theta} + \hat{\psi}'\cos\hat{\theta}\right]\chi ds \\ &+ \gamma\left[\lambda_x - \left(\hat{\theta}'(\hat{\rho})^2 + \hat{\psi}'(\hat{\rho})^2 + \alpha\hat{\phi}'(\hat{\rho})^2\right)/2\right] \end{aligned} \tag{7.17}$$

where $F_y = 2F\int_0^{\hat{\ell}_l}\cos\hat{\theta}\sin\hat{\psi}d\xi$, $F_z = -2F\int_0^{\hat{\ell}_l}\sin\hat{\theta}d\xi$ and H(s) is the Heaviside function. By vanishing (7.17) for the three independent variations $\eta(s)$, $\zeta(s)$, $\chi(s)$, the system of the governing equations of the elastica is accordingly obtained

$$\begin{aligned}-\theta'' + \psi'^2\sin 2\theta\,(\alpha-1)/2 - \phi'\psi'\cos\theta - \mathcal{R}_x\sin\theta\cos\psi \\ -\mathcal{R}_x\sin\theta\cos\psi - \mathcal{R}_y\sin\theta\sin\psi - \mathcal{R}_z\cos\theta = 0\end{aligned} \tag{7.18}$$

$$\begin{aligned}-\psi''\left(\cos^2\theta + \alpha\sin^2\theta\right) + \psi'\sin 2\theta\,(1-\alpha) + \alpha\left(\phi''\sin\theta + \phi'\cos\theta\right) \\ -\mathcal{R}_x\cos\theta\sin\psi + \mathcal{R}_y\cos\theta\cos\psi = 0\end{aligned} \tag{7.19}$$

$$\psi''\sin\theta + \psi'\cos\theta = 0 \tag{7.20}$$

where $\hat{}$ is omitted, $\mathcal{R}_x = \mathcal{Q} + \lambda_x$, $\mathcal{R}_y = \lambda_y - F_y H\,(s-\ell_l)$ and $\mathcal{R}_z = \lambda_z - F_z H\,(s-\ell_l)$ are the internal forces and $s \in [0,\rho]$. From this derivation, it is deduced that the applied axial force $\mathcal{Q}$ does not coincide with internal axial force $\mathcal{R}_x$. Their difference is the configurational or Eshelby-like force $P = \mathcal{R}_x - \mathcal{Q} = \left(\theta'(\rho)^2 + \psi'(\rho)^2 + \alpha\phi'(\rho)^2\right)/2$, which develops at the insertion point of the sliding sleeve.

7.3 Optimal control

The analytical derivation of the potential energy of a Kirchhoff rod model is explained in Chapter 5. The optimal control formulation for the constained buckling problem of a variable length elastica can be written as

$$\begin{cases} \text{Minimize} \quad J\left[\mathbf{x}(\cdot),\mathbf{u}(\cdot)\right] = \frac{1}{2}\int_0^{1+\bar{\delta}} \left(\kappa_2^2(s)+\kappa_3^2(s)\right) ds + \frac{\alpha}{2}\int_0^{1+\bar{\delta}} \kappa_1^2(s) ds \\ \text{subject to} \\ \qquad\qquad x' = \cos\theta(s)\cos\psi(s) \\ \qquad\qquad y' = \cos\theta(s)\sin\psi(s) \\ \qquad\qquad z' = -\sin\theta(s) \\ \qquad\qquad \psi' = u_1 \\ \qquad\qquad \theta' = u_2 \\ \qquad\qquad \phi' = u_3 \\ \qquad x(0) = y(0) = z(0) = y(1+\bar{\delta}) = z(1+\bar{\delta}) = 0 \\ \psi(0) = \psi(1+\bar{\delta}) = \theta(0) = \theta(1+\bar{\delta}) = \phi(0) = \phi(1+\bar{\delta}) = 0 \\ \qquad x(1+\bar{\delta}) = 1 \\ \qquad y^2(s) + z^2(s) \leq c^2 \end{cases} \tag{7.21}$$

where the state variables are the cartesian coordinates $\{x, y, z\}$ of the elastica and the Euler angles $\{\psi, \theta, \phi\}$, the control variables are the spatial derivatives of the Euler angles $\{\psi', \theta', \phi'\}$ and α is the ratio of the torsional to the bending moduli, while the rotational strains are given by (7.5).

Further analysis is omitted due to its similarity with the classical problem (see Chapter 5). For displacement-controlled loading conditions, the inserted length of the elastica gradually increases, while the applied load $\mathcal{Q}$ is given by

$$\mathcal{Q} = \mathcal{R}_x - P \tag{7.22}$$

where the internal horizontal force $\mathcal{R}_x$ is indirectly derived by the corresponding adjoint variable and the Eshelby-like force P is obtained by

$$P = \frac{\left(\theta'\left(1+\bar{\delta}\right)^2 + \psi'\left(1+\bar{\delta}\right)^2 + \alpha\phi'\left(1+\bar{\delta}\right)^2\right)}{2} \tag{7.23}$$

as shown in Section 7.2.

7.3.1 Example

In this Section, we investigate a clamped-clamped spatial elastica of variable length constrained by a cylindrical wall of $c = 0.1$ and $\alpha = 5/7$. The inserted length of the elastica gradually increases (increase of $\bar{\delta}$), while the applied load is indirectly obtained, as shown in Section 7.3.

The elastica remains unstressed until it buckles according to the first buckling mode of a clamped-clamped planar elastica at an applied load $\mathcal{Q}/\pi^2 = 4$. If we further increase the inserted

length, the applied load $\mathcal{Q}/\pi^2$ and the internal force $\mathcal{R}_x/\pi^2$ decrease until C2, where a discrete contact at the midpoint position occurs. This is a planar configuration of the elastica. At C3, the torsion starts increasing, leading to a spatial deformation with identical contact conditions. When C4 is reached, a second discrete contact appears. In particular, for symmetrical reasons, these discrete contacts lie in symmetrical positions next to the midpoint position. Then, at C5, a third discrete contact at the midpoint position takes place, which rapidly turns into a continuous contact when C6 is achieved. After further increase of the inserted length, a single continuous segment is obtained at C7, associated with a gradual reduction of the load (softening branch). Past C8, the single continuous segment is transformed to three shorter continuous segments. In Table 7.1, the points of evolution of the contact patterns are summarized, while the complete bifurcation diagram is shown in Figure 7.2.

Insertion Problem							
Points	$2, 2'$	$3, 3'$	$4, 4'$	$5, 5'$	$6, 6'$	$7, 7'$	$8, 8'$
δ	0.024	0.028	0.054	0.112	0.12	0.30	0.43
$\mathcal{R}_x/\pi^2$	3.86	7.59	7.32	8.45	8.62	10.35	6.32
$\mathcal{Q}/\pi^2$	3.68	7.45	6.85	7.44	7.55	8.46	5.15

Table 7.1: Points of evolution of the contact patterns for the bifurcation diagram of a constrained clamped-clamped spatial elastica of variable length with clearance $c = 0.1$

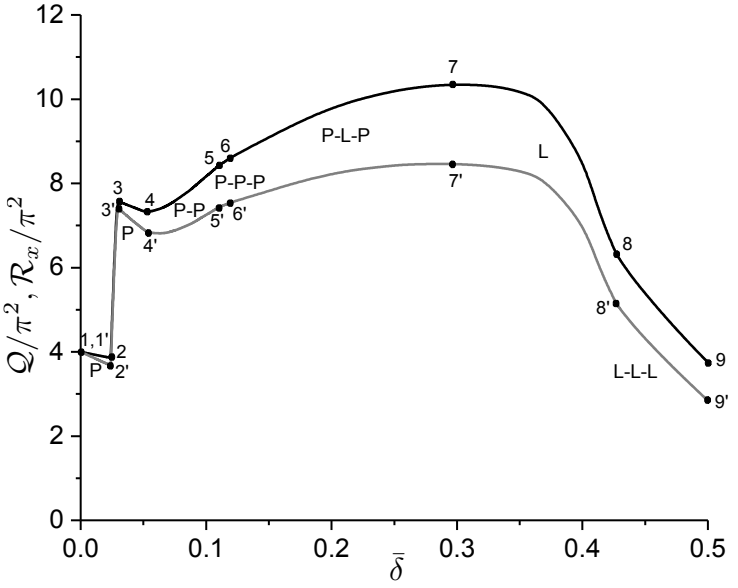

Figure 7.2: Bifurcation diagram for a constrained clamped-clamped elastica of variable length with clearance $c = 0.1$; (1-2) Planar one point (P), (3-4) Spatial one point, (4-5) Two discrete contacts (P-P), (5-6) Three discrete contacts (P-P-P), (6-7) Point-Line-Point (P-L-P), (7-8) Line contact (L) and (8-9) Line-Line-Line (L-L-L) (Same holds for the corresponding points denoted by $'$). The black and grey lines represent the evolution of the internal force $\mathcal{R}_x/\pi^2$ and the applied load $\mathcal{Q}/\pi^2$ with respect to the change of the inserted length $\bar{\delta}$, respectively.

7.4 Conclusions

This Chapter presents the generation of a configurational or Eshelby-like force at the insertion point of the sliding sleeve as the elastica is progressively inserted inside the conduit. This causes a reduction in the applied load. Its effect is also illustrated through a representative example of a clamped-clamped elastica constrained by a cylindrical wall of clearance $c = 0.1$.

Chapter 8

Conclusions

8.1 Summary

Slender elastic structures subjected to inside or outside constraints under various loading and boundary conditions forms a class of problems that has attracted a great deal of attention. For instance, the stability behavior of drillstrings inside a rigid conduit is of major concern in the oil and gas industry. In the medical field, the insertion of guidewire and catheters for interventional radiology operations is also a crucial problem and requires a real-time simulation rather than a stability analysis.

Motivated by the buckling problem in oil wells, our main focus is placed on the stability analysis of a constrained elastica, which is an inextensible-unshearable elastic rod. This is an appropriate choice in our case due to the large length/clearance ratio. Two distinct problems are mainly analyzed: (1) the classical buckling problem and (2) the insertion buckling problem. The bifurcation diagram is obtained in both cases. In the former case, the bifurcation diagram is expressed in terms of the axial force-end-shortening (i.e., distance between the two supports of the elastica), while in the latter case, the end-shortening is replaced by the change of the length of the elastica. Several alternatives in terms of loading, boundary conditions and clearances of the walls are investigated.

The analysis of these problems involves two steps; (i) the derivation of an equilibrium state of the elastica under particular loading and boundary conditions and (ii) the stability analysis of (i). Due to the presence of the unilateral constraints several numerical difficulties are encountered. Some remarkable numerical techniques can be found in literature (Lazarus et al., 2015; Ro et al., 2010; Manning and Bulman, 2005). One way is to transform the infinite dimensional problem to a finite dimensional system of equations by applying some discretization method and then derive the stability of an equilibrium configuration by computing the spectrum of the Hessian matrix (Lazarus et al., 2015). Nevertheless the potential existence of weakly active constraints

and the abrupt changes of the structure of the Hessian matrix, when the contact patterns evolve discontinuously, makes the analysis very sensitive to numerical errors. In our situation, an additional numerical issue is met. Even if a deformation shape is stable (i.e., positive-definite Hessian matrix), the condition number of the Hessian matrix can be remarkable high (i.e., at least one eigenvalue close to zero). This is true when the derived axial loads are very close to the Euler-buckling loads. For instance, this is a common issue when we analyze the post-buckling response of a planar weightless elastica with symmetrically located walls. Hence, if we apply a classical continuation method, an extremely small step length is required and even in this case the accuracy of the results is questionable.

For these reasons the majority of the research works preserves the infinite dimensionality of the problem. The most notable studies have been performed by (Domokos et al., 1997; Ro et al., 2010; Manning and Bulman, 2005). Domokos et al. (1997) solved the problem using two different methods; (1) an analytical technique using elliptic integrals and (2) a numerical method applying a classical linear programming method, the simplex method (Holmes et al., 1999). The problem was only partially solved, because the stability of the derived equibrium states was not investigated. Manning and Bulman (2005) reformulated Domokos et al. (1997)'s problem by replacing the unilateral constraint with a smooth potential and accordingly applied a conjugate point theory on the unconstrained problem. Even though the stability analysis is complete, the approach remains approximate due to the assumption of smooth contact. In addition, the method is not generic since it should be adjusted whenever Neumann-Neumann boundary conditions are present, as explained by Manning (2009).

On the other hand, Ro et al. (2010) provided an Eulerian description of the problem in order to take into account the potential variation of the contact points between the elastica and the rigid obstacles during vibration. Then a shooting method was applied, which can provide information regarding the stability of the problem. This method also involves numerical difficulties. First of all, it is known that the shooting method is always sensitive to initial guesses of the involved variables. This becomes very evident as the number of the unknown variables increases. Secondly, the derivation of the mathematical formulation of every distinct problem requires a lot of effort.

Based on above observations we tried to solve this constrained stability problem, taking into account two prerequisites; (i) there are no further assumptions in the formulation of the problem (e.g., the assumption of a smooth constraint) and (ii) the methodology is as simple and generic as possible. First, in Chapter 2, we show why the use of the calculus of variations is not recommended. Accordingly, two novel approaches are suggested, namely a geometry-based method that provides an equilibrium map of the problem and the optimal control method, which completely solves the constrained stability problem. These two contributions are summarized next.

The post-buckling response of the planar elastica constrained by rigid horizontal walls relies

on the proposed geometry-based method. We first define a specific sequence of deformation shapes of the elastica for a given buckling mode. For a known configuration the phase portait of the elastica (i.e., inclination θ- curvature θ') is then determined. Based on it, the elastica is divided into distinct segments consistent with a single canonical segment with clamped-pinned boundary conditions. The complete solution is accordingly calculated by solving all distinct subproblems and satisfying the continuity properties at the common extremities of these segments. The solution of these subproblems is obtained by applying an asymptotic analysis, or by using elliptic integrals.

In Chapter 3, the analysis is presented for both classes of problem; (1) the classical problem (some supplementary material can be also found in Appendix B) and (2) the insertion problem. In the latter case, a configurational force is generated at the insertion point that leads to a reduced value of the axial applied force, which is not present in the classical problem. This effect is also illustrated through concrete examples.

The same approach can be also adopted for the analysis of different equilibrium problems of inflectional elastica as far as the phase portrait of the elastica can be determined (known positions of zero inflection points $\theta' = 0$ and zero inclination angles $\theta = 0$). An alternative option is to discretize the elastica by applying a finite-difference scheme, leading to the so-called "discrete elastica" (Domokos and Holmes, 1993). This idea in combination with an asymptotic analysis was first suggested by Challamel et al. (2015) for the post-buckling analysis of an unconstrained elastica. It can be also adopted herein for the solution of the subproblems.

Another geometry-based contribution of the present work is a stability rule for the planar case, which is based on the number of the inflection points and the number and nature of the contact conditions. Its verification was achieved by using previous research works (Ro et al., 2010; Manning and Bulman, 2005) and applying the optimal control method. However, this rule has not been formally demonstrated and therefore remains a conjecture. As explained in Chapter 3, we can deduce about the stability of a given configuration of the planar elastica purely by its geometry without the need of any futher analysis. This stability criterion, however, cannot be adopted for a zero value of clearance, because the lower wall functions as an additional stabilization factor in this case and different contact patterns are obtained. The latter observation is explained in Chapter 6.

The application of the optimal control to the stability analysis of elastic structures is not very well-known yet. Maurer and Mittelmann (1991) were the first to derive preliminary results for the stability behavior of a nonlinear beam constrained by two symmetrically located longitudinal obstacles using an optimal control method. Maurer and Mittelmann (1991)'s innovative idea remained quasi unknown for years. Even though the equivalence between a calculus of variations and an optimal control problem was proved as early as in 1960, see for instance (Berkovitz, 1961, 1962), only recently the optimal control has started being used for the stability analysis of an elastic structure (Liberzon, 2012; Sachkov, 2008b,a; O ' Reilly and Peters, 2011).

In short, the optimal control formulation for our constrained stability problem involves the following parts; (1) the functional, which is the Lagrangian of the problem (i.e., the potential energy of the elastica), (2) the spatial dynamics, which is deduced from the inextensibility-unshearability constraints, (3) the control variables, which are the spatial derivatives of the Euler angles (e.g., the curvature for the planar elastica), (4) the unilateral constraints (i.e, rigid obstacles) and (5) the boundary conditions. Based on Hamiltonian mechanics, the optimality conditions, which constitute the Pontryagin's minimum principle, are then derived. These necessary optimality conditions consist of the minimization of the Hamiltonian with respect to the control, the canonical equations of the (augmented) Hamiltonian and the satisfaction of the boundary conditions. Detailed derivation of the Pontryagin's theorem can be found in Chapter 4.

The main advantage of the optimal control method when compared to calculus of variations is the assumption of strong rather than weak variation of the involved variables. This leads to the additional Weierstrass necessary condition, which provides the minimization of the Hamiltonian with respect to the control, see Chapter 4. Based on it, we obtain the "optimal" equilibrium state that minimizes the total energy of a system rather than just an equilibrium configuration, as in calculus of variations. Hence, we can deduce about the stability behavior of an equilibrium state even if we just apply the first-order optimality conditions. The inclusion of the unilateral constraints is also an additional reason to choose an optimal control method. In our constrained stability problem, the unilateral constraints are pure-state constraints of second order, which implies that set-valued functions of the adjoint equations are present. Physically, this means that discontinuous shear forces are obtained whenever a contact with the wall is present. Even in this case, the use of optimal control is straightforward while in calculus of variations several assumptions are required, such as the assumption of smooth constraints, or the addition of slack variables. For all these reasons, the optimal control method is a more efficient technique when compared to the classical calculus of variations.

A variety of examples is analyzed in Chapters 5 , 6 and 7 using the optimal control method. These involve the classical and insertion stability problems while several factors such as the gravity, the clearances of the walls and the boundary conditions are also investigated. Before referring to some remarkable results, it is important to point out that every distinct stability problem can be formulated without any special effort. For instance, let us explain how we can transform the classical to the insertion stability problem for displacement-controlled conditions. In the classical problem, we predefine the distance between the extremities of the elastica by keeping fixed the length of the elastica, while in the insertion problem exactly the opposite holds. This is the only difference between these problems, which shows how easy it is to switch from one formulation to another. In addition there is no need for any special treatment regarding the boundary conditions, or the types of the constraints. All above indicate that the optimal control method is simple and generic at the same time.

Based on the optimal control method some notable results were obtained. One important conclusion is that the classical and the insertion stability problems lead to the same sequence of contact patterns if the elastica is weightless. Some differences are observed when the self-weight is non-negligible. Another interesting result is the comparison between the stability behavior of the planar elastica and the spatial elastica with or without the unilateral constraints. In particular, the stability behavior of the unconstrained spatial elastica coincides with the planar elastica until the onset of out-of-plane deformation, which depends on the ratio of the torsional over the bending moduli. Past this point, the buckling response of the spatial elastica is entirely different. Similar conclusions are reached by solving the constrained problem, see Chapters 5 and 7.

The effect of the weight has been also investigated using the optimal control method. Only partial analysis of this effect can be found in the literature (Wicks et al., 2008; Gao and Huang, 2015). Based on the self-weight and the clearances of the walls, two possible initial configurations of the elastica can be obtained; (1) an unconstrained shape, or (2) a constrained shape with a discrete, or continuous contact with the lower wall. An unconstrained, or a constrained shape is obtained if the maximum height derived by buckling of the elastica under its own weight is higher, or lower than the clearance of the lower wall, respectively.

Another important observation is the case of one-sided foundation with a high value of self-weight and low or zero value of clearance. Initially, the elastica remains unstressed on the rigid foundation and an infinite axial force is required for the formation of a "ruck" (see Chapter 6). After the onset of buckling, the height of this ruck increases while the axial force initially decreases with increasing the end-shortening until it reaches a minimum value. Beyond this point, the axial force starts increasing and the height of the ruck gradually reaches a plateau. If an upper wall is also present and its clearance is lower than this plateau, a sequence of contact patterns is obtained. Otherwise, its behavior is identical to the stability problem with one-sided foundation. Several other interesting results are also available in Chapters 5, 6 and 7.

To summarize, the geometry-based method is only applicable to the planar case and for particular kinds of problems when compared to the optimal control problem whose use is more generic. The major contributions of the present work are summarized below.

8.2 Major contributions

The most notable contributions of this thesis are:

- **Development of a geometry-based technique for the analysis of the classical stability problem:** A geometry-based segmentation technique is applied to derive the bifurcation diagram, including the sequence of contact patterns. A simple geometry-based stability criterion based on the number of the inflection points and the nature of contact conditions

is also conjectured.

- **Analysis of the insertion problem:** The constrained buckling problem of a variable length elastica is solved. Based on the calculus of variations, we show that an Eshelby-like or configuration force is generated at the insertion point of the sliding sleeve, which was ignored in previous studies (Ro et al., 2010). Its effect for the constrained buckling problem of a spatial elastica is also illustrated.

- **Application of optimal control in the stability analysis of constrained thin elastic structures:** Optimization-based stability analysis of a planar, or a spatial elastica constrained by rigid horizontal walls is performed. Derivation of bifurcation diagrams for different loading and boundary conditions is achieved for both the classical and insertion stability problems.

- **Weight considerations in the stability analysis of constrained elastica:** To the best of our knowledge, the weight effect has not been investigated before. The problem is only partially solved as in the oil-drilling community, it is assumed that the drillstring is always in contact with the borehole.

8.3 Future work

Further analysis could also include second-order sufficient conditions. This would require an indirect method rather than a direct approach. In particular, after solving the first order optimality conditions of the problem, the second-order optimality conditions can be derived by applying a sensitivity analysis of the shooting mapping. This mapping should include a regular structure with a finite number of contact points and the strict complementarity conditions has to be also satisfied such that the implicit function theorem is applicable, as explained in detail in (Malanowski and Maurer, 2001; Maurer and Oberle, 2002). This could give a more complete solution of our problem. However, the comparison of our results with other studies has shown that the first-order optimality conditions are sufficient enough in order to derive accurate bifurcation diagrams without any exception.

The optimal control method can be also used to analyze the quasi-static, or buckling response of an elastic rod under complex loading and boundary conditions, including a non-uniform density and/or discontinuities along its arclength (e.g., kinks) and in the presence of bilateral and/or unilateral constraints. It can be also adopted for the stability analysis of any other elastic structure, such as shells and plates. Hence, we anticipate that this novel approach (see (Maurer and Mittelmann, 1991; Liberzon, 2012)) will gain more attention in the future.

Except for its application to the analysis of a stability problem, we can also use it to optimize the design (i.e., optimization of material or mechanical properties) of an elastic structure, such

that any catastrophic failure (i.e., buckling) is avoided or its optimal performance is achieved (Bendsoe and Sigmund, 2003; Huang and Xie, 2010). For instance, this analysis is essential in medical and engineering applications, such as the insertion of a guide-wire (Tang et al., 2012) or in oil-drilling operations (Wicks et al., 2008). A comprehensive literature review about the latter application is included in Appendix A.

The main limitation of the current study is that the effect of friction is ignored (frictionless rigid walls are only studied here). The effect of friction in a constrained buckling problem can be better understood if a dynamic stability analysis is performed, as explained by (Su et al., 2013). A classical stability analysis can only partially solve this problem (Gao and Miska, 2009a). Some preliminary study about it (particularly in oil-drilling operations) can be found in (Liu and Chen, 2013; Liu et al., 2015) (see also Appendix A). As explained in (Liu et al., 2015), the effect of friction in the buckling response of an elastic rod is complex as it can be beneficial or catastrophic, depending on the initial, boundary and loading conditions under consideration. Hence, further numerical and experimental analysis is necessary. This analysis, however, requires a different approach rather than the optimal control method as a history-dependent response of the elastic rod is expected.

Bibliography

Alderliesten, T., M. K. Konings, and W. J. Niessen (2007, January). Modeling Friction, Intrinsic Curvature, and Rotation of Guide Wires for Simulation of Minimally Invasive Vascular Interventions. *IEEE Transactions on Biomedical Engineering 54*(1), 29–38.

Alfutov, N. A. (2000). *Stability of Elastic Structures*. Foundations of Engineering Mechanics. Berlin, Heidelberg: Springer Berlin Heidelberg.

Antman, S. S. (2005). *Nonlinear problems of elasticity*. New York, NY: Springer.

Arslan, M., M. E. Ozbayoglu, S. Z. Miska, M. Yu, N. Takach, and R. F. Mitchell (2012). Buckling of Bouyancy Assisted Tubular. Society of Petroleum Engineers.

Atanackovic, T. (1997). *Stability Theory of Elastic Rods*. Stability, Vibration and Control of Systems, Series A.

Athisakul, C., T. Monprapussorn, and S. Chucheepsakul (2011, mar). A variational formulation for three-dimensional analysis of extensible marine riser transporting fluid. *Ocean Engineering 38*(4), 609–620.

Augustin, D. and H. Maurer (2001). Computational sensitivity analysis for state constrained optimal control problems. *Annals of Operations Research 101*(1/4), 75–99.

Barclay, A., P. E. Gill, and J. B. Rosen (1998). SQP methods and their application to numerical optimal control. In *Variational Calculus, Optimal Control and Applications*, pp. 207–222. Birkhauser Basel.

Barquins, M. (1985, August). Sliding friction of rubber and Schallamach waves - a: review. *Materials Science and Engineering 73*, 45–63.

Bendsoe, M. P. and O. Sigmund (2003). *Topology Optimization*. Springer-Verlag Berlin Heidelberg New York.

Benson, D. A., G. T. Huntington, T. P. Thorvaldsen, and A. V. Rao (2006, nov). Direct trajectory optimization and costate estimation via an orthogonal collocation method. *Journal of Guidance, Control, and Dynamics 29*(6), 1435–1440.

Berkovitz, L. D. (1961, aug). Variational methods in problems of control and programming. *Journal of Mathematical Analysis and Applications 3*(1), 145–169.

Berkovitz, L. D. (1962, dec). On control problems with bounded state variables. *Journal of Mathematical Analysis and Applications 5*(3), 488–498.

Berkovitz, L. D. and N. G. Medhin (2012). *Nonlinear Optimal Control Theory (Chapman & Hall/CRC Applied Mathematics & Nonlinear Science)*. Chapman and Hall/CRC.

Bernoulli, D. (1742). The 26th letter to euler. in correspondence mathematique et physique, volume 2. p. h. fuss,.

Bernoulli, J. (pp. 223-227, 1692). *Die Werke von Jakob Bernoulli: Bd. 5: Differentialgeometrie "Quadratura curvae, e cujus evolutione describitur inflexae laminae curvatura"*. Birkhauser.

Betts, J. T. (1998, mar). Survey of numerical methods for trajectory optimization. *Journal of Guidance, Control, and Dynamics 21*(2), 193–207.

Betts, J. T. (2010, jan). *Practical Methods for Optimal Control and Estimation Using Nonlinear Programming*. Society for Industrial and Applied Mathematics.

Biegler, L. and V. Zavala (2009, mar). Large-scale nonlinear programming using IPOPT: An integrating framework for enterprise-wide dynamic optimization. *Computers & Chemical Engineering 33*(3), 575–582.

Bigoni, D. (Ed.) (2016). *Extremely deformable structures*. Number Vol. 562 in Courses and lectures / International Centre for Mechanical Sciences. Wien: Springer.

Bigoni, D., F. D. Corso, F. Bosi, and D. Misseroni (2015, jan). Eshelby-like forces acting on elastic structures: Theoretical and experimental proof. *Mechanics of Materials 80*, 368–374.

Bonnans, J. F. (Ed.) (2006). *Numerical optimization: theoretical and practical aspects* (2nd ed ed.). Universitext. Berlin ; New York: Springer.

Bonnans, J. F. and A. Hermant (2007a, jul). No-gap second-order optimality conditions for optimal control problems with a single state constraint and control. *Mathematical Programming 117*(1-2), 21–50.

Bonnans, J. F. and A. Hermant (2008, feb). Stability and sensitivity analysis for optimal control problems with a first-order state constraint and application to continuation methods. *ESAIM: Control, Optimisation and Calculus of Variations 14*(4), 825–863.

Bonnans, J. F. and A. Hermant (2009, feb). Second-order analysis for optimal control problems with pure state constraints and mixed control-state constraints. *Annales de Institut Henri Poincare (C) Non Linear Analysis 26*(2), 561–598.

Bonnans, J. F. B. and A. Hermant (2007b, jan). Well-posedness of the shooting algorithm for state constrained optimal control problems with a single constraint and control. *SIAM Journal on Control and Optimization 46*(4), 1398–1430.

Born, M. (1906). *Untersuchungen uber die Stabilitaet der elastischen Linie in Ebene und Raum, under verschiedenen Grenzbedingungen.* Ph. D. thesis, University of Goettingen.

Bosi, F., D. Misseroni, F. D. Corso, and D. Bigoni (2015, jul). Self-encapsulation, or the 'dripping' of an elastic rod. *Proceedings of the Royal Society A: Mathematical, Physical and Engineering Science 471*(2179), 20150195.

Bosi, F., D. Misseroni, F. Dal Corso, and D. Bigoni (2015, September). Development of configurational forces during the injection of an elastic rod. *Extreme Mechanics Letters 4*, 83–88. 00005.

Bryson, A. (2016). *Applied optimal control: Optimization, estimation and control.* CRC Press.

Bryson, A. E. and W. F. Denham (1964, jan). Optimal programming problems with inequality constraints. ii - solution by steepest-ascent. *AIAA Journal 2*(1), 25–34.

Bryson, A. E., W. F. Denham, and S. E. Dreyfus (1963, nov). Optimal programming problems with inequality constraints. *AIAA Journal 1*(11), 2544–2550.

Bulirsch, R. and J. Stoer (2010). *Introduction to Numerical Analysis.* Springer.

Byrd, R. H., N. I. Gould, J. Nocedal, and R. A. Waltz (2003, may). An algorithm for nonlinear optimization using linear programming and equality constrained subproblems. *Mathematical Programming 100*(1).

Byrd, R. H., J. Nocedal, and R. A. Waltz (2006). *Knitro: An Integrated Package for Nonlinear Optimization*, pp. 35–59. Boston, MA: Springer US.

Chai, H. (1998, July). The post-buckling response of a bi-laterally constrained column. *46*(7), 1155–1181.

Challamel, N., A. Kocsis, and C. Wang (2015, December). Discrete and non-local elastica. *International Journal of Non-Linear Mechanics 77*, 128–140.

Cheatham, J. B. (1984, August). Helical Postbuckling Configuration of a Weightless Column Under the Action of m Axial Load. *Society of Petroleum Engineers Journal 24*(04), 467–472.

Chen, J., J. Wu, M. Luo, and J. Zhang (2014, jun). A knitro-based real-time locomotion method for imitating the caterpillar-like climbing strategy. *11th IEEE International Conference on Control & Automation (ICCA)*.

Chen, J.-S. and J. Fang (2013, October). Deformation sequence of a constrained spatial buckled beam under edge thrust. *International Journal of Non-Linear Mechanics 55*, 98–101.

Chen, J.-S. and Y.-C. Lin (2013, April). Vibration and stability of a long heavy elastica on rigid foundation. *International Journal of Non-Linear Mechanics 50*, 11–18.

Chen, J.-S., C.-J. Lu, and C.-Y. Lee (2015, November). On the use of energy method with element splitting to determine the stability of a constrained elastica. *International Journal of Non-Linear Mechanics 76*, 77–86.

Chen, J.-S. and H.-H. Wu (2011, January). Deformation and stability of an elastica under a point force and constrained by a flat surface. *53*(1), 42–50.

Chen, V., V. Lin, and J. Cheatham (1989). An Analysis of Tubing and Casing Buckling in Horizontal Wells. Offshore Technology Conference.

Chucheepsakul, S., S. Buncharoen, and T. Huang (1995, jul). Elastica of simple variable-arc-length beam subjected to end moment. *Journal of Engineering Mechanics 121*(7), 767–772.

Chucheepsakul, S. and T. Monprapussorn (2000, aug). Divergence pf variable arc-length elastica pipes transporting fluid. *Journal of Fluids and Structures 14*(6), 895–916.

Chucheepsakul, S., T. Monprapussorn, and T. Huang (2003, feb). Large strain formulations of extensible flexible marine pipes transporting fluid. *Journal of Fluids and Structures 17*(2), 185–224.

Chucheepsakul, S. and B. Phungpaigram (2004, jan). Elliptic integral solutions of variable-arc-length elastica under an inclined follower force. *ZAMM 84*(1), 29–38.

Clauvelin, N., B. Audoly, and S. Neukirch (2009, May). Elasticity and Electrostatics of Plectonemic DNA. *Biophysical Journal 96*(9), 3716–3723.

Comninou, M. (1978). The interface crack in a shear field. *Journal of Applied Mechanics 45*(2), 287.

Cunha, J. (2004, March). Buckling of Tubulars Inside Wellbores: A Review on Recent Theoretical and Experimental Works. *SPE Drilling & Completion 19*(01), 13–19.

Davies, M. A. and F. C. Moon (1993, jan). 3-d spatial chaos in the elastica and the spinning top: Kirchhoff analogy. *Chaos: An Interdisciplinary Journal of Nonlinear Science 3*(1), 93–99.

Daviet, G., F. Bertails-Descoubes, and L. Boissieux (2011). A hybrid iterative solver for robustly capturing coulomb friction in hair dynamics. pp. 1. ACM Press.

Dawson, R. (1984, October). Drill Pipe Buckling in Inclined Holes. *36*(10), 1734–1738.

Denoel, V. and E. Detournay (2011, February). Eulerian formulation of constrained elastica. *International Journal of Solids and Structures 48*(3-4), 625–636.

Dichmann, D. J. and J. H. Maddocks (2000). An Impetus-Striction Simulation of the Dynamics of an Elastica. In Journal of Nonlinear Science (Ed.), *Mechanics: From Theory to Computation*, pp. 217–238. New York, NY: Springer New York.

Dichmann, D. J., J. H. Maddocks, and R. L. Pego (1996, December). Hamiltonian dynamics of an elastica and the stability of solitary waves. *Archive for Rational Mechanics and Analysis 135*(4), 357–396.

Domokos, G., W. B. Fraser, and I. Szeberenyi (2003, November). Symmetry-breaking bifurcations of the uplifted elastic strip. *Physica D: Nonlinear Phenomena 185*(2), 67–77.

Domokos, G. and P. Holmes (1993, December). Euler's problem, Euler's method, and the standard map; or, the discrete charm of buckling. *Journal of Nonlinear Science 3*(1), 109–151.

Domokos, G., P. Holmes, and B. Royce (1997, June). Constrained euler buckling. *Journal of Nonlinear Science 7*(3), 281–314.

Doraiswamy, S., K. R. Narayanan, and A. R. Srinivasa (2012, January). Finding minimum energy configurations for constrained beam buckling problems using the Viterbi algorithm. *International Journal of Solids and Structures 49*(2), 289–297.

Duriez, C., S. Cotin, J. Lenoir, and P. Neumann (2006, November). New approaches to catheter navigation for interventional radiology simulation. *Computer Aided Surgery 11*(6), 300–308.

Elnagar, G., M. Kazemi, and M. Razzaghi (1995). The pseudospectral legendre method for discretizing optimal control problems. *IEEE Transactions on Automatic Control 40*(10), 1793–1796.

Euler, L. (1744). *Methodus inveniendi lineas curvas maximi minimive proprietate gaudentes, sive solutio problematis isoperimetrici lattissimo sensu accepti, chapter Additamentum 1.* Lausanne & Geneve, apud Marcum-Michaelem Bousquet & socios.

Falugi P., K. E. and van Wyk (2010). Imperial college london optimal control software user guide (iclocs). Technical report, Department of Electrical Engineering, Imperial College London, London, UK.

Fang, J., S.-Y. Li, and J.-S. Chen (2013, November). On a compressed spatial elastica constrained inside a tube. *Acta Mechanica 224*(11), 2635–2647.

Fletcher, R. (1970, mar). A new approach to variable metric algorithms. *The Computer Journal 13*(3), 317–322.

G. Fasano, J. P. (2012). *Modeling and Optimization in Space Engineering*. Springer-Verlag GmbH.

Gao, D.-L. and W.-J. Huang (2015, August). A review of down-hole tubular string buckling in well engineering. *Petroleum Science 12*(3), 443–457.

Gao, G., Q. Di, S. Z. Miska, and W. Wang (2011). Stability Analysis of Pipe with Connectors in Horizontal Wells. Society of Petroleum Engineers.

Gao, G. and S. Miska (2010, September). Dynamic Buckling and Snaking Motion of Rotating Drilling Pipe in a Horizontal Well. *15*(3), 867–877.

Gao, G. and S. Z. Miska (2009a, December). Effects of Boundary Conditions and Friction on Static Buckling of Pipe in a Horizontal Well. *SPE Journal 14*(4), 782–796.

Gao, G. and S. Z. Miska (2009b). Effects of Friction on Post Buckling Behavior and Axial Load Transferring of Pipe in a Horizontal Well. In *SPE Journal*. Society of Petroleum Engineers.

Gao, G. and S. Z. Miska (2009c). Effects of Friction on Post Buckling Behavior and Axial Load Transferring of Pipe in a Horizontal Well. In *SPE Journal*. Society of Petroleum Engineers.

Gelfand, I. M. (2000). *Calculus of variations*. Mineola, N.Y: Dover Publications.

Gill, P. E., W. Murray, and M. A. Saunders (2002, jan). SNOPT: An SQP algorithm for large-scale constrained optimization. *SIAM Journal on Optimization 12*(4), 979–1006.

Goh, C. and K. Teo (1988, jan). Control parametrization: A unified approach to optimal control problems with general constraints. *Automatica 24*(1), 3–18.

Goldfarb, D. (1970, jan). A family of variable-metric methods derived by variational means. *Mathematics of Computation 24*(109), 23–23.

Goldstein, H., C. P. Poole, and J. L. Safko (2002). *Classical mechanics*. San Francisco: Addison Wesley.

Goss, V. G. A. (2008, jul). The history of the planar elastica: Insights into mechanics and scientific method. *Science & Education 18*(8), 1057–1082.

Goyal, S., N. Perkins, and C. Lee (2005, oct). Nonlinear dynamics and loop formation in kirchhoff rods with implications to the mechanics of DNA and cables. *Journal of Computational Physics 209*(1), 371–389.

Hartl, R. F., S. P. Sethi, and R. G. Vickson (1995, jun). A survey of the maximum principles for optimal control problems with state constraints. *SIAM Review 37*(2), 181–218.

He, X. and A. Kyllingstad (1995, March). Helical Buckling and Lock-Up Conditions for Coiled Tubing in Curved Wells. *10*(1), 10–15.

Hermant, A. (2009a, jun). Homotopy algorithm for optimal control problems with a second-order state constraint. *Applied Mathematics and Optimization 61*(1), 85–127.

Hermant, A. (2009b, jan). Stability analysis of optimal control problems with a second-order state constraint. *SIAM Journal on Optimization 20*(1), 104–129.

Holmes, P., G. Domokos, J. Schmitt, and I. Szeberenyi (1999, March). Constrained Euler buckling: an interplay of computation and analysis. *Computer Methods in Applied Mechanics and Engineering 170*(3-4), 175–207.

Huang, W. and D. Gao (2014, July). Helical buckling of a thin rod with connectors constrained in a cylinder. *84*, 189–198.

Huang, W., D. Gao, and F. Liu (2015, April). Buckling Analysis of Tubular Strings in Horizontal Wells. *SPE Journal 20*(02), 405–416. 00005.

Huang, W., D. Gao, and Y. Liu (2016, nov). A study of tubular string buckling in vertical wells. *International Journal of Mechanical Sciences 118*, 231–253.

Huang, W., D. Gao, and Y. Liu (2017, apr). Inter-helical and intra-helical buckling analyses of tubular strings with connectors in horizontal wellbores. *Journal of Petroleum Science and Engineering 152*, 182–192.

Huang, W., D. Gao, S. Wei, and P. Chen (2015, December). Boundary Conditions: A Key Factor in Tubular-String Buckling. *SPE Journal 20*(06), 1409–1420.

Huang, X. and M. Xie (2010). *Evolutionary Topology Optimization of Continuum Structures: Methods and Applications*. John Wiley & Sons.

Humer, A. and H. Irschik (2009, may). Large deflections of beams with an unknown length of the reference configuration. In *50th AIAA/ASME/ASCE/AHS/ASC Structures, Structural Dynamics, and Materials Conference*. American Institute of Aeronautics and Astronautics.

Humer, A. and H. Irschik (2011, may). Large deformation and stability of an extensible elastica with an unknown length. *International Journal of Solids and Structures 48*(9), 1301–1310.

Hunt, G. W. and A. Blackmore (1997, nov). Homoclinic and heteroclinic solutions of upheaval buckling. *Philosophical Transactions of the Royal Society A: Mathematical, Physical and Engineering Sciences 355*(1732), 2185–2195.

Huntington, G. T. and A. V. Rao (2008, mar). Comparison of global and local collocation methods for optimal control. *Journal of Guidance, Control, and Dynamics 31*(2), 432–436.

Huynen, A., E. Detournay, and V. Denoel (2016). Eulerian formulation of elastic rods. *Proceedings of the Royal Society A: Mathematical, physical and engineering sciences 472*(2190).

Jacobson, D., M. Lele, and J. Speyer (1971, aug). New necessary conditions of optimality for control problems with state-variable inequality constraints. *Journal of Mathematical Analysis and Applications 35*(2), 255–284.

Jaculli, M. A., J. R. P. Mendes, and K. Miura (2017, may). Dynamic buckling with friction inside directional wells. *Journal of Petroleum Science and Engineering 153*, 145–156.

Jae Ho Jung, Tae Jin Kang, and Kwan Soo Chung (2004, October). An Analytical Solution to the Lateral Buckling of an Elastica with Self-Contact. *Textile Research Journal 74*(10), 899–904.

Jin, M. and Z. Bao (2008, April). Sufficient conditions for stability of Euler elasticas. *Mechanics Research Communications 35*(3), 193–200.

Jin, M. and Z. Bao (2014, July). A proof of instability of some Euler elasticas. *Mechanics Research Communications 59*, 37–41.

Jin, M. and Z. B. Bao (2013, July). Extensibility Effects on Euler Elastica ' s Stability. *Journal of Elasticity 112*(2), 217–232.

Jorge Nocedal, S. W. (2006). *Numerical Optimization*. Springer New York.

Kameswaran, S. and L. T. Biegler (2007, nov). Convergence rates for direct transcription of optimal control problems using collocation at radau points. *Computational Optimization and Applications 41*(1), 81–126.

Kirchhoff, G. (1859). Uber das gleichgewicht und die bewegung eines unendlich dunnen elastischen stabes. *Journal fur Mathematik (Crelle) 56*, 285–313.

Klarbring, A. (1988, January). On discrete and discretized non-linear elastic structures in unilateral contact (stability, uniqueness and variational principles). *International Journal of Solids and Structures 24*(5), 459–479.

Kolinski, J. M., P. Aussillous, and L. Mahadevan (2009, October). Shape and Motion of a Ruck in a Rug. *Physical Review Letters 103*(17).

Konings, M. K., E. B. Kraats, T. Alderliesten, and W. J. Niessen (2003, November). Analytical guide wire motion algorithm for simulation of endovascular interventions. *Medical & Biological Engineering & Computing 41*(6), 689–700.

Kopp, C., C. D. Rahn, and F. W. Paul (2000, oct). Measuring deformations of limp fabrics for material handling. *Textile Research Journal 70*(10), 920–932.

Kornienko, I., L. T. Paiva, and M. do Rosário de Pinho (2014). Introducing state constraints in optimal control for health problems. *Procedia Technology 17*, 415–422.

Kraft, D. (1985). On converting optimal control problems into nonlinear programming problems. *Computational Mathematical Programming*, 261–280.

Kuru, E., A. Martinez, S. Miska, and W. Qiu (2000). The Buckling Behavior of Pipes and Its Influence on the Axial Force Transfer in Directional Wells. *122*(3), 129.

Kuznetsov, V. and S. Levyakov (2002, September). Complete solution of the stability problem for elastica of Euler's column. *International Journal of Non-Linear Mechanics 37*(6), 1003–1009.

Lazarus, A., C. Maurini, and S. Neukirch (2015). Stability of discretized nonlinear elastic systems. pp. 1–53.

Lazarus, A., J. T. Miller, and P. M. Reis (2013, August). Continuation of equilibria and stability of slender elastic rods using an asymptotic numerical method. *Journal of the Mechanics and Physics of Solids 61*(8), 1712–1736.

Lee, A. A., C. Le Gouellec, and D. Vella (2015, December). The role of extensibility in the birth of a ruck in a rug. *Extreme Mechanics Letters 5*, 81–87.

Lenoir, J., S. Cotin, C. Duriez, and P. Neumann (2006, June). Interactive physically-based simulation of catheter and guidewire. *Computers & Graphics 30*(3), 416–422.

Levenberg, K. (1944, jul). A method for the solution of certain non-linear problems in least squares. *Quarterly of Applied Mathematics 2*(2), 164–168.

Levien, R. (2008). *The elastica: a mathematical history.* Ph. D. thesis, University of California at Berkeley.

Levyakov, S. V. and V. V. Kuznetsov (2010, April). Stability analysis of planar equilibrium configurations of elastic rods subjected to end loads. *Acta Mechanica 211*(1-2), 73–87.

Li, S., J. Qin, J. Guo, Y.-P. Chui, and P.-A. Heng (2011a). A Novel FEM-Based Numerical Solver for Interactive Catheter Simulation in Virtual Catheterization. *International Journal of Biomedical Imaging 2011*, 1–8.

Li, S., J. Qin, J. Guo, Y.-P. Chui, and P.-A. Heng (2011b). A Novel FEM-Based Numerical Solver for Interactive Catheter Simulation in Virtual Catheterization. *International Journal of Biomedical Imaging 2011*, 1–8.

Liberzon, D. (2012). *Calculus of variations and optimal control theory: a concise introduction*. Princeton University Press.

Liu, C.-W. and J.-S. Chen (2013, January). Effect of friction on the planar elastica constrained inside a circular channel with clearance. *50*(1), 270–278.

Liu, J., T. Su, N. Wicks, J. Pabon, and K. Bertoldi (2015, October). The Instability Mechanism of a Confined Rod Under Axial Vibrations. *Journal of Applied Mechanics 83*(1).

Lloyd, D., W. Shanahan, and M. Konopasek (1978, jan). The folding of heavy fabric sheets. *International Journal of Mechanical Sciences 20*(8), 521–527.

Love, A. E. H. (2013). *A treatise on the mathematical theory of elasticity*. Cambridge: Cambridge University Press.

Lu, Z.-H. and J.-S. Chen (2008, may). Deformations of a clamped–clamped elastica inside a circular channel with clearance. *International Journal of Solids and Structures 45*(9), 2470–2492.

Lubinski, A. (1950, January). A Study of the Buckling of Rotary Drilling Strings.

Lubinski, A. and W. Althouse (1962, June). Helical Buckling of Tubing Sealed in Packers. *14*(6), 655–670.

Maddocks, J. (1984). Stability of nonlinearly elastic rods. *Archive for Rational Mechanics and Analysis 85*(4).

Mahadevan, L. and J. B. Keller (1999, jan). Periodic folding of thin sheets. *SIAM Review 41*(1), 115–131.

Majumdar, A. and A. Goriely (2013, jun). Static and dynamic stability results for a class of three-dimensional configurations of kirchhoff elastic rods. *Physica D: Nonlinear Phenomena 253*, 91–101.

Majumdar, A., C. Prior, and A. Goriely (2012, September). Stability Estimates for a Twisted Rod Under Terminal Loads: A Three-dimensional Study. *Journal of Elasticity 109*(1), 75–93.

Malanowski, K. (1995, sep). Stability and sensitivity of solutions to nonlinear optimal control problems. *Applied Mathematics & Optimization 32*(2), 111–141.

Malanowski, K. (1997, jan). Sufficient optimality conditions for optimal control subject to state constraints. *SIAM Journal on Control and Optimization 35*(1), 205–227.

Malanowski, K. and H. Maurer (2001). Sensitivity analysis for optimal control problems subject to higher order state constraints. *Annals of Operations Research 101*(1/4), 43–73.

Malanowski, K., H. Maurer, and S. Pickenhain (2004, dec). Second-order sufficient conditions for state-constrained optimal control problems. *Journal of Optimization Theory and Applications 123*(3), 595–617.

Maltby, T. and C. Calladine (1995a, September). An investigation into upheaval buckling of buried pipelines - ii. theory and analysis of experimental observations. *International Journal of Mechanical Sciences 37*(9), 965–983.

Maltby, T. and C. Calladine (1995b, sep). An investigation into upheaval buckling of buried pipelines-ii. experimental apparatus and some observations. *International Journal of Mechanical Sciences 37*(9), 943–963.

Manning, R. S. (2009, February). Conjugate Points Revisited and Neumann - Neumann Problems. *SIAM Review 51*(1), 193–212.

Manning, R. S. (2014, April). A Catalogue of Stable Equilibria of Planar Extensible or Inextensible Elastic Rods for All Possible Dirichlet Boundary Conditions. *Journal of Elasticity 115*(2), 105–130. 00003.

Manning, R. S. and G. B. Bulman (2005, August). Stability of an elastic rod buckling into a soft wall. *Proceedings of the Royal Society A: Mathematical, Physical and Engineering Sciences 461*(2060), 2423–2450.

Manning, R. S., K. A. Rogers, and J. H. Maddocks (1998, December). Isoperimetric conjugate points with application to the stability of DNA minicircles. *Proceedings of the Royal Society A: Mathematical, Physical and Engineering Sciences 454*(1980), 3047–3074.

Martinez, A., S. Miska, E. Kuru, and J. Sorem (2000). Experimental Evaluation of the Lateral Contact Force in Horizontal Wells. *122*(3), 123.

Maurer, H. (1979, mar). Differential stability in optimal control problems. *Applied Mathematics & Optimization 5*(1), 283–295.

Maurer, H. and K. Malanowski (1998, feb). Sensitivity analysis for state constrained optimal control problems. *Discrete and Continuous Dynamical Systems 4*(2), 241–272.

Maurer, H. and H. D. Mittelmann (1991, jan). The non-linear beam via optimal control with bounded state variables. *Optimal Control Applications and Methods 12*(1), 19–31.

Maurer, H. and H. J. Oberle (2002, jan). Second order sufficient conditions for optimal control problems with free final time: The Riccati approach. *SIAM Journal on Control and Optimization 41*(2), 380–403.

Maurer, H. and S. Pickenhain (1995, sep). Second-order sufficient conditions for control problems with mixed control-state constraints. *Journal of Optimization Theory and Applications 86*(3), 649–667.

McCann, R. and P. Suryanarayana (1994). Experimental Study Of Curvature And Frictional Effects On Buckling. Offshore Technology Conference.

McCourt, I., T. Truslove, and J. Kubie (2004, September). On the penetration of tubular drill pipes in horizontal oil wells. *Proceedings of the Institution of Mechanical Engineers, Part C: Journal of Mechanical Engineering Science 218*(9), 1063–1081.

Menand, S., H. Sellami, J. Akowanou, C. Simon, L. P. Y. Macresy, P. Isambourg, and D. C. Dupuis (2008). How Drillstring Rotation Affects Critical Buckling Load ? Society of Petroleum Engineers.

Mesterton-Gibbons, M. (2009). *A Primer on the Calculus of Variations and Optimal Control Theory*. American Mathematical Society.

Miersemann, E. and H. Mittelmann (1991, June). Stability and continuation of solutions to obstacle problems. *Journal of Computational and Applied Mathematics 35*(1-3), 5–31.

Miersemann, E. and H. D. Mittelmann (1989, June). Continuation for parametrized nonlinear variational inequalities. *Journal of Computational and Applied Mathematics 26*(1-2), 23–34.

Miersemann, E., H. D. Mittelmann, and W. Tornig (1986). A free boundary problem and stability for the nonlinear beam. *Mathematical Methods in the Applied Sciences 8*(1), 516–532. 00012.

Mikata, Y. (2007, May). Complete solution of elastica for a clamped-hinged beam, and its applications to a carbon nanotube. *Acta Mechanica 190*(1-4), 133–150.

Miller, J., T. Su, E. Dussan V., J. Pabon, N. Wicks, K. Bertoldi, and P. Reis (2015, October). Buckling-induced lock-up of a slender rod injected into a horizontal cylinder. *International Journal of Solids and Structures 72*, 153–164.

Miller, J. T. (2014). *Mechanical behavior of elastic rods under constraint*. Thesis, Massachusetts Institute of Technology. Thesis: Ph. D., Massachusetts Institute of Technology, Department of Civil and Environmental Engineering, 2014.

Miska, S. and J. Cunha (1995). An Analysis of Helical Buckling of Tubulars Subjected to Axial and Torsional Loading in Inclined Wellbores. Society of Petroleum Engineers.

Miska, S., W. Qiu, L. Volk, and J. Cunha (1996). An Improved Analysis of Axial Force Along Coiled Tubing in Inclined/Horizontal Wellbores. Society of Petroleum Engineers.

Misseroni, D., G. Noselli, D. Zaccaria, and D. Bigoni (2015, September). The deformation of an elastic rod with a clamp sliding along a smooth and curved profile. *International Journal of Solids and Structures 69-70*, 491–497.

Mitchell, R. (1982, October). Buckling Behavior of Well Tubing: The Packer Effect. *22*(5), 616–624.

Mitchell, R. (1986, December). Simple Frictional Analysis of Helical Buckling of Tubing. *1*(6), 457–465.

Mitchell, R. (1988, September). New Concepts for Helical Buckling. *3*(3), 303–310.

Mitchell, R. F. (2005). The Pitch of Helically Buckled Pipe. Society of Petroleum Engineers.

Morse, M. (2013). *Introduction to Analysis in the Large*. Literary Licensing, LLC.

Nocedal, J. (2006). *Numerical optimization* (2nd ed ed.). Springer series in operations research. New York: Springer.

O ' Reilly, O. M. and D. M. Peters (2011, November). On Stability Analyses of Three Classical Buckling Problems for the Elastic Strut. *Journal of Elasticity 105*(1-2), 117–136.

O Reilly, O. and T. Tresierras (2011, February). On the static equilibria of branched elastic rods. *International Journal of Engineering Science 49*(2), 212–227.

O'Keefe, A. (2015). *Determining the feasibility of building Len Lye's kinetic artwork sun, land and sea*. Ph. D. thesis, University of Kanterbury.

O'Keefe, A. N. and S. D. Gooch (2015, feb). On the properties of a traveling ruck in a flexible strip. *Journal of Applied Mechanics 82*(4).

O'Reilly, O. M. and D. M. Peters (2012, January). Nonlinear stability criteria for tree-like structures composed of branched elastic rods. *Proceedings of the Royal Society A: Mathematical, Physical and Engineering Sciences 468*(2137), 206–226.

Paiva, L. T. and F. Fontes (2015, apr). Adaptive time–mesh refinement in optimal control problems with state constraints. *Discrete and Continuous Dynamical Systems 35*(9), 4553–4572.

Paslay, P. R. and D. B. Bogy (1964). The Stability of a Circular Rod Laterally Constrained to Be in Contact With an Inclined Circular Cylinder. *31*(4), 605.

Peterson, K. and R. Manning (2010, March). Ineffective perturbations in a planar elastica. *Involve, a Journal of Mathematics 2*(5), 559–580.

Plaut, R. H. (2015, may). Formulas to determine fabric bending rigidity from simple tests. *Textile Research Journal 85*(8), 884–894.

Pocheau, A. and B. Roman (2004, June). Uniqueness of solutions for constrained Elastica. *Physica D: Nonlinear Phenomena 192*(3-4), 161–186.

Pulngern, T., T. Sudsanguan, C. Athisakul, and S. Chucheepsakul (2013, mar). Elastica of a variable-arc-length circular curved beam subjected to an end follower force. *International Journal of Non-Linear Mechanics 49*, 129–136.

Reddien, G. W. (1979, mar). Collocation at gauss points as a discretization in optimal control. *SIAM Journal on Control and Optimization 17*(2), 298–306.

Ro, W.-C., J.-S. Chen, and S.-Y. Hong (2010, August). Vibration and stability of a constrained elastica with variable length. *International Journal of Solids and Structures 47*(16), 2143–2154.

Roman, B. and A. Pocheau (1999, June). Buckling cascade of thin plates: Forms, constraints and similarity. *Europhysics Letters (EPL) 46*(5), 602–608.

Ross, M. I. (2015). *A Primer on Pontryagin's Principle in Optimal Control*. Collegiate Publishers.

Sachkov, Y. L. (2007, December). Optimality of Eulerâs elastica. *Doklady Mathematics 76*(3), 817–819.

Sachkov, Y. L. (2008a, July). Conjugate Points in the Euler Elastic Problem. *Journal of Dynamical and Control Systems 14*(3), 409–439.

Sachkov, Y. L. (2008b, April). Maxwell strata in the Euler elastic problem. *Journal of Dynamical and Control Systems 14*(2), 169–234.

Santillan, S. T., L. N. Virgin, and R. H. Plaut (2006). Post-buckling and Vibration of Heavy Beam on Horizontal or Inclined Rigid Foundation. *Journal of Applied Mechanics 73*(4), 664.

Schallamach, A. (1971, April). How does rubber slide? *Wear 17*(4), 301–312.

Schulz, M. and S. Pellegrino (2001). Equilibrium Paths of Mechanical Systems with Unilateral Constraints I. Theory. In *Mathematical, Physical and Engineering Sciences*, Volume 456, pp. 2223–2242.

Shanno, D. F. (1970, sep). Conditioning of quasi-newton methods for function minimization. *Mathematics of Computation 24*(111), 647–647.

Sorenson, K. G. and J. B. Cheatham (1986). Post-Buckling Behavior of a Circular Rod Constrained Within a Circular Cylinder. *53*(4), 929.

Spillmann, J. and M. Teschner (2007). CoRdE: Cosserat rod elements for the dynamic simulation of one-dimensional elastic objects. In *In Proc. ACM Siggraph/Eurographics Symposium of computer animation*, pp. 63–72.

Stuart, I. M. (1966, September). A loop test for bending length and rigidity. *British Journal of Applied Physics 17*(9), 1215–1220.

Su, T., N. Wicks, J. Pabon, and K. Bertoldi (2013, July). Mechanism by which a frictionally confined rod loses stability under initial velocity and position perturbations. *50*(14), 2468–2476.

Sun, Y., Y. Yu, and B. Liu (2015, January). Closed form solutions for predicting static and dynamic buckling behaviors of a drillstring in a horizontal well. *European Journal of Mechanics - A/Solids 49*, 362–372.

Tang, W., T. R. Wan, D. A. Gould, T. How, and N. W. John (2012, August). A Stable and Real-Time Nonlinear Elastic Approach to Simulating Guidewire and Catheter Insertions Based on Cosserat Rod. *IEEE Transactions on Biomedical Engineering 59*(8), 2211–2218.

Thongyothee, C. and S. Chucheepsakul (2015, jun). Postbuckling of unknown-length nanobeam considering the effects of nonlocal elasticity and surface stress. *International Journal of Applied Mechanics 07*(03).

Timoshenko, S. (2009). *Theory of elastic stability* (2nd ed., Dover ed ed.). Mineola, N.Y: Dover Publications.

Ulbrich, S. (2003, nov). On the superlinear local convergence of a filter-SQP method. *Mathematical Programming 100*(1).

Vaillette, D. P. and G. G. Adams (1983). An Elastic Beam Contained in a Frictionless Channel. *Journal of Applied Mechanics 50*(3), 693.

van der Heijden, G., S. Neukirch, V. Goss, and J. Thompson (2003, jan). Instability and self-contact phenomena in the writhing of clamped rods. *International Journal of Mechanical Sciences 45*(1), 161–196.

van der Heijden, G. H. M. (2001, March). The static deformation of a twisted elastic rod constrained to lie on a cylinder. *457*(2007), 695–715.

Vella, D., A. Boudaoud, and M. Adda-Bedia (2009, October). Statics and Inertial Dynamics of a Ruck in a Rug. *Physical Review Letters 103*(17).

Viswanathan, K., A. Mahato, and S. Chandrasekar (2015, jan). Nucleation and propagation of solitary schallamach waves. *Physical Review E 91*(1).

Vlassenbroeck, J. and R. V. Dooren (1988, apr). A chebyshev technique for solving nonlinear optimal control problems. *IEEE Transactions on Automatic Control 33*(4), 333–340.

von Stryk, O. (1993). Numerical solution of optimal control problems by direct collocation. *ISNM International Series of Numerical Mathematics: Optimal control*, 129–143.

Wachter, A. and L. T. Biegler (2005, apr). On the implementation of an interior-point filter line-search algorithm for large-scale nonlinear programming. *Mathematical Programming 106*(1), 25–57.

Waltz, R., J. Morales, J. Nocedal, and D. Orban (2005, nov). An interior algorithm for nonlinear optimization that combines line search and trust region steps. *Mathematical Programming 107*(3), 391–408.

Wang, C. (1984a, January). Buckling and postbuckling of the lying sheet. *International Journal of Solids and Structures 20*(4), 351–358.

Wang, C. (1997, November). Post-buckling of a clamped-simply supported elastica. *International Journal of Non-Linear Mechanics 32*(6), 1115–1122.

Wang, C. M., C. M. Wang, C. Y. Wang, and J. N. Reddy (2004). *Exact solutions for buckling of structural members*. Number 6 in CRC series in computational mechanics and applied analysis. Boca Raton, FL: CRC Press.

Wang, C.-Y. (1981a). Folding of Elastica-Similarity Solutions. *Journal of Applied Mechanics 48*(1), 199.

Wang, C. Y. (1981b, January). The Ridging of Heavy Elastica. *ZAMM - Journal of Applied Mathematics and Mechanics 61*(2), 125–126.

Wang, C. Y. (1984b, June). On Symmetric Buckling of a Finite Flat-Lying Heavy Sheet. *Journal of Applied Mechanics 51*(2), 278–282.

Wang, C. Y. (1986). A critical review of the heavy elastica. *International Journal of Mechanical Sciences 28*(8), 549–559.

Weiss, H. (2002). Dynamics of Geometrically Nonlinear Rods: I. Mechanical Models and Equations of Motion. *Nonlinear Dynamics 30*(4), 357–381.

Wicks, N., B. L. Wardle, and D. Pafitis (2008, March). Horizontal cylinder-in-cylinder buckling under compression and torsion: Review and application to composite drill pipe. *International Journal of Mechanical Sciences 50*(3), 538–549.

Wu, J. and H. Juvkam-Wold (1995a, mar). Coiled tubing buckling implication in drilling and completing horizontal wells. *SPE Drilling & Completion 10*(01), 16–21.

Wu, J. and H. C. Juvkam-Wold (1993). Helical Buckling of Pipes in Extended Reach and Horizontal Wells Part 2: Frictional Drag Analysis. *Journal of Energy Resources Technology 115*(3), 196.

Wu, J. and H. C. Juvkam-Wold (1995b). Buckling and Lockup of Tubulars in Inclined Wellbores. *117*(3), 208.

Wu, J. and H. C. Juvkam-Wold (1995c). The Effect of Wellbore Curvature on Tubular Buckling and Lockup. *Journal of Energy Resources Technology 117*(3), 214.

Wu, J., H. C. Juvkam-Wold, and R. Lu (1993). Helical Buckling of Pipes in Extended Reach and Horizontal Wells Part 1: Preventing Helical Buckling. *115*(3), 190.

Zhou, X., C. Majidi, and O. M. O'Reilly (2015, sep). Flexing into motion: A locomotion mechanism for soft robots. *International Journal of Non-linear Mechanics 74*, 7–17.

Appendix A

Constrained Buckling of Drillstrings

A.1 Introduction

The buckling of columns under compression, first investigated by Euler, is a well researched problem in structural and mechanical engineering (Timoshenko, 2009). However, the constrained buckling of a rod, a key problem in petroleum engineering, has not yet been fully explored, as other factors have to be taken into account when inserting a slender elastic rod, the so-called drillstring inside a rigid cylindrical conduit, the wellbore.

The main differences between the classical buckling of a column and the buckling of a drillstring are the constraint of the cylindrical conduit, the dominant role of gravity in the loading, and the effect of friction. These factors affect the force distribution within the drillstring depending on the geometry of the wellbore.

In a vertical, or steeply inclined well, the weight on the bit (i.e., the axial load transmitted by the drillstring to the bit) is the dominant factor that can cause buckling of the part of the drillstring under compression. In horizontal, or moderately inclined borehole, contact between the drillstring and the wellbore due to gravity leads to significant axial friction forces during insertion of the drillstring. Friction forces, which oppose the motion of the drillstring, cause a build-up of the axial force that could lead to buckling of the drillstring. In both cases, the rest of the length of the drillstring (i.e., away from the bit) is under tension and remains straight.

In early studies (Dawson, 1984; Paslay and Bogy, 1964) the effect of friction was neglected. Based on this assumption, and since the drillstring has a very large length/diameter ratio, the first buckling mode is expected to be sinusoidal. Past the critical load, or the sinusoidal buckling load, there is a transition of the configuration of the rod from a sinusoidal to a helical, or secondary buckling shape, which is observed due to the increasing contact force between the rod and the wellbore. This transition region is also called post-buckling region. Its understanding is crucial in oil-drilling operations (Cheatham, 1984; Sorenson and Cheatham, 1986) since any

potentiality of failure should be avoided.

Friction is the most important factor that affects the buckling response of drillstring in an inclined/horizontal well. When friction is under consideration (Gao and Miska, 2009c; Martinez et al., 2000; McCourt et al., 2004; Miller, 2014; Wu and Juvkam-Wold, 1993), past the first mode buckling load, the normal contact force between the rod and the wellbore increases significantly, causing a substantial increase of the friction force. Once secondary buckling is reached, limited additional insertion is feasible. When further insertion is impossible, a "sticking" behavior between the rod and the wellbore is recognized. This condition is the so-called 'lock-up failure' (He and Kyllingstad, 1995; Wicks et al., 2008; Wu and Juvkam-Wold, 1995b).

The Section starts with the description of the buckling response of a drillstring constrained by a vertical, or steeply inclined borehole. All stability factors are illustrated. Then we present the stability behavior of a drillstring constrained by a horizontal, or a moderately inclined borehole which is the main concern of the study. Special care is placed on the effect of friction.

A.1.1 Vertical boreholes

Since the 1950 pioneering work of Lubinski (1950) on the buckling of drillstrings, there have been various efforts aimed at assessing the critical weight on bit at which in-plane buckling takes place (Dawson, 1984; Gao and Miska, 2009b; Paslay and Bogy, 1964). The key question that arises when attempting to solve this problem is the determination of the characteristic length ℓ_* that scales the buckling wavelength.

In a vertical, or steeply inclined borehole, the drillstring does not contact the borehole prior to buckling, and the buckling problem is analogous to that of a beam buckling under its own weight. The characteristic length and the force scale are given by

$$\ell_*^v = \left(\frac{EI}{w}\right)^{1/3}, \quad f_*^v = \left(EIw^2\right)^{1/3} \tag{A.1}$$

where EI is the flexural rigidity of the bottom-hole assembly (BHA) and w is the effective weight/length of the BHA (after subtracting the weight of the displaced drilling fluid). This leads to the dimensionless quantities $\varsigma = s/\ell_*^v$ and $\mathcal{Q} = F/f_*^v$, where s is the arc-length of the drillstring and F is the axial force. Assigning the origin at the so-called neutral point at which the axial force vanishes and neglecting the frictional effect, the axial force $\mathcal{Q}$ is identical to the distance ς, or in other words the weight $W = ws$ is identical to the axial force F.

Considering that the drillstring is initially stress-free and increasing gradually the weight on the bit, Lubinski (1950) calculated the critical weight on bit W_c that causes buckling of the BHA. In particular, the drillstring first buckles in a planar deformation shape which is consistent with a first-order buckling mode with critical length $\varsigma_c = 1.94$. Lubinski (1950) also calculated the secondary critical length $\varsigma_c = 3.75$ for a second-order buckling mode.

Later, Lubinski and Althouse (1962) mentioned that the drillstring does not buckle into a higher-order planar buckling mode. Instead the onset of a spatial deformation is met. Lubinski and Althouse (1962) assumed that the drillstring is in continuous contact with the borehole and more particularly a helical deformation shape is predefined. In this paper, based on geometric considerations, a force-pitch relationship is derived for a weightless pipe as

$$F = \frac{8\pi^2 EI}{p^2} \tag{A.2}$$

where p is a constant pitch (i.e., distance between spirals) throughout and F is the applied axial compression force at the lower end of the tubing which is above the helical buckling load. Additionally, the same expression can be applied to non-weightless pipes, where the pitch is not constant but varies with the distance from the neutral point. Typically, in oil drilling operations, the distance of the lower end to the neutral point is very large (i.e., several thousands of feet) leading to a number of spirals around $100 \sim 200$ (Lubinski and Althouse, 1962).

Cheatham (1984) also investigated the case when the axial load starts decreasing from its helical buckling load for a weightless pipe. During unloading from (A.2), the pitch remains initially constant until the load reaches the value $4\pi^2 EI/p^2$. Any further decrease of the axial load is then accompanied by an increase of the pitch length and the pipe starts losing contact with the wall. This leads to the bounds of the force in terms of the pitch length $4\pi^2 EI/p^2 \leq F \leq 8\pi^2 EI/p^2$, which was later verified by Miska and Cunha (1995).

Recently, Huang et al. (2016) demonstrated a more comprehensive stability analysis of a drillstring constrained by a vertical wellbore. Huang et al. (2016) provides five distinct deformation shapes of the drillstring depending on the weight on the bit; (1) the straight configuration, (2) the planar shape with discrete contacts, (3) the spatial shape with discrete contacts, (4) the spatial shape with discrete contacts and a single continuous segment, and (5) the helical shape. These configurations are successively obtained as we gradually increase the weight on the bit. The sequence of the deformation shapes is shown in Figure A.1.

For the planar and spatial deformation shapes with discrete contacts, a finite number of distinct segments is obtained. Every configuration is then solved by the beam-column model (see Section A.2). The complete solution is finally obtained by applying the necessary continuity conditions at the common extremities. Nevertheless when a continuous segment is also present, its solution is obtained by the buckling differential equation (see Section A.2).

To clarify the procedure followed by Huang et al. (2016), we need to denote two distinct positions which are the extremities of the drillstring; (1) $\varsigma_o \leq 0$ is the length on the hook (i.e., upper end) and (2) $\varsigma_c \geq 0$ is the length on the bit (i.e., lower end), where the origin is assigned at the neutral point, as before (Lubinski, 1950). In this manner, the critical length on the bit ς_c ranges between two limits; (1) the lower limit $\varsigma_c^{(l)}$ is derived by assuming $\varsigma_o \to -\infty$ and (2) the upper limit $\varsigma_c^{(u)}$ is obtained by setting $\varsigma_o = 0$. These limits are identical to the lower and upper

bounds of the axial force $\varsigma_c^{(l)} \leq \mathcal{Q}_c \leq \varsigma_c^{(u)}$ for a frictionless vertical borehole. Depending on the weight on the bit, distinct deformation shapes are obtained with different associated bounds.

Let us now describe in more detail the buckling mode transition for a drillstring with weight constrained by a vertical borehole, as explained by Huang et al. (2016). Initially the drillstring is unstressed, as shown in Figure A.1(a). When the axial force reaches the value of $1.8546 \leq \mathcal{Q}_{2d}^v \leq 2.6012$, the drillstring buckles into a planar deformation shape which is in contact with the borehole. When the drillstring is weightless a first-order buckling mode is only present with a single discrete contact. This is not the case when the drillstring is non-weightless. As we increase the weight on the bit, the drillstring comes in contact with the borehole in more than one discrete contact implying that higher-order buckling modes can be gradually obtained. The first two-order buckling modes are illustrated in Figure A.1(b,c). If $3.9494 \leq \mathcal{Q}_{3d}^v \leq 4.3758$ is reached, the planar deformation shape becomes unstable and a spatial deformation shape appears, see Figure A.1(d). This configuration involves several discrete contact points with the borehole. As shown in Figure A.1(e), the discrete contact at the middle part of the drillstring is successively transformed to a line, or continuous segment when $5.2497 \leq \mathcal{Q}_l^v \leq 6.1864$ is achieved. If we further increase the weight on the bit, the axial load becomes $8.3954 \leq \mathcal{Q}_h^v \leq 9.2453$ and one pitch of helix is developed leading to a helical deformation shape, as indicated in Figure A.1(f). The analytical derivation can be found in Huang et al. (2016).

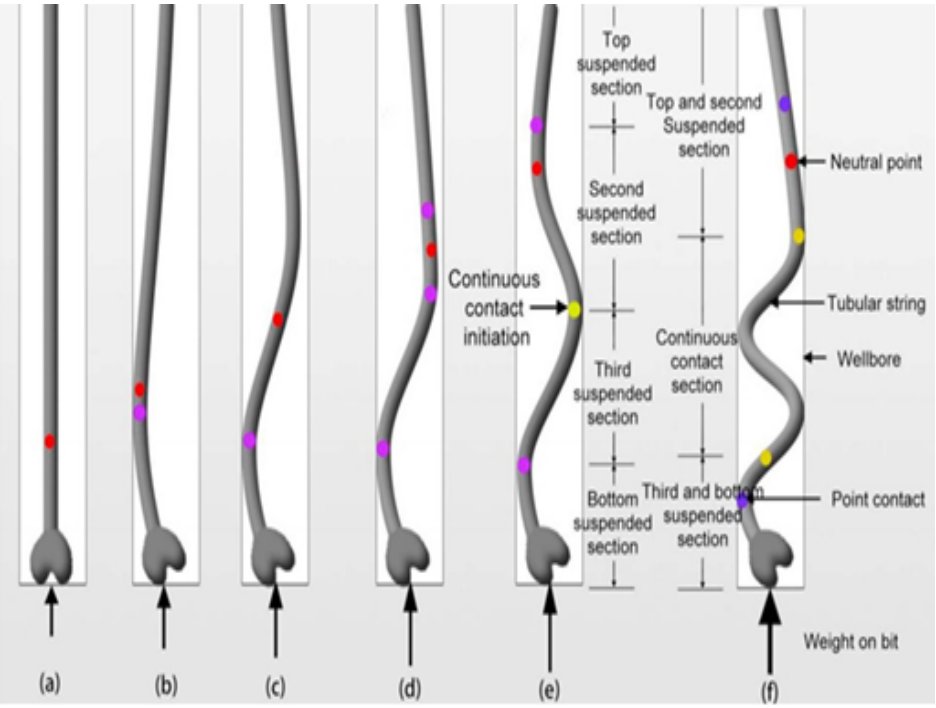

Figure A.1: Configurations of the drillstring constrained by a vertical well; (a) Initial straight configuration, (b) first-order planar shape, (c) second-order planar shape, (d) spatial shape, (e) spatial shape with a continuous segment, and (f) helical shape Huang et al. (2016).

Taking into account the buckling differential equation for a helical deformation shape, the contact force can be also computed. In particular, using (A.2) Mitchell (1988) derived the contact force between the drillstring and the vertical borehole for a helical shape when the frictional effect is omitted;

$$\mathcal{N} = \frac{\varrho Q_h^2}{4} \tag{A.3}$$

where $\mathcal{N} = N/w$ is the contact force per unit length of the drillstring and $\varrho = r/\ell_*^v$ is the dimensionless radial clearance.

Nevertheless if the friction is present, the axial force $\mathcal{Q}$ does not coincide with the distance ς. In this case, the differential equation of the axial force can be expressed as follows

$$\frac{d\mathcal{Q}}{d\varsigma} = 1 - \frac{\mu\varrho}{4}\mathcal{Q}^2 \tag{A.4}$$

where μ is the friction coefficient (Mitchell, 1986). Integrating (A.4) Mitchell (1986) calculated

an analytical expression of the axial force for a helical shape;

$$\mathcal{Q} = \frac{2}{\sqrt{\mu\varrho}} \left[\tanh\left(\frac{1}{2}\varsigma\sqrt{\mu\varrho} + c \right) \right] \tag{A.5}$$

where c is an integral constant. Recently, Huang et al. (2016) defined this constant c by assigning the position of the entry point of the line, or continuous contact ς_l, leading to the following analytical formula

$$Q(\varsigma) = \frac{2}{\sqrt{\mu\varrho}} \tanh\left(\frac{1}{2}\left(\varsigma - \varsigma_l\right)\sqrt{\mu\varrho} + \operatorname{arctanh}\left(\frac{1}{2}\varsigma_l\sqrt{\mu\varrho} \right) \right) \tag{A.6}$$

More details can be found in Huang et al. (2016).

A.1.2 Horizontal/Inclined boreholes

In a horizontal, or moderately inclined borehole, the characteristic length arises from consideration involving the transverse deflection of a horizontal beam under its own weight relative to the clearance between the drillstring and the borehole wall.

By assuming a sinusoidal deflection of the drillstring of specific mode, the critical buckling load for a drillstring constrained by a horizontal borehole subject to both compression and gravity is derived by Paslay and Bogy (1964);

$$F_s = \frac{EI\pi^2}{\lambda^2}\left(4 + \frac{\lambda^4}{4\pi^4}\frac{w}{EIr} \right) \tag{A.7}$$

where r is the clearance between the drillstring and the borehole and λ is the wavelength. The critical buckling load (A.7) is equivalent to the buckling load of a beam on an elastic foundation of stiffness $\beta = w/r$.

After reaching the critical buckling load and if we further increase the axial force, the sinusoidal deformation shape becomes unstable and a new configuration of helical shape appears. Chen et al. (1989) derived a formula similar to (A.7) for the initiation of secondary, or helical buckling in inclined/horizontal wellbores assuming constant axial load along the helical buckling process;

$$F_h = EI\frac{\pi^2}{\lambda^2}\left(4 + \frac{\lambda^4}{\pi^4}\frac{w}{2EIr} \right) \tag{A.8}$$

Adopting as length and force scales

$$\ell^h_* = \left(\frac{EIr}{w} \right)^{1/4}, \quad f^h_* = \left(\frac{EIw}{r} \right)^{1/2} \tag{A.9}$$

we get $\varsigma = s/\ell^h_*$, $\sigma = \lambda/\ell^h_*$ and $\mathcal{Q} = F/f^h_*$, where s is the arc-length of the drillstring, λ is the wavelength and F is the axial force. The dimensionless form of the sinusoidal and helical

buckling loads can be written as follows

$$\mathcal{Q}_s = \frac{\pi^2}{\sigma_s^2}\left(4 + \frac{\sigma_s^4}{4\pi^4}\right), \quad \mathcal{Q}_h = \frac{\pi^2}{\sigma_h^2}\left(4 + \frac{\sigma_h^4}{2\pi^4}\right)$$

For a sufficiently long cylinder (Wicks et al., 2008) the asymptotic length-independent loads are given by $\mathcal{Q}_s = 2$ and $\mathcal{Q}_h = 2\sqrt{2}$ with wavelengths $\sigma_s = 2\pi$ and $\sigma_h = 2\sqrt{2}\pi$ for sinusoidal and helical buckling, respectively. For inclined wells the same formula can be applied if we replace w by $w\cos\alpha$ with $\alpha = 0,\ \alpha = \pi/2$ for a horizontal and a vertical wellbore, respectively.

Several studies for the derivation of the sinusoidal and helical buckling loads can be found which are typically based on predefined displacement fields (Wicks et al., 2008; Gao and Huang, 2015; Cunha, 2004; Arslan et al., 2012). Even though the critical buckling loads are well-established, there is no complete understanding of the transition stage from the sinusoidal buckling load $\mathcal{Q}_s$ to the onset of secondary buckling $\mathcal{Q}_h$. Nevertheless several suggestions are available. According to (Wu et al., 1993) the axial force increases linearly from the sinusoidal buckling load $\mathcal{Q}_s = 2$ to the helical buckling load $\mathcal{Q}_h = 2\sqrt{2} - 1$. Miska et al. (1996) suggested a linear increase of the axial force for the entire loading process which leads to higher values of buckling load $\mathcal{Q}_s = 3.75$ and $\mathcal{Q}_h = 4\sqrt{2}$. Similar assumptions can be found in (Gao and Miska, 2009b; Wicks et al., 2008; Gao and Huang, 2015). The difference between these works clearly indicates that further examination is required.

Effect of boundary conditions

The effect of boundary conditions on the stability analysis of a drillstring constrained by a horizontal borehole is an important factor, as explained by (Mitchell, 1982; Wu and Juvkam-Wold, 1995a; Huang et al., 2015; Gao and Miska, 2009a). The main concern is the influence of the boundary conditions when a sinusoidal, or a helical deformation shape has been developed. In particular, it is assumed that the configuration of the drillstring is composed by two parts; (1) a transition region close to the extremities of the drillstring and (2) a fully-developed sinusoidal, or helical segment in the middle (Huang et al., 2015).

Mitchell (1982) was the first who attempted to involve this transition region in the buckling analysis of the drillstrings. In particular, Mitchell (1982) assumed that the transition region involves a single suspended segment which is solved by the beam-column method while the helical shape is derived by solving the buckling differential equation. A similar idea was also adopted by Sorenson and Cheatham (1986) and Mitchell (2005). From these studies it was found that the transition region is smaller than one pitch of helix. Hence, if a drillstring has at least 3.5 pitches of helix, the transition section can be considered to be negligible (Wu and Juvkam-Wold, 1995c). The derived lengths of the transition section for fixed and pinned ends based on different approaches are summarized in Huang et al. (2015).

Recently, Huang et al. (2015) classified the boundary conditions based on a virtual work approach. The first type of boundary conditions corresponds to zero virtual work of the bending moment and lateral force. In this case, the fully-developed helical deformation shape is unaffected by the boundary conditions if the drillstring is sufficiently long $L/\ell_*^h \geq 5\pi$, as explained in detail by Gao and Miska (2009a,b). This assumption is typically adopted in previous studies (Wicks et al., 2008; Gao and Miska, 2009a). Nevertheless in the second type of boundary conditions, the virtual work of the bending moment and lateral force is non-negligible and it can influence the helical configuration. More precisely, the stability of the helical buckling shape may change depending on the boundary conditions. For instance, the helical buckling direction can abruptly reverse whenever the virtual work of the bending moment and/or the lateral force goes across some critical values. These critical conditions are analytically derived by (Huang et al., 2015,?).

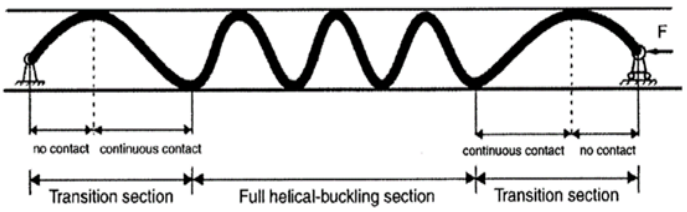

Figure A.2: Configuration of a weightless drillstring constrained in a straight borehole Huang et al. (2015)

Effect of friction

Most studies on the constrained stability analysis of a drillstring do not consider the frictional effect (Cunha, 2004; Gao and Huang, 2015). In fact, an energy approach is typically adopted which provides the critical and secondary buckling loads for the frictionless case (Wicks et al., 2008). Nevertheless friction alters the buckling response of a confined drillstring. In the presence of friction, the buckling load of a confined drillstring has been reported to be substantially higher than the frictionless case (Gao and Miska, 2009b,a; Jaculli et al., 2017). The unloading process also reveals a hysteresis behavior which cannot be predicted by the classical frictionless theory (McCann and Suryanarayana, 1994).

While the friction has been shown to enhance the critical buckling load, its effect can be also catastrophic. After initiation of the buckling, the friction can cause a diminishing transfer of the axial force which may subsequently lead to a lock-up failure. This phenomenon was first studied by Wu et al. (1993) who computed an analytical expression of the axial force in horizontal and inclined wells. Other studies are also available which additionally consider the effect of boundary

conditions (Gao and Miska, 2009b; Jaculli et al., 2017).

Recently, Su et al. (2013) studied the buckling behavior of a drillstring constrained by a horizontal borehole based on a dynamic perspective. Using the buckling differential equation and applying a Fourier series theory, a second-order ODE is deduced similar to a mass-spring system. Based on this approach, Su et al. (2013) investigated how friction affects the dynamics of the system and accordingly the buckling behavior of the confined rod. It was proved that the friction enhances the critical buckling loads, as expected. Interestingly, the initial conditions were found to be the key-factor in the buckling response of the confined drillstring when friction is non-negligible. Liu et al. (2015) extended this study in order to understand the additional effect of the axial vibration. Liu et al. (2015) found that this factor is essential, but its trend is very complex.

The Section starts with the demonstration of the frictional effect by performing a static analysis of a confined drillstring. The critical buckling loads and approximate analytical expressions of the axial force are provided, including the theoretical derivation of the lock-up failure. Some methods that improve the axial force transfer are also included. We then present a more realistic methodology to capture the effect of friction which involves the dynamics of the constrained drillstring. Special focus is placed on the effect of axial vibration which is commonly thought as a means to further improve the stability behavior of the drillstring.

Static analysis

The effect of friction in horizontal and low inclination wellbores has been shown recently to be a dominant factor on the stability behavior of drillstrings. On the one hand, friction force may be a stability factor since it usually delays the onset of the buckling. Nevertheless, after initiation of buckling the friction force can cause an abrupt reduction in axial force transfer and eventually "lock up", as explained by Kuru et al. (2000).

The fruitful effect of the friction in the critical buckling load was first confirmed by experimental results (McCann and Suryanarayana, 1994). Based on an energy approach, Gao and Miska (2009b) then computed the sinusoidal and helical buckling loads in a horizontal borehole by applying the Coulomb's law of sliding friction;

$$\mathcal{Q}_s^f = \mathcal{Q}_s \left[1 + 1.233\mu^{2/3}\right] \tag{A.10}$$

$$\mathcal{Q}_h^f = \sqrt{2}\mathcal{Q}_s \left(1 + \frac{\left(30 + 7\pi^2\right)}{30\pi}\mu\right) \tag{A.11}$$

where the dimensionless axial force is denoted as $\mathcal{Q}^f$ to indicate the frictional effect. These theoretical results are found to be consistent with experimental results.

Even though the critical and secondary buckling loads can be easily computed by an energy

approach, the derivation of the axial force distribution function requires a different methodology. The understanding of the axial force transfer is crucial since a lock-up failure can occur under the action of friction. To investigate the axial force transfer in the presence of the friction, a new length scale is adopted, the so-called lock-up length;

$$\ell_*^f = \frac{1}{\mu}\left(\frac{EI}{wr}\right)^{1/2} \tag{A.12}$$

which leads to $\varsigma^f = s/\ell_*^f$ while the force scale f_*^h (A.9) remains unchanged.

Wu et al. (1993) was the first who investigated the axial force transmission in horizontal and inclined wells under the action of the friction force. Wu et al. (1993) distinguished the frictional drag for an unbuckled and a helically buckled drill-pipe, ignoring the first critical buckling. Based on Coulomb friction law Wu et al. (1993) derived the following differential equation of the axial load

$$\frac{dQ^f}{d\varsigma^f} = (\cos\alpha + \mathcal{N}) - \sin\alpha/\mu \tag{A.13}$$

where μ is the friction coefficient, $\mathcal{N} = N/w$ is the contact force per unit length for helically buckled weightless drillpipes with $\mathcal{N} \approx \mathcal{Q}_h^2 \cos\alpha/4$. Based on Wu et al. (1993)'s approach the axial force distribution function in a horizontal borehole can be written as follows

$$\mathcal{Q}_h^f(\varsigma) = 2\tan(c - \varsigma) \tag{A.14}$$

where c is an integral constant. A similar expression can be also derived in an inclined wellbore. More details can be found in Wu et al. (1993). Quite recently, (Gao and Miska, 2009b) also calculated the axial force function in a horizontal borehole for sinusoidal and helical buckling, respectively;

$$\mathcal{Q}_s^f(\varsigma) = 2\left[-a_3 + \frac{1}{a_2}\tan\left(-\frac{a_1 a_2}{2}\varsigma + c\right)\right], \quad \mathcal{Q}_h^f(\varsigma) = \mathcal{Q}_h \frac{1}{1 - \mathcal{Q}_h\varsigma} \tag{A.15}$$

where $a_1 = 0.79 + 0.043\mu^{2/3}$, $a_2 = 0.446 - 0.17\mu^{2/3}$, $a_3 = 1.16 - 0.093\mu^{2/3}$ and c is an integral constant.

Taking into account the differential equation of the axial load (A.13) and assuming that a cylinder is pushed into an already existing horizontal wellbore (i.e., with no load on the bit), the total lock-up failure length can be approximated. In this particular case, the lock-up failure length is defined as the maximum distance that the drill-pipe can be pushed inside the wellbore due to the frictional effect (Wicks et al., 2008). Under these conditions, the total lock-up failure length is approximately $\varsigma_L = 3\sqrt{2}\ell_f$ in a horizontal borehole.

There is a variety of methods that can improve the transfer of axial force and consequently

eliminate the lock-up failure. For instance, the rotation of the drillstring can modify the direction of the friction force, leading to a substantial reduction of the axial friction force. Nevertheless the rotation can also affect the critical buckling loads, as explained by Menand et al. (2008). In particular, Menand et al. (2008) showed that rotation can remarkably reduce the helical buckling load when compared to a non-rotating case under the presence of friction, while Gao and Miska (2010) deduced that the critical buckling load is unaffected by the rotation in the frictionless case. Recently, other techniques are also adopted which can minimize the unfavorable effect of friction on the transmission of axial force, namely the hydraulic vibration and the use of connectors (Huang et al., 2017; Huang and Gao, 2014; Gao et al., 2011). More details can be found in (Gao and Huang, 2015).

Dynamic analysis

Let us now investigate the buckling behavior of a drillstring constrained by a horizontal borehole including inertia effects. More precisely, we assume that the drillstring is in continuous contact with the horizontal borehole. Hence, the governing equation of the drillstring is based on the buckling differential equation (see Section A.2) which can be approximated as follows

$$EIr\frac{\partial^4\theta}{\partial s^4} + rF\frac{\partial^2\theta}{\partial s^2} + w\theta + mr\frac{\partial^2\theta}{\partial t^2} + F_f\text{sign}(\dot{\theta}) = 0 \tag{A.16}$$

neglecting higher order terms and assuming a sliding friction force per unit length $F_f = \mu N$. Taking into account the length and force scales (A.9) and a time scale $t_*^h = (r/g)^{1/2}$, we get the dimensionless quantities $\varsigma = s/\ell_*^h$, $\tau = t/t_*^h$, $\mathcal{Q} = F/f_*^h$ and $\mathcal{F}_f = F_f/\left(f_*^h/\ell_*^h\right)$. In this manner, (A.16) becomes

$$\frac{\partial^4\vartheta}{\partial\varsigma^4} + \mathcal{Q}\frac{\partial^2\vartheta}{\partial\varsigma^2} + \frac{\partial^2\vartheta}{\partial\tau^2} + \vartheta + \mathcal{F}_f\text{sign}(\dot{\vartheta}) = 0 \tag{A.17}$$

Let us now apply a Fourier series expansion on the angular displacement $\vartheta(\varsigma,\tau)$ and the sign function with respect to the angular term $\dot{\vartheta}(\varsigma,\tau)$

$$\vartheta(\varsigma,\tau) = \sum_{i=1}^{\infty} A_i(\tau)\sin\omega_i\varsigma, \quad \text{sign}\left(\dot{\vartheta}\right) = \sum_{i=1}^{\infty} B_i(\tau)\sin\omega_i\varsigma \tag{A.18}$$

where A_i, B_i are the time dependent coefficients for the i-mode with frequency $\omega_i = i\pi/\varsigma_L$. Assuming that one mode k is dominant, the coefficient B_k can be approximated as follows

$$B_k \approx \text{sign}\left(\dot{A}_k\right)\frac{2}{\varsigma_L}\int_0^{\varsigma_L}|\sin\omega_k\varsigma|\,d\varsigma = \frac{4}{\pi}\text{sign}\left(\dot{A}_k\right) \tag{A.19}$$

Substituting (A.18) and (A.19) into (A.17), we get the second-order ODE

$$\ddot{A}_k + \omega_k^2 \left[\omega_k^2 + \omega_k^{-2} - \mathcal{Q}\right] A_k + \frac{4\mathcal{F}_f}{\pi}\text{sign}\left(\dot{A}_k\right) = 0 \Rightarrow$$
$$\ddot{A}_k + \mathcal{K}_k A_k + \tilde{\mathcal{F}}_f \text{sign}\left(\dot{A}_k\right) = 0 \tag{A.20}$$

where $\tilde{\mathcal{F}}_f$ is the "effective" value of the sliding friction force per unit length and $\mathcal{K}_k$ describes the stiffness of the system and is a linear function of the axial force $\mathcal{Q}$.

Let us first investigate the frictionless case $\mathcal{F}_f = 0$. In this case, three distinct cases are possible; (1) $\mathcal{K}_k > 0$, (2) $\mathcal{K}_k = 0$ and (3) $\mathcal{K}_k < 0$. The first and third cases lead to periodic and hyperbolic functions, respectively. This implies that the first case is only stable. In the special case of $\mathcal{K}_k = 0$, the onset of instability is obtained with critical buckling load $\mathcal{Q}_c = \omega_k^2 + \omega_k^{-2}$. The critical load is minimized by setting $d\mathcal{Q}_c/d\omega_k = 0$. This leads to $\mathcal{Q}_c = 2$ which coincides with the critical, or sinusoidal buckling load $\mathcal{Q}_s$, as explained in Section A.1.2.

When the friction is present, the response of the drillstring does not only depend on the sign of $\mathcal{K}_k$ but also the initial conditions $A_k, \dot{A}_k$. In particular, the initial conditions define the length of the stationarity line and accordingly the area of the stable zone. The stationarity line represents the so-called "sticking condition" which leads to a dissipation of the system.

Let us first demonstrate the special case of $\mathcal{K}_k = 0$. As $\mathcal{K}_k \to 0$ any solution tends to a stationary line independently of the initial perturbation A_k. This indicates that the case of $\mathcal{K}_k = 0$ does not provide the onset of instability in the frictional case. Instead, the onset of instability occurs for $\mathcal{K}_k < 0$. Decreasing $\mathcal{K}_k$ the axial $\mathcal{Q}$ accordingly increases and becomes obviously higher than $\mathcal{Q}_s$. Even if $\mathcal{K}_k < 0$, a stable zone can be also derived whose size depends on the initial conditions. Hence, the onset of instability is not uniquely derived but it clearly depends on the initial perturbation (Su et al., 2013). In addition, the analysis shows that friction can strongly affect the number of the dominant buckling mode. The higher the friction force $\mathcal{F}_f$ is the higher the buckling mode is obtained.

Recently, Liu et al. (2015) extended the above analysis in order to additionally investigate the effect of the axial vibration in the stability behavior of the confined rod as it is said to be capable of delaying buckling and lock-up in the oil field. To incorporate the axial vibration into the above derivation, an axial vibration force $d\mathcal{Q}\sin\tau_a$ is included with $\tau_a = \omega\tau$. The frequency ω is chosen in such a way that $\sqrt{E/\rho} \geq \omega L/2\pi$ (i.e., the period of the vibration force is much larger than the time for an axial wave to travel through the rod Liu et al. (2015)). The axial vibration force is added into (A.17), leading to the new form

$$\frac{\partial^4\vartheta}{\partial\varsigma^4} + \left[\mathcal{Q} + d\mathcal{Q}\sin\tau_a\right]\frac{\partial^2\vartheta}{\partial\varsigma^2} + \frac{\partial^2\vartheta}{\partial\tau_a^2} + \vartheta + \bar{\mathcal{F}}_f \text{sign}(\dot{\vartheta}) = 0 \tag{A.21}$$

with $\bar{\mathcal{F}}_f = \mu_\theta\left(\varsigma, \tau_a\right) N/\left(f_*^h/\ell_*^h\right)$ a more realistic representation of the sliding friction force per

unit length. $\mu_\theta(\varsigma, \tau_a)$ is the transverse friction coefficient which depends on the constant friction coefficient μ and the ratio of shear to the axial velocity components. This is a reasonable representation of the friction force when we only seek the critical buckling loads, because at the instant of buckling initiation the shear velocity approaches infinity and the shear friction becomes accordingly dominant, as explained by (Gao and Miska, 2009b). Its derivation is shown in Section A.2. In this study, μ_θ is assumed to be constant and a simple approximation is contained in (Liu et al., 2015).

After applying a Fourier series expansion (A.18-A.19), (A.21) becomes

$$\ddot{A}_k + \left[\bar{\mathcal{K}}_k - \bar{\mathcal{P}}_k \sin\tau_a\right] A_k + \widetilde{\mathcal{F}}_f \text{sign}\left(\dot{A}_k\right) = 0 \tag{A.22}$$

where $\bar{\omega}_k = \omega_k/\omega$, leading to the new stiffness $\bar{\mathcal{K}}_k = \bar{\omega}_k^2\left[\bar{\omega}_k^2 + \bar{\omega}_k^{-2} - \mathcal{Q}\right]$, $\bar{\mathcal{P}}_k = \bar{\omega}_k^2 d\mathcal{Q}$ and $\widetilde{\mathcal{F}}_f = 4\bar{\mathcal{F}}_f/\pi$.

In the case of a frictionless system with $d\mathcal{Q} \neq 0$, (A.22) is the well-known Mathieu's equation for the k-mode. Its stability depends on the two parameters $\bar{\mathcal{K}}_k$ and $\bar{\mathcal{P}}_k$ and not on the initial conditions. We cannot also assume that a dominant mode is present in this case. Hence, the stability analysis is obviously a more difficult task herein as the derivation of the stable modes requires the investigation of several combinations of $\bar{\mathcal{K}}_k$ and $\bar{\mathcal{P}}_k$.

From the stability analysis remarkable conclusions can be withdrawn. One main result is that the negative value of the stiffness $\bar{\mathcal{K}}_k < 0$ implies instability of the system, as above. The stability analysis also shows that by increasing any of the quantities ω, or $\mathcal{Q}$, or $d\mathcal{Q}$, the system may become unstable as some of the modes fall outside the stable region. More precisely, if we increase the amplitude of the vibrational force $d\mathcal{Q}$, the stable region shrinks, especially when $d\mathcal{Q}$ reaches the value of $0.5\mathcal{Q}_c$. On the other hand, the effect of the frequency ω is complex. In particular, for a given value of $d\mathcal{Q}$ the range of frequencies for which the rod is stable is unclear. For instance, there are some frequencies for which the drillstring is stable even for large axial forces $\mathcal{Q}$ while for other frequencies the instability may initiate for very low values of $\mathcal{Q}$.

In the frictional case $\bar{\mathcal{F}}_f \neq 0$, the stability behavior of k-mode of the confined drillstring is controlled by four parameters, namely the coefficients $\bar{\mathcal{K}}_k$, $\bar{\mathcal{P}}_k$, $\bar{\mathcal{F}}_f$ and the initial velocity $\dot{A}_k(0)$. Let us first investigate the effect of the friction $\bar{\mathcal{F}}_f$. For low values of friction the buckling response is close to the frictionless case while the stability is enhanced when we increase the value of $\bar{\mathcal{F}}_f$. This also implies that the negative value of $\bar{\mathcal{K}}_k$ does not imply instability, as above. Keeping the value of friction constant, the stability behavior of the confined drillstring is affected by the quantities $d\mathcal{Q}$,ω in a similar manner to the frictionless case. Surprisingly, in the frictional case the stability region remains unchanged if we increase the axial force $\mathcal{Q}$ while keeping constant the value of friction $\bar{\mathcal{F}}_f$. On the other hand, the effect of the initial velocity $\dot{A}_k(0)$ is dominant. In particular, as we decrease the initial velocity $\dot{A}_k(0)$ the stable domain is remarkably enhanced even for negative values of $\bar{\mathcal{K}}_k$.

A.2 Drilling equations

The stability problem of drillstrings constrained by a straight borehole is analyzed in this Section. Based on the contact conditions with the borehole two distinct models can be adopted; (1) the beam-column model and (2) the so-called buckling differential equation. The two-dimensional beam-column model is applied when there is no contact with the wellbore, or only a few discrete contact points are present. Nevertheless when a continuous contact is present, it is preferable to assume a cylindrical coordinate system, meaning that the lateral displacements can be expressed as $u_2 = r\cos\theta$ and $u_3 = r\sin\theta$, where θ is the angular displacement and r is the known clearance of the borehole. In this particular case, the governing equation of the drillstring becomes one-dimensional (it is only a function of θ). These models are analyzed in short in the following Sections.

A.2.1 Beam-column model

The clearance of the wellbore is much smaller than the total length of the tubular string. Hence the linear elastic theory assuming small displacements can be applied in this case. In particular, the governing equation of an inclined straight wellbore is derived by adopting the beam-column model (Timoshenko, 2009; Gao and Huang, 2015);

$$\frac{d^4u_2}{ds^4} + \frac{d}{dS}\left(\frac{F_1 - ws\sin\alpha}{EI}\frac{du_2}{ds}\right) - \frac{w\cos\alpha}{EI} = 0$$

$$\frac{d^4u_3}{ds^4} + \frac{d}{ds}\left(\frac{F_1 - ws\sin\alpha}{EI}\frac{du_3}{ds}\right) = 0$$

where u_2 and u_3 are the lateral displacements along Y and Z coordinates, respectively; s is the axial distance; F_1 is the axial compressive force at the bottom end; EI is the bending stiffness; w is the weight per unit length of the tubular string; $\alpha = 0$ for a horizontal well and $\alpha = \pi/2$ for a vertical well.

A.2.2 Buckling differential equation

When the drillstring is in continuous contact with the wellbore, it is more convenient to express the governing equations of the drillstring with respect to the angular displacement θ rather than the two lateral displacements $u_{2,}u_3$ as a constant clearance r is present. Based on this simplification, two distinct approaches can be adopted to derive the buckling differential equation (Gao and Huang, 2015); (1) the energy principle (Gao and Miska, 2009a) and (2) the general theory of elastic rods (Gao and Miska, 2010; Mitchell, 1988). In the former case, the virtual works of shear force and bending moment at the extremities of the drillstring are neglected while in the latter case the higher-order terms of the curvature and twist are considered to be

negligible. Both methods lead to the same buckling differential equation.

In the next Section, we demostrate the static and dynamic analysis of the drillstring by applying the general theory of elastic rods (Gao and Miska, 2010). An improved model that includes higher-order terms can be found in (Huang et al., 2015).

Static analysis

Let us suppose that the reference configuration $\{\mathbf{e}_1, \mathbf{e}_2, \mathbf{e}_3\}$, where $\mathbf{e}_1 = \{1, 0, 0\}$, $\mathbf{e}_2 = \{0, 1, 0\}$ and $\mathbf{e}_3 = \{0, 0, 1\}$. In the reference configuration the rod is located at $(s, 0, -r)$, where s is the arclength and r is the uniform clearance of the wellbore. If we denote $\theta(s)$ the angular displacement and $u_1(s)$ the axial linear displacement at a point s, the position vector can be written as follows

$$\mathbf{r}(s,t) = (s + u_1)\,\mathbf{e}_1 + r\sin\theta\mathbf{e}_2 - r\cos\theta\mathbf{e}_3 \tag{A.23}$$

which implies that the continuous contact with the wellbore $u_2 = r\sin\theta$ and $u_3 = -r\cos\theta$.

The spatial derivative of (A.23) gives the tangential direction of the pipe's axis is

$$\boldsymbol{\tau}(s) = \frac{\partial \mathbf{r}}{\partial s} = \mathbf{e}_1 + r\frac{\partial \theta}{\partial s}\mathbf{e}_\theta \tag{A.24}$$

where $\mathbf{e}_\theta = \cos\theta\mathbf{e}_2 + \sin\theta\mathbf{e}_3$ while the term $\partial u_s/\partial s \ll 1$ and it is neglected. The unit vectors in the normal direction $\mathbf{n}$ and binormal direction $\mathbf{b}$ are

$$\kappa\mathbf{n} = \frac{\partial \boldsymbol{\tau}}{\partial s} = \kappa_r\mathbf{e}_r + \kappa_\theta\mathbf{e}_\theta \tag{A.25}$$

and

$$\kappa\mathbf{b} = \boldsymbol{\tau} \times k\mathbf{n} = -\kappa_\theta\mathbf{e}_\mathrm{r} + \kappa_r\mathbf{e}_\theta \tag{A.26}$$

where $\mathbf{e}_r = \sin\theta\mathbf{e}_2 - \cos\theta\mathbf{e}_3$, $\kappa = \sqrt{\kappa_r^2 + \kappa_\theta^2}$ is the curvature of drillpipe and $\kappa_r = -r\left(\partial\theta/\partial s\right)^2$ and $\kappa_\theta = r\partial^2\theta/\partial s^2$ are the components of $\kappa\mathbf{n}$ on $\mathbf{e}_r$ and $\mathbf{e}_\theta$ axes, respectively.

The total displacement can be written as $u_1(s) = u_a(s) + u_b(s)$, where $u_a(s)$ is the axial displacement and $u_b(s)$ is the axial displacement due to the lateral buckling. Considering that the total change of length can be approximated as follows

$$\Delta L \approx -\frac{1}{2}\int_0^L \left[\left(\frac{\partial r_y(s,t)}{\partial s}\right)^2 + \left(\frac{\partial r_z(s,t)}{\partial s}\right)^2\right] ds = \frac{1}{2}r^2\int_0^1 \left(\frac{\partial\theta}{\partial\eta}\right)^2 d\eta$$

the displacement u_b of a material element ds is similarly derived

$$u_b(s) = -\frac{1}{2}r^2\int_0^s \left(\frac{\partial\theta}{\partial\eta}\right)^2 d\eta \tag{A.27}$$

The distributed pressure consists of the weight $\mathbf{W}$ and the normal contact pressure $\mathbf{N}$ can be expressed as follows

$$\mathbf{W} = -mg\cos\alpha\mathbf{k}ds = w\cos\alpha\left(\cos\theta\mathbf{e}_r - \sin\theta\mathbf{e}_\theta\right)ds \tag{A.28}$$

$$\mathbf{N} = -N\mathbf{e}_r ds \tag{A.29}$$

Using (A.28-A.29) the total body force becomes

$$\mathbf{f} = \left(mg\cos\alpha\cos\theta - N\right)\mathbf{e}_r - mg\cos\alpha\sin\theta\mathbf{e}_\theta \tag{A.30}$$

where $\alpha = 0$ for a horizontal well and $\alpha = \pi/2$ for a vertical well. In addition the forces $\mathbf{F}$, the moments $\mathbf{M}$ and their spatial derivatives yield to the following expressions

$$\mathbf{F} = F_1\mathbf{e}_1 + F_r\mathbf{e}_r + F_\theta\mathbf{e}_\theta \tag{A.31}$$

$$\mathbf{M} = M_r\mathbf{e}_r + M_\theta\mathbf{e}_\theta \tag{A.32}$$

$$\frac{\partial\mathbf{F}}{\partial s} = \frac{\partial F_1}{\partial s}\mathbf{e}_1 + \left(\frac{\partial F_r}{\partial s} - F_\theta\frac{\partial\theta}{\partial s}\right)\mathbf{e}_r + \left(\frac{\partial F_\theta}{\partial s} + F_r\frac{\partial\theta}{\partial s}\right)\mathbf{e}_\theta \tag{A.33}$$

$$\frac{\partial\mathbf{M}}{\partial s} = \left(\frac{\partial M_r}{\partial s} - M_\theta\frac{\partial\theta}{\partial s}\right)\mathbf{e}_r + \left(\frac{\partial M_\theta}{\partial s} + M_r\frac{\partial\theta}{\partial s}\right)\mathbf{e}_\theta \tag{A.34}$$

The consistutive relations between the forces (moments) with the displacements (angular displacements) are required. In particular, Hooke's law is adopted to derive the relationship between the axial deformation and the axial compressive force F_1;

$$F_1(s) = -EA\frac{\partial u_a}{\partial s} = -EA\frac{\partial u_1}{\partial s} - \frac{1}{2}EAr^2\left(\frac{\partial\theta}{\partial s}\right)^2 \tag{A.35}$$

where E is the Young's modulus and A is the cross-sectional area. Similarly, we assume that the bending moment $M(s,t)$ is proportional to the curvature $\kappa\mathbf{b}$;

$$\mathbf{M}(s,t) = -EI\kappa\mathbf{b} \tag{A.36}$$

where EI is the bending stiffness.

The conservation of linear and angular momentum is then obtained;

$$\frac{\partial\mathbf{F}}{\partial s} - \mathbf{f} = 0 \tag{A.37}$$

$$\frac{\partial\mathbf{M}}{\partial s} + \boldsymbol{\tau}\times\mathbf{F} = 0 \tag{A.38}$$

which can be decomposed along the three orthogonal directions $\boldsymbol{\tau}, \mathbf{e}_{\mathrm{r}}$ and $\mathbf{e}_\theta$ respectively;

$$\frac{\partial F_1}{\partial s} = 0 \tag{A.39}$$

$$\frac{\partial F_r}{\partial s} - F_\theta \frac{\partial \theta}{\partial s} + N - w\cos\alpha\cos\theta = 0 \tag{A.40}$$

$$\frac{\partial F_\theta}{\partial s} + F_r \frac{\partial \theta}{\partial s} + w\cos\alpha\sin\theta = 0 \tag{A.41}$$

$$\frac{\partial M_r}{\partial s} - M_\theta \frac{\partial \theta}{\partial s} - F_\theta + F_s r \frac{\partial \theta}{\partial s} = 0 \tag{A.42}$$

$$\frac{\partial M_\theta}{\partial s} + M_r \frac{\partial \theta}{\partial s} + F_r = 0 \tag{A.43}$$

where (A.39) indicates that F_1 is uniform and

$$M_\theta = EIr\left(\frac{\partial \theta}{\partial s}\right)^2 \tag{A.44}$$

$$M_r = EIr\frac{\partial^2 \theta}{\partial s^2} \tag{A.45}$$

Substituting (A.44-A.45) into (A.42) and (A.43), we get

$$F_\theta = EIr\left[\frac{\partial^3 \theta}{\partial s^3} - \left(\frac{\partial \theta}{\partial s}\right)^3\right] + F_1 r\frac{\partial \theta}{\partial s} \tag{A.46}$$

$$F_r = -3EIr\frac{\partial \theta}{\partial s}\frac{\partial^2 \theta}{\partial s^2} \tag{A.47}$$

(A.46) and (A.47) are then substituted into (A.40) and (A.41), leading to the nonlinear buckling equations

$$\begin{aligned} N = -EIr&\left[\left(\frac{\partial \theta}{\partial s}\right)^4 - 3\left(\frac{\partial^2 \theta}{\partial s^2}\right)^2 - 4\frac{\partial \theta}{\partial s}\frac{\partial^3 \theta}{\partial s^3}\right] \\ &+ F_1 r\left(\frac{\partial \theta}{\partial s}\right)^2 + w\cos\alpha\cos\theta \end{aligned} \tag{A.48}$$

and

$$EIr\left[\frac{\partial^4 \theta}{\partial s^4} - 6\left(\frac{\partial \theta}{\partial s}\right)^2\frac{\partial^2 \theta}{\partial s^2}\right] + rF_1\frac{\partial^2 \theta}{\partial s^2} + w\cos\alpha\sin\theta = 0 \tag{A.49}$$

Dynamic analysis

If we extend the static analysis described in the previous Section, we need to modify the conservation of linear and angular momentum to include inertia effects

$$\frac{\partial \mathbf{F}}{\partial s} - \mathbf{f} + m\frac{\partial \mathbf{v}}{\partial t} = 0 \tag{A.50}$$

$$\frac{\partial \mathbf{M}}{\partial s} + \boldsymbol{\tau} \times \mathbf{F} + I\frac{\partial \boldsymbol{\omega}}{\partial t} = 0 \tag{A.51}$$

where $\mathbf{v}(x,t)$ is the linear velocity

$$\mathbf{v}(x,t) = \frac{\partial \mathbf{r}}{\partial t} = \frac{\partial u_1}{\partial t}\mathbf{e}_1 + r\frac{\partial \theta}{\partial t}\mathbf{q} \tag{A.52}$$

and $\boldsymbol{\omega}(x,t)$ involves two terms; (1) the angular velocity of the element rotating about the centerline of the drillstring ($\omega\boldsymbol{\tau}$) with ω the uniform angular velocity of the rod and (2) the angular velocity produced by the change in the direction of the centerline ($\partial\boldsymbol{\tau}/\partial x$);

$$\boldsymbol{\omega}(s,t) = \omega\boldsymbol{\tau} + \frac{\partial \boldsymbol{\tau}}{\partial t} = \omega\mathbf{e}_1 + \omega_r\mathbf{e}_r + \left(\omega r\frac{\partial \theta}{\partial s} + \omega_\theta\right)\mathbf{e}_\theta \tag{A.53}$$

where $\omega_r = -r\left(\partial\theta/\partial s\right)\left(\partial\theta/\partial t\right)$ and $\omega_\theta = r\partial^2\theta/\partial s\partial t$ whose absolute values are much smaller than ω.

The nonlinear buckling equations (A.48-A.54) are then modified, leading to the dynamic buckling equations;

$$+EA\frac{\partial u_1}{\partial s} + EAr^2\frac{\partial^2\theta}{\partial s^2}\frac{\partial\theta}{\partial s} - m\frac{\partial^2 u_1}{\partial t^2} = 0 \tag{A.54}$$

$$\begin{aligned} N = -EIr\left[\left(\frac{\partial\theta}{\partial s}\right)^4 - 3\left(\frac{\partial^2\theta}{\partial s^2}\right)^2 - 4\frac{\partial\theta}{\partial s}\frac{\partial^3\theta}{\partial s^3}\right] + F_1 r\left(\frac{\partial\theta}{\partial s}\right)^2 \\ + I\omega\left(\frac{\partial\omega_\theta}{\partial s} + \omega_r\frac{\partial\theta}{\partial s}\right) + w\cos\alpha\cos\theta + mr\left(\frac{\partial\theta}{\partial t}\right)^2 \end{aligned} \tag{A.55}$$

and

$$\begin{aligned} EIr\left[\frac{\partial^4\theta}{\partial s^4} - 6\left(\frac{\partial\theta}{\partial s}\right)^2\frac{\partial^2\theta}{\partial s^2}\right] + r\frac{\partial}{\partial s}\left(F_1\frac{\partial\theta}{\partial s}\right) \\ +I\omega\left(\frac{\partial\omega_r}{\partial s} - \omega_\theta\frac{\partial\theta}{\partial s}\right) + w\cos\alpha\sin\theta + mr\frac{\partial^2\theta}{\partial t^2} = 0 \end{aligned} \tag{A.56}$$

Friction

Based on (Gao and Miska, 2009b,a), the friction force can be also included in the above derivation. The friction force involves two components which are given by

$$\mathbf{F}_f(s,t) = F_{f_1}(s,t)\mathbf{e}_1 + F_{f_\theta}(s,t)\mathbf{e}_\theta \tag{A.57}$$

where $F_{f_1}(s,t)$, $F_{f_\theta}(s,t)$ are the axial and lateral components, respectively;

$$F_{f_1}(s,t) = -\text{sign}(\frac{\partial u_1}{\partial t})\mu_1 N ds, \quad F_{f_\theta}(s,t) = -\text{sign}(\frac{\partial \theta}{\partial t})\mu_\theta N ds \tag{A.58}$$

and μ_1, μ_θ are the corresponding friction coefficients on the axial and lateral directions. As shown in (Gao and Miska, 2009b), the friction coefficients μ_1, μ_θ can be derived by introducing a constant friction coefficient μ and taking into account that the ratio of μ_1 and μ_θ is proportional to the ratio of the corresponding speeds;

$$\mu_1 = \mu\frac{|v_1|}{\sqrt{v_1^2 + v_\theta^2}}, \quad \mu_\theta = \mu\frac{|v_\theta|}{\sqrt{v_1^2 + v_\theta^2}} \tag{A.59}$$

where $v_1 = \partial u_1/\partial t$ and $v_\theta = r\partial\theta/\partial t$. Substituting (A.59) and (A.58) into (A.57), the friction force can be written as follows

$$\mathbf{F}_f(s,t) = -\frac{\mu N ds}{\sqrt{\left(\frac{\partial u_1}{\partial t}\right)^2 + r^2\left(\frac{\partial \theta}{\partial t}\right)^2}}\left[\text{sign}(\frac{\partial u_1}{\partial t})\left|\frac{\partial u_1}{\partial t}\right|\mathbf{e}_1 + \text{sign}(\frac{\partial \theta}{\partial t})\left|r\frac{\partial \theta}{\partial t}\right|\mathbf{e}_\theta\right] \tag{A.60}$$

Based on (A.60), the final form of the dynamic buckling equations is derived;

$$+EA\frac{\partial u_1}{\partial s} + EAr^2\frac{\partial^2\theta}{\partial s^2}\frac{\partial\theta}{\partial s} - m\frac{\partial^2 u_1}{\partial t^2} - \frac{\mu\text{sign}(\frac{\partial u_1}{\partial t})\left|\frac{\partial u_1}{\partial t}\right|}{\sqrt{\left(\frac{\partial u_1}{\partial t}\right)^2 + r^2\left(\frac{\partial \theta}{\partial t}\right)^2}}N = 0 \tag{A.61}$$

$$\begin{aligned} &EIr\left[\frac{\partial^4\theta}{\partial s^4} - 6\left(\frac{\partial\theta}{\partial s}\right)^2\frac{\partial^2\theta}{\partial s^2}\right] + r\frac{\partial}{\partial s}\left(F_1\frac{\partial\theta}{\partial s}\right) \\ &+I\omega\left(\frac{\partial\omega_r}{\partial s} - \omega_\theta\frac{\partial\theta}{\partial s}\right) + w\cos\alpha\sin\theta + mr\frac{\partial^2\theta}{\partial t^2} - \frac{\mu\text{sign}(\frac{\partial\theta}{\partial t})\left|r\frac{\partial\theta}{\partial t}\right|}{\sqrt{\left(\frac{\partial u_1}{\partial t}\right)^2 + r^2\left(\frac{\partial\theta}{\partial t}\right)^2}}N = 0 \end{aligned} \tag{A.62}$$

$$N = -EIr\left[\left(\frac{\partial\theta}{\partial s}\right)^4 - 3\left(\frac{\partial^2\theta}{\partial s^2}\right)^2 - 4\frac{\partial\theta}{\partial s}\frac{\partial^3\theta}{\partial s^3}\right] + F_1 r\left(\frac{\partial\theta}{\partial s}\right)^2$$

$$+ I\omega \left(\frac{\partial \omega_\theta}{\partial s} + \omega_r \frac{\partial \theta}{\partial s} \right) + w \cos\alpha \cos\theta + mr \left(\frac{\partial \theta}{\partial t} \right)^2 \tag{A.63}$$

Appendix B

Supplementary material to Chapter 3

In this Appendix, we first present the principle of minimum energy for a particular example of a clamped-clamped variable-length elastica constrained by symmetrically located walls with clearance $c = 0.05$ (see Chapter 3 for its complete bifurcation diagram). We then derive the analytical solution of a clamped-clamped elastica of constant length (classical problem) constrained by symmetrically located walls. The complete bifurcation diagram for this particular problem is also computed by applying the geometry-based method, as proposed in Chapter 3.

B.1 Principle of minimum energy

The constrained buckling problem cannot be solved by applying the calculus of variations in the traditional manner. The reason behind that is the presence of the unilateral constraints, which affect the space of allowed variations. Hence, a second-order analysis cannot be easily performed. Even if the contact conditions are assumed to be known (i.e., closed contacts), the variation of the associated contact points should be included for a second-order analysis. Their inclusion is particularly crucial for the investigation of the bifurcation points, where a smooth or a nonsmooth evolution of the contact patterns is present under further loading. These issues are explained in detail in (Ro et al., 2010; Chen et al., 2015; Manning and Bulman, 2005).

As an alternative, we apply the principle of minimum energy, which is typically used to identify the most likely equilibrium state (see (Alfutov, 2000; Doraiswamy et al., 2012)). Even though this criterion does not address the stability problem rigorously, it can be used to deduce about the most favorable, or optimal equilibrium configuration among other candidates for particular loading conditions. An optimal solution is also called stable in the current study.

To illustrate this optimality criterion, we revisit the constrained buckling problem of a clamped-clamped elastica of variable length for a clearance $c = 0.05$ (see Chapter 3). Taking into account that there is no dissipation (i.e., system is conservative), the external work is given by

$$\mathcal{W} = \int_0^{\bar{\delta}} \mathcal{Q} d\bar{\delta} \tag{B.1}$$

is identical to the bending energy $\mathcal{U}$ (Antman, 2005). Hence, the principle of minimum energy can be applied by utilizing either the external work, or the bending energy. Here, the bending energy is computed in terms of two distinct bifurcations parameters, the applied load $\mathcal{Q}$ for force-controlled conditions or the change of the inserted length of the elastica $\bar{\delta}$ for displacement-controlled conditions. The corresponding diagrams $\mathcal{U}(\mathcal{Q})$, $\mathcal{U}(\bar{\delta})$ are shown in Figs. B.1 and B.2, respectively. Based on them, for a fixed value of a bifurcation parameter, an equilibrium state of the elastica is then called optimal if its energy is minimum when compared to other candidates.

Consider first displacement-controlled conditions. By increasing the inserted length of the elastica, a sequence of equilibrium configurations is obtained, indicated with black line in Fig. B.1. The corresponding contact patterns can be found in Fig. B.1. Special attention is placed on the bifurcation point $3'$, where the bending moment vanishes at the discrete contact and at the end-points of the elastica for symmetrical reasons. Beyond this point, the bending moments at the extremities of the elastica could possibly evolve in a symmetrical or anti-symmetrical manner, leading to the shapes $3-6$ and $3-4$, respectively. As shown in Fig. B.1, for a fixed $\bar{\delta}$, the energy of the asymmetric configuration $3-4$ is lower than the energy of the symmetrical shape $3-6$. In addition the initiation of a continuous contact is not feasible for the same reason. Hence, the asymmetric configuration $3-4$ is the optimal solution. The same conclusion has been deduced by (Ro et al., 2010).

For force-controlled conditions (see Fig. B.2), the main difference when compared to the displacement-controlled loading condition is that all softening branches are unstable here. In particular, at points $1'$ and $3'$, there is no smooth evolution of the contact patterns. Instead, there is a jump to the closest possible in terms of energy equilibrium configuration of the same applied load $\mathcal{Q}/\pi^2$. For instance, at $1'$, there is a jump to a point of the branch $2'-3'$ with the same applied load $\mathcal{Q}/\pi^2 = 4$.

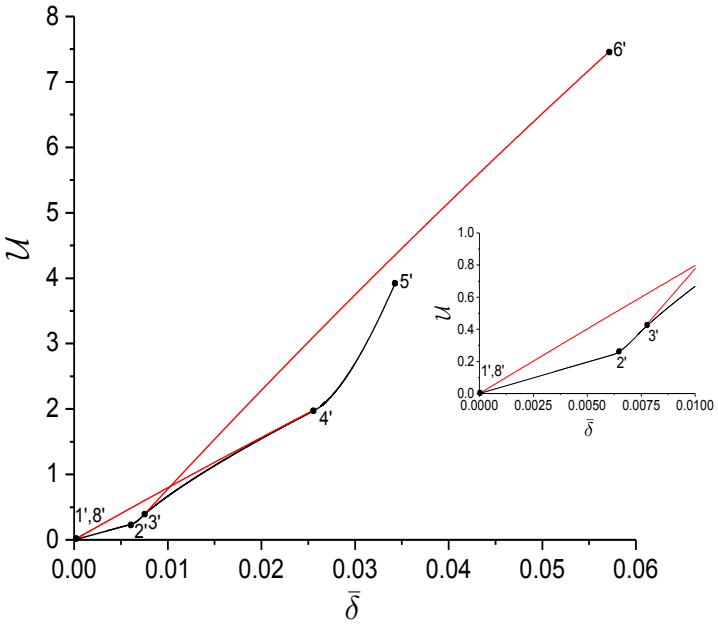

Figure B.1: Bending energy $\mathcal{U}$ with respect to $\bar{\delta}$

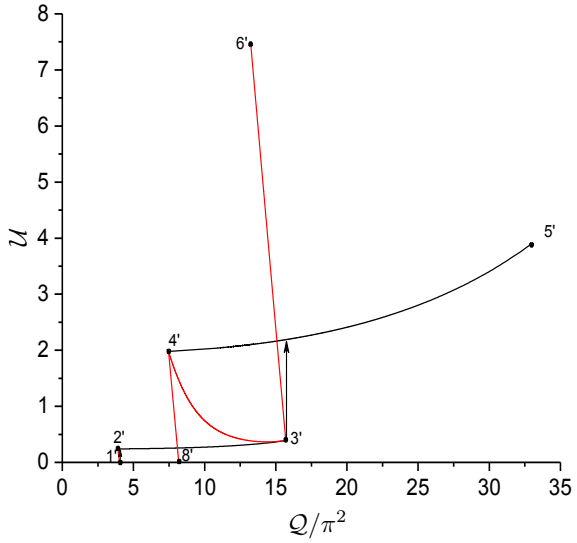

Figure B.2: Bending energy $\mathcal{U}$ with respect to $\mathcal{Q}$

B.2 Analytical solution of constrained clamped-clamped elastica

The analytical solution of the post-buckling behavior of the clamped-clamped elastica constrained by two symmetrically located walls at $y = \pm c$ is presented. The derivation is restricted to the symmetrical configurations of the elastica (odd buckling modes). Because of symmetry the elastica is divided by $1/4k$ segments where k is an odd number of buckling mode and thus the solution of the first segment is only illustrated below.

The anti-symmetrical configurations (even buckling modes) are not analyzed because they are similar to the clamped-pinned elastica which can be found in (Domokos et al., 1997).

B.2.1 Unconstrained case

The equilibrium equation of the unconstrained clamped-clamped elastica can be written as

$$\frac{\theta'^2}{2} - \mathcal{R}\cos\theta = -\mathcal{R}\cos\theta_{1/4k} \tag{B.2}$$

with boundary conditions $\theta(0) = \theta'(1/4k) = 0$, $\mathcal{R}$ is the compressive load with inclination angle $\alpha = 0$ and $k = 2\varrho - 1$ is the number of buckling mode with $\varrho \in \{1, 2, ...\}$.

Multiplying (B.2) by $\mathrm{d}\theta$ and integrating from $s = 0$ to $s = 1/4k$, the horizontal load $\mathcal{R}$ becomes

$$\sqrt{\mathcal{R}} = 4kK(\bar{k}) \tag{B.3}$$

where $\bar{k} = \sin\left(\theta_{1/4k}/2\right)$ is the modulus of elliptic integrals.

Accordingly the cartesian component $\bar{x}(1)$ at the right end of the elastica for the k buckling mode is given by

$$\frac{\bar{x}(1)}{4k} = \frac{1}{\sqrt{\mathcal{R}}}\left[2E(\bar{k}) - K(\bar{k})\right] \tag{B.4}$$

Combining (B.3) and (B.4) the horizontal component becomes $\bar{x}(1) = 2E(\bar{k})/K(\bar{k}) - 1$.

The above expressions are applicable until the elastica touches one of the horizontal walls. When a contact occurs in the absence of a contact force, the vertical component at $s = 1/4k$ becomes

$$\bar{y}(\frac{1}{4k}) = \int_0^{\frac{1}{4k}} \sin\theta d\zeta = \frac{c}{2} \tag{B.5}$$

Combining (B.3) and (B.5) a relation between the compressive load and the clearance can be derived $\sqrt{\mathcal{R}} = 4\sin\left(\theta^{(n)}_{1/4k}/2\right)/c$.

B.2.2 Point contact

Past the first contact event, a contact force appears which implies that $\alpha \neq 0$. The positions of the contact points on the elastica remain unchanged and the vertical component at the right end of the first segment is given by (B.5). In this situation, the governing equation of the elastica becomes

$$\frac{\psi'^2}{2} - \mathcal{R}\cos\psi = -\mathcal{R}\cos\psi_{1/4k} \tag{B.6}$$

with boundary conditions $\psi(0) = -\alpha$, $\psi'(1/4k) = 0$ and $\psi(1/4k) = \theta_{1/4k} - \alpha$.

Starting from (B.6) and applying the boundary conditions, the following expression is obtained

$$F\left(\pi/2;\bar{k}\right) + F\left(\phi_o;\bar{k}\right) = \frac{1}{4k}\sqrt{\mathcal{R}} \tag{B.7}$$

where $\bar{k} = \sin\left(\psi_{1/4k}/2\right)$ and $\phi_o = \arcsin\left[\sin\left(\alpha/2\right)/\sin\left(\psi_{1/4k}/2\right)\right]$.

For the k buckling mode the horizontal component $\bar{x}(1)$ and the clearance c can be expressed in terms of ψ, α as follows

$$\frac{\bar{x}(1)}{4k} = \int_0^{1/4k} \cos(\psi+\alpha)d\xi, \quad \frac{c}{2} = \int_0^{1/4k} \sin(\psi+\alpha)d\xi \tag{B.8}$$

where

$$\int_0^{1/4k} \cos\psi \mathrm{d}s = \frac{1}{\sqrt{\mathcal{R}}}\left\{2\left[E(\bar{k}) + E(\phi_o,\bar{k})\right] - \left[K(\bar{k}) + F(\phi_o,\bar{k})\right]\right\} \tag{B.9}$$

$$\int_0^{1/4k} \sin\psi \mathrm{d}s = \frac{2\bar{k}}{\sqrt{\tilde{\mathcal{R}}}}\cos\phi_o \tag{B.10}$$

B.2.3 Onset of continuous contact

For the special case where $\mathcal{R}$ passes through the contact point, a line contact (second contact event) initiates, and a geometrical expression is obtained $\tan\alpha = \tan\psi_{1/4k} = 2kc/\bar{x}(1)$, leading to $\sqrt{\mathcal{R}} = 8kK(\bar{k})$.

Further analysis other than the onset of the continuous contact is not required since past this point the elastica loses stability.

B.3 Geometry-based analysis of the constrained clamped-clamped Elastica

We consider next the case of a constrained elastica clamped at both ends. There are two important differences between this case and the pinned-pinned elastica analyzed above. First, there exist two distinct roots for the first buckling mode of a clamped-clamped elastica, with the smaller root corresponding to a stable symmetric configuration and the larger root to an

unstable anti-symmetric configuration. Second, the first symmetric buckling mode configuration with continuous contact is unstable, while it was stable for a pinned-pinned elastica. We analyze separately the symmetric, anti-symmetric, and asymmetric configurations.

B.3.1 First Buckling Mode (Symmetric Case)

Unconstrained Buckling

Referring to Figure B.3, the unconstrained elastica is divided into four identical segments for the first symmetric buckling mode. More generally, there are $m = 4k$ with $n_p = 2k$ for the symmetric k-buckling mode, with the inclination $\theta_1(s)$ and the horizontal force $\mathcal{R}_1$ of the first segment given by

$$\theta_1(s) = \theta_{[2]} \left\{ \cos\left[2k\pi\left(s - s_{[2]}\right)\right] + \frac{\theta_{[2]}^2}{192}\left(\cos\left[2k\pi\left(s - s_{[2]}\right)\right] - \cos\left[6k\pi\left(s - s_{[2]}\right)\right]\right) \right\}$$

$$\mathcal{R}_1 = 4(k\pi)^2 \left[1 + \frac{\theta_{[2]}^2}{8}\right] \tag{B.11}$$

and $\theta_{[2]}$ viewed here as the loading parameter. Using symmetry considerations, the solution is trivially extended to the other segments.

Constrained Buckling with Discrete Contact

This first contact event is characterized by contact force $F_{[j]} = 0$, $j \in \mathcal{I}_w$ and $\Delta y_i = c/2$, $i \in \mathcal{I}_\ell$ for each segment. Past this first contact event, increasing $\theta_{[2]}$ leads to the build-up of contact force $F_{[j]} > 0$, $j \in \mathcal{I}_w$ at the discrete contacts and the progressive decrease of the moment at the location of the contacts. The derivation is similar to the pinned-pinned case presented in Section 3.4.4 and is thus omitted.

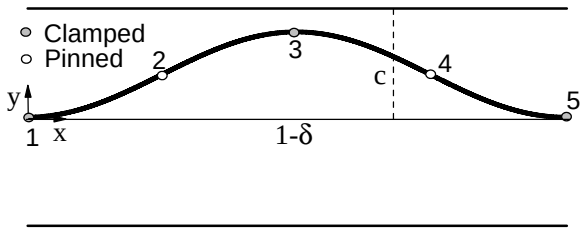

Figure B.3: Symmetrical first buckling mode of clamped-clamped elastica

Secondary Buckling

With increasing $\theta_{[2]}$, the moment at the discrete contact eventually vanishes. In contrast to the pinned-pinned elastica, this condition does not mark the onset of continuous contact as this configuration of the elastica become unstable ($n_p^{(l)} = 2m_e^{(l)}$). In addition the same holds for the secondary buckling described below, for which $n_p^{(d)} = m_e^{(d)} + 2$. Due to vanishing moments of both ends, the secondary buckling corresponds to a change in the sign of the moment at the clamped ends, as reflected in the deformed configuration shown in Fig. B.4.

To construct the solution for the secondary buckling with one discrete contact, only one half of the elastica needs to be considered. As shown in Fig. B.4, there are two distinct clamped-clamped segments with an inflection point at the midpoint of each segment. Two distinct canonical problems have thus to be solved, corresponding to segments 2 (bounded by nodes 2 and 3) and 3 (bounded by nodes 3 and 4), with a combined length $\ell_2 + \ell_3 = 1/4$. The segments have relative inclinations $\psi_2(s) = \theta_2(s) + \alpha_2$ and $\psi_3(s) = \theta_3(s) - \alpha_3$, respectively with $\alpha_2 \geq 0$, $\alpha_3 > 0$. As the resultant force $\boldsymbol{\mathcal{R}}_i$, $i \in \mathcal{I}_\ell$ is uniform, $\alpha_i = \alpha_{i+1}$, $i \in \mathcal{I}_\ell$. Due to continuity of the bending moment at node 3, $\beta_2 = -\beta_3$, and a relation between length ℓ_i and angle β_i is derived

$$\ell_i = \frac{1}{4\pi} \arccos \beta_i \tag{B.12}$$

Hence, $\mathcal{R}_i = 16\pi^2$, $i \in \mathcal{I}_\ell$.

The contact constraints for the segments are $\Delta y_1 = \Delta y_2 = -\gamma c/2$ and $\Delta y_3 = \Delta y_4 = c\,(1+\gamma)\,/2$ with $0 \leq \gamma < 1$. Number γ increases with end-displacement δ, starting at 0 at the onset of secondary buckling up to 1 when the elastica contacts the opposite wall at two symmetric points. With three discrete contacts, the segmentation remains the same. However the relative inclination for the second segment is modified according to $\psi_2(s) = \theta_2(s) - \alpha_2$ and the transverse components of the force transmitted by the segments are related by

$$\mathcal{R}_2 \sin \alpha_2 = \mathcal{R}_3 \sin \alpha_3 + F_{[3]} \tag{B.13}$$

This means that the inclination angles $\alpha_2 \neq \alpha_3$ are different. Using the continuity of the bending moment at node 3 and the uniformity of horizontal horizontal force, the complete solution can be easily derived.

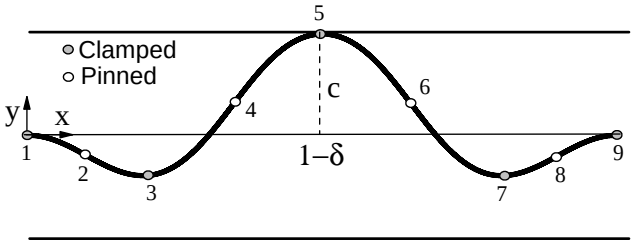

Figure B.4: Secondary buckling of clamped-clamped elastica.

B.3.2 First Buckling Mode (Anti-symmetric Case)

The anti-symmetric case of the second root differs remarkably from the symmetric one. It is a double clamped-pinned case, which requires some special consideration. An asymmetrical deformation shape similar to the anti-symmetric case is also discussed.

Unconstrained Buckling

The second root of the first buckling mode of a clamped-clamped elastica corresponds to the anti-symmetric configuration (see Fig. B.5). Hence, only one-half of the elastica has to be solved. Using the segmentation technique, one half of the elastica is divided into three distinct segments, with segments 1 (bounded by nodes 1 and 2) and 2 (bounded by nodes 2 and 3) being identical; the combined lengths $2\ell_2 + \ell_3 = 0.5$. Considering that the node 4 lies along the centerline, the sum of the vertical offsets of the segments satisfy

$$\sum_{i=1}^{3} \Delta y_i = 0 \tag{B.14}$$

In the absence of contact, the force in the elastica is uniform. The solution can be obtained by applying continuity of the bending moment at node 3.

Constrained Buckling with Discrete Contact

The contact event occurs when the contact force $F_{[3]} = 0$ and $\Delta y_3 = c$. The deflection of the segments is then constrained by $2\Delta y_1 = 2\Delta y_2 = \Delta y_3 = c$ and the segment lengths by $2\ell_2 + \ell_3 = 0.5$. Further increase of δ leads to $F_{[3]} > 0$ and thus to a jump in the transverse component of the force transmitted by segments 2 and 3.

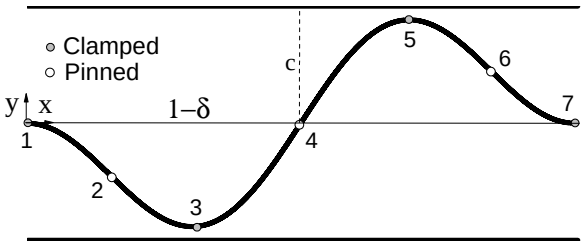

Figure B.5: Asymmetrical first buckling mode of clamped-clamped elastica

Asymmetrical configuration (displacement controlled)

For a displacement-controlled loading, an asymmetrical configuration of the elastica is observed beyond the point of vanishing moment at the discrete contact 3, as shown in Figure B.6. It is similar to the second root of first buckling mode but in an asymmetrical manner and with a single discrete contact. With increasing δ an abrupt decrease of the horizontal force R_o occurs. The position of the discrete contact varies (i.e., $s_{[3]} \leq 0.5$), while the vertical displacement of the two last segments (i.e., $\Delta y_5 + \Delta y_6$) increases until a second discrete contact develops at node 5 .

To derive the solution for the asymmetrical configuration, the elastica should be divided into three clamped-clamped segments with an inflection point at the midpoint of each segment. Three canonical problems should be solved, e.g., segments 2 (bounded by nodes 2 and 3), 4 (bounded by nodes 4 and 5) and 5 (bounded by nodes 5 and 6) with combined length $\ell_2+\ell_4+\ell_5 = 1/2$. The segments have relative inclinations $\psi_2(s) = \theta_2(s)-\alpha_2$, $\psi_4(s) = \theta_4(s)-\alpha_4$ and $\psi_5(s) = \theta_5(s)+\alpha_5$, respectively, assuming positive inclinations. The horizontal applied force $R_i \cos\alpha_i$, $i \in \mathcal{I}_\ell$ is uniform. In addition, $\mathcal{R}_4 = \mathcal{R}_5$ and thus $\alpha_4 = \alpha_5$. Due to continuity of the bending moment at node 5, $\beta_4 = -\beta_5$ and a relation between lengths ℓ_4, ℓ_5 and their resultant force is obtained

$$\ell_4 + \ell_5 = \frac{\pi}{\mathcal{R}_4^2} \tag{B.15}$$

Continuity of bending moment at the discrete contact at node 3 has also to be satisfied. The contact constraints for the segments are $\Delta y_1 = \Delta y_2 = -c/2$, $\Delta y_3 = \Delta y_4 = c\,(1+\gamma)\,/2$ and $\Delta y_5 = \Delta y_6 = \gamma c/2$ with $0 \leq \gamma < 1$. For $\gamma = 1$, the deformation configuration is characterized by two discrete contacts and the elastica should be divided differently, as explained in Section B.3.2.

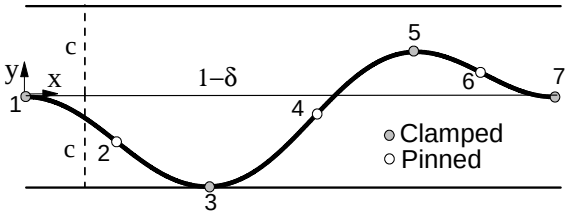

Figure B.6: Asymmetrical configuration of clamped-clamped elastica

B.3.3 Numerical Results

The calculated post-buckling response of a constrained clamped-clamped elastica for clearance $c = 0.05$ is in full agreement with the numerical results of Manning and Bulman (2005). The corresponding bifurcation diagram is shown in Fig.B.7.

The behavior for the first symmetric buckling mode shares some similarities with the pinned-pinned case. Due to symmetry the elastica comes in contact with the wall at the midpoint position at Point 2 ($\theta_{[2]} = 0.16$,$\delta = 0.0062$, $\mathcal{Q}/\pi^2 = 4$). This contact position remains unchanged until Point 3 ($\theta_{[2]} = 0.2$,$\delta = 0.0075$, $\mathcal{Q}/\pi^2 = 15.9$) for both force-controlled and displacement–controlled conditions. The Point 3 corresponds to the vanishing of the moment at the discrete contact. Nevertheless it does not continue to a line contact, as confirmed by the conjectured rule $n_p^{(l)} = 2m_e^{(l)}$ (see Chapter 3). In addition the simultaneous change of the moments of both ends is not feasible (Branch 3-7), noting also that $n_p^{(d)} = m_e^{(d)} + 2$.

For displacement controlled, beyond Point 3 the sign of the moment at the right end changes, leading to an asymmetrical configuration with one discrete contact point (i.e., $n_p^{(d)} = m_e^{(d)} + 1$). Along Branch 3-5, the horizontal load decreases with increasing δ (i.e., softening branch). This branch is present until a second discrete contact occurs at Point 5 ($\theta_{[2]} = 0.255$, $\delta = 0.026$, $\mathcal{Q}/\pi^2 = 8.3$), where the configuration becomes anti-symmetric with two discrete contacts. For force-controlled conditions the softening Branch 3-5 is not possible. Instead the elastica jumps to a point ($\theta_{[2]} = 0.266$, $\delta = 0.0285$, $\mathcal{Q}/\pi^2 = 16$) of Branch 5-6.

The second root of the first buckling mode, corresponding to an anti-symmetric configuration of the elastica is also shown in Figure B.7 (Branch 4-5). The unconstrained case is unstable ($n_p^{(u)} > 2$) . However, when the elastica comes in contact with the wall at Point 5 ($\theta_{[2]} = 0.40$,$\delta = 0.026$, $\mathcal{Q}/\pi^2 = 8.3$), the configuration becomes stable (i.e., Branch 5-6), noting that $n_p^{(d)} = m_e^{(d)}$.

Upon unloading, the response follows Branch 5-6 until one of the contact points vanishes. It unloads further according to its unconstrained first mode.

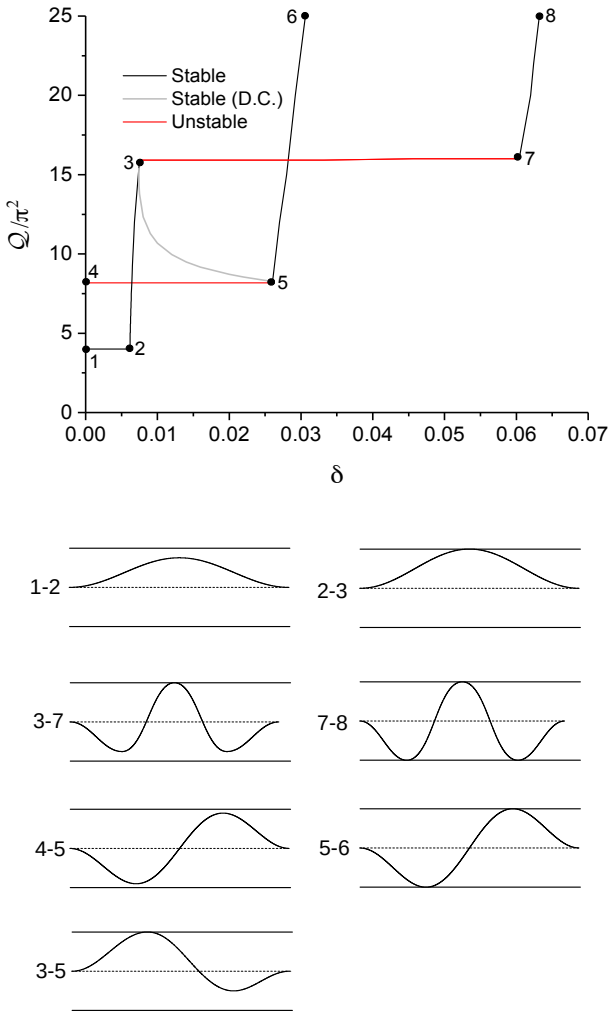

Figure B.7: Bifurcation diagram for a constrained clamped-clamped elastica with clearance $c = 0.05$

B.4 Clamped-pinned elastica

The post-buckling response of a constrained clamped-pinned elastica has also been computed. Results for clearance $c = 0.053$, chosen to enable comparison with the numerical and experimental results of Domokos et al. (1997) are shown in the bifurcation diagram of Fig. B.8. The numerical results are not shown since they coincide with the current study.

The elastica is stable for the first buckling mode. The elastica comes in contact with the

wall at Point 2 ($\theta_{[1]} = 0.215$,$\delta = 0.00735$, $\mathcal{Q}/\pi^2 = 2.05$) and the second configuration is is stable ($n_p^{(d)} = m_e^{(d)}$). The first two configurations are actually similar to those corresponding to the second root of the first buckling mode of a clamped-clamped elastica, except that the length of the clamped-pinned segment is here the total length of the elastica.

At Point 3 ($\theta_{[1]} = 0.32$,$\delta = 0.0098$, $\mathcal{Q}/\pi^2 = 8.8$), where the moment at the discrete contact vanishes, the configuration switches smoothly from 3 to 4 for a displacement-controlled loading. The switch is associated with a change in the sign of the moment at the clamped support changes. Along this branch the axial load decreases (i.e., softening) and the right segment approaches the lower wall. When it reaches Point 4 ($\theta_{[1]} = 0.387$,$\delta = 0.0293$, $\mathcal{Q}/\pi^2 = 6.7$), a discrete contact with the opposite wall appears, corresponding to configuration 4-5. For a force-controlled loading, Branch 3-4 is unstable (i.e., $n_p^{(d)} = m_e^{(d)} + 1$) and the elastica jumps from Point 3 to a point ($\theta_{[1]} = 0.4$,$\delta = 0.03$, $\mathcal{Q}/\pi^2 = 8.8$) of Branch 4-5. This response is in agreement with experimental results (Domokos et al., 1997).

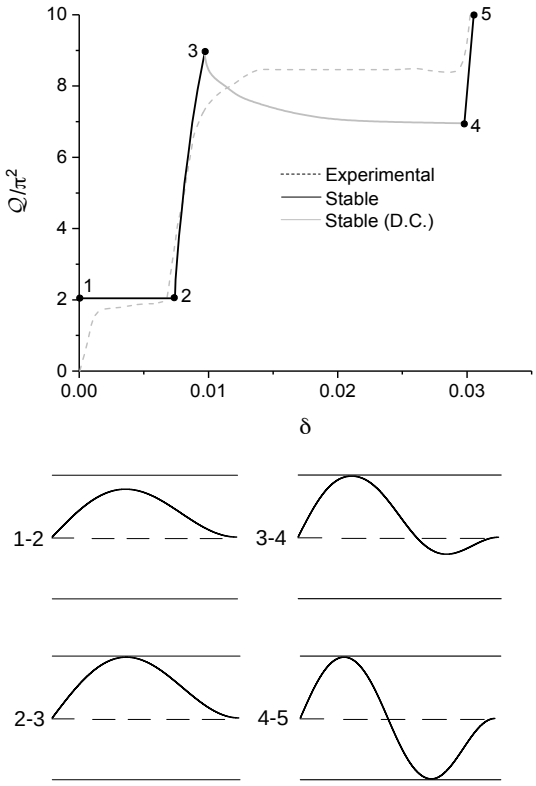

Figure B.8: Bifurcation diagram for a constrained clamped-pinned elastica with clearance $c = 0.053$